Unlocking the Higgs Potential: from Colliders to the Cosmos

vorgelegt von

Kateryna Radchenko Serdula

Hamburg, 2025

Gutachter/innen der Dissertation:	Prof. Dr. Georg Weiglein
	Prof. Dr. Géraldine Servant
Zusammensetzung der Prüfungskommission:	Prof. Dr. Georg Weiglein
	Prof. Dr. Géraldine Servant
	Dr. Thomas Konstandin
	Prof. Dr. Christian Schwanenberger
	Prof. Dr. Michael Potthoff
Vorsitzender der Prüfungskommission:	Prof. Dr. Michael Potthoff
Datum der Disputation:	04.07.2025
Vorsitzender Fach-Promotionsausschusses PHYSIK:	Prof. Dr. Wolfgang J. Parak
Leiter des Fachbereichs PHYSIK:	Prof. Dr. Markus Drescher
Dekan der Fakultät MIN:	Prof. Dr.-Ing. Norbert Ritter

Abstract

The upcoming decades in particle physics will offer an unprecedented amount of data, opening new avenues to deepen our understanding of the fundamental laws of nature. On one hand, the High-Luminosity Large Hadron Collider (HL-LHC) will significantly enhance our experimental reach at the energy frontier. On the other hand, the Laser Interferometer Space Antenna (LISA) will inaugurate the era of the early Universe gravitational wave astronomy. The data they will collect may shed light on some of the most profound open questions in physics. At the centre of many unresolved questions in the Standard Model (SM), which include the origin of electroweak symmetry breaking, the matter-antimatter asymmetry, and the nature of dark matter, lies the scalar potential. In particular, the trilinear Higgs self-coupling offers a unique window to determine the shape of this potential. While collider experiments probe it as realised today, cosmological observations can provide insights into its evolution in the early Universe. Together, they offer complementary perspectives on one of the most fundamental ingredients of particle physics.

This thesis investigates the phenomenological implications of deviations in the Higgs trilinear self-coupling within well-motivated Beyond the Standard Model (BSM) scenarios featuring extended scalar sectors, with a particular focus on the Two Higgs Doublet Model (2HDM). We perform a detailed study of Higgs pair production at the HL-LHC, the process most directly sensitive to trilinear scalar couplings, examining the effects of additional scalar states both through direct resonant production channels and through radiative corrections to the trilinear Higgs coupling. Our results show that interference effects between resonant and non-resonant contributions, affected by loop-induced modifications to scalar self-interactions, can significantly alter both the total production cross section and the invariant mass distribution, while remaining consistent with all current experimental and theoretical constraints. To account for these effects, we develop and apply dedicated computational frameworks that enable precision BSM analyses incorporating these significant loop effects.

Turning to the early Universe, we examine the thermal evolution predicted by BSM scenarios and identify conditions required for a strong first-order electroweak phase transition, which is a necessary ingredient for electroweak baryogenesis. We analyse the characteristic mass hierarchies that favour such transitions and identify the most important collider signatures capable of probing the relevant parameter space. At the same time, we explore the complementary reach of cosmological observables, focusing on stochastic gravitational wave (GW) backgrounds that may be sourced by such strong transitions. We find that space-based GW astronomy could become a complementary tool for exploring fundamental questions of particle physics.

Zusammenfassung

Die nächsten Jahrzehnte in der Teilchenphysik versprechen eine beispiellose Menge an Daten, die es ermöglicht, unser Verständnis der fundamentalen Naturgesetze deutlich zu vertiefen. Einerseits wird der High-Luminosity Large Hadron Collider (HL-LHC) unsere experimentellen Möglichkeiten im Hochenergiebereich erheblich erweitern. Andererseits wird die Laser Interferometer Space Antenna (LISA) das Zeitalter der Gravitationswellen-Astronomie des frühen Universums einläuten. Die auf diese Weise gesammelten Daten könnten Licht auf einige der tiefgreifendsten offenen Fragen der Physik werfen. Im Zentrum vieler offener Fragen im Standardmodell (SM)- darunter der Ursprung der elektroschwachen Symmetriebrechung, die Materie- Antimaterie-Asymmetrie sowie die Natur der Dunklen Materie - steht das skalare Potential. Insbesondere die trilineare Higgs-Selbstkopplung bietet einen einzigartigen Zugang zur Form dieses Potentials. Während Kolliderexperimente die heute realisierte Form des Potentials untersuchen, können kosmologische Beobachtungen Einblicke in dessen Entwicklung im frühen Universum geben. Gemeinsam bieten sie komplementäre Perspektiven auf eine der grundlegendsten Größen der Teilchenphysik.

Diese Dissertation untersucht die phänomenologischen Implikationen von Abweichungen in der trilinearen Higgs-Kopplung in theoretisch fundierten Szenarien des Standardmodells (BSM) mit erweiterten skalaren Sektoren, mit besonderem Fokus auf das Zwei-Higgs-Doublett-Modell (2HDM). Wir führen eine detaillierte Studie zur Produktion von Higgs-Paaren am HL-LHC durch, da dieser Prozess besonders sensi- tiv auf die trilineare skalare Kopplung ist, und untersuchen die Auswirkungen zusätzlicher skalarer Zustände sowohl durch direkte resonante Produktionskanäle als auch durch radiative Korrekturen zur trilinearen Higgs-Kopplung. Unsere Ergebnisse zeigen, dass Interferenzeffekte zwischen resonanten und nicht-resonanten Beiträgen, beeinflusst durch schleifeninduzierte Modifikationen der skalaren Selbstwechselwirkungen, sowohl den gesamten Produktionswirkungsquerschnitt als auch die invariante Massenverteilung signifikant verändern können, während sie dennoch mit allen derzeitigen experimentellen und theoretischen Einschränkungen vereinbar bleiben. Um diesen Effekten Rechnung zu tragen, entwickeln und verwenden wir spezielle Analysecodes, die eine präzise BSM-Analyse unter Berücksichtigung dieser signifikanten Schleifen-Effekte ermöglichen.

Im Hinblick auf das frühe Universum untersuchen wir die von BSM-Scenarios vorhergesagte thermische Entwicklung und identifizieren Bedingungen, die für einen starken elektroschwachen Phasenübergang erster Ordnung erforderlich sind, eine notwendige Voraussetzung für die elektroschwache Baryogenese. Wir analysieren charakteristische Massenhierarchien, die solche Übergänge ermöglichen, und identifizieren charakteristische Kollider-Signaturen, mit denen sich der relevante Parameterraum untersuchen lässt. Gleichzeitig erforschen wir die komplementäre Sensitivität kosmologischer Beobachtungen, insbesondere stochastischer Gravitationswellenhintergründe (GW), die durch einen solchen starken Phasenübergang erzeugt werden könnten. Wir stellen fest, dass weltraumbasierte Gravitationswellenastronomie zu einem komplementären Werkzeug werden könnte, um die fundamentalen Fragen der Teilchenphysik zu untersuchen.

List of Publications

This thesis is based on the following scientific articles:

Journal articles:

[1] F. Arco, S. Heinemeyer, M. Mühlleitner, and K. Radchenko, *Sensitivity to triple Higgs couplings via di-Higgs production in the 2HDM at the (HL-) LHC*, Eur. Phys. J. C 83 (2023) 1019 [2212.11242]

[2] T. Biekötter, S. Heinemeyer, J.M. No, K. Radchenko, M.O. Olea Romacho and G. Weiglein, *First shot of the smoking gun: probing the electroweak phase transition in the 2HDM with novel searches for $A \to ZH$ in $\ell^+\ell^- t\bar{t}$ and $\nu\nu b\bar{b}$ final states*, JHEP 01 (2024) 107 [2309.17431]

[3] S. Heinemeyer, M. Mühlleitner, K. Radchenko, and G. Weiglein, *Higgs Pair Production in the 2HDM: Impact of Loop Corrections to the Trilinear Higgs Couplings and Interference Effects on Experimental Limits*, Eur. Phys. J. C. 85 (2025) 437 [2403.14776]

Preprints / in preparation:

[4] H. Bahl, J. Braathen, M. Gabelmann, K. Radchenko and G. Weiglein, `anyH3` *and* `anyHH`*: precise predictions for trilinear Higgs couplings and double Higgs production in extended scalar sectors*

[5] H. Bahl, T. Biekötter, S. Heinemeyer, K. Radchenko and G. Weiglein, `HiggsTools` *for LHC Run-3 and Beyond*

[6] M. Frank, S. Heinemeyer, M. Mühlleitner, and K. Radchenko, *Experimental determination of BSM Triple Higgs Couplings at the HL-LHC with Neural Networks* [2506.18981]

Declaration on oath

I hereby declare and affirm that this doctoral dissertation is my own work and that I have not used any aids and sources other than those indicated.

If electronic resources based on generative artificial intelligence (gAI) were used in the course of writing this dissertation, I confirm that my own work was the main and value-adding contribution and that complete documentation of all resources used is available in accordance with good scientific practice. I am responsible for any erroneous or distorted content, incorrect references, violations of data protection and copyright law or plagiarism that may have been generated by the gAI.

15-05-2025
_____
Date

_____
Signature of doctoral candidate

Acknowledgements

First and foremost, I would like to express my deepest gratitude to my supervisors, Georg Weiglein and Sven Heinemeyer, for their invaluable guidance throughout my PhD. I am especially thankful to Sven for his mentorship during my bachelor's and master's thesis projects. I thank him for his constant support and persistent encouragement, and in particular for suggesting that I pursue a PhD in Hamburg. This has been a life-changing experience and will remain a core memory for me. I also want to thank Sven for inviting me to HiggsDays. I am profoundly grateful to Georg for the trust he placed in me when he accepted me as a student, for his support, and for the countless opportunities he has provided over the years. I particularly appreciate his ability to relieve pressure during challenging moments. To both of them, I owe being introduced to the passion for particle physics, and I am grateful to have learned so much under their guidance.

I want to sincerely thank Maggie Mühlleitner for her insightful contributions to our discussions, her kindness, and her encouragement. I am also grateful for her thoughtfulness in always considering me, for inviting me to the conference she organized in Karlsruhe, and for the trust she placed in me when she invited me to give a plenary talk at the LHCHWG. I truly appreciate her availability and support during my PhD and postdoc applications.

I would also like to thank Géraldine Servant for kindly agreeing to be my co-supervisor and for reviewing my thesis. I extend my gratitude to Michael Potthoff for chairing my defense committee, and to its members, Thomas Konstandin, my mentor, and Christian Schwanenberger, for their valuable involvement in this process.

I thank my friends and collaborators for their brilliant input to our projects and all I learned from them: Fran Arco, Thomas Biekötter, Olalla Olea, Jose Miguel No, Markus Frank, Henning Bahl, Johannes Braathen and Martin Gabelmann. They have each contributed to making me a better scientist, and their replies always came quickly. I especially want to mention Olalla and Thomas for their warm welcome when I arrived at DESY. I am particularly grateful to Johannes for his continuous feedback on my postdoc applications and many of my talks, as well as for always taking the time to answer my questions, even when it meant staying late at the office instead of heading home. I also want to thank Martin for his patience, kindness, and for always being available for discussions.

I want to thank Gudi Moortgat-Pick for organizing the working group meetings and always bringing the cookies. I also sincerely thank Venus Keus for inviting me to CATCH 2022+2 and for inspiring me to approach science more mindfully.

To my friends at DESY and beyond, whom I met during my PhD, thank you for making this period of my life so much brighter: Andrii, Romal, Panos, Julia, Guilherme, Mohamed, Jonas, Monika, Marten, Alain, Max, Mathias, Sara, Lisa, Julian, Jacopo, Felix, Pedro, and many others. I thank them for always showing their support and enthusiasm for making

room for both fun and hard work. I want to thank Julia, Andrii, and Panos for never turning down a coffee break. I want to thank Panos in particular for always helping me as though my problems were his own. I especially appreciate his help in reviewing my postdoc applications and parts of this thesis. I also want to thank Monika for her feedback on some sections of the thesis.

I am deeply grateful to my family for always remaining by my side while I explored my own path. In particular, I want to thank those I cannot see often for their love and encouragement. Above all, I thank my parents for giving me the tools to navigate this life, their unconditional love, and their constant efforts to be there for me. Any strengths I have and anything I have done right is because of them. Anything I have failed at is despite their best efforts. I want to thank my sister, Polina, for being my confidante and my first call in both joy and challenge. Being able to rely on her throughout my life has been a true pillar of my success. Finally, my heartfelt gratitude goes to my life partner, Fran, for his love, presence, and support. I am deeply grateful for the sacrifices and efforts he made to stay close and be part of my life. His perspective, morals, and advice are always present in my decisions. The achievement this thesis represents is therefore as much his as it is mine.

Contents

Chapter 1

Introduction

> We've basically got it all worked out, except for small stuff, big stuff, hot stuff, cold stuff, fast stuff, heavy stuff, dark stuff, turbulence, and the concept of time.
>
> — *Zach Weinersmith*

The development of the physical theories that anchor human knowledge is fundamentally driven by curiosity. This deep desire to understand nature is supported by principles intrinsic to our species, such as critical thinking, abstraction, and creativity. Throughout our exploration of the natural world, we have come to recognise that mathematics is, in fact, nature's language of choice, one that not only describes physical reality but often anticipates it [7]. In the historical course of physical sciences, mathematical frameworks constructed to interpret natural phenomena have revealed truths about the universe before experimental confirmation, thereby advancing our understanding of the fundamental laws governing nature.

One of the most successful physical theories developed so far is Quantum Field Theory (QFT), which is the result of contributions from some of the most brilliant minds in human history. Over decades, if not centuries[1], they have assembled the pieces of the unified picture we possess today. Born out of the need to reconcile the principles of quantum mechanics with those of special relativity, it postulates that particles are excitations of underlying quantum fields that pervade spacetime [8–10]. While quantum mechanics, established in the 1920s, successfully described the behaviour of particles at atomic scales, it was intrinsically non-relativistic and could not accommodate key relativistic phenomena such as particle creation and annihilation.

The first steps toward QFT were taken by Paul Dirac, who formulated a relativistic equation for the electron [11]. This not only predicted the existence of antimatter, subsequently confirmed with the discovery of the positron [12], but also laid the groundwork for field quantisation. When applied to the electromagnetic field, it led to the formulation of Quantum Electrodynamics (QED), the first complete quantum field theory. However, early calculations in QED revealed infinite results of some basic physical quantities, casting

---

[1]While the origins of quantum mechanics date to the early 20th century, the idea of an atomic description of nature can be traced back to ancient civilisations.

doubt on the theory's consistency. It was not until the 1940s and 1950s that these issues were resolved through the development of renormalisation theory by Feynman [13,14], Schwinger [15–18], Tomonaga [19], and Dyson [20]. These techniques allowed for the absorption of infinities into redefined physical parameters, rendering QED a predictive and experimentally well-tested theory.

The success of QED inspired efforts to describe other fundamental forces using similar principles. In 1954, Yang and Mills introduced non-Abelian gauge theories [21], generalising the idea of local symmetries and setting the stage for modern descriptions of the weak and strong interactions. A major challenge was the incorporation of particle masses within gauge-invariant frameworks, a problem ultimately resolved in the 1960s through the Brout-Englert-Higgs (BEH) mechanism [22,23] and the theory of spontaneous symmetry breaking (SSB). A byproduct of the Higgs mechanism was a fundamental scalar particle called the Higgs boson [23], the quantum excitation of the Higgs field, which interacts with other fundamental particles to give them mass.

These theoretical breakthroughs culminated in the formulation of the Standard Model (SM) of particle physics, a renormalisable gauge theory based on the symmetry group $SU(3)_C \times SU(2)_L \times U(1)_Y$, which successfully incorporates the strong, weak and electromagnetic interactions [24–26] . The discovery of a Higgs boson in 2012 at the LHC [27,28] was a historic milestone that provided the experimental evidence of the BEH mechanism. We provide a brief introduction to the ingredients and principles behind the SM in Sec. 2.1.

One such foundational principle of the SM is symmetry, which lies at the heart of modern physics, shaping our understanding of fundamental interactions.[2] Symmetry is often paired with the principle of simplicity, commonly referred to as Occam's Razor: a heuristic guiding principle in both philosophy and natural sciences [29]. The SM exemplifies this philosophy by offering a minimal and elegant framework. However, its economy of content, guided by symmetry principles and validated by experimental success, is shaped by historical development and does not arise from a deeper, intrinsic necessity, but rather from an *ad hoc* construction.

This is exemplified by the shape of its scalar potential, the part responsible for electroweak symmetry breaking (EWSB). Despite its simplicity, the shape of this potential remains unexplained in any deeper sense, lacking a compelling fundamental origin of the EWSB. We provide a comprehensive introduction to the SM scalar potential in Sec. 2.2. More fundamentally, despite its tremendous success, the SM leaves many deep questions unanswered: What is the nature of dark matter and dark energy? Why are neutrinos massive? Why is our universe composed of matter rather than antimatter? Why does the electroweak (EW) scale reside so far below the Planck scale? These questions and many others, discussed in more detail in Sec. 2.4, suggest that the SM is, at best, an effective low-energy theory of a more complete framework.

Perhaps the most significant flaw of the SM is that it does not incorporate the gravitational interaction within its framework. Our most successful description of gravity is General Relativity (GR), which captures the dynamics of space and time with unmatched

---

[2]On a philosophical note, one could argue that symmetry might be a bias inherent in our current understanding, potentially blurring the true nature of reality. Nonetheless, in light of its historical successes, our approach is to emphasise its strengths while maintaining the critical perspective essential to scientific progress.

elegance. Yet, it remains fundamentally incompatible with a QFT description, eluding the unification that has gathered theoretical efforts for nearly a century.

From these limitations of the SM, the need for Beyond the SM (BSM) physics arises clearly. The uniqueness of the Higgs field and the relation of its potential to several aspects of the theory, such as the origin of the EWSB and the fate of the vacuum, place the Higgs sector in a central role of many BSM theories. One compelling and testable class of models involves extending the particle content of the SM with extra scalars [30], often referred to as Higgses for simplicity. These include singlet, doublet, or higher multiplet scalar fields added to the theory, often motivated by the solutions they provide to the aforementioned shortcomings of the SM. A richer scalar sector can lead to modified electroweak dynamics, offer dark matter candidates [31–36], enable electroweak baryogenesis [37–40], and alter the vacuum structure of the theory [41]. We discuss extended scalar sectors in Sec. 2.5.

One example of such scenarios is the minimal extension of the SM by one additional complex doublet, named Two Higgs Doublet Model (2HDM) [30,42–44], which we introduce in Sec. 2.7. We will refer to it frequently throughout this work, as a simple, yet phenomenologically rich, theoretical framework for BSM phenomena. One of them is the viability of a strong first order electroweak phase transition (SFOEWPT) [45–47] that emerges due to the presence of additional scalar degrees of freedom. Such a transition is a necessary condition for explaining the baryon asymmetry of the Universe through electroweak baryogenesis [48] (EWBG).

To explore such new physics and ultimately to deepen our understanding of nature and to find the answers to the open questions, we must explore complementary experimental avenues. On one hand, we need the high-energy precision laboratories, such as particle accelerators, where experiments can be performed in controlled environments. On the other hand, we have the natural cosmic laboratory, offering a plethora of phenomena that we aim to observe and understand.

Looking at the starred sky is, in essence, looking back in time. Light from distant galaxies has travelled millions of years to reach our detectors, carrying information from the evolution of the Universe. The oldest light we can observe is the cosmic microwave background (CMB), which was emitted approximately 380,000 years after the Big Bang, when photons decoupled from the primordial plasma. This is as far as we can *see*. We do know however what happened before that, in particular we can trace back the history of the Universe up to three minutes after the Big Bang, when Big Bang Nucleosynthesis (BBN) occurred and gave rise to the light elements. The remarkable agreement between BBN predictions and observed abundances is a major success of the ΛCDM model [49,50], our current standard cosmological paradigm, that we introduce in Sec. 2.3.

Anything that happened before BBN, and in particular the EWSB, remains a mystery. Despite the discovery of a scalar particle with the properties of a Higgs boson and therefore of the confirmation of the Higgs mechanism, the details of the SSB are yet unsettled. The shape of the Higgs potential today could provide insights into the cosmological history of the Universe and the pattern of symmetry breaking. This places the investigation focus heavily on the shape of the scalar potential, which is mostly unknown. As of today, only the location of the global minimum at the vacuum expectation value of the electroweak field, and the curvature around it given by the mass of the discovered Higgs boson are known. The shape of the potential can be constrained further by precision high energy

collider experiments, in particular by measurements of the trilinear Higgs self-interactions. We provide a description of this type of interactions in Sec. 2.6

However, we are now beginning to peer even further back, beyond the reach of electromagnetic radiation. The next exciting frontier for cosmological observations lies in non-photonic messengers, such as gravitational waves (GWs). GWs were first detected by the LIGO collaboration in 2015 [51], opening a new observational window to the distant past that could provide information about such early times as inflation or even the Big Bang itself. More recently, in 2023, the first hints of a stochastic gravitational wave background have been detected in pulsar timing array observations by the NANOGrav collaboration [52]. These signals, in the nano-Hertz regime, could be the cosmic analogue of the CMB: a gravitational wave background sourced by phenomena such as phase transitions, cosmic strings, or inflation.

Today we are entering an exciting era for fundamental physics. At the energy frontier, the High-Luminosity Large Hadron Collider (HL-LHC) is expected to deliver unprecedented amounts of data [53, 54], enabling precision tests of the SM and opening new opportunities to discover physics beyond it. Simultaneously, on the cosmological frontier, the Laser Interferometer Space Antenna (LISA) [55] will be the first space-based GW observatory. Its launch will trigger a new era of precision cosmology and GW astronomy.

This thesis lies at the intersection of these two frontiers: collider phenomenology and early-universe cosmology. At the core of our investigation is the scalar potential, due to its possible connections to proposed solutions for the open problems of the SM. Specifically, this thesis focuses on the study of trilinear Higgs self-interactions, which are beginning to come within reach of current collider experiments. We carry out a thorough investigation of the phenomenological implications of deviations in these couplings with respect to the SM, caused by the presence of additional BSM scalar states. Particular attention is given to BSM extensions capable of supporting a SFOEWPT, an essential ingredient for electroweak baryogenesis and thus an attractive feature for addressing the matter–antimatter asymmetry of the Universe. Additionally, we investigate the observable imprints of such a phase transition in both collider experiments and cosmological observables such as GWs.

Guided by the ultimate goal of understanding the shape and nature of the scalar potential, we study the process most sensitive to the Higgs self-coupling at hadron colliders: double Higgs production via gluon fusion. This process provides a unique window into the Higgs potential and its interactions with additional scalar states. The central question is:

Q1: *What are the phenomenological signatures of extra scalar particles in Higgs pair production at the HL-LHC?*

To answer this, we perform a detailed analysis of how new physics affects the couplings involved in this process, with a focus on the radiative corrections to the trilinear couplings. We examine whether these effects alter the expected phenomenological signatures at hadron colliders and how future experiments can probe such deviations. In particular, we study the potential of the HL-phase of the LHC to constrain or measure both the SM-like trilinear Higgs coupling and the scalar self-couplings involving BSM particles.

We then turn to the practical application of future experimental data on di-Higgs production. Specifically, we address the question:

Q2: *How can we use experimental data from the HL-LHC in theoretical developments?*

The answer unfolds along two lines: in Sec. 4.1, we focus on how experimental di-Higgs data can be used to constrain the BSM parameter space of general models with extended scalar sectors; in Sec. 4.2, we explore the possibility of extracting BSM trilinear couplings from HL-LHC data using modern machine learning techniques.

On the cosmology side, we examine the relation between modifications to the Higgs self-coupling and the conditions required for a SFOEWPT. First, we study the possible thermal histories predicted by BSM theories and the role of these modifications in the early Universe in Sec. 5.1. Then, we scrutinise the possible observational probes of a SFOEWPT. Collider probes are discussed in Sec. 5.2, including direct searches for BSM particles and deviations in trilinear scalar couplings. Cosmological probes are explored in Sec. 5.3, focusing on gravitational waves. The complementarity between these collider and cosmological probes provides unique insights into the conditions for a SFOEWPT. This leads to our third guiding question:

Q3: *If a strong first order electroweak phase transition occurred, what observable consequences could we detect today?*

Following the general considerations outlined in this introduction, this thesis is structured in four main chapters. In Chapter 2, we provide an overview of the theoretical background and introduce key concepts relevant to the subsequent analysis. Chapter 3 focuses on Higgs pair production and addresses question **Q1**. We begin with a general study of parameter variations in Sec. 3.1, followed by a detailed analysis within the 2HDM in Sec. 3.2, including experimental challenges in Sec. 3.3. We analyse the impact of radiative corrections and interference effects on the cross section predictions in Sec. 3.4 and confront them with experimental data in Sec. 3.5. We then generalise the inclusion of loop corrections to arbitrary BSM theories in Sec. 3.6. Chapter 4 bridges theory and experiment, addressing question **Q2**. Chapter 5 provides a detailed investigation of probes for a strong first order electroweak phase transition, addressing question **Q3**, with a focus on both collider and cosmological observables.

Chapter 2

Particle Physics: Current Knowledge and Open Questions

Contents

2.1 Brief introduction to the Standard Model

The **Standard Model** of particle physics is the state-of-the-art theory that describes $\sim$ 15% of the matter in the Universe and 3 out of the 4 known fundamental interactions in a unified mathematical framework.[1] This framework is **Quantum Field Theory**, which combines the principles of quantum mechanics and special relativity. In this description the fundamental components of nature are fields that are defined at every point in spacetime. Particles are quantum excitations (or ripples) of fundamental fields.

The 15% percent of matter described by the SM is what we call ordinary matter, which is divided into two main categories: fermions, which are the main building blocks of matter,

---

[1]This section is based on [8, 56, 57] and personal notes from Elementary Particle Physics and Quantum Field Theory at Universidad Autonoma de Madrid (UAM), as well as master courses of BSM phenomenology and Spontaneously Broken Gauge Theories at the University of Hamburg.

and bosons, which act as force carriers. This distinction arises from the quantum nature of the particles, which in the quantum mechanical formalism can be described as wavefunctions. For two particles to be identical, the exchange symmetry of their wavefunction must be either symmetric $(+)$ or antisymmetric $(-)$ under particle exchange:

$$\Psi(x_1, x_2) = \pm\Psi(x_2, x_1). \tag{2.1}$$

The former case corresponds to bosons, and the latter to fermions. One can immediately see that if two fermions occupy the same quantum state, their wavefunction must vanish, making it physically impossible. This observation directly leads to the Pauli exclusion principle, which explains that electrons arrange in atomic orbitals, shaping the structure of the periodic table and leading to the rich chemistry of the elements. The difference between fermions and bosons also impacts their statistical behaviour: while multiple bosons can occupy the same state and thus they follow Bose-Einstein statistics, fermions have to follow Fermi-Dirac statistics because of the Pauli exclusion principle. The spin–statistics theorem proves that particles that follow BE statistics can be described with integer spins, while particles that follow FD statistics are characterised by half-integer spins. An intuitive way to understand this is through rotation symmetry: fermions require a 4π rotation to return to their original state, while bosons return to their original state after only a 2π rotation. This behaviour is precisely described by the spin quantum number, an intrinsic property of each elementary particle.

As of today, we know about the existence of three families (or generations) of fermions, each with the same quantum numbers but different masses. Each family contains an up-type quark (u, c, t), a down-type quark (d, s, b), a charged lepton (e, μ, τ) and a neutrino $(\nu_e, \nu_\mu, \nu_\tau)$, these types are usually called flavours.

The remaining 85% of the known matter is "dark", because it can only be inferred so far through its gravitational effects on visible matter, such as galaxy rotation curves and gravitational lensing. If it were to interact in any other way, this would have to be very weakly in order to accommodate the limits from the current experimental bounds.

The forces described in the SM are the electromagnetic, the strong and the weak force. Gravity is described by the theory of **General Relativity**, which however cannot be consistently unified in the quantum description, and therefore is not part of the SM. Each of the forces described in the SM, is mediated by a corresponding force carrier, a spin-one boson. In particular, the photon is the force carrier of electromagnetism, the $W^\pm$ and Z bosons mediate the weak force, and the eight gluons mediate the strong force.

A special role is played by the detected **Higgs boson**, the only scalar (spin-zero) particle discovered so far. It provides consistency to the SM through the **Brout-Englert-Higgs mechanism** [22,23]. The Higgs boson is an excitation of the Higgs field, which has a non-zero **vacuum expectation value** (vev), meaning that the vacuum state of the field is not zero, contrary to the rest of the fields in the SM. This non-zero vev enables the generation of mass for the weak gauge bosons via their gauge interactions, and for fermions through Yukawa couplings to the Higgs field. The magnitude of the mass of a given fundamental particle is thus proportional to the strength of its coupling to the Higgs field.

The mathematical description of the SM unifies the principles of special relativity and quantum mechanics. The basic idea is that particles, the elementary constituents of the matter in the Universe, are excitations of their respective fields. A cornerstone of the description of the fundamental interactions in terms of relativistic quantum field theories is

Noether's Theorem [58], which links symmetries of the physical system (a mathematical description) to conserved laws (a physical outcome). Noether's theorem establishes that invariance under time translations leads to energy conservation, spatial translations lead to the conservation of linear momentum, rotational symmetry leads to the conservation of angular momentum, and a phase shift symmetry leads to the conservation of charge. A symmetry can be global or local, in the first case it is applied uniformly across all points in spacetime. For example if we describe a particle as a wavefunction ψ (for instance of the electron), our physical system is automatically symmetric under phase shifts

$$\psi \rightarrow e^{i\alpha}\psi, \tag{2.2}$$

where α is an arbitrary constant. In mathematical terminology, this is a global $U(1)$ symmetry, which leads to charge conservation in quantum electrodynamics via Noether's theorem. The fact that this is a global symmetry implies that the associated electromagnetic force should be a background effect that exists uniformly everywhere in the Universe. This contradicts the observations: electromagnetism must have a dynamical field (the photon) that propagates and only interacts where sources (charges) exist. This can be described mathematically by promoting the $U(1)$ to a local symmetry (also called **gauge symmetry**), which depends on each particular spacetime coordinate,

$$\psi(x) \rightarrow e^{i\alpha(x)}\psi(x). \tag{2.3}$$

In this case the local $U(1)$ symmetry introduces the electromagnetic field, which ensures charge conservation dynamically. A local symmetry requires the introduction of a force carrier, in the case of the electromagnetism it is the photon field, A_μ. This requirement comes from the fact that the derivative of the field $\partial_\mu\psi(x)$ is no longer invariant under $U(1)$ transformations. To ensure that the kinetic terms in the Lagrangian, which depend on the derivatives of the fields, stays invariant and the theory is consistent, a covariant derivative is introduced

$$D_\mu = \partial_\mu + ieA_\mu(x). \tag{2.4}$$

where e is the electric charge. With this definition, the derivative of the field transforms in the same way under the same symmetry group as the field itself, and the equations of motion can be consistently derived.

Identifying the symmetries of a system therefore becomes the first step to simplify a mathematical description of a physical system. Based on observations, we could determine the conserved quantities around us, and this leads to the establishment of the symmetries that exist in our Universe. These symmetries will in turn restrict the terms that are allowed in the Lagrangian description of the theory, as all the terms will have to obey them. This reduces the number of free parameters of the theory by constraining the type of interactions. Finally, they have a predictive power, such as historically the prediction of $W^\pm$ and Z gauge bosons was obtained from the symmetry group of the electroweak interactions.

The SM is built to respect the symmetries of spacetime, namely translational and rotational invariance as well as invariance under boosts, the latter two encompass the so called Lorentz group of transformations in special relativity and the three of them form the Poincaré group. This implies 10 conserved quantities, namely, energy, spatial momentum,

angular momentum and Lorentz boosts. Furthermore, it is a gauge theory based on three
local symmetries:

SU(3)$_\mathbf{C}$: Describes **strong interactions** for particles that have a colour charge: quarks
and gluons. The subindex $_\mathbf{C}$ stands for colour, the conserved charge of the strong
interactions.

SU(2)$_\mathbf{L}$: Describes the **weak interactions** between the $W^\pm$ and Z gauge bosons and left-
handed leptons, which is responsible for radioactive decay processes. The right-handed
leptons do not participate in those interactions, therefore the subindex $_\mathbf{L}$ stands for
left. This makes the weak interactions of the SM chiral, as discovered by Chien-Shiung
Wuin 1956 in the groundbreaking experiment involving the β decay of the Cobalt-60
isotope [59]. Only particles with a half-integer spin (i.e. fermions) can be chiral, as
this property refers to the alignment of their spin and momenta: if these two vector
quantities point in the same direction, the fermion is right-handed, while if they point
in opposite directions, it is said to be left-handed. Mathematically, we arrange the
particles charged under $SU(2)_L$ in doublets, like for example the first fermion family:

$$L_L = \begin{pmatrix} \nu_e \\ e^- \end{pmatrix}, Q_L = \begin{pmatrix} u_L \\ d_L \end{pmatrix}, \tag{2.5}$$

while singlets like the right-handed quarks u_R, d_R and leptons e_R do not transform
under this symmetry group. The associated conserved quantity is the weak isospin,
usually denoted as T_3.

U(1)$_\mathbf{Y}$: Describes the **weak hypercharge** interactions. It is one of the two gauge sym-
metries that mix to form the electroweak interaction. After SSB, $U(1)_Y$ and $SU(2)_L$
combine to produce the photon, γ, associated with $U(1)_{\text{EM}}$, and the weak bosons,
$W^\pm$ and Z. The subindex $_\mathbf{Y}$ stands for the corresponding conserved quantity, the
weak hypercharge.

The usual electric charge arises after the SSB of the electroweak SM gauge symmetry
groups, which will be described in detail in the next section (Sec. 2.2). For the moment, it is
sufficient to note that the conventional electromagnetic charge is related to the hypercharge
and the weak isospin via the Gell-Mann-Nishijima [60] relation

$$Q = T_3 + \frac{Y}{2}. \tag{2.6}$$

These symmetry groups are called Lie groups, and they have an associated Lie algebra
that mathematically describes the infinitesimal transformations of the fields under their
respective symmetry group. The algebras can be Abelian, meaning that the elements of
the group commute with each other, or non-Abelian, meaning that the elements do not
commute. In an Abelian gauge theory, self-interactions between the gauge bosons are not
possible, as in electromagnetism, where the photon does not interact with itself. Conversely,
non-Abelian groups like $SU(2)_L$ for the weak interaction, or $SU(3)_C$ for colour interactions
have non-commuting elements, which means that the force carriers can interact with them-
selves. Non-Abelian gauge theories are described by the Yang-Mills framework [61], which

generalises electromagnetism to include self-interacting gauge fields. These gauge fields correspond to the generators of the Lie algebra in the fundamental representation, $A_\mu = A_\mu^a T^a$, and the generators satisfy the commutation relations

$$[T^a, T^b] = i f^{abc} T^c, \tag{2.7}$$

with f^{abc} being the antisymmetric structure constants of the Lie algebra corresponding to the generators.

The global symmetries of the SM also play an important role in physics, despite not leading to the manifestation of fundamental interactions. There are some fundamental discrete symmetries, for example C stands for change conjugation, P for parity and T for time reversal. C conservation means that particles and antiparticles behave in the same way, P conservation means the system is invariant under spatial reflections. Both are violated by the weak interactions. T is the time reversal symmetry. Only the combination of the three of them, CPT, is an exact symmetry in any QFT, as it ensures locality and causality. Other symmetries that can arise in the Lagrangian will be discussed throughout this thesis.

The fundamental role of symmetry in the mathematical description of a physical system has motivated extensive efforts to unify all fundamental interactions under a single symmetry group. One example are **Grand Unified Theories** (GUT) that aim to unify the strong and electroweak forces within a larger symmetry group such as $SU(5)$ or $SO(10)$. Another possibility is **Supersymmetry** (SUSY), the most general extension of the Poincaré group (the super-Poincaré group) that leads to a unique, consistent QFT [62]. SUSY introduces an R symmetry that relates bosons and fermions: each bosonic degree of freedom has a fermionic partner and vice-versa. Broader theoretical frameworks like supergravity and string theory also commonly predict SUSY. While theoretically very compelling, these theories remain unconfirmed experimentally, making them a lively area of research and a significant fraction of experimental searches.

But in order to first understand the SM, we need to start from its **Lagrangian**, which can be constructed from the particle content - dictating the kinetic terms - and the interactions allowed between them, which we have described above. Its classical part can be separated in the following terms

$$\mathcal{L}_{\text{SM}} = \mathcal{L}_{\text{gauge}} + \mathcal{L}_f + \mathcal{L}_h. \tag{2.8}$$

$\mathcal{L}_{\text{gauge}}$: The **gauge** part describes the kinetic terms and the self-interactions between gauge bosons, as discussed above. These terms depend on the electroweak symmetry group but not on the matter content

$$\mathcal{L}_{\text{YM}} = -\frac{1}{4} G_{\mu\nu}^a G^{a\,\mu\nu} - \frac{1}{4} W_{\mu\nu}^i W^{i\,\mu\nu} - \frac{1}{4} B_{\mu\nu} B^{\mu\nu}, \tag{2.9}$$

where the field strength tensors are

$$\begin{aligned}
B_{\mu\nu} &= \partial_\mu B_\nu - \partial_\nu B_\mu, \\
W_{\mu\nu}^i &= \partial_\mu W_\nu^i - \partial_\nu W_\mu^i + g_2 \epsilon^{ijk} W_\mu^i W_\nu^k, \\
G_{\mu\nu}^a &= \partial_\mu G_\nu^a - \partial_\nu G_\mu^a + g_s f^{abc} G_b^i G_c^k,
\end{aligned} \tag{2.10}$$

for the $U(1)_Y, SU(2)_L$ and $SU(3)_C$, respectively. The ϵ^{ijk} and the f^{abc} are the anti-symmetric structure constants of the Lie algebra of $SU(2)_L$ and $SU(3)_C$ respectively, that give rise to the self-interaction terms among the weak gauge bosons and the gluons, while g_2 and g_s are the weak and the strong coupling constants, respectively.

$\mathcal{L}_f$: The **fermionic part** depends on the matter content and includes the kinetic terms for the fermions and their interactions with the gauge bosons via covariant derivatives

$$\mathcal{L}_f = \sum_f \bar{f} i \slashed{D} f, \qquad (2.11)$$

where f stand for the fermionic fields and $\bar{f}$ indicates antifermionic field, the slash means that the vector quantities are contracted with gamma matrices $\slashed{k} := \gamma_\mu k^\mu$. We note that, according to the gauge groups of the SM, the covariant derivative acting on the fermion fields in the above equation is defined in analogy to Eq. (2.4) as

$$D_\mu = \partial_\mu - ig_1 \frac{Y}{2} B_\mu - ig_2 W_\mu^i \tau^i - ig_s G_\mu^a t^a, \qquad (2.12)$$

where Y is the generator of the $U(1)_Y$ group and g_1 its associated coupling constant. τ^i are the normalised Pauli matrices, $\tau^i = \sigma^i/2$, which are the generators of $SU(2)_L$ in the fundamental representation. t^a are the normalised generators of the $SU(3)_C$, expressed in terms of the Gell-Mann matrices λ^a, i.e. $t^a = \lambda^a/2$.

$\mathcal{L}_h$: Finally, the **Higgs part** can be described by the kinetic energy of the Higgs field, the scalar potential and the Yukawa interactions of the Higgs with the fermion matter,

$$\mathcal{L}_h = (D_\mu \Phi)^\dagger (D^\mu \Phi) + V(\Phi) + \mathcal{L}_{\text{Yukawa}}, \quad \text{where} \quad \Phi = \begin{pmatrix} \phi^+ \\ \phi^0 \end{pmatrix} \qquad (2.13)$$

is a complex doublet, often called Higgs doublet, under $SU(2)_L$ with hypercharge $Y = 1$.

The **Yukawa terms** in the Lagrangian are proportional to the vev, meaning they are zero before spontaneous symmetry breaking. After symmetry breaking, the vev becomes nonzero, causing these terms to appear in the Lagrangian and explicitly breaking the gauge invariance. More about this mechanism and how it influenced the choice of the scalar potential $V(\Phi)$ will be discussed in Sec. 2.2. The explicit expression of the Yukawa term is[2]

$$\mathcal{L}_{\text{Yukawa}} = -y_u \bar{Q}_L \tilde{\Phi} u_R - y_d \bar{Q}_L \Phi d_R - y_e \bar{L}_L \Phi e_R + \text{h.c.}, \qquad (2.14)$$

where $\tilde{\Phi} = i\sigma^2 \Phi^*$ is the conjugate Higgs doublet that has the opposite hypercharge, thereby allowing for the correct electric charge combinations in the up-type quark terms. The left-handed quark Q_L, and lepton L_L doublets are defined in Eq. (2.5), u_R, d_R and e_R represent the right-handed quark and lepton singlets respectively. y_u, y_d

---

[2] We use the notation u, d and l for all up-type quarks, down-type quarks and leptons in three fermionic generations respectively.

and y_e are the Yukawa couplings for up-type, down-type and electrons, respectively.[3] h.c. stands for hermitian conjugate, i.e. the complex conjugate transpose.

Though we do not describe the mechanism of the electroweak symmetry breaking in detail here, we note that after the Higgs field gets a vev, the gauge bosons of the electroweak symmetry group $SU(2)_L \times U(1)_Y$ mix to give rise to the known gauge bosons, namely

$$
\begin{aligned}
\text{the photon}: \quad & A_\mu = \cos\theta_W B_\mu + \sin\theta_W W_\mu^3, \\
\text{the } Z \text{ boson}: \quad & Z_\mu = -\sin\theta_W B_\mu + \cos\theta_W W_\mu^3, \\
\text{the } W^\pm \text{ bosons}: \quad & W_\mu^\pm = \frac{1}{\sqrt{2}}(W_\mu^1 \mp i W_\mu^2),
\end{aligned}
\tag{2.15}
$$

where θ_W is the weak mixing angle. Only the photon A_μ remains massless due to the unbroken $U(1)_{\text{EM}}$ symmetry.

Now that we have constructed the Lagrangian based on the symmetries and matter content of the SM, we can proceed to compute observable quantities like the **scattering amplitudes**. These describe the probabilities of particle collisions or decays and are the key predictions of the theory and measurements of the experiment. For this we will only briefly outline the methods developed in the QFT framework.

We will use the **path integral formalism**, that defines the amplitudes as a sum over all possible classical field configurations weighted by the exponential of the classical action S. The idea behind this formalism can be understood from the double split experiment. In that experiment, a particle seems to follow both possible paths through two slits in the wall simultaneously.[4] However, if there was no wall, the natural inference is that the particle in fact follows simultaneously *any possible path* connecting two points. Therefore, to compute the amplitude we need to sum (integrate) over all possible quantum histories, and the probability of a particle going from an initial state, $|i\rangle$, to a final state, $\langle f|$, is the squared magnitude of this amplitude.

In this weighted sum over paths, the action appears in the exponent as a phase factor because each path contributes a wavefunction with a phase proportional to its action. The total amplitude at a point arises from the sum of all these phases. For most paths, especially those far from the classical trajectory, the phases vary rapidly and interfere destructively, effectively cancelling out. However, near the path of least action, small deviations lead to only small changes in phase, allowing nearby paths to interfere constructively. This constructive interference around the classical path explains why we observe definite trajectories. For example, the visible path of a laser beam arises from the constructive interference of many possible photon paths clustered near the classical path: a manifestation of the principle of least action, a foundational concept in classical mechanics. This **action** can be extracted from the Lagrangian as

$$
\mathcal{S} = \int d^4 x \mathcal{L} + \sum_V J_V V_\mu + \sum_\phi J_\phi + \sum_\psi \left(J_\psi \psi - \bar{\psi} J_{\bar{\psi}} \right),
\tag{2.16}
$$

---

[3]Since neutrinos are massless in the SM, only the electron component of the lepton doublet has a Yukawa interaction with the Higgs.

[4]For a comprehensive explanation see e.g. Ref. [56]

where we added the sources $J(x)$ to capture the presence of external vector J_V, scalar J_ϕ and fermion J_ψ fields.

With this action we can compute the **generating functional** (or partition function), $Z[J]$, which sums over all possible quantum field configurations, in analogy to the canonical partition function in statistical mechanics, as

$$\mathcal{Z}\left[J_V, J_\phi, J_\psi\right] = \int \mathcal{D}V\mathcal{D}\phi\mathcal{D}\bar{\psi}\mathcal{D}\psi e^{i\mathcal{S}}, \qquad (2.17)$$

where $\mathcal{D}V$ encodes all possible configurations of the vector field V, and equivalently for the fermion and scalar fields. This integral is not computed exactly but rather expanded in a perturbative series of the exponential, which will eventually give rise to the **Feynman diagrams**, which are pictorial representations of the terms in this expansion. In these diagrams, the vertices correspond to interactions, internal lines to propagators and external lines (called legs) to the incoming and outgoing particles. The Feynman rules are extremely useful and lie at the basis of any calculations in QFT, as they can be derived directly from the Lagrangian and provide a convenient way to calculate the contributions to the scattering amplitude at different orders (also called loops) in the perturbative expansion.

It must be pointed out that the gauge symmetry implies that many field configurations are in fact physically equivalent. Therefore, to properly define the path integral, one has to fix a gauge, e.g. the photon field A_μ in the Lorentz gauge is defined as

$$\partial^\mu A_\mu = 0. \qquad (2.18)$$

The **gauge fixing** introduces a non trivial Jacobian in the path integral, accounted for by the Faddeev-Popov determinant. In gauge symmetries with redundant degrees of freedom, this determinant depends on the gauge fields and can be rewritten as a path integral over additional scalar anti-commuting fields called **ghosts**. The appearance of the ghosts is an artefact of the mathematical methods in the theory. They can only contribute in the internal loops of a process and ensure that the predicted quantities remain consistent and well behaved, as well as renormalisable, a concept we will introduce properly further below. Eventually, this procedure leads to the appearance of two additional terms in the Lagrangian, the gauge fixing and the Fadeev-Popov terms that we have not mentioned until now.

The definition of the generating functional will allow us to compute correlation functions (also called **Green functions**) for different sources. These correlation functions describe the propagation of quantum fields at n spacetime points and they are defined as

$$G_n\left(x_1, \ldots, x_n\right) = \langle 0|T\left\{\phi(x_1)\ldots\phi(x_n)\right\}|0\rangle = \left.\frac{\delta^n \mathcal{Z}[J]}{i^n \delta J(x_1)\ldots\delta J(x_n)}\right|_{J=0}$$
$$= \frac{1}{\mathcal{Z}[0,0,0]} \int \mathcal{D}V\mathcal{D}\phi\mathcal{D}\bar{\psi}\mathcal{D}\psi e^{iS}\phi\left(x_1\right)\ldots\phi\left(x_2\right), \qquad (2.19)$$

where $\langle 0|T\left\{\phi(x_1)\ldots\phi(x_n)\right\}|0\rangle$ is the vacuum expectation value of the time-ordered product of the field evaluated at n points in spacetime, "time-ordered" means

$$T\left\{\phi(x_1)\phi(x_2)\right\} = \begin{cases} \phi(x_1)\phi(x_2) & \text{if } t_1 > t_2, \\ \phi(x_2)\phi(x_1) & \text{if } t_2 > t_1, \end{cases} \qquad (2.20)$$

which enforces causality.

Now the **Lehmann-Symanzik-Zimmermann** (LSZ) formula allows us to relate the n-point Green functions (mathematical artefacts describing propagation of fields with encoded interactions and sources) to the scattering amplitudes (physical observables).

$$\langle i|S|f \rangle = (2\pi)^4 \delta^4 \left(p_i - p_f \right) G_n^{\text{trunc}} \left(p_1, \ldots p_n \right)\big|_{p_j^2 = m_j^2}, \tag{2.21}$$

where $G_n^{\text{trunc}} \left(p_1, \ldots p_n \right)$ is the truncated (i.e. only the interaction parts without the external legs) Green function in the momentum space (obtained by taking the Fourier transform), and S is the scattering amplitude or simply the S-matrix. It describes the probability of an initial state to transition to a final state, both of which are asymptotically free particles in the Hilbert space. It can be rewritten as

$$S = \mathbb{I} + iT, \tag{2.22}$$

where the first term represents the free, non-interacting term and T is the transition matrix that accounts for interactions between the states. The relation between the S-matrix and the scattering amplitude $\mathcal{M}$ is given by

$$\langle f|S|i \rangle = \delta_{fi} + i(2\pi)^4 \delta^{(4)}(p_f - p_i)\mathcal{M}_{fi}, \tag{2.23}$$

which means that the transition probability from the initial state i to a final state f is equal to the free term (i.e. the Kronecker delta δ_{ij}), plus the interaction strength encoded in $\mathcal{M}$, with the conservation of four-momenta of the initial p_i and final p_f states.

Finally, with the value of $\mathcal{M}$, the cross section of a scattering process can be computed simply as

$$\sigma = \int \frac{1}{F} \mathcal{M} d\Pi, \tag{2.24}$$

where F is a flux factor describing the incoming particles and $d\Pi$ is the phase space for the outgoing particles.

However, the order by order calculation in perturbative QFT involve loop diagrams that typically suffer from ultraviolet (high-momentum) divergences, giving rise to the crucial point of the **renormalisability** [8, 63]. The appearance of infinities in the formalism of QFTs was a bustling topic of research in the 20th century. QED was the first successful renormalisable theory, developed in the early 1940s by Julian Schwinger [15–18], Richard Feynman [13, 14], and others. To intuitively understand this concept, we can consider the classical electromagnetic mass of the electron:

$$m_e = \frac{e^2}{4\pi r_e}, \tag{2.25}$$

which describes a point-like particle with charge e and radius r_e. Despite being divergent at $r_e \to 0$, an experimental measurement of the electron mass never yields an infinite result, hinting at the need to reinterpret the mass parameter. In QED, this happens to all the free parameters of the theory, the electron mass, its charge and the field itself. Considering the electron charge, we say that it has a *bare* value, e_0, which is infinite, and the vacuum around it is constantly polarised due to higher order corrections (creation and annihilation of virtual particle-antiparticle pairs), which align their electromagnetic

charges and screen the bare charge. The experiments are only sensitive to the effective, or renormalised charge of the electron, which includes the charged cloud induced around the electron by the vacuum polarisation. Increasing the energy of a scattering experiment is equivalent to resolving smaller scales of the electron, which stripes the measured charge from these quantum corrections and we can measure an effective increase of the electric charge with energy, a phenomenon called the running of the coupling constants. The way physical parameters change with energy is paramerised by the **renormalisation group equation** (RGE). This is described by the beta functions:

$$\beta(g) = \frac{dg}{d\ln\mu}, \tag{2.26}$$

where g is the coupling constant and μ is the energy scale. The form of the beta function depends on the symmetries, field content, and interactions in the theory, and determines whether a coupling increases or decreases with energy. In the case of the strong interaction, the beta function is negative, causing the strong coupling to decrease with energy. This behaviour, known as asymptotic freedom, means that quarks and gluons are free of interaction at very small scales but become strongly interacting at larger scales, forcing them to come closer together and making it impossible for quarks and gluons to exist freely without hadrons, which leads to confinement. By contrast, the beta function the electroweak couplings is positive, meaning that these couplings become weaker at higher energies, which allows electrons and leptons to exist as free particles. Additionally, the massive nature of $W^\pm$ and Z makes the electroweak force a short ranged force and prevents them from being confined.

In practice, the procedure of renormalisation is a very specific algorithm that allows to cancel the infinities arising in the quantum corrections of the theory. Through observable processes masses and certain couplings are fixed, and with their input we are able to predict the numerical values of physical observables. The most important aspect of renormalisation is that the physical meaning of the free parameters is defined order by order. This algorithm consists of two steps:

Regularisation: introduces a temporary modification to the equations to make the expressions mathematically meaningful. Usual choices are (1) **cut-off regularisation**, which introduces a physical scale Λ as an upper bound of the momentum integrals and is particularly helpful to understand the order of the divergencies, and (2) **dimensional regularisation**, which extends the integrals to d dimensions and then takes the limit of $d \to 4 - 2\epsilon$. Since the spacetime is deformed, a renormalisation scale μ must be introduced to maintain the correct dimensional analysis, this is the energy scale that appears in the running of the coupling constants in Eq. (2.26).

Renormalisation: removes the infinities by introducing counterterms (CTs). These parameters in general depend on the renormalisation scale [5] and relate the bare couplings (denoted with a subindex 0) to the renormalised quantities (denoted by a subindex R):

$$g_0 = Z_g(\mu)g_R \simeq (1 + \delta Z_g(\mu))g_R,$$
$$\psi_0 = Z_\psi^{1/2}(\mu)\psi_R \simeq \left(1 + \frac{1}{2}\delta Z_\psi(\mu)\right)\psi_R, \tag{2.27}$$

---

[5]With the exception of the on-shell renormalisation scheme defined below.

where the second equalities are only valid to the first perturbative order. This re-definition allows to split the Lagrangian into two pieces, one with the renormalised couplings and fields, and one with the counterterms:

$$\mathcal{L}(\psi_0, g_0) = \mathcal{L}(\psi_R, g_R) + \mathcal{L}_{\mathrm{CT}}(\psi_R, g_R, \delta Z_\psi, \delta Z_g). \qquad (2.28)$$

The bare terms and the counterterms are infinite, but the cancellation of the infinities renders a finite renormalised parameter. There is not a unique way of cancelling the infinities, some common choices are: (1) **Minimal subtraction (MS)**, in which the CTs are defined in such a way as to only cancel the poles of the theory, keeping the finite pieces as they are. This makes the scheme mass-independent, meaning that the renormalisation procedure does not explicitly depend on particle masses. As a result, when comparing physical quantities defined at different energy scales, for example, a mass parameter defined in the infrared (IR) at scale m versus one defined in the ultraviolet (UV) at scale M, a matching procedure must be applied. This involves converting parameters from one renormalisation scheme or scale to another to consistently account for the physical mass thresholds and ensure accurate predictions across scales. And (2) **On-shell (OS)**, which enforces that renormalised mass is equal to the physical mass of the particle and that the propagator has a pole at this mass.

Overall, the SM is an overwhelmingly powerful and predictive theory. For instance the gluon was predicted by Harald Fritzsch, Murray Gell-Mann and Heinrich Leutwyler in the 1970s [64] and experimentally confirmed in 1979 at the PETRA collider at DESY [65] via the observation of three-jet events in e^+e^- collisions consistent with the predictions of gluon Bremsstrahlung. Similarly, the $W^\pm$ and Z bosons, the mediators of the weak force, were also postulated by Sheldon Glashow, Abdus Salam and Steven Weinberg in the seventies [24–26] and experimentally confirmed in $p\bar{p}$ collisions at CERN in 1973 [66], the Z boson appeared as an excess in the invariant mass of lepton pairs and the $W^\pm$ as an excess of leptons and missing energy (corresponding to the neutrinos). The fact that these gauge bosons were massive, contrary to the photons and the gluons, was puzzling, since a mass term in the Lagrangian would break gauge invariance. The solution to the puzzle was developed over the sixties and consisted in suggesting a spontaneous breaking of the gauge symmetry, which was early explored in the work of Guralnik, Hagen, and Kibble [67] and expanded by François Englert and Robert Brout [22] as well as independently by Peter Higgs [23], who suggested the existence of a scalar particle. This mechanism became known as the Brout-Englert-Higgs, or simply Higgs mechanism. More than half a century later, their prediction was confirmed by the discovery of a particle with the predicted properties in 2012 [27, 28]. Among the numerical predictions of the SM, the agreement of the electron magnetic moment with the prediction up to the 12th decimal is remarkable, which exemplifies the interplay between theory and experiment [68].

2.2 The scalar potential

The scalar potential[6] in the SM takes the form

$$V(\Phi) = -\mu^2 \Phi^\dagger \Phi + \lambda (\Phi^\dagger \Phi)^2, \tag{2.29}$$

where μ^2 and λ are real and positive parameters. This potential is chosen because of two reasons: it includes all the possible renormalisable and gauge invariant terms for an $SU(2)_L$ doublet, Φ, and it has the form that allows for the mechanism of **spontaneous symmetry breaking**.

SSB is a common phenomenon in physics and a necessary ingredient for the **BEH** mechanism [22, 23]. The SSB refers to a symmetry that is possessed by the interactions governing the dynamics of a physical system but not by the ground state of the system. A common example of this phenomenon are ferromagnetic materials. At high temperatures, a ferromagnetic material has an average zero magnetisation because the magnetic spins of individual atoms are randomly oriented and therefore the material is rotationally invariant. Below the Curie temperature, exchange interactions between the atoms overpower thermal fluctuations, causing neighbouring atomic spins to align parallel to each other. This induces a net magnetisation and spontaneously breaks the rotational symmetry of the ground state of the system. This behaviour can be interpreted in therms of the Ginzburg-Landau theory [70], which phenomenologically describes ferromagnetism as a phase transition. The magnetisation (the so called order parameter) of the material close to the Curie temperature can be parametrised by a free energy density with a potential energy of the form

$$V(\vec{M}) = \alpha_1 (T - T_C)(\vec{M}\vec{M}) + \alpha_2 (\vec{M}\vec{M})^2 \quad \text{and} \quad \alpha_{1,2} > 0. \tag{2.30}$$

By minimising the above potential w.r.t. the magnetisation we obtain the magnetisation condition of the ground state

$$\vec{M}\big(\alpha_1 (T - T_C) + 2\alpha_2 (\vec{M}\vec{M})\big) = 0. \tag{2.31}$$

It is clear that for $T > T_C$ the term in parenthesis is positive and the only solution is null net magnetisation $\vec{M} = 0$, leading to a symmetric potential with a minimum at $V(0) = 0$. For $T < T_C$, i.e. after SSB, $\vec{M} = 0$ becomes a local maximum, and the minimum is achieved at an infinite number of solutions with the same magnetisation,

$$|\vec{M}| = \sqrt{\frac{\alpha_1 (T_C - T)}{2\alpha_2}}. \tag{2.32}$$

This leads to a potential of the shape of a "mexican hat", and the system needs to chose between one of the rotationally non-invariant ground states above. In the case of the SM scalar potential, the minimisation condition leads to the infinite states of vacuum configurations for the field doublet Φ, that must satisfy

$$\Phi^\dagger \Phi = \frac{\mu^2}{2\lambda} := \frac{v^2}{2}, \tag{2.33}$$

---

[6]This section is based on Ref. [69].

where v is defined as the vacuum expectation value and is the ground energy state of the Universe today. It is extracted from the Fermi constant G_F, which is the effective weak interaction strength, as $v^2 = 1/\sqrt{2}G_F \sim (246 \text{ GeV})^2$. The value of G_F is measured experimentally via muon decay. The minimum of the potential is thus an arbitrary state that lies on a circle of radius v from $\Phi = 0$, analogously to the magnetisation potential. We show a sketch of the scalar potential shape in the SM before and after symmetry breaking in Fig. 2.1.
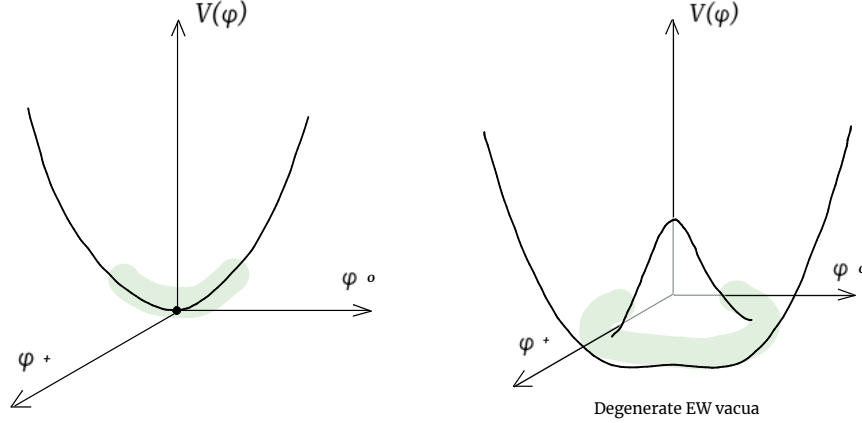

Figure 2.1

SM scalar potential before (left) and after (right) SSB. The potential is symmetric before SSB with a unique vacuum configuration at the origin of field space. After SSB there are multiple energetically favourable EW vacua, and the chosen ground state will break the symmetry of the system.

In the unitary gauge, the components of the field doublet Φ are non-zero only in the neutral component, so that the vacuum preserves the unbroken QED gauge symmetry group $U(1)_{\text{EM}}$,

$$\langle \Phi \rangle = \begin{pmatrix} 0 \\ \frac{v}{\sqrt{2}} \end{pmatrix}. \tag{2.34}$$

The similarities between Eq. (2.29) and Eq. (2.30) are manifest, as they describe the same phenomena in nature. The Ginzburg-Landau theory is thus a precursor for the BEH mechanism in QFTs. The latter requires however an additional ingredient, which is the **Goldstone theorem** [71–73]. The Goldstone theorem states that if the Lagrangian of a theory has a global symmetry that is not a symmetry of the vacuum, a massless scalar or pseudoscalar boson appears associated to each generator that does not annihilate the vacuum. These modes are called Goldstone bosons. In the case of the BEH mechanism, the $SU(2)_L \times U(1)_Y$ symmetry of the Lagrangian is not a global symmetry but rather a gauge symmetry. Therefore the would-be-Goldstone bosons are not physical particles but rather they mix with the massless gauge bosons to give rise to their longitudinal component,

which makes them massive vector particles. The number of vector bosons that aquire a mass through the BEH mechanism is equal to the number of would-be-Goldstone bosons.

Therefore, the Higgs mechanism breaks the symmetry group of the Lagrangian $SU(2)_L \times U(1)_Y$ down to $U(1)_{\rm EM}$. In this process the weak gauge bosons aqcuire a mass, while the photon remains massless as it corresponds to the gauge boson of the unbroken $U(1)_{\rm EM}$.

The Goldstone modes appear as excitations of the vacuum state along the tangent direction of the circle with equivalent vacuum states. Since this direction is flat, the Goldstone modes are massless. On the other hand, the excitations along the radial direction around the vev are massive because there is a curvature. The mass is given by the second derivative of the potential. This corresponds to the massive physical Higgs boson.

The SM is really the minimal configuration that allows for a successful SSB pattern. In theories **Beyond the Standard Model**, where there are multiple field dimensions and multiple scalar self-interactions, the scalar potential can have a richer structure. For a pictorial representation see Fig. 2.2, where deeper minima can coexist with the EW vacuum v. In Sec. 2.4 we will list some of the shortcomings of the SM that point to the need for such BSM physics that could be probed via modifications of the SM scalar potential.
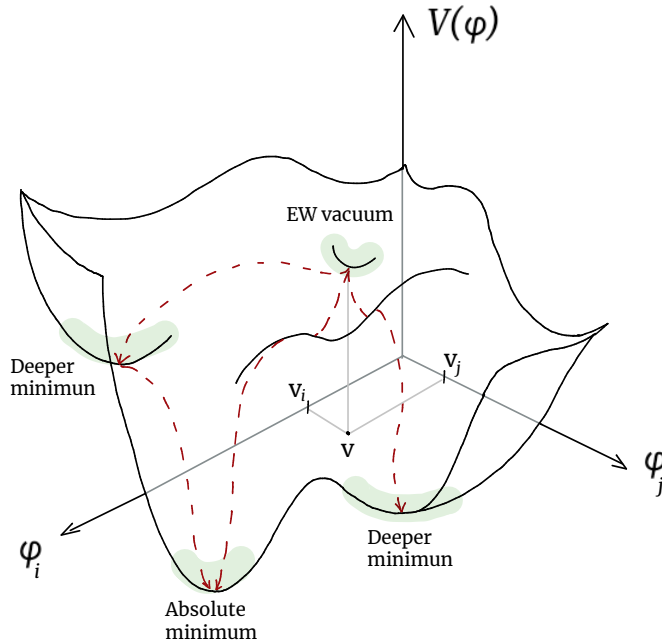

Figure 2.2

Example representation of a scalar potential $V(\varphi)$ in a BSM theory with two scalar fields φ_i and φ_j. Indicated in red are the possible tunnelling directions from the EW vacuum to deeper minima.

2.3   The ΛCDM model and the Cosmological History

The Λ cold dark matter model, or ΛCDM model, is the current state-of-the-art model for describing the cosmological history and evolution of the Universe.[7] This theory adds to the SM of particle physics by incorporating two observationally motivated components: dark energy, represented by the cosmological constant Λ, which drives the accelerated expansion of the Universe, and non-relativistic (i.e. "cold") dark matter.

Our current, widely accepted understanding of the Universe is built on a few assumptions:

Cosmological principle: defines the general symmetries based on observations: the Universe is homogeneous (translation invariant) and isotropic (rotation invariant) on large scales. Mathematically, this is described by the Friedman-Lemaitre-Robertson-Walker (FLRW) metric

$$ds^2 = -dt^2 + a(t)^2 \left(\frac{dr^2}{1 - kr^2} + r^2(d\theta^2 + \sin^2\theta d\phi^2) \right), \tag{2.35}$$

which is a solution to the Einstein equations of GR. The FLRW metric also allows for an expanding or collapsing Universe, its evolution is encoded in the time-dependent scale factor $a(t)$.

Cosmic expansion: describes the evolution of the Universe based on Hubble's observation that the space between galaxies is expanding, leading to the establishment of the Hubble law. Mathematically, this means that the Hubble parameter is defined as the expansion rate of the Universe, normalised by the distance

$$H(t) := \frac{\dot{a}(t)}{a(t)}. \tag{2.36}$$

Assuming that the Universe is thermodynamically isolated, it seems reasonable to assume that this expansion is adiabatic[8], i.e. there is no heat loss and the entropy is conserved.

Properties of matter: determines what is the content of the Universe. Einstein's GR equations allow to relate the geometry of space time (the FLRW metric) to the matter energy-momentum tensor: *matter determines the curvature of spacetime, and the curvature of spacetime dictates the motion of matter.* To describe the properties of matter we need to assume an equation of state. We assume the equation of state for barotropic fluids, for which the pressure P and energy density ρ have a linear relation given by $P = w\rho$, with the parameter w depending on the type of matter: $w = 1/3$ for radiation, $w = 0$ for collisionless matter, $w = -1$ for vacuum energy and $w = -1/3$ for curvature. Using the first law of thermodynamics and the continuity equation, we can derive the relation between the energy density ρ and the scale factor at each moment of time,

$$\rho \propto a(t)^{-3(1+w)}. \tag{2.37}$$

---

[7]This section is based on Ref. [50,74] and my personal notes from the Cosmology lectures at the IFT [75].

[8]This is also confirmed by the homogeneity of the temperature distribution of the Cosmic Microwave Background. Furthermore, a net heat flow would be pointing towards a preferred direction, which violates the cosmological principle.

We can measure the different components of matter in terms of their density today: the vacuum energy density is $\Omega_{\Lambda,0} = 0.685 \pm 0.007$, the matter energy density is $\Omega_{m,0} = 0.315 \pm 0.007$, the curvature density is $\Omega_{K,0} = 0.001 \pm 0.002$ (i.e. our Universe is flat) and the radiation density is negligible [49].[9] Looking at the evolution of the different components of the Universe, we see that it has only recently become vacuum-dominated, which has a constant energy density as can be seen in Eq. (2.37). Before it was in a period of matter domination, and at the very beginning it was radiation dominated.

The Big Bang: defines the initial conditions. It is assumed that the Universe began from a singularity $13.8 \cdot 10^9$ years ago in an extremely hot and dense state, which later cooled down due to the accelerated expansion. Inflation is also thought to be responsible for the the seeds of large-scale-structure formation: small quantum fluctuations generate overdensities that are amplified and eventually grow into galactic structures.[10]

We also rely on a few <u>physical concepts</u>, some of the most relevant ones are:

Energy budget: The temperature of the Universe sets the available thermal energy. The temperature will therefore govern the types of particles that are present at each moment and their energy density. At high temperatures, the thermal energy of the particles is much larger than their rest mass energy, $T \gg m$, therefore they effectively behave as massless, i.e. relativistic, particles. The number density of a relativistc particle in thermal equilibrium is

$$n = K\frac{\zeta(3)}{\pi^2}gT^3, \qquad (2.38)$$

where $\zeta(3) \sim 1.202$ is the Riemann zeta function, $K = 1$ for bosons and $K = 3/4$ for fermions and g is the number of internal degrees of freedom of the species. As the Universe cools down, the thermal energy decreases and the rest mass starts dominating the total energy of each particle species, therefore when $T \approx m$, the particle becomes non-relativistic. This energy density of a non-relativistic species is

$$n = g\left(\frac{mT}{2\pi}\right)^{3/2}e^{\left[\frac{\mu-m}{T}\right]}, \qquad (2.39)$$

where μ is the chemical potential.[11] One can see that the non-relativistic number density is Botlzmann suppressed, therefore some other physical process needs to happen to prevent it from completely diluting and resulting in a radiation-filled Universe. This process is the decoupling from the thermal bath described below. We also note here that the energy of the particles is Boltzmann distributed.

---

[9]See Ref. [76] for the latest experimental results from the Dark Energy Spectroscopic Instrument (DESI) collaboration, which suggest a time evolution of the vacuum energy density.

[10]This remains a theoretical model that cannot be directly tested at the moment but is consistent with all current observations. Inflation could potentially be probed in the future if it left some observable imprints such as a primordial magnetic field or a gravitational wave stochastic background.

[11]In the early Universe, the chemical potential μ can generally be neglected because $\mu \ll T$. In particular, photons have zero chemical potential ($\mu_\gamma = 0$) and they dominate the energy density during the radiation-dominated era, making this approximation especially valid.

Thermal equilibrium: It refers to a state of a physical system in which energy exchange is efficient. The particles in the early Universe can convert from one another rapidly and continuously. They interact with each other through the weak, strong and electromagnetic forces (gravity is neglected at atomic scales). Their interaction rate is Γ, which is proportional to the particle number density, the cross section of the interaction, and the relative velocity between the interacting particles. In the early Universe the interaction rate is greater than the Hubble rate, $\Gamma \gg H$, and the particles can maintain in thermal equilibrium.

As the Universe expands, the Hubble rate decreases and when $\Gamma \ll H$, which means that the Universe is expanding too quickly for the particles to have enough time to interact, as a result thermal equilibrium is not kept and this leads to the decoupling of this particle species from the thermal plasma. Its number density is thus fixed or "frozen" until present time.

This describes the so called freeze-out, which happens for weakly interacting particles, like neutrinos or Weakly Interacting Massive Particles (WIMPs). The latter are hypothetical dark matter candidates that can account for the observed dark matter because, contrary to the neutrinos, they decouple from the thermal bath while being non-relativistic, and thus could potentially constitute cold dark matter. Another alternative for a number density of a species remaining constant until today is the freeze-in, which describes how particles that were not in thermal equilibrium start to slowly acquire a larger number density as a result of a relative increase in their interaction rate.

Phase transitions: A further important notion is phase transitions. In the early Universe they occur when the properties of the cosmic medium change in a sharp or discontinuous way. If this change is smooth then we talk about a crossover. A first order phase transition is characterised by an abrupt change in the properties of the medium. We already introduced the electroweak phase transition (EWPT) in the context of the SM as a breaking of a gauge symmetry, which changes the properties of the vacuum. If this transition was of first order, the vev would have a discontinuity in its evolution with the temperature. A second order transition (or a crossover) implies a slow and continuous change of the properties, meaning the medium is always in a state close to thermal equilibrium. There is also the Quantum Chromodynamics (QCD) phase transition related to the confinement of quarks into hadrons. Both these transitions in the SM are smooth crossovers.

With these ingredients the overall picture of the evolution of the Early Universe can be chronologically described in the following <u>milestones</u>:

$T = ?$ − **Inflation:** It is strongly believed that the Universe underwent a period of rapid expansion called inflation, as it efficiently solves the flatness and the horizon problems. During inflation, the Universe expands exponentially, smoothing out any initial irregularities and causing a nearly homogeneous and isotropic Universe. Radiation is the main component of the Universe, the energy density scales as $\rho \propto R^{-4}$.

$T \sim \mathbf{100}$ **GeV** $(t = \mathbf{10\,ps})$ – **EWPT:** The SSB of the $SU(2)_L \times U(1)_Y$ group into $U(1)_{\text{EM}}$ is a necessary ingredient of the SM.[12] At finite temperatures, the Higgs potential in Eq. (2.29) is modified by including temperature corrections (see App. A). When the particles become massive, the top quark becomes non-relativistic because its mass is of the same order of magnitude as the temperature, and its number density becomes Boltzmann suppressed.

$T \sim \mathbf{150}$ **MeV** $(t = \mathbf{20\,\mu s})$ – **QCDPT:** Before this point, the quarks and gluons are free particles, due to the asymptotic freedom of the $SU(3)_C$. As the Universe cools down, it undergoes the QCD Phase Transition (QCDPT), where quarks and gluons become confined into hadrons (protons and neutrons). After this point, the Universe has a sufficient number of protons and neutrons for the onset of Big Bang Nucleosynthesis.

$T \sim \mathbf{0.8}$ **MeV** $(t = \mathbf{1\,s})$ – $\boldsymbol{\nu}$**-decoupling:** Since the neutrinos are the most weakly interacting particles of the SM, they decouple first from the thermal plasma, while still being relativistic. After decoupling, neutrinos remain relativistic and travel freely through the Universe, forming the cosmic neutrino background.

$T = \mathbf{500}$ **keV** $(t = \mathbf{6\,s})$ – e^+e^- **annihilation:** As the Universe cools down below the electron mass threshold, electrons and positrons became non-relativistic and annihilate into photon pairs. This process transferred entropy to the photon bath, increasing its temperature relative to that of the neutrinos. While the number of massive particles decreased, the photon number increased.

$T = \mathbf{100}$ **keV** $(t = \mathbf{3\,m})$ – **BBN:** Big Bang Nucleosynthesis is a crucial component of the ΛCDM model, and its ability to predict the observed abundances of light elements (like deuterium, helium, and lithium) is one of its major successes.

$T = \mathbf{800}$ **meV** $(t \sim \mathbf{60\,kyr})$ – **Matter-radiation equality:** Matter becomes the main component of the Universe. The energy density scales as $\rho \propto R^{-3}$.

$T = \mathbf{310}$ **meV** $(t \sim \mathbf{300\,kyr})$ – **Recombination and** $\boldsymbol{\gamma}$**-decoupling:** Photons are coupled to the thermal bath via Thomson scattering. In equilibrium, protons and electrons can combine to form hydrogen atoms and release photons, and the reverse process also occurs. As the Universe cools, it becomes energetically favourable for hydrogen atoms to remain bound. Recombination refers to the epoch when electrons and protons form neutral hydrogen atoms. This does not occur exactly at the hydrogen binding energy of 13.6 eV, due to the large excess of photons relative to baryons in the thermal (blackbody) spectrum. Recombination only proceeds efficiently once the number of photons energetic enough to ionize hydrogen becomes sufficiently suppressed. After recombination, photons no longer scatter off free charged particles and begin to travel freely, imprinting the anisotropies observed in the CMB.

$T = \mathbf{5}$ **meV** $(t \sim \mathbf{250\,Myr})$ – **Reionisation:** The formation of the first stars light the Universe after a period of darkness after the emission of the CMB. The emitted photons ionise the surrounding gas clouds.

---

[12]BSM scenarios with electroweak symmetry-non-restoration are physically viable [77]. Even if the particles do have a mass they would still be relativistic as long as the temperature of the Universe is much larger than their mass.

$T = 300\ \mu$eV$(t \sim 9$ Gyr$) - \Lambda$-matter equality: The vacuum energy becomes the main component of the Universe, with a constant evolution of the energy density.[13] If this era persists, it will eventually imply the dilution of all matter and radiation.

$T = 240\ \mu$eV$(t \sim 13.8$ Gyr$) -$ today: Today we can measure imprints of the past through electromagnetic waves (up to the CMB), gravitational waves and primordial magnetic fields.

Some missing milestones in this chronology are the baryogenesis, which presumably took place before the EWPT and the dark matter freeze out. These are highly active areas of research, but strictly not part of the well established chronology.

2.4   Open problems of the SM

The remarkable success of the SM in describing the fundamental particles and high-energy interactions necessitates that any alternative BSM theory must also provide predictions compatible with current experimental data. The fact is, however, that a vast number of observations remain unaccounted in the SM, which highlights the pressing need for an extended BSM framework. In the following, we provide a non-exhaustive list of these problems.

$-$ As mentioned in the introduction, the SM does not incorporate one of the known fundamental forces: **gravity**. The main problem is that when gravity is described in a QFT language as a gauge theory mediated by a massless spin-2 particle, the resulting theory is non-renormalisable. This means that at each loop order, new counterterms are required to absorb divergences. Consequently, the number of free parameters that must be fixed by experiment increases indefinitely, making the theory non-predictive at high energies at the Planck scale.

$-$ Another notable mismatch with observations is the complete lack of a **dark matter** candidate. Assuming a particle nature of dark matter[14], it must be non baryonic, non-relativistic, stable, electrically neutral and interacting via the weak force, or only via gravity.

$-$ There are some purely theoretical shortcomings related to the SM called **naturalness problems** [78]. The main idea is that the parameters of the theory should be of the same order: this is called full naturalness [79]. As we discussed in the introduction of the SM in Sec. 2.1, QFTs are based on the concepts of symmetry. An exact symmetry of the Langrangian will make some of the coefficients of certain operators in the Lagrangian vanish. If this symmetry is softly broken by some small parameter, then the quantum corrections will be proportional to that small amount. The latter observation is a rough statement of the so called technical naturalness derived by 't Hooft [80]. Some observed differences between the scales can indeed be explained. For example the proton mass scale is much smaller than the Planck scale because of the logarithmic evolution of the gauge coupling of the $SU(3)_C$ (the RGE running) that suppresses the QCD scale with respect to the Planck scale. The requirement of full naturalness can seem *ad hoc* and could be argued

---

[13]See footnote 9.

[14]Other proposed solutions include primordial black holes, that do not rely on a particle nature of the dark matter and therefore could be in principle compatible with the SM.

to disappear with anthropic reasoning. However, historical examples render naturalness a guiding principle for new physics. These are the currently remaining naturalness problems: the hierarchy problem, the strong CP problem and the cosmological constant problem. We provide more details on these problems below:

- The **Hierarchy problem** refers to the smallness of the Higgs mass compared to higher energy scales in nature. Thinking of the SM as effective field theory of a more complete description, like for example one that includes gravity, the Higgs mass will recieve quantum corrections from loop diagrams involving all particles that couple to it, same as the other parameters in the theory. However, unlike some other masses in the SM (e.g. the photon or the electron), there is no symmetry that protects the Higgs mass from large corrections, from the physics at higher scales, such as the Planck mass, M_P.

  For instance, the photon mass is exactly zero at all orders due to the unbroken $U(1)_{\text{EM}}$ gauge symmetry of the SM. Similarly, the smallness of the electron mass can be understood from the approximate chiral symmetry of the Lagrangian, which is restored when the electron mass is set to zero, rendering it technically natural in the definition above. In contrast, there is no such symmetry in the SM that would protect the Higgs mass from getting arbitrarily large corrections from some physics at a heavier scale, e.g. the Planck scale at $M_P \sim 1.2 \times 10^{19}$ GeV. This sensitivity implies that, unless there is some mechanism to cancel or suppress these large corrections, an unnatural fine-tuning of the Higgs mass is required to keep the physical mass at the electroweak scale. This issue becomes especially relevant if the SM is viewed as an effective field theory (EFT), valid only below some cut-off scale Λ, potentially as high as M_P. Supporting this view, the SM is known to become inconsistent in the ultraviolet: for example, the hypercharge gauge coupling associated with $U(1)_Y$ runs toward a Landau pole at high energies, indicating that the theory cannot remain valid arbitrarily far into the UV.

  A concrete manifestation of the hierarchy problem arises from the fact that the radiative corrections to the Higgs mass are quadratically divergent. In the Wilsonian approach to EFTs, such divergences are interpreted not merely as a mathematical artefact, but as a reflection of our ignorance about the UV completion of the theory. They signal the physical sensitivity of low-energy observables, like the Higgs mass, to whatever dynamics exists at high energy. Even in a broader fully UV-complete theory that includes the SM in some limit, where calculations can be done using dimensional regularisation (which formally avoids power divergences), the corrections to the Higgs mass still scale with the mass of the heavy particles in the theory. Therefore, any predictive theory of the Higgs sector is necessarily subject to large threshold corrections proportional to the cut-off scale or the mass scale of new physics, making the presence of such terms unavoidable. This is what makes the smallness of the Higgs mass appear unnatural without a protective symmetry or a dynamical mechanism that explains it.

  Thus, the hierarchy problem raises the question: *"What new physics enters at or below the cut-off scale to stabilise the Higgs mass and ensure the consistency of the theory?"* The answer to this question is a bustling topic of research, just to list some solutions, (1) symmetry between fermions and bosons in SUSY protects the Higgs mass from being sensitive to larger mass scales and thus explains the smallness of

the measured Higgs mass. This happens because superpartners cancel the quadratic divergences in the radiative corrections to the Higgs mass. (2) The composite Higgs models in which the Higgs is a bound state of more fundamental constituents, similar to how pions emerge as bound states of quarks in QCD. The small mass of the neutral pion, protected by approximate chiral symmetry, serves as an analogy: the Higgs can be understood as a pseudo-Nambu–Goldstone boson of a spontaneously broken global symmetry, naturally explaining its lightness compared to the compositeness scale, and (3) Extra space dimensions, which effectively lower the cut-off scale by embedding the Universe into a higher-dimensional space.

– The **strong CP problem** refers to the smallness of a term in the Lagrangian that is allowed by all symmetry considerations, but appears to be tiny in nature [81,82]:

$$\mathcal{L}_\theta = \theta_{\text{QCD}} \frac{g_s^2}{32\pi^2} G_{\mu\nu}^a \tilde{G}^{a\,\mu\nu}, \tag{2.40}$$

where θ_{QCD} is a CP-violating parameter usually called theta angle, and $\tilde{G}^{a\,\mu\nu} = \frac{1}{2}\epsilon^{\mu\nu\rho\sigma} G_{\rho\sigma}^a$ is the dual of the gluon field strength tensor. EDM experiments have set an upper bound on the magnitude of the theta angle, $\theta_{\text{QCD}} < 10^{-10}$ [83,84].

A way to dynamically explain its smallness is with the so called Peccei-Quinn mechanism, which introduces a symmetry in the Lagrangian whose physical consequence is the manifestation of a light "axion" particle [85,86].

– The **cosmological constant problem** refers to the large discrepancy between the observed small value of the cosmological constant and the much larger value predicted by QFT, which scales with the fourth power of the Planck scale, M_P^4 [87,88].

– The **masses of the neutrinos** are zero in the SM, which contradicts the observations of neutrino oscillations. In the SM the neutrinos do not have a right-handed component because they are massless, in BSM extensions a very massive right-handed neutrino is postulated in order to explain the experimentally observed small neutrino masses via a dynamical Seesaw mechanism.

−There are also some tensions between experimental measurements and theoretical predictions of the SM; perhaps the most well known example is the **muon $g-2$ anomaly**. It refers to the magnetic moment of the muon, given by

$$\vec{\mu} = \frac{e}{2m_\mu} g \vec{S}, \tag{2.41}$$

where $g = 2$ is the tree-level prediction from the Dirac equation. Higher-order quantum corrections lead to deviations from this value, quantified by the anomalous magnetic moment $a_\mu = (g-2)/2$. Experimental measurements of a_μ [89] differ from the SM prediction [90], potentially hinting at the existence of new heavy particles contributing via loop effects. However, recent lattice calculations show better consistency with the Fermilab measurement [91] coming from an improved lattice calculation of the QCD contributions to a_μ (for a short review see Ref. [92]).

− There is a lack of a description of the observed matter-antimatter asymmetry of the Universe, a problem known as the **baryon asymmetry of the Universe** (BAU). The

exact CPT symmetry of any QFTs ensures that particles and antiparticles are created in pairs to preserve their quantum numbers like charge, baryon number and lepton number. If this had been the case throughout the thermal evolution of our Universe, the produced particles and antiparticles would have annihilated, resulting in a radiation filled Universe. Assuming that the Universe was generated *ad hoc* with this asymmetry does not help in solving the problem, since any initial asymmetry would have been washed out (diluted) by inflation. Thus we know there must have been a mechanism by which the asymmetry between baryons (components of matter) and antibaryons was generated, a process called baryogenesis [93,94]. The way to measure this asymmetry makes use of the so called baryon to photon ratio, whose independent measurements from primordial element abundances and the cosmic microwave background agree. A quantity that remains constant over the evolution of the Universe is

$$\eta_s = \frac{n_B - n_{\bar{B}}}{s} \sim 6 \cdot 10^{-10}, \tag{2.42}$$

where n_B is the number of baryons, $n_{\bar{B}}$ is the number of antibaryons and s is the entropy. All of these quantities scale as $1/a^3$ as the Universe expands, so the ratio remains constant.

In 1967, Sakharov summarised the necessary conditions for any viable baryogenesis mechanism [48]: 1) parity P and charge parity CP violation, 2) baryon number violation and 3) out of equilibrium dynamics, needed in order to avoid the inverse process. Even though all of these conditions are *a priori* present in the SM, they are insufficient to guarantee a successful baryogenesis.[15] In the following, we address the reasons for this, considering each individual condition separately.

Baryon number violation: Baryon number conservation is an accidental global symmetry of the SM, it is accidental because it is not imposed *a priori*, but follows from the invariance of the Lagrangian under common phase rotations of all quark fields. This symmetry impedes tree-level baryon number violating processes. However, in 1976, 't Hooft showed that in the SM the triangle anomaly violates baryon number through non-perturbative effects [95] with the corresponding baryon number current being:

$$\partial^\mu j_\mu^B = 3\frac{g^2}{32\pi^2} V^{\mu\nu\,a} \tilde{V}_{\mu\nu}^a, \tag{2.43}$$

where $V_{\mu\nu}^a = \partial_\mu V_\nu^a - \partial_\nu V_\mu^a + g\epsilon^{abc} V_\mu^b V_\nu^c$ is the field strength of the $SU(2)_L$ gauge fields ($V = W^\pm, Z$) and $\tilde{V}_{\mu\nu}^a = \frac{1}{2}\epsilon_{\mu\nu\rho\sigma} V^{\rho\sigma\,a}$ is the dual tensor and g is the coupling constant of the $SU(2)_L$ gauge group. The reason for this anomaly is that only left-handed fermions interact with the electroweak gauge field, in fact strong interactions do preserve baryon number.[16] The outcome of this is that there is spontaneous production of 9 quarks and 3 leptons per each generation.

This is related to the fact that the electroweak vacuum is not unique, but rather consists of different topologically distinct vacua with the same energy configuration, as pointed out in Sec. 2.2. Field configurations can interpolate between these vacua, leading to stable or unstable *extended* objects. An example of the former would be soliton solutions, which are solutions to the field equations that give rise to cosmic

---

[15]In particular the third condition is incompatible with the experimental measurement of the Higgs mass, see the forthcoming discussion for a detailed explanation.

[16]A similar discussion follows also for the different lepton families.

strings or magnetic monopoles. An example of the latter are sphalerons[17], which are unstable field configurations that exist at high energy and disappear when the Universe cools. Standard perturbation theory can only describe point-like particles as small excitations around the ground state. These are the elementary constituents of nature and for these the methods developed by Feynman diagrams come at hand to make accurate predictions. However, these methods cannot be applied to the aforementioned non-perturbative solutions, which arise when solving the classical field equations exactly [96], and therefore non-perturbative methods or lattice calculations are used. Each of these degenerate minima is a valid perturbative vacuum state of the theory, the height of the energy barrier between them is

$$E_{\text{sph}} = \frac{2m_W(T)}{\alpha_W} f\left(\frac{m_h}{m_W}\right), \tag{2.44}$$

where $m_W(T)$ is the temperature-dependent mass of the $W^\pm$ gauge boson, $\alpha_W = g^2/4\pi \cong 1/30$ and $f(m_h/m_W \ll 1) = 1.56$, $f(m_h/m_W \gg 1) = 2.72$ and $f(m_h/m_W) = 2.4$ for $m_h = 125$ GeV. E_{sph} is a saddle point, meaning that the energy increases along one field direction but decreases in the others. At $T = 0$, transitions between the vacua are possible only through quantum tunnelling (these solutions are called instantons) and are very suppressed, which implies that there is no baryon number violation today. At finite temperature, the probability of a given configuration is determined by the free energy, meaning that the thermal energy can hop over the barrier instead of tunnelling through it. The transition rate between the vacua in this case is [97]

$$\Gamma_{\text{sph}} = CT^4 e^{-E_{\text{sph}}/T}, \tag{2.45}$$

where E_{sph} is given in Eq. (2.44), and for estimation purposes we set $C \sim 1$. This formula is only valid for temperatures lower than the energy barrier $T \lesssim E_{\text{sph}}$. Above that, the exponential suppression is absent, in fact for temperatures above the EWSB $m_W(T \gg 100 \text{ GeV}) \sim gT$, as it only has a mass from the thermal corrections and not from the Higgs mechanism, because $m_W(T = 0) \propto v$ and $v = 0$ before SSB. For high temperatures, the following transition rate should be used

$$\Gamma_{\text{sph}} = \kappa \alpha_W^5 T^4, \tag{2.46}$$

which is based on lattice simulations and dimensional analysis. An extra factor of α_W is added to account for plasma effects and $\kappa \sim 18$ is a constant value determined by lattice calculations. If we compare the sphaleron rates in Eq. (2.46) and Eq. (2.45) to the Hubble rate, we can roughly estimate at which temperature the sphaleron processes are in thermal equilibrium, which happens to be between $T \sim 10^{12}$ GeV and $T \sim 100$ GeV.

At temperatures close to the EWSB, we can estimate that sphalerons are active if

$$\frac{\Gamma_{\text{sph}}}{T^3} \lesssim H(T) = \frac{T^2}{M_P} \rightarrow \frac{m_W(T)}{T} \lesssim \frac{\alpha_W}{2f(m_h/m_W)} \log\left(\frac{M_P}{T}\right), \tag{2.47}$$

---

[17]In Greek σφαλερός means unstable, ready to fall.

where $H(T)$ is the Hubble rate and M_P is the Planck mass. By inverting the second inequality in Eq. (2.47), we can establish the condition for shpaleron decoupling, which effectively means that they "switch off" and are not efficient in producing a baryon asymmetry. We get the necessary condition that baryon number violation is "switched off" in the broken phase after the electroweak phase transition only if

$$\xi_n := \frac{v_n}{T_n} \gtrsim 1, \tag{2.48}$$

where v_n and T_n are the vacuum expectation value and the temperature at the transition. This condition alone puts a bound on the Higgs mass that would allow for baryon number violation during an electroweak phase transition, which is not fulfilled in the SM [94]. From a rough estimate of the vacuum expectation value at the nucleation temperature that one gets from the one-loop effective thermal potential (see App.A) this mass should be [98]

$$m_h < 35 - 40 \,\mathrm{GeV}. \tag{2.49}$$

This condition also puts a bound on the temperature of the electroweak phase transition. If it happens below 100 GeV it cannot lead to a successful electroweak baryogenesis (see the discussion below for a detailed explanation), regardless of the other conditions.

C and CP violation: A theory has CP violation (i.e. the CP symmetry is not exact) if it has complex couplings in the Lagrangian which lead to a phase that cannot be removed by field redefinitions. In the SM the CP violation happens in weak interactions through the phase of the Cabibbo-Kobayashi-Maskawa (CKM) matrix, which is a unitary matrix that describes the mixing between the different quark flavors. Effectively, the CKM matrix can be parametrised with three mixing angles and one phase $\delta_{\mathrm{CKM}} = 1.147 \pm 0.026$ [99] , measured in experiments like B meson decays. Another way to measure CP violation in nature is by measuring the electric dipole moment (EDM) of the particles, as it measures the charge distribution within that particle. The predicted EDM of the electron in the SM is $\mathcal{O}(10^{-38})$ while experimental bounds are $\mathcal{O}(10^{-29})$. Another source of CP violation is the complex phase of the Pontecorvo-Maki-Nakagawa-Sakata (PMNS) matrix, that describes the mixing of the three generations of neutrinos analogously to the CKM matrix but in the leptonic sector. Its effects on CP violation are very small [100]. An additional source of CP violation would be the θ-term in QCD, which would induce an EDM in the neutron and the proton. In particular the neutron EDM puts the most stringent bound on the smallness of the θ-term, thus further constraining the amount of CP violation in the SM. The bounds on neutron and proton EDMs are [99]

$$|d_n| < 1.8 \times 10^{-26} \, e \cdot \mathrm{cm} \quad \text{and} \quad |d_p| < 10^{-25} \, e \cdot \mathrm{cm}. \tag{2.50}$$

Any BSM theory with additional sources of CP violation has to respect these bounds. A way to parametrise the CP-violating phase in a basis-independent way is with the Jarlskog invariant, defined in terms of the commutator of the up-type and down-type mass matrices squared as

$$J = \det[m_u^2, m_d^2] \sim \frac{1}{8} \sin \delta_{\mathrm{CKM}}. \tag{2.51}$$

If J = 0 there is no CP violation. In the SM the result is 10 times smaller than the amount necessary for baryogenesis [101]. Further BSM sources of CP violation can also be searched for in the Higgs sector, as a CP-mixed character of the Higgs boson is compatible with experiments. So far the measurements are compatible with the SM predictions, but the amount of CP violation in the SM is insufficient for a successful baryogenesis. Thus, all of our current understanding of physics is, in essence, incapable of explaining our existence.

Departure from thermal equilibrium: None of the above conditions could, by themselves, explain a baryon surplus in the Universe, as in thermal equilibrium any generated baryon or CP asymmetry would be immediately erased by the inverse process. Some common scenarios that lead to out-of-equilibrium conditions include first order phase transitions, decays of very heavy particles out of equilibrium, topological defects, and others.

In this thesis, we focus in the first scenario, and in particular on the phase transition associated to the SSB of the electroweak gauge group. This mechanism is called electroweak baryogenesis. There are also proposed mechanism for baryogenesis during the QCD phase transition [102, 103], which we will not discuss here.

A first order phase transition between the symmetric and broken phases of the electroweak vacuum can occur if the finite temperature scalar potential develops a barrier between the false and true vacua. In that case, the transition releases a significant amount of energy and cannot proceed uniformly throughout space. Instead, it occurs via the spontaneous nucleation of bubbles of true vacuum. These bubbles grow and collide, creating the necessary out-of-equilibrium conditions.
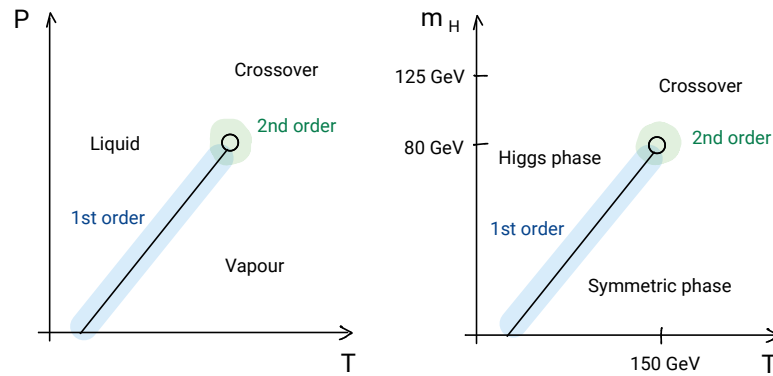
Figure 2.3
Comparison between the phase diagram of water (left) and the SM Higgs (right), showing the different patterns of phase transition depending on the parameters.

A familiar analogy of a first order phase transition is the boiling of water. In the water phase-diagram the liquid-gas transition becomes second order at the critical point at a particular pressure and temperature. Above this point the change in the water properties is continuous and homogenous and is called a crossover. In the

cosmological phase transition the point at which the transition becomes second order depends on the Higgs mass and the temperature. Lattice calculations show that the mass of the Higgs must be below 80 GeV in the SM [104,105]. This means that a first order electroweak phase transition is not possible in the SM, as the Higgs mass is too heavy, and therefore BSM physics is needed. Similarly to the water analogy, above this mass, the transition is a crossover.[18] We illustrate this analogy in Fig. 2.3, where we plot the phase diagram of the SM and of water describing the different nature of the transition (first order, second order or crossover).

To summarise, a first order phase transition is essential for generating out-of-equilibrium dynamics. It is through the formation and evolution of true vacuum bubbles that these conditions arise. The requirement of a *strong* first order transition for a successful electroweak baryogenesis arises because of the condition of baryon number washout inside the symmetric phase, as previously discussed.

Any explanation of the aforementioned problems will necessarily involve new physics, which we introduce in the following section. Some proposed explanations of baryogenesis are listed below [93,99,106,107]:

GUT baryogenesis: The the asymmetry is generated by the asymmetric decay of a very heavy GUT particle. The main challenge of GUT theories is the prediction of a rapid proton decay, which fortunately was not observed experimentally.

Affleck-Dine mechanism: It involves the decay of flat directions in supersymmetric models that generate more baryons than antibaryons [108].

Leptogenesis: In this case an asymmetry in lepton number generated by the out-of-equilibrium decay of a superheavy right-handed neutrino in the Seesaw mechanism is converted to a baryon number asymmetry by sphalerons, which preserve B-L symmetry [107].

Electroweak baryogenesis: If the baryon asymmetry was generated during the electroweak phase transition, it is called electroweak baryogenesis. The SM would in principle belong to this class of models if it had sufficient CP violation and out of equilibrium conditions. In order to explain the baryon asymmetry with electroweak baryogenesis the BSM theory must contain two ingredients, additional sources of CP violation, and a **strong first order electroweak phase transition**. Both can be realised in models with extended scalars sectors as will be discussed in detail in the next section. Other possibilities include composite Higgs models, which additionally solve the hierarchy problem. Some proposals also include phase transitions in the dark sector.

We describe how EWBG would take place in a nutshell [38, 94]. As soon as the Universe cools down to the electroweak temperatures, it undergoes the SSB of the electroweak gauge symmetry group. In BSM models, the energy barrier between the symmetric false minimum and the broken EW minimum of the scalar potential can be quite large. Since the potential is the free energy per unit volume of the primordial

---

[18]It is usually impossible to distinguish a crossover from a second order electroweak phase transition via their phenomenology.

plasma, the change in the properties of the plasma is so big that in cannot happen everywhere simultaneously. Instead, it proceeds through spontaneous nucleation of bubbles that have the broken phase inside while the exterior plasma is still in the unbroken phase, see Fig. 2.4 for a graphic illustration of this process.
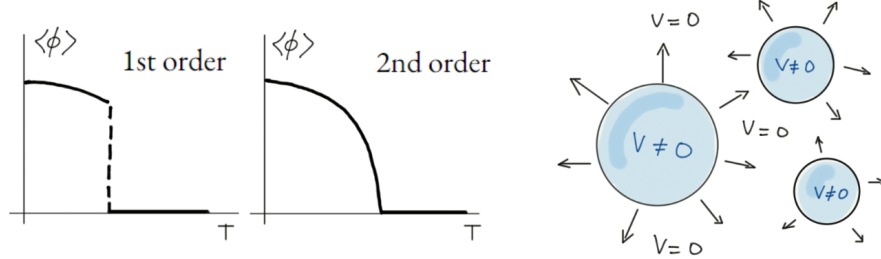

Figure 2.4
Evolution of the vacuum expectation value with temperature in a first order and a second order phase transition (left). Bubble nucleation of the EW vacuum in a Universe with a zero vev (right).

As these bubbles expand, the particles in the plasma scatter off the walls. Provided there are additional sources of CP violation, there would be a different transmission and reflection coefficient for particles and antiparticles. The net overdensity of left-handed particles would build up in front of the wall, which will then be transformed into a baryon asymmetry by the sphalerons. Since the bubbles are expanding, they will absorb the excess baryons and because the sphalerons in the broken phase are suppressed, they will be frozen until the present day. An attractive feature of the electroweak baryogenesis scenario is its falsifiability. On one hand, the additional scalar particles required to generate a strong first order electroweak phase transition can be tested at particle accelerators. On the other hand, the expansion of the bubbles and the resulting bulk motion of the thermal plasma may produce a stochastic gravitational wave background, provided the transition is sufficiently violent. Remarkably, the characteristic frequency of these GWs lies within the sensitivity range of the space-based interferometer LISA [109, 110], offering a complementary probe of the EWBG mechanism [97]. In addition, the movement of the plasma can source a primordial magnetic field background, potentially contributing to the origin of a primordial magnetic field background.

2.5 Extended scalar sectors

The existence of *at least one* Higgs boson is necessary for two reasons: the first one is to give masses to the gauge bosons and fermions, for which the mass terms violate the $SU(2)_L \times U(1)_Y$ symmetry with weak hypercharge $Y = 1$. The second reason is the scattering amplitude of longitudinal gauge bosons ($V_L V_L \to V_L V_L$, where $V = W^\pm, Z$), that requires the Higgs-boson exchange contribution to be unitary and not diverge proportionally to the centre of mass energy squared. One Higgs boson completes the minimum electroweak theory.

The existence of *several* scalars is an appealing possibility for many reasons [111], which we briefly outline below in the context of specific models. Perhaps the most widely studied model that has an extended scalar sector is the Minimal Supersymmetric SM (MSSM). It addresses the hierarchy problem by introducing a fermionic partner for each bosonic field and a bosonic partner for each fermion, thereby cancelling the divergent quantum corrections to the Higgs mass. Additionally, it predicts the unification of the gauge couplings and provides a dark matter candidate. Although exact Supersymmetry conflicts with current experimental evidence, MSSM with spontaneously broken supersymmetry and its extensions can solve these issues while remaining consistent with experimental constraints. The possibility of realising a SFOEWPT in the MSSM is affected by severe constraints from the non-observation of light stops and the necessity of accommodating a Higgs with SM-like properties at a mass of 125 GeV [112].

On the contrary, many studies are focused on models that feature extended scalar sectors without additional supersymmetric particles. A model that shares the scalar sector witht the MSSM is the Two Higgs Doublet Model, which has been widely studied and can also accommodate a first order electroweak phase transition. CP violating versions of the 2HDM can also accommodate the necessary amount of CP violation for baryogenesis, but have been recently subject to strong constraints from EDM bounds and collider searches [113]. Inert versions of the 2HDM can accommodate a dark matter candidate [34–36]. Perhaps the simplest scalar extension of the SM is a singlet extension [114], that is also appealing due to possibly being a dark matter candidate [31–33] or accommodating a SFOEWPT [115–117]. Other possibilities include several singlets [118], doublets [119] or triplets [120].

The phenomenological consequences of extended scalar sectors are in particular the physical particles that can directly be found at collider experiments. These can be neutral or charged and are commonly referred to as Higgs bosons. Their existence could also lead to measurable imprints in the electroweak precision measurements, therefore these need to be investigated for any BSM theory. Furthermore the presence of such fields could potentially lead to deviations in the couplings of the observed Higgs boson h at 125 GeV. Of particular interest are the self-interactions, since they are not symmetry protected and can receive large corrections from the presence of the additional heavy states. Finally, these states can also leave cosmological imprints, for instance if they lead to a SFOEWPT, the produced stochastic gravitational wave background could be observable by space based gravitational wave telescopes.

As mentioned in Sec. 2.4, the electroweak baryogenesis cannot take place in the SM. The presence of additional scalar states can provide the missing sources of CP violation and the conditions for a strong first order electroweak phase transition.

2.6   The Trilinear Higgs Self-Coupling

The SM predicts triple and quartic Higgs self-interactions, both related and uniquely defined once the vev and the Higgs mass are measured. After SSB, we can rewrite the scalar potential in Eq. (2.29) expanding the Higgs doublet around the minimum in a unitary gauge:

$$\Phi = \begin{pmatrix} 0 \\ \frac{v+h}{\sqrt{2}} \end{pmatrix}, \tag{2.52}$$

as

$$V(h) \propto v(\lambda v^2 - \mu^2)h + \frac{1}{2}(3\lambda v^2 - \mu^2)h^2 + \lambda v h^3 + \frac{\lambda}{4}h^4 \qquad (2.53)$$

$$\equiv t_h h + \frac{m_h^2}{2}h^2 + \frac{m_h^2 - t_h/v}{2v}h^3 + \frac{m_h^2 - t_h/v}{8v^2}h^4, \qquad (2.54)$$

where we dropped the constant terms. After the equality we defined the mass of the Higgs boson as the coefficient in front of the quadratic term $m_h^2 := 3\lambda v^2 - \mu^2$, and the tadpole as the coefficient in front of the first term $t_h := v(\lambda v^2 - \mu^2)$. We thus replace the Lagrangian parameters, λ and μ, for the physical mass, m_h, tadpole t_h and vev, v, of the Higgs boson:

$$\mu^2 = \frac{m_h^2 - 3t_h/v}{2}, \quad \lambda = \frac{m_h^2 - t_h/v}{2v^2}. \qquad (2.55)$$

Usually the tadpole is removed by requiring $t_h = 0$, which is equivalent to imposing the minimisation condition in Eq. (2.33). This can be done at tree-level, but at higher order the tadpole equations need to be included via the definition of a tadpole counterterm. An on-shell renormalisation condition usually refers to keeping the $t_h = 0$ condition true at higher loop orders, i.e. the radiatively corrected vacuum remains the true vacuum of the theory. We will set $t_h = 0$ for the moment and mention tadpoles again in the renormalisation discussion in Sec. 3.6.1.

The SM trilinear coupling is thus given by $\lambda_3 \equiv m_h^2/(2v)$ and the quartic $\lambda_4 \equiv m_h^2/(8v^2)$, where $\lambda_3 = 4v\lambda_4$. Comparing the trilinear Higgs self-interaction with the general QFT interaction term

$$\mathcal{L}_{\text{int}} = \frac{-g}{n!}h^n, \qquad (2.56)$$

where the denominator is a symmetry factor and the Feynman rule for the vertex is given by $-ig$, we can get the Feynman rule for the trilinear Higgs self-interaction as $g = n!\lambda_3 = 6v\lambda = 3m_h^2/v \sim 190$ GeV. In order to use a dimensionless parameter, we will absorb the vacuum expectation value in the definition of the Feynman rule $-ig := -ivn!\lambda_{\text{SM}}$, where $\lambda_{\text{SM}} = m_h^2/(2v^2) \simeq 0.13$.

In BSM theories, the presence of additional degrees of freedom makes scalar self-interactions depend on additional Lagrangian parameters and thus a window to new physics. In general, the trilinear and quartic coupling involving h will deviate from the SM prediction depending on the parameters of the theory. Furthermore, additional BSM couplings between h and the rest of the scalars are possible and interesting parameters to test BSM sectors. The generic trilinear Higgs coupling $\lambda_{hh_ih_j}$, involving at least one SM-like Higgs boson h, is defined such that the Feynman rule is given by
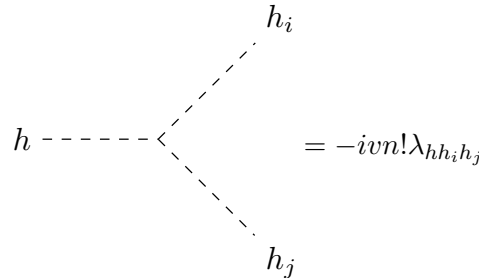
$$h \dashleftarrow \begin{array}{c} h_i \\ \\ h_j \end{array} = -ivn!\lambda_{hh_ih_j}, \qquad (2.57)$$

where n is the number of identical particles in the vertex (relevant for our analysis here are λ_{hhh} and λ_{hhH}). We adopt this convention in Eq. (2.57) so that the light Higgs trilinear coupling λ_{hhh} in BSM theories has the same normalisation as λ_{SM}. For convenience we define the parameter κ_λ as

$$\kappa_\lambda \equiv \lambda_{hhh}/\lambda_{\mathrm{SM}}^{(0)}. \tag{2.58}$$

Throughout this thesis, h will represent the Higgs boson found at 125 GeV and its properties will be SM-like.

2.6.1 Current experimental status

The current experimental sensitivity to the 125 GeV Higgs self-interaction places constraints on the trilinear Higgs coupling (THC), for convenience we will use the coupling relative to the SM, κ_λ. At 95% confidence level (C.L.), the allowed range is $-1.2 < \kappa_\lambda < 7.2$ (AT-LAS [121]) and $-1.4 < \kappa_\lambda < 7.8$ (CMS [122]). These limits are primarily derived from searches for Higgs boson pair production, assuming a SM–like top Yukawa coupling.

A detailed discussion of how Higgs pair production is sensitive to the trilinear coupling can be found in Chapter 3. For now, it is important to note that the production of Higgs boson pairs has not been observed directly so far. As a result, current measurements only provide upper bounds on the production cross section.

These bounds are illustrated in Fig. 2.5, where the intersection of the solid black line (experimental upper bound) with the red line (theoretical prediction of the cross section for the different values of κ_λ) determines the experimentally allowed rage for κ_λ.
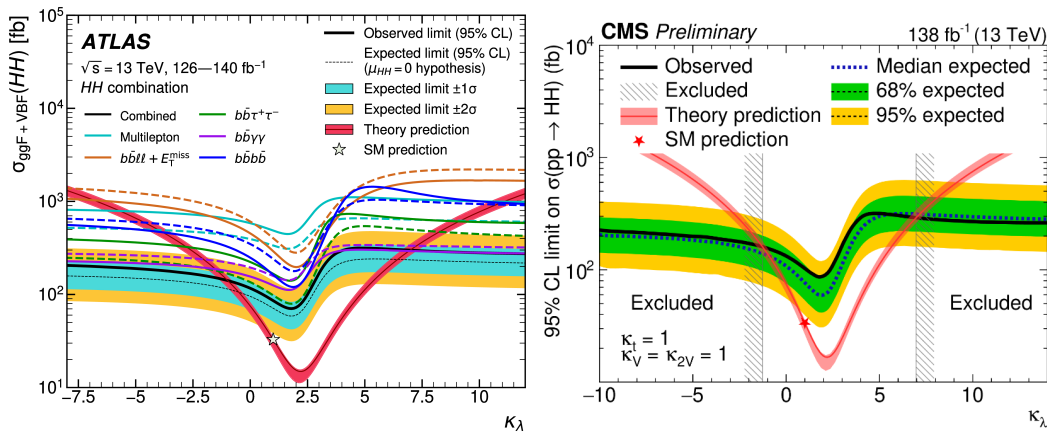
Figure 2.5
Experimental bounds on the values of κ_λ from ATLAS [121] (left) and CMS [122] (right) from non-resonant di-Higgs combinations.

While the measurements remain compatible with the SM within current experimental and theoretical uncertainties, they also leave ample room for interpretations involving physics beyond the SM [123]. A further step to establish this would be a precise measurement of the THC, which directly provides information about the scalar potential. This observation aligns with the objective of the Run 3 and the High Luminosity phase of the LHC.

2.6.2   One-loop corrections

Direct observation of heavy physics might be difficult because of the energy needed to produce it. However, its effects in the experimental results can be large in the radiative corrections to different physical processes. Therefore, it is important to measure such processes precisely and compare to theoretical predictions that go beyond the leading order (LO). One can think of the Higgs boson mass, or the top quark, as SM examples of particles whose mass ranges could be induced indirectly though their effects on physics at a lower mass scale. Thus radiative corrections provide a powerful tool to understand the structure of the underlying theory. Such is the case for THCs in BSM theories.

In scalar extensions of the SM with somewhat large couplings due to splittings in the mass scales of the BSM particles, the tree-level scalar potential is not sufficient to properly capture the interactions among the particles. This effect is often called *mass-splitting* effect, it was pointed out in [124,125] and occurs quite generally in BSM theories [126–133]. These corrections are driven by couplings of the form

$$g_{hh\phi\phi} \propto \frac{(m_\phi^2 - M^2)}{v^2}, \tag{2.59}$$

where h is the SM-like Higgs and ϕ is a BSM scalar field with mass m_ϕ. M is an intrinsic BSM mass scale, and v is the vev. An example of this behaviour will be discussed later in Chapter 3 for the particular case of a doublet extension of the SM. For the moment we just want to note that the appearance of large loop corrections in this model is not a sign of the breakdown of perturbation theory, but an inclusion of a new class of contributions from the heavy physics that are only captured at one-loop. This is confirmed by calculations of the THCs at two loops [134–136], that follow the expected perturbative behaviour, as no new interactions enter in the process.

This shows the need to include at least one-loop corrections to the trilinear couplings in our analysis, either diagrammatically or with an effective potential approach:

Effective potential approach: the THCs are extracted from the one-loop-corrected effective potential,

$$V_{\text{eff}} = V_{\text{tree}} + V_{\text{CW}} + V_{\text{CT}} . \tag{2.60}$$

In this equation, V_{tree} is the tree-level potential, V_{CW} is the one-loop Coleman–Weinberg potential [137, 138] at zero temperature, and V_{CT} is the counterterm potential defined within a given renormalisation scheme. The loop-corrected THCs can be computed as the third derivative of the effective potential with respect to the Higgs fields evaluated at the minimum

$$\lambda_{hhh}^{(1)} = \frac{1}{3!v} \left. \frac{\partial^3 V_{\text{eff}}}{\partial h^3} \right|_{h,H=0} . \tag{2.61}$$

This coupling is obtained at zero external leg momenta, and only includes so-called genuine one-loop corrections, that refer to the Three-Point C (TPC) and Three-Point B (TPB) functions.[19]

---

[19] These functions are known as Passarino–Veltman loop integrals [139], used to simplify one-loop Feynman diagram calculations. The A-functions correspond to diagrams with one external leg (e.g. tadpole corrections), B-functions involve two external legs (e.g. self-energy corrections), C-functions correspond to three external legs (e.g. vertex corrections), and D-functions are used for diagrams with four external legs (e.g. box diagrams).

A tool that performs this calculation within specific BSM models is `BSMPT` [140–142]. In this tool, the counterterm potential is chosen such that the masses and mixing angles are kept at their tree-level values by means of the conditions:

$$
\begin{aligned}
0 &= \partial_{\phi_i} \left(V_{\text{CW}} + V_{\text{CT}} \right) \big|_{v=v_{\text{tree}}} \ , \\
0 &= \partial_{\phi_i} \partial_{\phi_j} \left(V_{\text{CW}} + V_{\text{CT}} \right) \big|_{v=v_{\text{tree}}} \ .
\end{aligned}
\tag{2.62}
$$

Diagrammatic approach: alternatively, one could use a fully diagrammatic approach by calculating the one-loop corrections to the three-point functions. This gives a more precise understanding on the type of corrections included, and allows to include in particular wave function renormalisation (WFR) corrections, as well as tadpole contributions. It also allows to keep track of full momentum dependence and to define a convenient renormalisation scheme to obtain a consistent result. This calculation can be conveniently performed in general renormalisable extended scalar models with the public tool `anyH3` [131], which provides loop corrections to λ_{hhh}. In general BSM models multiple scalar self-interactions are possible. Their one-loop corrections can also be computed in a general way in terms of the contributions to the renormalised scalar three-point function, $\hat{\Gamma}_{ijk}$, as

$$
\lambda_{ijk} = -\hat{\Gamma}_{ijk}(p_i^2, p_j^2, p_k^2) = \lambda_{ijk}^{(0)} + \delta_{\text{genuine}}^{(1)}\lambda_{ijk} + \delta_{\text{tadpoles}}^{(1)}\lambda_{ijk} + \delta_{\text{WFR}}^{(1)}\lambda_{ijk} + \delta_{\text{CT}}^{(1)}\lambda_{ijk}, \tag{2.63}
$$

where i, j, k stands for general scalar particles h_i, h_j and h_k. The superscripts (0) are used for the tree-level values and (1) for the one-loop ones. Therefore $\lambda_{ijk}^{(0)}$ is the tree-level result as in Eq. (2.57) and $\delta_{\text{genuine}}^{(1)}\lambda_{ijk}$, $\delta_{\text{tadpoles}}^{(1)}\lambda_{ijk}$, $\delta_{\text{WFR}}^{(1)}\lambda_{ijk}$, and $\delta_{\text{CT}}^{(1)}\lambda_{ijk}$ are the several one-loop contributions. In particular, $\delta_{\text{genuine}}^{(1)}\lambda_{ijk}$ is the correction from the genuine three-point vertex functions (TPC on the left and TPB on the right):

where the solid line is a place holder for the different types of particles: scalars, fermions, gauge bosons, would-be Goldstone bosons and Faddeev-Popov ghosts. These type of diagrams are the ones included in the Coleman-Weinberg potential V_{CW}, where they are computed at zero external momentum.

The wave function renormalisation corrections enter in $\delta_{\text{WFR}}^{(1)}\lambda_{ijk}$

These contributions can be computed in terms of the self energies, $\sum_{ij}$, of the particles i, j, k as follows

$$
\begin{aligned}
\delta^{(1)}\lambda_{ijk}^{\text{WFR}}(p_i^2, p_j^2, p_k^2) &= \frac{1}{2}\left(\Sigma_i'(p_i^2)\lambda_{ijk}^{(0)} + \Sigma_j'(p_j^2)\lambda_{ijk}^{(0)} + \Sigma_k'(p_k^2)\lambda_{ijk}^{(0)}\right) \\
&\quad + \sum_{l \neq i}\frac{\Sigma_{il}(p_i^2)}{p_i^2 - m_l^2}\lambda_{ljk}^{(0)} + \sum_{l \neq j}\frac{\Sigma_{jl}(p_j^2)}{p_j^2 - m_l^2}\lambda_{ilk}^{(0)} + \sum_{l \neq k}\frac{\Sigma_{kl}(p_k^2)}{p_k^2 - m_l^2}\lambda_{ijl}^{(0)} \\
&\equiv \frac{1}{2}\left(\delta^{(1)}Z_i(p_i^2)\lambda_{ijk}^{(0)} + \delta^{(1)}Z_j(p_j^2)\lambda_{ijk}^{(0)} + \delta^{(1)}Z_k(p_k^2)\lambda_{ijk}^{(0)}\right) \\
&\quad + \sum_{l \neq i}\delta^{(1)}Z_{il}\lambda_{ljk}^{(0)} + \sum_{l \neq j}\delta^{(1)}Z_{jl}\lambda_{ilk}^{(0)} + \sum_{l \neq k}\delta^{(1)}Z_{kl}\lambda_{ijl}^{(0)},
\end{aligned}
\tag{2.64}
$$

where the prime means the derivative of the self energy with the respect to the momentum squared. Thus in the first line we compute the contributions of all the diagonal self-energies in the three external legs evaluated at a given momenta and in the second line we sum over all the possibilities of the off-diagonal self energies in the three external legs. After the equivalence sign we define the field renormalisation constants in terms of the corresponding diagonal or off-diagonal self-energies. The WFR corrections to a particular coupling such as the one involving two light Higgs bosons (h) and one heavier heavy CP-even Higgs boson (H), are given by:

$$
\begin{aligned}
\delta^{(1)}\lambda_{hhH}^{\text{WFR}}(p_1^2, p_2^2, p_3^2) &= \frac{1}{2}\delta^{(1)}Z_h(p_1^2)\lambda_{hhH}^{(0)} + \frac{1}{2}\delta^{(1)}Z_h(p_2^2)\lambda_{hhH}^{(0)} + \frac{1}{2}\delta^{(1)}Z_H(p_3^2)\lambda_{hhH}^{(0)} \\
&\quad + \delta^{(1)}Z_{hH}(p_1^2)\lambda_{hHH}^{(0)} + \delta^{(1)}Z_{hH}(p_2^2)\lambda_{hHH}^{(0)} + \delta^{(1)}Z_{Hh}(p_3^2)\lambda_{hhh}^{(0)}.
\end{aligned}
\tag{2.65}
$$

The contributions from the tadpole diagrams are captured in $\delta^{(1)}_{\text{tadpoles}}\lambda_{ijk}$,

where the first term is a contribution to the vertex and a second term is a contribution to the WFR correction, which can be included in the $\delta^{(1)}_{\text{WFR}}\lambda_{ijk}$ term (but not double counted).

Finally, the counterterm contributions to renormalise the result will depend on the chosen renormalisation scheme and is encoded in the term $\delta^{(1)}_{\text{CT}}\lambda_{ijk}$.

$$\left.\begin{array}{c} h_i \dashv\!\!\!\!\dashv\otimes \begin{array}{c} \diagup\,h_j \\ \diagdown\,h_k \end{array} \end{array}\right\}\ \delta_{\mathrm{CT}}^{(1)}\lambda_{ijk},$$

More about this approach and the automation followed in this tool will be discussed in Sec. 3.6.

2.6.3 Relation to the Early Universe

The importance of precise measurements of the trilinear Higgs self-coupling lies not only in unveiling the shape of the scalar potential today, which has implications for vacuum stability, but also in paving the way for a deeper understanding of the electroweak phase transition, i.e. the evolution of the scalar potential with temperature.

It is clear that a strong first order electroweak phase transition is required for a successful electroweak baryogenesis. It is also clear that this can only occur if the effective potential develops a significant barrier so that the change in the vacuum expectation value is abrupt. This barrier can be generated already in the tree-level scalar potential, e.g in the case of a singlet extension without a $\mathbb{Z}_2$ symmetry. Alternatively, this barrier can be generated by radiative or thermal corrections. In the former case, these corrections will also alter the trilinear self-couplings at $T = 0$.

The occurrence of a SFOEWPT is therefore often correlated with a deviation of the trilinear Higgs self-interaction, as has been shown in a vast class of toy models applicable to concrete UV complete models in Ref. [143]. There, $\mathcal{O}(1)$ deviations were realised whenever BSM physics was introduced to accommodate a SFOEWPT. Three possible mechanisms are explored: (1) large quantum corrections to the Higgs potential through large couplings to the Higgs, (2) presence of non-renormalisable terms in the potential and (3) tree-level scalar mixing. Another quite general analysis [144] showed that different types of modifications of the scalar potential (including exponential and logarithmic terms beyond polynomial ones[20]) that lead to SFOEWPT also necessarily imply 50% modification of the THC w.r.t the SM, which is precisely within the sensitivity of HL-LHC [145]. We will now briefly mention the three possible types of models introduced above.

Models with extended scalar sectors with a significant splitting between the mass scales can feature a very enhanced value of the Higgs self-coupling due to loop corrections, therefore they belong to the first class of models analysed in Ref. [143]. As an example, in a doublet extension of the SM, the condition of the strong first order phase transition necessarily leads to the deviation of the trilinear Higgs self-coupling of at least 10% from the SM prediction [146]. Quite generally, models with extended scalar sectors with large mass splitting feature large self-couplings [131] and we expect phase transitions to show up in these regions.

The second class of models contains the so called Effective field theories and composite Higgs models. For instance the Effective Field Theory of the SM (SMEFT) [147–149] can

---

[20]Logarithmic dependence of the potential on the fields is inspired by Coleman Weinberg potentials. On the other hand, the presence of exponentials of the inverse of the field are a signature of non-perturbative regimes.

accommodate first order electroweak phase transitions if non-renormalisable operators of dimension six are taken into account. These contribute directly to deviations in the trilinear couplings up to $\mathcal{O}(1)$ in κ_λ [150]. For a catalogue of different ways to generate an EWPT in SMEFT see [151]. In this case, however, the requirement of large Wilson coefficients signals the inadequacy of describing the dynamics of the phase transitions at electroweak scales with the Wilsonian EFT approach. A way to overcome this is by considering the Higgs Effective Field Theory (HEFT) [152–154]. In HEFT the THC is in fact relatively unconstrained and can become large [155].

While in the first two classes of models the relationship between the potential barrier and the trilinear Higgs coupling κ_λ is direct, this connection becomes less straightforward in the third. In models with tree-level scalar mixing (such as singlet-extended models), the dependence of κ_λ on model parameters is more complex. If all other parameters are fixed, the phase transition typically strengthens with increased mixing [156]. However, even in the absence of mixing, a strong first-order EWPT can still occur if the singlet field acquires a temporary vacuum expectation value at finite temperature that vanishes at zero temperature [157]. This illustrates that the thermal history of the early universe can differ substantially from zero-temperature collider physics, and that signatures of the electroweak phase transition may be accessible primarily through cosmological probes rather than at particle colliders.

To conclude this section we want to stress that a measurement of a deviation of the Higgs self-couplings at the LHC is quite generally an indirect probe of a first order phase transition, but cannot conclusively prove it. Therefore multimessenger probes need to be considered simultaneously. Conversely, a measurement of a THC consistent with the SM cannot completely exclude the SFOEWPT, but will substantially narrow the possible models that feature it, including in particular two Higgs doublets models.

2.7 Two Higgs Doublet Model

As introduced in Sec. 2.5, the 2HDM is one of the simplest and most common scalar extensions of the SM.[21] It adds to the SM particle content one complex doublet (Φ_1 and Φ_2) under the $SU(2)_L$ symmetry. This results in four additional degrees of freedom, two for each real and two for each charged components of the doublet, that mix together to give rise to the physical fields. The total number of physical states in the 2HDM is five: two CP-even states h and H, one CP-odd A and two charged scalars $H^\pm$. In the following our convention will be $m_h < m_H$ and h has the properties of the measured Higgs particle at 125 GeV.

The most general renormalisable[22] theory with two complex doublets contains 14 free parameters. However, an unrestricted 2HDM would lead to flavour changing neutral currents (FCNC), which are severely disfavoured by experiments. If both doublets couple to the same type of fermions, then after electroweak symmetry breaking, the mass matrices and Yukawa couplings are not simultaneously diagonalisable. This misalignment in flavour space leads to FCNCs because of the appearance of couplings between neutral Higgs bosons with different flavour fermions. To avoid this problem, we can restrict that each fermionic

---

[21]This section is based on my personal notes from the BSM Phenomenology couse by Prof. Dr. Georg Weiglein and Physics beyond the Standard Model course by Prof. Dr. M. Mühlleitner

[22]In the classical sense, meaning that all the operators have a dimension ≤ 4.
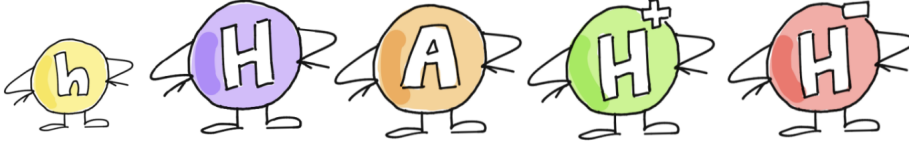
Figure 2.6
Artistic view of the scalar sector of the 2HDM: two CP-even states h and H,
one CP-odd A and two charged scalars $H^{\pm}$.

	u_R	d_R	ℓ_R	Q_L, L_L
Type I	-	-	-	+
Type II	-	+	+	+
Type III (lepton specific)	-	-	+	+
Type IV (flipped)	-	+	-	+

Table 2.1: $\mathbb{Z}_2$ charge assignments in the 2HDM.

family can only couple to one of the doublets. At the tree-level, such a behaviour can be achieved by imposing a $\mathbb{Z}_2$ symmetry [158, 159].[23] Under this symmetry, the two complex Higgs doublet fields transform as $\Phi_1 \to \Phi_1$ and $\Phi_2 \to -\Phi_2$. FCNC can still be avoided if the symmetry is softly broken by a mass term m_{12}^2. There is a total of four unique possibilities of $\mathbb{Z}_2$ charge assignments depending on which doublet couples to each fermion within a generation. The different variants depending on the Yukawa sector of 2HDM are shown in Tab. 2.1, where we specify the charge under $\mathbb{Z}_2$ of each fermionic multiplets. We notice that by convention Φ_2 couples to the up-type quark. The number of free parameters in the theory reduces to 10 after applying the $\mathbb{Z}_2$ symmetry, as it forbids the terms where there is mixing between the doublets.

For simplicity, we will assume a CP-conserving 2HDM [30, 42–44]. Neglecting the terms that explicitly break CP symmetry will further reduce the number of free parameters in the theory to 8, these are the real coefficients $m_{11}, m_{22}, m_{12}, \lambda_{1,\dots,5}$ that appear in the general form of the $\mathbb{Z}_2$ symmetric 2HDM tree-level potential ,

$$
\begin{aligned}
V \;=\;& m_{11}^2(\Phi_1^\dagger \Phi_1) + m_{22}^2(\Phi_2^\dagger \Phi_2) - m_{12}^2(\Phi_1^\dagger \Phi_2 + \Phi_2^\dagger \Phi_1) + \frac{\lambda_1}{2}(\Phi_1^\dagger \Phi_1)^2 + \frac{\lambda_2}{2}(\Phi_2^\dagger \Phi_2)^2 \\
&+ \lambda_3(\Phi_1^\dagger \Phi_1)(\Phi_2^\dagger \Phi_2) + \lambda_4(\Phi_1^\dagger \Phi_2)(\Phi_2^\dagger \Phi_1) + \frac{\lambda_5}{2}[(\Phi_1^\dagger \Phi_2)^2 + (\Phi_2^\dagger \Phi_1)^2] \, .
\end{aligned}
\tag{2.66}
$$

---

[23]The Paschos–Glashow–Weinberg theorem states that tree-level FCNCs are avoided if all fermions with the same charge and helicity transform under the same $SU(2)_L$ representation, have the same isospin, and receive mass from a single source in some basis. For a SM-like Yukawa sector, this means all right-handed quarks of a given charge must couple to one Higgs doublet. This leads to two options in the 2HDM: all quarks couple to the same doublet (Type I), or up-type and down-type right-handed quarks couple to different doublets (Type II). Variants like Type-III or IV differ in how leptons couple, which is not constrained by the theorem.

The fields Φ_1 and Φ_2 can be conveniently parametrised as

$$\Phi_1 = \begin{pmatrix} \phi_1^+ \\ \frac{1}{\sqrt{2}}(v_1 + \rho_1 + i\eta_1) \end{pmatrix}, \qquad \Phi_2 = \begin{pmatrix} \phi_2^+ \\ \frac{1}{\sqrt{2}}(v_2 + \rho_2 + i\eta_2) \end{pmatrix}, \qquad (2.67)$$

in terms of their respective vacuum expectation values, v_1 and v_2 (with $v_1^2 + v_2^2 \equiv v^2 \sim 246^2$ GeV), and the interaction fields $\phi_{1,2}^\pm$, $\rho_{1,2}$ and $\eta_{1,2}$. After rotating the fields from the interaction to the mass basis the degrees of freedom $\phi_{1,2}^\pm$, $\rho_{1,2}$ and $\eta_{1,2}$ mix to give rise to five physical scalar fields $(h, H, A, H^\pm)$ and three would-be-Goldstone bosons $(G^0, G^\pm)$. The mixing matrices diagonalising the CP-even and CP-odd/charged Higgs mass matrices can be expressed in terms of the mixing angles α and β, respectively, with $t_\beta \equiv v_2/v_1$.[24]

Additionally, two minimisation conditions can be applied to introduce the tadpoles

$$\left.\frac{\partial V}{\partial \rho_1}\right|_{\substack{\Phi_1=\langle\Phi_1\rangle \\ \Phi_2=\langle\Phi_2\rangle}} \overset{!}{=} T_1, \; \left.\frac{\partial V}{\partial \rho_2}\right|_{\substack{\Phi_1=\langle\Phi_1\rangle \\ \Phi_2=\langle\Phi_2\rangle}} \overset{!}{=} T_2, \; \text{where} \; \langle\Phi_1\rangle = \begin{pmatrix} 0 \\ \frac{v_1}{\sqrt{2}} \end{pmatrix}, \langle\Phi_2\rangle = \begin{pmatrix} 0 \\ \frac{v_2}{\sqrt{2}} \end{pmatrix}, \; (2.68)$$

and usually the tadpoles $T_1 = T_2 = 0$ at tree-level, but they will play a role in the renormalisation of the one-loop result (See Sec. 3.6).

In the following we will restrict ourselves to the physical basis of the 2HDM, where the free parameters are the masses, mixing angles and vacuum expectation values

$$c_{\beta-\alpha}, \; t_\beta, \; v, \; m_h, \; m_H, \; m_A, \; m_{H^\pm}, \; m_{12}^2. \qquad (2.69)$$

$m_h, m_H, m_A, m_{H^\pm}$ being the masses of the physical scalars $h, H, A, H^\pm$ respectively. We sometimes also use $M^2 \equiv m_{12}^2/(s_\beta c_\beta)$ instead of m_{12}^2 when convenient.

The decoupling limit of the 2HDM: The mass terms for the heavier Higgses can be expressed as

$$m_\phi^2 = M^2 + \lambda_\phi v^2 \left(+\mathcal{O}(v^4/M^2)\right), \qquad (2.70)$$

where $\phi = H, A, H^\pm$ and λ_ϕ is a linear combination of $\lambda_{1,\dots,5}$. If the first term in Eq. (2.70) is much larger than the second term, i.e. $M^2 \gg \lambda_\phi v^2$, the effective theory below the soft symmetry breaking scale M is described by one Higgs doublet. Effectively the heavy states "decouple" as the effects of the heavy states in the loops vanish and h properties become SM-like. This is described by the decoupling theorem [160]. If the value of the soft symmetry breaking parameter M is close to the electroweak scale $M^2 \lesssim \lambda_\phi v^2$, the mass of the heavy states can be enhanced by the occurrence of large quartic couplings.[25] The inapplicability of the decoupling theorem leads to large contributions of the heavy scalars in the radiative corrections of the process, leading to the so called *non-decoupling effect*. In this scenario, it is important to make sure that perturbative unitarity is fulfilled, because λ_i cannot be arbitrarily large in order to fulfill theoretical constraints, which will be discussed in greater detail in Sec. 2.7.2.

The alignment limit of the 2HDM: The *alignment limit* [161] corresponds to $c_{\beta-\alpha} \to 0$, where the light Higgs boson h has couplings to fermions and gauge bosons at lowest order that exactly correspond to the ones in the SM.

---

[24]In the following, we use the short-hand notation $s_x \equiv \sin x$, $c_x \equiv \cos x$, $t_x \equiv \tan x$.

[25]We will call the quartic couplings the parameters λ_i entering in the potential in analogy to the SM λ that determines the SM quartic coupling up to a prefactor.

	type I	type II	type III	type IV
ξ_u	$\cot\beta$	$\cot\beta$	$\cot\beta$	$\cot\beta$
ξ_d	$\cot\beta$	$-\tan\beta$	$\cot\beta$	$-\tan\beta$
ξ_l	$\cot\beta$	$-\tan\beta$	$-\tan\beta$	$\cot\beta$

Table 2.2: Factors appearing in the Yukawa couplings in the four 2HDM Types.

2.7.1 Couplings

The richer scalar content of the 2HDM implies that the mixing between the additional states will alter the couplings of the scalars to the other fermionic and bosonic fields w.r.t. the SM.

Couplings to fermions: The couplings of the neutral Higgs bosons to fermions are

$$
\begin{aligned}
\mathcal{L}_Y \;=\; & -\sum_{f=u,d,l} \frac{m_f}{v} \left[\xi_h^f \bar{f}fh + \xi_H^f \bar{f}fH + \xi_A^f \bar{f}\gamma_5 fA \right] \\
& - \frac{\sqrt{2}}{v} \left[\bar{u}(\xi_d V_{\mathrm{CKM}} m_d P_R)dH^+ + \xi_l \bar{\nu} m_l P_R l H^+ + \text{h.c.} \right],
\end{aligned}
\tag{2.71}
$$

where m_f are the fermion masses, V_{CKM} is the CKM matrix and $P_{R,L} = (1 \pm \gamma^5)/2$ are the right and left chiral projectors, respectively. The values of $\xi_f^{h,H,A}$ are called Yukawa coupling modifiers and they are given by,

$$
\xi_f^h = s_{\beta-\alpha} + \xi_f c_{\beta-\alpha}, \quad \xi_f^H = c_{\beta-\alpha} - \xi_f s_{\beta-\alpha}, \quad \xi_u^A = -i\xi_u \quad \text{and} \quad \xi_{d,l}^A = i\xi_{d,l}, \tag{2.72}
$$

where the factors ξ_f depend on the 2HDM Type, their explicit values are given in Tab. 2.2 [162].

Couplings to gauge bosons: The couplings of the neutral scalars with the massive gauge bosons $V = W^\pm, Z$ are given by the terms

$$
\mathcal{L} \supset \sum_{h_i=h,H} \left[gm_W \xi_{h_i}^W W_\mu W^\mu h_i + \frac{1}{2} gm_Z \xi_{h_i}^Z Z_\mu Z^\mu h_i \right]. \tag{2.73}
$$

where m_W and m_Z are the masses of the gauge bosons $W^\pm$ and Z, g is the coupling constant corresponding to $SU(2)_L$ and the gauge coupling modifiers $\xi_{V=W,Z}$ are defined as

$$
\xi_V^h = s_{\beta-\alpha}, \quad \text{and} \quad \xi_V^H = c_{\beta-\alpha}. \tag{2.74}
$$

Note that $\xi_V^A = 0$, and the sum rule $\sum_i (\xi_V^{h_i})^2 = 1$ automatically holds. The latter condition ensures that the scattering amplitude of longitudinal gauge bosons in longitudinal gauge bosons is unitarised. Therefore sum rules are a general theoretical constraint in models with extended scalar sectors.

Scalar self-couplings: The explicit expressions of the possible tree-level trilinear Higgs couplings in the 2HDM are given by

$$\lambda_{hhh} = \frac{1}{2v^2} \left\{ m_h^2 s_{\beta-\alpha}^3 + \left(3m_h^2 - 2M^2\right) c_{\beta-\alpha}^2 s_{\beta-\alpha} + 2\cot 2\beta \left(m_h^2 - M^2\right) c_{\beta-\alpha}^3 \right\},$$
(2.75)

$$\lambda_{hhH} = -\frac{c_{\beta-\alpha}}{2v^2} \left\{ \left(2m_h^2 + m_H^2 - 4M^2\right) s_{\beta-\alpha}^2 + 2\cot 2\beta \left(2m_h^2 + m_H^2 - 3M^2\right) s_{\beta-\alpha} c_{\beta-\alpha} \right.$$
$$\left. - \left(2m_h^2 + m_H^2 - 2M^2\right) c_{\beta-\alpha}^2 \right\},$$
(2.76)

$$\lambda_{hHH} = \frac{s_{\beta-\alpha}}{2v^2} \left(s_{\beta-\alpha}^2 \left(m_h^2 + 2m_H^2 - 2M^2\right) + 2s_{\beta-\alpha} c_{\beta-\alpha} \cot 2\beta \left(m_h^2 + 2m_H^2 - 3M^2\right) \right),$$
(2.77)

$$\lambda_{HHH} = \frac{1}{2v^2} \left(c_{\beta-\alpha}^3 m_H^2 + s_{\beta-\alpha}^2 c_{\beta-\alpha} \left(3m_H^2 - 2M^2\right) - 2s_{\beta-\alpha}^3 \cot 2\beta \left(m_H^2 - M^2\right) \right),$$
(2.78)

$$\lambda_{hAA} = \frac{1}{2v^2} \left(s_{\beta-\alpha} \left(2m_A^2 + m_h^2 - 2M^2\right) + 2c_{\beta-\alpha} \cot 2\beta \left(m_h^2 - M^2\right) \right),$$
(2.79)

$$\lambda_{HAA} = \frac{1}{2v^2} \left(c_{\beta-\alpha} \left(2m_A^2 + m_H^2 - 2M^2\right) - 2s_{\beta-\alpha} \cot 2\beta \left(m_H^2 - M^2\right) \right),$$
(2.80)

$$\lambda_{hH^+H^-} = \frac{1}{v^2} \left(s_{\beta-\alpha} \left(m_h^2 + 2m_{H^\pm}^2 - 2M^2\right) + 2c_{\beta-\alpha} \cot 2\beta \left(m_h^2 - M^2\right) \right),$$
(2.81)

$$\lambda_{HH^+H^-} = \frac{1}{v^2} \left(c_{\beta-\alpha} \left(m_H^2 + 2m_{H^\pm}^2 - 2M^2\right) - 2s_{\beta-\alpha} \cot 2\beta \left(m_H^2 - M^2\right) \right).$$
(2.82)

These represent all the possible couplings that are both electrically neutral and CP-even. If the 2HDM potential included CP-violating terms, couplings such as λ_{Ahh} or λ_{AHH} would be allowed. However, they are forbidden in the CP-conserving scenario considered here. Note that the tree-level dependence of the trilinear couplings on $c_{\beta-\alpha}$ ensures that λ_{hhh} approaches the SM value in the alignment limit, and that the BSM trilinear coupling λ_{hhH} vanishes, while the other BSM couplings remain non-zero and will have an impact in loop calculations. These couplings will receive significant corrections at one-loop as discussed in Sec. 2.6.2 and as will be analysed in detail in the context of the 2HDM in Sec. 3.2.

In the 2HDM, it has been shown that the loop contributions to the THCs involving the heavy BSM Higgs bosons can give rise to corrections of the order of 100% and

larger [124, 125] w.r.t. their tree-level values. More recently, also two-loop corrections have been computed [134] enhancing in some parts of the parameter space the value of κ_λ to the sensitivity of current and future runs of the LHC [126]. The occurrence of large loop corrections should, however, not been regarded as a sign of the breakdown of perturbation theory, as large corrections at one-loop order are present mainly due to new contributions involving couplings of the Higgs boson h to heavier BSM Higgs bosons that do not appear at tree-level [125], while the size of the two-loop corrections relative to the one-loop result follows the expected perturbative behaviour [126, 134, 135] (see Sec. 2.6.2). In view of these findings the impact of these large higher-order corrections on the Higgs pair production process will be investigated in Chapter 3.

2.7.2   Constraints

There is no strong reason for the scalar sector in nature to be minimal. On the contrary, an extended scalar sector is very well motivated by the shortcomings of the SM. However, there are some requirements that need to be satisfied so that the extended sector theory is theoretically consistent and experimentally allowed. In this subsection we briefly summarise the various theoretical and experimental constraints that need to be taken into account when working in extended scalar sectors and in particular how they are applied in the 2HDM in this analysis.

2.7.2.1   Theoretical constraints

Custodial symmetry: The custodial symmetry is an approximate symmetry of the SM that protects the relationship between the $W^\pm$ and the Z masses. It prevents large quantum corrections to the ratio of these masses, preserving the tree-level mass ratio

$$\rho = \frac{m_W}{m_Z \cos \theta_W} \approx 1, \tag{2.83}$$

which is in agreement with the measurement $\rho = 1.01016 \pm 0.00009$ [99]. In a more general theory, with n scalar multiples ϕ_i with weak isospin I_i, weak hypercharge Y_i and vev of the neutral components v_i, the tree-level ρ parameter is

$$\rho = \frac{\sum_{i=1}^{n} [I_i(I_i + 1) - \frac{1}{4} Y_i^2] v_i}{\sum_{i=1}^{n} \frac{1}{2} Y_i^2 v_i}. \tag{2.84}$$

Since the $SU(2)_L$ doublets with $Y = 1$ present in the 2HDM satisfy the relation

$$I(I + 1) = \frac{3}{4} Y^2, \tag{2.85}$$

$\rho = 1$ holds automatically at tree-level.

Perturbative unitarity: It is required that the S-matrix defined in Eq. (2.22) is unitary, as it represents the probability amplitudes for transitions between asymptotic quantum states. We will translate this condition on the parameters of the Lagrangian, and in particular on the quartic couplings in order to set a theoretical bound on their

values, this will give us an upper bound above which the couplings become too large for perturbative unitarity to be a trustworthy procedure.

Using the relation between the S-matrix and the scattering amplitude $\mathcal{M}$ given in Eq. (2.23), and imposing the unitarity condition on the S-matrix, one can arrive at the optical theorem [163], which relates the scattering cross section with the imaginary part of the scattering amplitude for a 0 scattering angle

$$\sigma = \frac{1}{s}\text{Im}\mathcal{M}(\theta = 0), \tag{2.86}$$

where θ is the scattering angle. Additionally, we can expand a general wave function in terms of partial waves by means of Legendre polynomials P_ℓ, where ℓ is the order of the polynomial that represents the orbital angular momentum quantum number. We take the limit of large distance from the scattering center, which is an accurate limit for our purposes, and we perturb the wave by some scattering $S_\ell(k)$, which leads to the following expression [164]

$$\psi(\vec{r}) \simeq e^{ikr\cos\theta} + \left[\sum_{\ell=0}^{\infty}(2\ell+1)\frac{S_\ell(k)-1}{2ik}P_\ell(\cos\theta)\right]\frac{e^{ikr}}{r} \equiv e^{ikr\cos\theta} + f(\theta)\frac{e^{ikr}}{r}, \tag{2.87}$$

where $\vec{r}$ is the position vector and k is the wavenumber or the momentum p in the center of mass (c.m.) frame. The first term is the original incident plane wave and the second term is the outgoing spherical wave, where we define $f(\theta)$ as the coefficient that determines the scattering strength.

By definition, the partial wave amplitude is

$$a_\ell(k) \equiv \frac{S_\ell(k)-1}{2ik}. \tag{2.88}$$

Therefore the condition on the unitarity of the scattering $|S_\ell(k)| \leq 1$ can be translated into the following conditions on a_ℓ

$$|a_\ell| \leq 1, \quad |\text{Re}(a_\ell)| \leq 1/2 \quad \text{and} \quad 0 \leq \text{Im}(a_\ell) \leq 1, \tag{2.89}$$

which defines the area inside a circle in the complex plane centered at $(0, i/2)$ and radius $1/2$.

We can translate these bounds to some measurable quantities, such as the cross section for a given process. Recalling the definition of the differential cross section

$$\frac{d\sigma}{d\Omega} = |f(\theta)|^2, \tag{2.90}$$

and in QFT in the c.m. frame, where the energy is $E_{\text{CM}} \approx 2p$, the cross section is

$$\left(\frac{d\sigma}{d\Omega}\right)_{\text{CM}} = \frac{|\mathcal{M}|^2}{64\pi^2 E_{\text{CM}}^2}, \tag{2.91}$$

from where we derive

$$\mathcal{M}(\theta) = 16\pi \sum_{l=0}^{\infty} a_\ell (2l + 1) P_\ell(\cos\theta), \qquad (2.92)$$

which holds in a full result and a_ℓ must lie within the bounds in Eq. (2.89). Usually in QFT we can compute $\mathcal{M}$ up to a particular order in perturbation theory, and if we truncate the calculation at a specific order, it does not need to satisfy the bounds on a_ℓ. In general a_ℓ are matrices, so the bounds are imposed on their eigenvalues. They are also always real, therefore usually the first two conditions in Eq. (2.89) are used. Strictly speaking, the tree-level results will then automatically break perturbative unitarity, as only the minimum of the complex circle is in the real axis, and this at an $a_\ell = 0$, but it is expected that perturbative corrections to the imaginary part of a_ℓ will restore unitarity.

A commonly used scattering amplitude is the scalar $2 \to 2$ scattering, which are the relevant ones to constrain the interactions. We can get rid of the angular dependence in a_ℓ and therefore keep the only contributing mode a_0. Then taking for instance the first bound in Eq. (2.89) and substituting it in Eq. (2.92) and taking into account that $P_0(x) = 1$ we get

$$|\mathcal{M}_{2\to2}^i| \leq 16\pi, \qquad (2.93)$$

where the index i runs over the eigenvalues of the scattering matrix elements in any basis. If the second condition in Eq. (2.89) was chosen, the limits will be 8π and both are used in the literature.

If these tree-level conditions are violated, then perturbative corrections need to be also large to unitarise the result, this usually signals that the couplings on which perturbative expansion is made are too large. Therefore we can say that a violation of unitarity in some parameter regions signals a breakdown of perturbation theory, and the results cannot be trusted above this threshold.

Historically, the requirement of perturbative unitarity was applied to predict an upper bound on the Higgs mass at around 1 TeV [165, 166], which served as a rationale for the construction of the LHC.[26]

In the 2HDM these bounds have been derived at tree-level [167–169] and can be conveniently written in terms of the quartic couplings as

---

[26] As mentioned before, the Higgs boson unitarises the scattering amplitude of longitudinal gauge bosons.

$$\left| \frac{1}{2} \left(3\lambda_1 + 3\lambda_2 \pm \sqrt{9(\lambda_1 - \lambda_2)^2 + 4(2\lambda_3 + \lambda_4)^2} \right) \right| \leq 16\pi,$$

$$|\lambda_3 + 2\lambda_4 \pm 3\lambda_5| \leq 16\pi,$$

$$\left| \frac{1}{2} \left(\lambda_1 + \lambda_2 \pm \sqrt{(\lambda_1 - \lambda_2)^2 + 4\lambda_5^2} \right) \right| \leq 16\pi,$$

$$|\lambda_3 + 2\lambda_4 \pm 3\lambda_5| \leq 16\pi, \qquad (2.94)$$

$$\left| \frac{1}{2} \left(\lambda_1 + \lambda_2 \pm \sqrt{(\lambda_1 - \lambda_2)^2 + 4\lambda_4^2} \right) \right| \leq 16\pi,$$

$$|\lambda_3 + 2\lambda_4 \pm 3\lambda_5| \leq 16\pi,$$

$$|\lambda_3 \pm \lambda_4| \leq 16\pi,$$

$$|\lambda_3 \pm \lambda_5| \leq 16\pi,$$

These conditions can be extended to NLO [170, 171] by tracking the dependence of the couplings on the energy scale with the RGE running of the couplings, which leads to similar but more complicated equations to bound the quartic couplings in terms of the correponding beta-functions.

We also note here that the parameter space allowed by perturbative unitarity can be enlarged, if we allow for a mass term breaking the imposed $\mathbb{Z}_2$ symmetry softly, i.e. we choose a non-zero m_{12}^2. In some of the sample scenarios that we will investigate later, we chose m_{12}^2 as

$$m_{12}^2 = \frac{m_H^2 c_\alpha^2}{t_\beta}. \qquad (2.95)$$

This choice prevents λ_1 from recieving large corrections for large t_β and ensures a larger allowed region by theoretical constraints when close to the alignment limit [172] (see also [162]).

Constraints on the electroweak vacuum: There are additional theoretical constraints arising from the shape of the scalar potential, in particular two things need to be ensured: that the potential is bounded from below, and that it contains a *sufficiently* stable minimum at the location of the EW vev.

A stable electroweak minimum is a requirement of a consistent perturbation theory, therefore the scalar potential needs to be bounded from below to prevent tunnelling to an unstable vacuum configuration. In the SM, the boundedness from below is satisfied if

$$\lambda > 0, \qquad (2.96)$$

where λ is defined in Eq. (2.29). A positive quartic coupling thus ensures that at large values of ϕ the potential stays positive. This directly impacts the trilinear Higgs coupling as well, as it only differs from λ by an additional factor of v.

In the 2HDM there are eight field directions. Therefore the conditions for boundedness from below are more involved, as they need to prevent the potential from becoming

arbitrarily large at large field values in any of these field directions. The conditions
on the quartic couplings that ensure boundedness from below at tree-level are [173]

$$\lambda_1, \lambda_2 > 0, \quad \lambda_3 + \lambda_4 - |\lambda_5| > -\sqrt{\lambda_1 \lambda_2}, \quad \lambda_3 < -\sqrt{\lambda_1 \lambda_2}. \tag{2.97}$$

Since the trilinear Higgs coupling is a more complicated relation of the quartic cou-
plings, this means in particular that negative values of the trilinear coupling are viable,
as long as the conditions in Eq. (2.97) are fulfilled.

An additional constraint related to the vacuum of the theory comes from the fact that
the minimum of the potential should be at ~ 246 GeV, as this is the experimentally
required value. However, it does not need to be an absolute minimum of the potential
as long as it is sufficiently stable. The possibility of tunnelling to deeper minima
remains viable, as long as the vacuum lifetime exceeds the age of the Universe. To
study the dynamics of the vacuum, the tree-level potential is insufficient, and the
zero-temperature effective potential has to be evaluated. In the SM in the leading
logarithmic approximation, and taking into account only the heaviest particles in the
theory (top quark, $W^\pm$, Z and the Higgs itself) this potential is [27]

$$V(\phi) = \lambda(\mu)\phi^4 + \frac{3m_Z^4 + 6m_{W^\pm}^4 - 12m_t^4 + 3m_h^4}{16\pi^2 v^4}\phi^4 \ln(\frac{\phi^2}{\mu^2}). \tag{2.98}$$

where μ is the renormalisation scale. We see that the second term is negative due
to the large mass of the top. This means that the vacuum at one-loop is not stable
but metastable in the SM for μ values above $\simeq 10^{10}$ GeV. Taking into account the
RGE running of the quartic coupling λ up to three-loops, stability would occur at the
border of a 3σ region [174,175]. This however is not a big problem, as the decay rate is
much smaller than the inverse of the age of the Universe. This decay occurs through
spontaneous nucleation of bubbles of the vacuum, which is a tunnelling process at
$T = 0$ and therefore quite suppressed. A proper calculation is derived from the decay
rate per unit volume and unit time

$$\Gamma \sim A e^{-S_4}, \tag{2.99}$$

where S_4 is the so called bounce action, which is a semiclassical solution to the equa-
tions of motion of the Euclidean action (i.e. the action with imaginary time) and
A is a subleading dimensionful parameter. An approximate calculation with the SM
parameters leads to a vacuum decay probability of $P \sim 10^{-340}$ [94].

In BSM models without RGE running, an estimate of the result for vacuum stability
in terms of the bounce action was made in Ref. [41,176], where a vacuum is considered
unstable if

$$S_4 < 390. \tag{2.100}$$

---

[27]This is an approximation of the full CW potential, details in App. A

In the 2HDM a stronger constraint can be imposed without the need to compute the bounce action, by requiring that the minimum is a global minimum. In that case a simpler condition can be applied [177]

$$m_{12}^2 \left(m_{11}^2 - m_{22}^2 \sqrt{\frac{\lambda_1}{\lambda_2}} \right) \left(t_\beta - \sqrt[4]{\frac{\lambda_1}{\lambda_2}} \right) \geq 0. \tag{2.101}$$

Constraints from electroweak precision data: The electroweak precision observables (EWPO) are a set of parameters in the electroweak sector that are highly senstive to deviations from the SM prediction from possible new physics, they include the gauge boson masses m_Z, m_W, the Z decay width Γ_Z, the Fermi constant G_F, among others. For SM extensions based solely on extensions of the Higgs sector, some of the constraints from the EWPO can be expressed in terms of the oblique parameters S, T and U [178, 179], which parametrise deviations from the SM.

S: is sensitive to new physics that affect the photon and the Z boson propagators, therefore related to anomalies in neutral currents.

T: is sensitive to deviations in the ratio of the $W^\pm$ and the Z masses, reflecting the amount of custodial symmetry breaking in the theory. In particular [180],

$$\rho - 1 = \frac{1}{1 - \alpha T} - 1 \simeq \alpha T, \tag{2.102}$$

where $\alpha = 1/137$ is the fine structure constant.

U: it is related to the $W^\pm$ boson propagator and is usually less sensitive than the others.

These parameters are constrained from experimental measurements with relatively high precision [99]

$$S = -0.04 \pm 0.10, \ T = 0.01 \pm 0.12, \ U = -0.01 \pm 0.09, \tag{2.103}$$

Most constraining in the 2HDM is the T parameter, requiring either $m_{H^\pm} \approx m_A$ or $m_{H^\pm} \approx m_H$. Therefore in the simplest scenarios analysed in this thesis we will assume mass degeneracy, i.e. $m_H = m_{H^\pm} = m_A$. Alternatively the combinations of $m_{H^\pm} = m_A$ and $m_{H^\pm} = m_H$ will usually ensure that EWPO constraints are fulfilled.

In practice, compatibility with EWPO can be tested by direct comparison of experimental data with the predicted values of the electroweak observables for a specific parameter point. These observables are in particular the W-mass, the total decay width of the Z boson and the effective weak mixing angle at the Z-boson resonance. In the 2HDM, such calculations can be performed in an automated way using the software `THDM_EWPOS` [181–183], which includes the full one-loop corrections and the leading non-standard two-loop contributions from the top-Yukawa coupling and the scalar self-couplings, the latter only in the aligment limit of the 2HDM. In our analysis, these predictions are required to be in a 2σ agreement with the experimental measurements (by default the prediction for m_W is checked against the average value from the LHC–TeV m_W Working Group [184], which does not include the latest CDF

m_W result). Alternatively, a statistical χ^2 fit in terms of the parameters S, T and U can be performed and again a 2σ agreement between measurements and prediction is required. In contrast to precise calculations provided in `THDM_EWPOS` (even though the most precise calculations are only available in the alignment limit), the S, T and U parameters are evaluated only at the one-loop level according to Ref. [185]. The experimental fit values of the oblique parameters, their uncertainties and correlations are taken from Ref. [186].

2.7.2.2   Experimental constraints

The search for new physics is an active branch of the activities of particle physics colliders, and a motivation to pursue future experiments. These limits cover a wide range of masses and couplings for possible new physics candidates, many of which cover specific targets of the extra scalars predicted in extended scalar models and the 2HDM in particular.

Therefore, every BSM sector that either contains additional scalars or modifications of the SM-like Higgs couplings to the other particles, has to be tested against the experimental data of the past and present collider experiments. The amount of the available experimental data makes it unfeasible to perform such analysis *by hand* whenever considering extended scalar sectors. Therefore, the need arises to develop automated tools that contain these large experimental datasets and facilitate the comparison with the theory predictions within a given model.

Such tools have been available for a long time. Notably, the `HiggsBounds` dataset, which includes existing BSM searches in several colliders such as LEP (Large Electron-Positron Collider) and LHC, was first developed in 2008 [187] and subsequently updated in newer versions [187–191] (see also Ref. [192]). The idea behind `HiggsBounds` is to incorporate the experimental searches for BSM scalar particles. So far these searches have not lead to a discovery, therefore they result in exclusion limits that constrain the parameter space of BSM models.

In 2022, CMS [193] and ATLAS [194] published summary papers of all the properties of the Higgs boson that have been measured in 10 years since the Higgs discovery. This includes the main Higgs boson production cross sections and branching ratios of the decays. It also includes the intervals of the couplings of the Higgs to the other SM particles in the so called $\kappa-$framework, which paramaterises deviations from the SM prediction. Any model beyond the SM has to accommodate a Higgs boson with mass and signal strengths as the ones measured at the LHC.

Recently, `HiggsBounds` was integrated with `HiggsSignals` [191,195–197], which checks the compatibility of BSM parameter points with precision measurements of the discovered Higgs boson, h. Similarly to `HiggsBounds`, `HiggsSignals` constraints the BSM sectors that despite having a Higgs with a mass at the measured 125 GeV, predict deviations of some of its couplings. The resulting combined tool, named `HiggsTools` [191], is written in modern `C++` and includes `Python` and `Mathematica` interfaces for the user convenience. Additionally, `HiggsTools` incorporates a new package, `HiggsPredictions`, which calculates cross sections and branching ratios directly from the provided couplings in a given BSM model.

In the following we will briefly outline how each of these tests is performed.

HiggsBounds: It includes the experimental exclusion limits at the 95% confidence level of all relevant BSM Higgs boson searches (at LEP and LHC). As input it requires some specific model predictions, either production cross sections and branching ratios of the specified BSM state to the other particles, or alternatively their effective couplings, normalised to the SM ones. The former can be computed via effective couplings in the `HiggsPredictions` framework or directly provided in case specific and more refined prediction tools are available for that model. In particular, in the 2HDM there are two commonly used public codes for the computation of branching ratios, `2HDMC-1.8.0` [198] and `HDECAY` [199,200]. For a comparison of the two codes, see [201].

For a parameter point in a particular model, the code selects which are the applied searches depending on the BSM particles involved. It determines on the basis of expected limits which is the most sensitive channel to test each BSM Higgs boson. This is determined by selecting the search with the highest expected ratio

$$R_{\mathrm{exp}} = \frac{(\sigma \times \mathrm{BR})_{\mathrm{model}}}{(\sigma \times \mathrm{BR})_{\mathrm{expected}}}, \tag{2.104}$$

where the expected numbers are taken from the experimental data. Then, based on this most sensitive channel, `HiggsBounds` determines whether the point is allowed or not at the 95% CL, which is equivalent to excluding the points with an observed ratio larger than one

$$R_{\mathrm{obs}} = \frac{(\sigma \times \mathrm{BR})_{\mathrm{model}}}{(\sigma \times \mathrm{BR})_{\mathrm{obs}}} > 1, \tag{2.105}$$

where again the observed quantities are taken from experimental data.

HiggsSignals: Provides a statistical χ^2 analysis of Higgs boson predictions within a certain model compared to the experimentally measured signal rates and masses. If not stated otherwise, our criterium for allowed scenarios in the 2HDM will be that the corresponding χ^2 value of the parameter point is within $2\,\sigma$ ($\Delta\chi^2 = 6.18$) from the SM fit: $\chi^2_{\mathrm{SM}} = 151.70$.

Constraints from flavour physics: In the 2HDM, the presence of the charged Higgs boson can significantly alter the prediction for flavour changing processes. Some flavour observables like rare B decays, mixing parameters of B mesons, and LEP constraints on Z decay partial widths are sensitive to the contributions of charged Higgs bosons [202, 203]. The most constraining decays are usually

$$\begin{aligned} \mathrm{BR}(B \to X_s \gamma) &= 3.49 \cdot 10^{-4} \pm 0.19 \cdot 10^{-4}, \\ \mathrm{BR}(B_s \to \mu^+ \mu^-) &= 3.45 \cdot 10^{-9} \pm 0.29 \cdot 10^{-9}. \end{aligned} \tag{2.106}$$

In our analysis, the experimental values are taken from Ref. [204]. To compare with the theoretical predictions in the 2HDM we use the code `SuperIso` [205–207].

In order to take into account all these constraints we developed a specific code in the 2HDM (with real parameters and a softly-broken $\mathbb{Z}_2$ symmetry): `thdmtools` [2]. It is a python package that allows the user to check the compatibility of a particular parameter

point with the aforementioned constraints. The input for the code is given in terms of the free parameters of the model (see Eq. (2.69)). During the installation of this package the following external codes will also be downloaded and installed: `AnyHdecay` [199, 200, 208], which computes the branching ratios and decay widths of all Higgs bosons contained in the model, `HiggsTools` [191] (if not already installed in the current `python` environment of the user), `THDM_EWPOS` [181–183] and `SuperIso` [205–207].

2.7.3 Electroweak Baryogenesis

In the 2HDM the phase transition giving rise to EW symmetry breaking can be rendered to be a sufficiently strong first-order transition, providing the out-of-equilibrium conditions required for EW baryogenesis [39, 40, 77, 209–212]. The presence of the heavier scales leads to an alteration of the Higgs potential that allows for a SFOEWPT even for the light Higgs-boson mass up to 200-300 GeV [39, 40], provided that a sufficient mass splitting with the heavier mass scales is realised. This possibility is excluded now by the measurement of the Higgs at 125 GeV, but it is interesting to note that the presence of the extra scalars pushes the upper bound for the Higgs mass compatible with a SFOEWPT (which is 80 GeV in the SM) to such high values. In the CP violating 2HDM it is shown that low values of t_β are preferred for a successful baryogenesis [40], since the baryon asymmetry is suppressed by a factor of $\sim t_\beta^2$. A favoured mass hierarchy of the heavier scalars was established in Ref. [213], in particular $m_{H^+} < m_H < m_A$, with $m_A \sim 400$ GeV. Also a preference of a SFOEWPT towards the alignment limit is established in Refs. [213, 214]. In Ref. [214] correlations between the zero temperature effective potential and the finite temperature potential are made, earlier noted in Ref. [146]. In Chapter 5 we will investigate in greater detail the scenarios of a SFOWPT in the 2HDM and present ways to probe them phenomenologically.

Chapter 3

Higgs pair production at the (HL-)LHC

Contents

The measurement of the Higgs pair production cross section constitutes a primary motivation for the High Luminosity upgrade of the LHC. This physical process gains its importance due to the direct access it provides to the trilinear Higgs coupling, which in turn probes the structure of the Higgs sector through the shape of the scalar potential. Producing two Higgses simultaneously has been challenging so far because of the small cross section, the main reason being that the main production mode is a loop-induced process at LO, where the contributing diagrams interfere destructively. Furthermore, the phase space is small, as two heavy particles need to be produced in the final state. Additionally, the large backgrounds of the dominant decay modes, for instance to 4 bottom quarks ($hh \to b\bar{b}b\bar{b}$),

further difficult the measurement. This is the reason why higher luminosity is required in order to study this process with enough statistics.

The dominant production mode in a hadron collider, such as the LHC [215,216], is gluon fusion: $gg \to hh$. Other production modes are [216] (1) vector boson fusion (VBF), $qq \to VV^*qq \to hhqq$ ($V = W, Z$) [1], which in the SM constitutes 10% of the total production, but can become relevant at higher energies or in certain BSM theories depending on the specific parameters, (2) double Higgs-strahlung, $q\bar{q} \to V^* \to Vhh$ ($V = W, Z$), which accounts for less than 1% of all the cross sections, and (3) associated production of two Higgs bosons with a top quark pair, $gg \to t\bar{t}hh$, that is also within 5% of the total contribution but can become more relevant than VBF at higher energies. In Fig. 3.1 we show the total cross section of Higgs pair production for all these processes in the SM in terms of the center-of-mass (c.m) energy of the proton collider, thus emphasising the importance of gluon fusion.
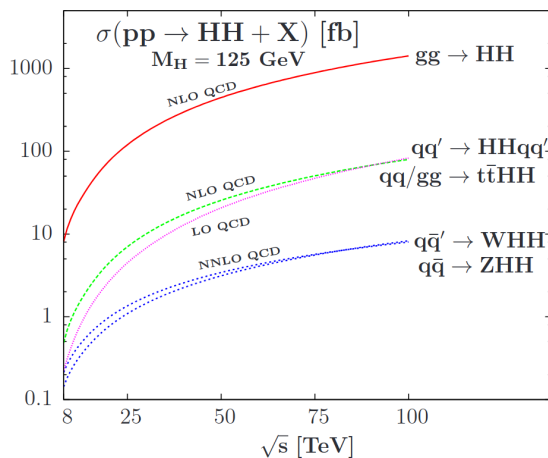

Figure 3.1

Total cross sections for Higgs pair production in proton collisions in the SM for different processes assuming a Higgs mass of $m_h = 125$ GeV, shown as a function of the c.m. energy. Taken from Ref. [216].

We should also mention that a small sensitivity to the trilinear Higgs coupling can be achieved via higher orders in single Higgs production. This is possible when next-to-leading order (NLO) electroweak corrections that depend on κ_λ are included [217]. Experimental collaborations usually combine both single and double Higgs production, where in the latter case only gluon fusion and VBF are taken into account [122,218]. In di-Higgs production, κ_λ contributes already at LO, and a $\pm 100\%$ deviation from the SM value ($\kappa_\lambda = 1$) can result in a 50% change in the cross section. In contrast, for single Higgs production at $\sqrt{s} = 13$ TeV, the same variation in κ_λ would affect the cross section by only about 1%.

With all these considerations, Higgs pair production via gluon fusion remains the most sensitive channel to the trilinear Higgs coupling at the LHC and therefore it will be the main focus of the present work.

The first leading order calculation of $\sigma(gg \to hh)$ was performed in the SM in 1987 in Refs. [219, 220]. Ten years later it was extended to NLO QCD in the large m_t limit Ref. [221]. It took nearly two more decades before the full NLO corrections were calcu-

---

[1]The asterisk * indicates that the vector boson is off-shell.

lated [222–227]. These corrections were found to be significant in the SM, approximately doubling the predicted total cross section compared to the LO result[2].

Currently, the highest order prediction in the SM is [229]

$$\sigma(gg \to hh) = 30.77^{+6\%}_{-23\%} \text{ fb at } \sqrt{s} = 13 \text{ TeV},$$

which is obtained at the NNLO_FTapprox for $m_h = 125$ GeV and the renormalisation and factorisation scales at half the invariant mass of the Higgs pair. At NNLO_FTapprox, the cross section is computed at next-to-next-to-leading order (NNLO) QCD in the heavy-top limit [230–232] with full LO and NLO mass effects [222–224, 226, 227] and full mass dependence in the one-loop double real corrections at NNLO QCD [233]. The uncertainty of the result combines the uncertainty from the renormalisation and factorisation scale variations with the uncertainty due to the choice of the renormalisation scheme and scale of the mass of the top quark [227, 234], which is by far the dominant source of the total uncertainty, and is of the order of 20%.

NLO electroweak corrections to gluon fusion hh-production have been recently provided in Ref. [235], resulting in a -4% decrease of the total cross section. Differential distributions were found to be enhanced by 15% close to hh threshold and decrease by -10% at high energies. A cross check of these results would be desirable and is currently under investigation, for partial EW corrections see Refs. [236–240].

In BSM models, the first calculation at LO was done in 1996 in Ref. [241] in the MSSM. NLO QCD corrections in the MSSM in the heavy-top-mass (HTL) limit were also considered in Ref. [221]. The NLO electroweak corrections have been investigated in the NMSSM in Refs. [242, 243].

3.1   General effects in Higgs pair production

In this section we detail the effects of the different parameters involved in gluon fusion hh-production. We will assume that deviations in the relevant couplings w.r.t the SM are possible, and we will additionally explore the possibility of a heavy resonance produced in the s-channel, that is absent in the SM but present in many BSM scenarios, in particular in singlet and doublet extensions of the SM.

In Fig. 3.2 we show the LO diagrams contributing to the gluon fusion into Higgs pairs, which is mediated by heavy quark loops. The two diagrams on the left are present in the SM and are usually called non-resonant or continuum contribution, the first diagram is the so-called box, which we will denote with the symbol $\Box$, and the second diagram is the SM-like triangle diagram which we will label with the symbol h. The right diagram shows a BSM contribution from a heavy CP-even scalar, we will call it resonant diagram and label with the symbol H. Generally, more than one resonant contributions are possible, e.g. in models with doublets and singlets. The quark loop is represented with Q, which is dominantly the top quark due to the Yukawa hierarchy. The bottom quark contribution in the SM only plays a subleading role, accounting for less than 1% of the total cross section [216].

In the 2HDM, the bottom contribution in the process can be enhanced for large values of t_β within the regions allowed by all the constraints, therefore we will take into account both contributions in our LO analysis. The trilinear coupling enters through the s-channel

---

[2]For a review of higher-order corrections to SM di-Higgs production, see [228]

SM-like triangle diagram. In the SM, the triangle and box diagram interfere destructively leading to a small cross section. In BSM models this interference pattern can be altered, leading to deviations in the expected value of the cross section.
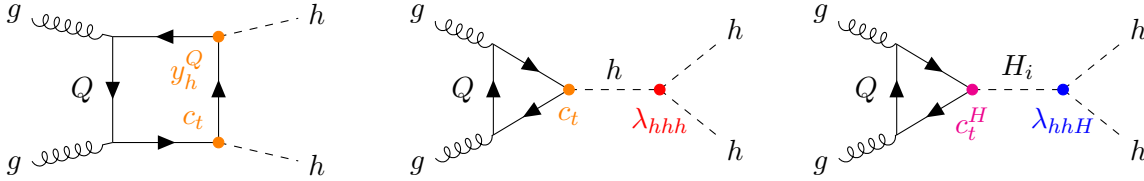

Figure 3.2
Generic diagrams contributing to Higgs pair production in gluon fusion, all mediated by heavy quark loops $Q = b, t$. The first and second diagram correspond to the non-resonant contribution, present in the SM. The first diagram is the box, and the second is the h triangle diagram. The third diagram shows possible resonant contributions in BSM models with heavy CP-even scalars, H_i. The trilinear Higgs couplings λ_{hhh} and λ_{hhH_i} are depicted by red/blue dots respectively. They can be evaluated at tree-level or at one-loop. Other couplings involved are the (top/bottom) Yukawas of the light/heavy Higgses, $y_h^Q/y_{H_i}^Q$, denoted by orange/pink dots.

In BSM models, there are two potential sources of changes of the gluon fusion Higgs pair production cross section w.r.t. the SM. Firstly, the couplings in the SM-like diagrams can differ from the SM values. While the Yukawa couplings, in particular the deviations of the top-Yukawa coupling, are restricted by the current constraints to about $\pm 10\%$ (at 1σ) of the SM value, there is still room for substantial changes in the trilinear Higgs self-coupling λ_{hhh}, while being compatible with all relevant constraints [244]. Changes in λ_{hhh} can alleviate the SM suppression of the hh-production cross section by altering the interference pattern of the continuum diagrams.

Secondly, there is an additional s-channel contribution from a heavy Higgs boson, involving the trilinear coupling λ_{hhH} and the top Yukwawa coupling of the H. In case its mass, m_H, exceeds twice the mass of the lighter Higgs boson, $m_H > 2m_h \sim 250$ GeV, it can lead to resonant hh-production, in which case the corresponding diagram is referred to as "resonant diagram" (for simplicity we will call it resonant diagram also for non-resonant scenarios). Thereby, the cross section can be significantly enhanced. Furthermore, depending on the involved couplings, the additional s-channel diagram can also lead to destructive interference with the SM-like diagram.

From this discussion it becomes clear, that the involved coupling values play a crucial role for the size of the cross section, in particular the trilinear Higgs self-couplings. Moreover, in the 2HDM there can be substantial EW corrections to these couplings, implying sizeable effects on the cross section, to which future high-luminosity LHC measurements will possibly become sensitive.

We can distinguish between the partonic cross section, which concerns the process $\sigma(gg \to hh)$, and the hadronic one, $\sigma(pp \to gg \to hh)$, which is obtained by integrating over the parton distribution functions (PDFs). The partonic cross section at a given a c.m. energy squared is given by

$$\hat{\sigma}(\hat{s}) = \int \frac{d\hat{\sigma}}{d\hat{t}} d\hat{t}, \tag{3.1}$$

where we used the hat, ˆ, to indicate that the corresponding variables refer to the partonic process. In particular, the partonic c.m. energy squared is $\hat{s} = x_1 x_2 s$, where s is the total (or hadronic) c.m. energy squared. At present, the LHC is operating at a c.m. energy of $\sqrt{s} = 13$ TeV. In the case of Higgs pair production, the partonic c.m. energy corresponds to the invariant mass of the hh system, i.e. $\hat{s} = m_{hh}^2$. The variable $\hat{t}$ is the Mandelstam variable for the partonic transverse momentum transfer, for $gg \to hh$ collisions it is given by $\hat{t} = (p_g - p_h)^2$, where p_g is the momentum of an incoming gluon and p_h the momentum of the outgoing Higgs boson.

On the other hand, the hadronic cross section is defined as

$$\sigma(s) = \int_0^1 dx_1 \int_0^1 dx_2 f_g(x_1, Q^2) f_g(x_2, Q^2) \hat{\sigma}(\hat{s}) \equiv \int_0^1 d\tau \mathcal{L}_{gg}(\tau) \hat{\sigma}(\hat{s} = \tau s), \qquad (3.2)$$

where we integrate over all possible combinations of gluon momentum fractions x_1 and x_2. The functions $f_g(x_i, Q^2)$ are the gluon PDFs, which have been determined experimentally and represent the probability density of finding a gluon with momentum x_i at a certain factorisation scale Q. On the right hand side of the equation we define $\tau \equiv \hat{s}/s = x_1 x_2$, and rewrite the expression in terms of the gg luminosity:

$$\mathcal{L}_{gg}(\tau) = \int_\tau^1 \frac{dx_1}{x_1} f_g(x_1, Q^2) f_g\left(\frac{\tau}{x_1}, Q^2\right), \qquad (3.3)$$

which can be interpreted as the probability density for producing a partonic system with invariant mass squared $\hat{s} = \tau s$ via gluon-gluon collisions.

In this thesis we will always provide the hadronic cross section. We will use the public tool LHAPDF [245] for evaluating the gluon PDFs. We also evaluated the LO in QCD cross section with LO PDFs and the strong coupling α_s at LO, and the NLO QCD cross section with NLO PDFs and α_s at NLO. If not stated otherwise, we used the sets CT14lo (for LO QCD) and CT14nlo (for NLO QCD) [245–247].

In the following, we will discuss one by one the contributions to the scattering matrix element from each of these diagrams and will further elucidate the dependence of the cross section on the above mentioned parameters on a toy model with one scalar resonance. We will allow for variations of the SM couplings λ_{hhh} and y_h^t (for simplicity we will restrict ourselves to the top loop for this discussion) in the case of non-resonant production, and of the BSM couplings, λ_{hhH} and y_H^t, as well as the heavy Higgs mass, m_H, and total decay width, Γ_H, in the case of the resonant production. These are the main parameters that intervene in the process and can get modifications in extended scalar sectors. It is worth noting that we assume only extensions of the scalar sector of the SM, in particular, we assume that no modifications in the SM QCD sector through coloured particles or interactions with them are introduced. While this restricts some interesting BSM scenarios, we do capture the effects in the most common extensions of the SM.

We will discuss two different observables which we analysed together as they provide the greatest sensitivity to the trilinear couplings, these are the total cross section and the invariant mass distributions of two Higgses in the final state.

3.1.1   Non-resonant production

We start with the analysis of the SM-like box diagram, whose scattering amplitude element $\mathcal{M}_\square$ is given by
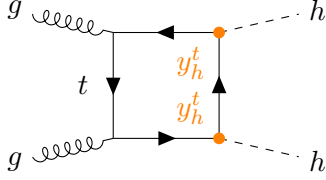

$$\mathcal{M}_\square \propto F_\square(s)(y_h^t)^2,$$

where y_h^t is the top Yukawa of the SM-like Higgs dependent on the top mass, m_t and the vev, v,

$$y_h^t = \frac{\sqrt{2}m_t}{v}, \tag{3.4}$$

and $F_\square(s)$ is the box form factor that depends on the energy. In fact, the contributions to the box form factor can be split into two gauge-invariant pieces according to the allowed gluon-gluon polarisation: $F_\square(s)$ corresponds to spin zero and $G_\square(s)$ to spin 2. The latter contribution won't mix with the other diagrams and therefore its overall contribution to the partonic cross section will be $\propto (y_h^t)^4 G_\square^2(s)$, a term that we wont discuss further. These form factors are rather lengthy complex functions that we define in App. B. Finally, because the external lines are scalar particles, they contribute with a factor of 1 in the amplitude.

The triangle diagram contribution to the scattering matrix, $\mathcal{M}_h$ be written as
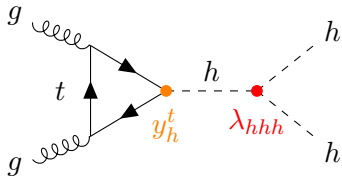
$$\mathcal{M}_h \propto F_\triangle(s)\frac{y_h^t\lambda_{hhh}}{s - m_h^2 + im_h\Gamma_h},$$

where $F_\triangle(s)$ is the energy dependent triangle form factor, and the propagation of the internal h particle is given by the scalar propagator

$$\frac{1}{s - m_h^2 + im_h\Gamma_h},$$

where m_h and Γ_h are the mass and width of the SM-like Higgs. Since these two parameters are measured quite precisely[3], we will keep them fixed in our analysis. Their values are [99]

$$m_h = 125.20 \pm 0.11 \text{ GeV} \quad \text{and} \quad \Gamma_h = 3.7^{+1.9}_{-1.4} \text{ MeV}.$$

The combined matrix element of the non-resonant production can be written as

$$\mathcal{M}_{\text{no res.}} = \mathcal{M}_\square + \mathcal{M}_h, \tag{3.5}$$

and therefore the squared element, which will contribute to the cross section according to Eq. (2.91), is

---

[3]The width measurement is based on the assumption of equal on-shell and off-shell effective couplings, which enables an indirect yet precise determination of such a narrow quantity [248].

$$|\mathcal{M}_{\text{no res}}|^2 = |\mathcal{M}_\square|^2 + |\mathcal{M}_h|^2 + 2\text{Re}(\mathcal{M}_h\mathcal{M}_\square^*). \tag{3.6}$$

Therefore, the full non-resonant matrix element of the process also includes the interference term between the two diagrams, given by $2\text{Re}(\mathcal{M}_h\mathcal{M}_\square^*)$. We can explicitly isolate the dependence of the squared matrix element on the interesting to us couplings by power counting in the respective diagrams. For convenience, we will now switch to working with the coupling modifiers w.r.t. the SM, i.e. κ_λ instead of λ_{hhh} and $\xi_h^t \equiv y_h^t/(y_h^t)^{\text{SM}}$, so we can describe any non-resonant squared matrix element in terms of these couplings,

$$\begin{aligned}|\mathcal{M}_{\text{no res}}|^2(\xi_h^t, \kappa_\lambda) &= (y_h^t)^4|\mathcal{M}_\square^{\text{SM}}|^2 + (\xi_h^t)^2(\kappa_\lambda)^2|\mathcal{M}_h^{\text{SM}}|^2 + 2(\xi_h^t)^3\kappa_\lambda\text{Re}(\mathcal{M}_h^{\text{SM}}\mathcal{M}_\square^{\text{SM}*}) \\ &\equiv (\xi_h^t)^4\mathcal{A}_1 + (\xi_h^t)^2\kappa_\lambda^2\mathcal{A}_2 + (\xi_h^t)^3\kappa_\lambda\mathcal{A}_3,\end{aligned} \tag{3.7}$$

where in the first line we use the upper index SM to account for the fact that these are the matrix elements with the SM couplings, and in the second line we simplify the notation of the squared matrix element of each contribution with the coefficients $\mathcal{A}_i$, $i = \{1, 2, 3\}$. These coefficients will be fixed for us because we only allow for variations of the couplings and we took it into account in Eq. (3.7).

In order to illustrate the effects discussed in this section w.r.t the couplings involved we have computed the total Higgs pair production cross section, and the differential distribution of the invariant mass of the two Higgses in a toy model, where each of the couplings can be modified *ad hoc*. In Fig. 3.3 we show the dependence of the total cross section (left) and the invariant mass distributions of two Higgses in the final state, m_{hh} (right) on κ_λ, in the first case we normalise the result to the SM prediction. The blue curve on the left corresponds to the red curve in the experimental limits on κ_λ shown in Fig. 2.5, i.e. the theory prediction, although the latter also includes the vector boson fusion cross section. In practice, we plot (besides the normalisation to the SM value σ_{SM})

$$|\mathcal{M}_{\text{no res}}|^2(1, \kappa_\lambda) = \mathcal{A}_1 + \kappa_\lambda^2\mathcal{A}_2 + \kappa_\lambda\mathcal{A}_3. \tag{3.8}$$

The gray regions on the left plot show the experimentally excluded regions at 2σ by ATLAS [121]. We observe a minimum at the value of $\kappa_\lambda \sim 2.5$, which happens due the increase in the destructive interference between the triangle and box diagrams, which we will discuss in greater detail below. We can see that currently, the maximum deviations from the SM cross section σ_{SM} are roughly a 4-times enhancement for negative κ_λ and a 6-times enhancement for positive values of κ_λ. We have selected some points to represent their differential cross section with respect to the invariant mass, $\partial\sigma_{hh}^{\text{LO}}/\partial m_{hh}$, we use the symbol σ_{hh} here for the cross section to make explicit that it is the cross section in the hh-final state and the superscript LO to refer to the leading order in QCD result[4]. These points are the SM case, $\kappa_\lambda = 1$, which is represented with a red star on the left, the extrema of the experimentally allowed interval, $\kappa_\lambda = -1.2$ and $\kappa_\lambda = 7.2$, and the value for the maximal destructive interference $\kappa_\lambda = 2.5$.

On the right plot of Fig. 3.3 we see the invariant mass distributions corresponding to these points. The SM distribution, shown in red, presents a cancellation of the triangle and box form factors right below the kinematic threshold of hh-production, which reduces the

---

[4]While applying an NLO-QCD K-factor of 2 is justified for the total cross section, it is less so for the differential invariant mass distribution, for more details see the discussion in Sec. 3.1.5
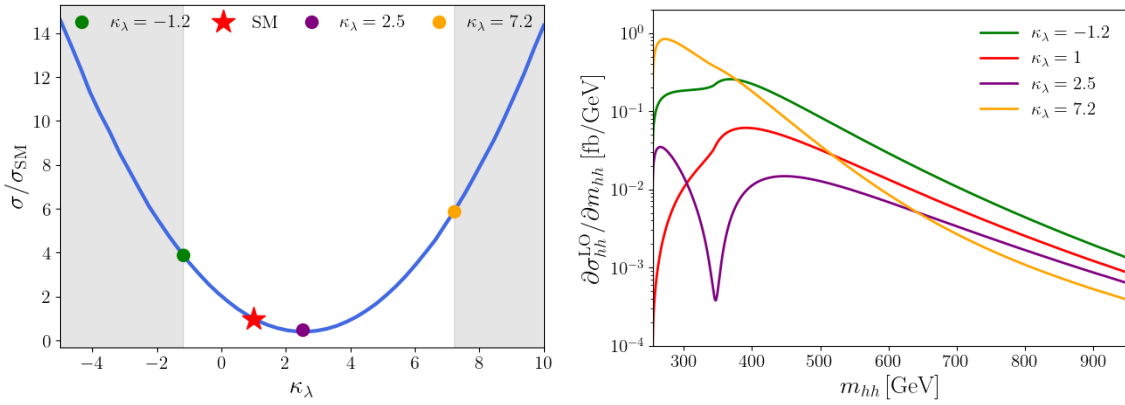
Figure 3.3
Cross sections for non-resonant Higgs pair production depending on the trilinear coupling κ_λ. Left: total cross section. Right: invariant mass distribution of four selected benchmark points for a fixed κ_λ, the value is indicated in the legend.

cross section at that region. It is later enhanced at around 400 GeV, which corresponds to the di-top production threshold and is also present in single Higgs production via gluon fusion (see e.g. Ref. [249]). It further decreases for larger c.m energies. If the trilinear coupling is modified to a more negative value as in the $\kappa_\lambda = -1.2$ case (green curve), the triangle and box diagrams cancel much below the kinematic threshold, which results in an apparent enhancement of the cross section at threshold. If the coupling can reach larger values than in the SM, in particular at the minimum where $\kappa_\lambda = 2.5$, the cancellation of the form factors is shifted to higher c.m. energies and results in a dip at around the di-top threshold, as can be observed in the purple curve. Finally, for the largest allowed value of κ_λ, the distribution follows a steadily decreasing slope with no significant dips, at threshold the contribution is enhanced over 4 orders of magnitude w.r.t. the SM and then decreases monotonously.

In Fig. 3.4 we show the dependence of the total (left) and differential (right) cross section on the SM-like top Yukawa coupling modifier, ξ_h^t, i.e.

$$|\mathcal{M}_{\text{no res}}|^2(\xi_h^t, 1) = \mathcal{A}_1 + (\xi_h^t)^2 \mathcal{A}_2 + (\xi_h^t)^3 \mathcal{A}_3. \tag{3.9}$$

We again shade the regions of the top Yukawa coupling that is experimentally excluded at 2σ C.L. [193] and normalise the total cross section to the SM prediction σ_{SM}.

In this case we see an increase of about 100% for the largest possible top Yukawa coupling at $\xi_h^t = 1.2$ and a cross section very close to zero for the smallest allowed top Yukawa of $\xi_h^t = 0.8$. We chose these points as representatives of for the invariant mass distribution, which we show on the right plot of Fig. 3.4, compared again to the SM distribution in red. We can see that the shape of the invariant mas distribution is not altered by the largest allowed deviations in the top Yukawa coupling, only an overall shift to larger values happens for the 20% increase of the coupling, corresponding to the increase of around 100% in total cross section, and a similar decrease in the opposite case.
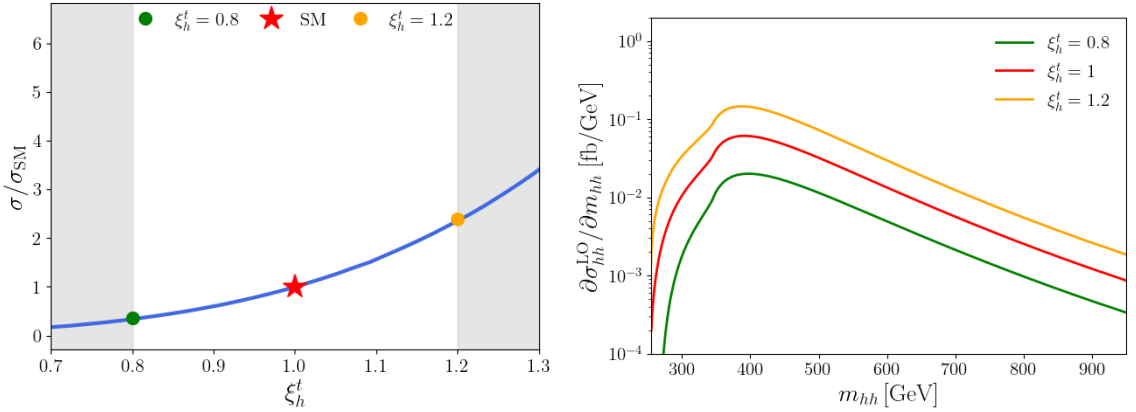
Figure 3.4
Non-resonant Higgs pair production depending on the top Yukawa coupling modifier ξ_t^h. Left: total cross section. Right: invariant mass distribution of three selected benchmark points for a fixed ξ_t^h, the value is indicated in the legend.

Finally, we discuss the interference term in Eq. (3.7), i.e. $(\xi_h^t)^3 \kappa_\lambda \mathcal{A}_3$ in terms of κ_λ, which we plot in Fig. 3.5. We also show three different values of the ξ_h^t coupling. In Fig. 3.5 we see that the interference becomes more negative as κ_λ increases due to the negative sign of $\mathcal{A}_3$. The slope is bigger for a larger ξ_h^t as well, therefore in general the interference grows when the couplings are larger.
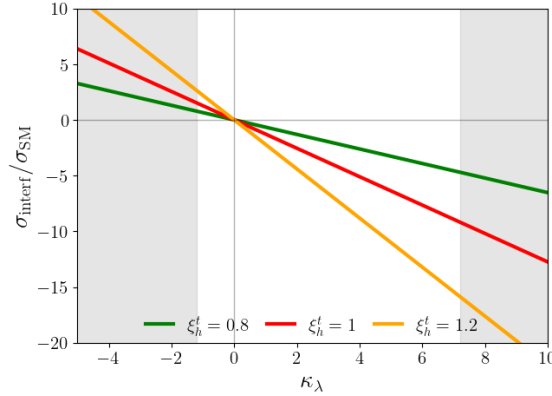
Figure 3.5
Non-resonant Higgs pair production interference term for different values of κ_λ and ξ_h^t.

The lowest-order interference term $\mathcal{A}_3$ in the SM, i.e. $\kappa_\lambda = \xi_h^t = 1$ would be ~ -39.23 fb, but this is a tree-level analysis. At a higher precision this number will change and in fact the LHC Higgs Working Group (LHCHWG) recommendation is –48.37 fb (see also Sec. 4.1.1).

3.1.2   Resonant production

Here we analyse the contribution of the resonant diagram in the total cross section, given by
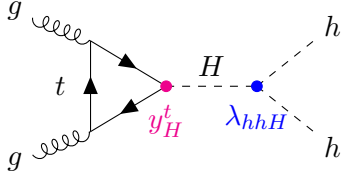
$$\mathcal{M}_h \propto F_\triangle(s) \frac{y_H^t \lambda_{hhH}}{s - m_H^2 + im_H\Gamma_H},$$

where the matrix element is defined analogously to the SM-triangle case, except that now the scalar propagator includes the resonant BSM scalar mass m_H and decay width Γ_H, and the matrix element is proportional to the BSM couplings y_H^t and λ_{hhH}. All of these are new free parameters of the theory that will complicate a possible experimental analysis of the process, although we can simplify the problem a bit by combining the BSM couplings in a variable that we call $\xi_H^t \times \lambda_{hhH}$, as they will enter together everywhere in this process. Here again we use the Yukawa coupling modifier w.r.t the SM Yukawa, i.e. $\xi_h^t \equiv y_h^t/(y_h^t)^{\text{SM}}$, and the notation of Eq. (2.57) to define λ_{hhH}. The heavy scalar top Yukawa interaction could be measured in a simpler production process. Isolating this dependence in the squared matrix element we get

$$|\mathcal{M}_{\text{res}}|^2(\xi_H^t \times \lambda_{hhH}, m_H, \Gamma_H) = (\xi_H^t \times \lambda_{hhH})^2 \mathcal{A}_4(m_H, \Gamma_H), \tag{3.10}$$

where now the coefficient $\mathcal{A}_4$ is a function of m_H and Γ_H, which we plot in Fig. 3.6 in terms of m_H for different values of $\xi_H^t \times \lambda_{hhH}$ (left) and of the total decay width Γ_H (right).
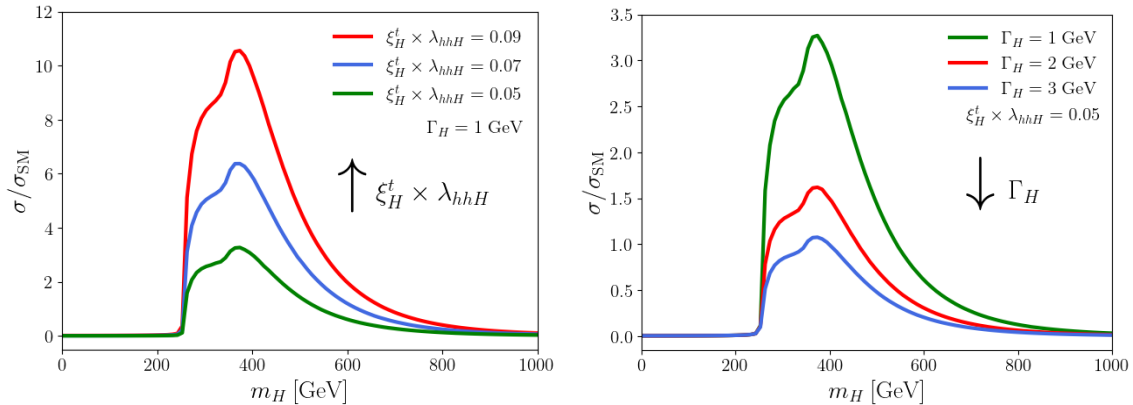
Figure 3.6

Resonant Higgs pair production cross section as a function of m_H. The left plot shows the dependence on the involved BSM couplings $\xi_H^t \times \lambda_{hhH}$ for a fixed width $\Gamma_H = 1$ GeV and the right plot the dependence on the total decay width of the heavy Higgs, Γ_H, for a fixed value of $\xi_H^t \times \lambda_{hhH} = 0.05$.

In Fig. 3.6 we show the cross section of the resonant only contribution normalised to the SM. The values of the y-axis are irrelevant because they refer to a toy model, and

the couplings are set to arbitrary values. We can however clearly see the impact of the resonance on the cross section. The effect of the resonant diagram is inexistent below the kinematic threshold, as there is not enough phase space to produce the hh system. As soon as the channel opens up, the cross section increases drastically and we see a peak at around the $t\bar{t}$ mass threshold, again resembling the single Higgs production. If we analyse the dependence of the cross section with the couplings, it increases with an increase of the product $\xi_H^t \times \lambda_{hhH}$. On the contrary, it diminishes with an increase in the total decay width of the heavy Higgs, as it enters in the denominator. These effects are indicated in the left and right plots of Fig. 3.6, respectively.

3.1.3 Interference terms

The full process will include, besides the contributions outlined above, two BSM interference terms: $\Box - H$ and $h - H$ which will arise in the presence of a resonant scalar. The SM-like interference $\Box - h$ was already defined. The total scattering amplitude is therefore,

$$\mathcal{M}_{\text{total}} = \mathcal{M}_{\Box} + \mathcal{M}_h + \mathcal{M}_H \equiv \mathcal{M}_{\text{no res}} + \mathcal{M}_{\text{res}}, \tag{3.11}$$

and the squared amplitude is

$$|\mathcal{M}_{\text{total}}|^2 = |\mathcal{M}_{\text{no res}}|^2 + |\mathcal{M}_{\text{res}}|^2 + 2\text{Re}(\mathcal{M}_H \mathcal{M}_{\Box}^*) + 2\text{Re}(\mathcal{M}_H \mathcal{M}_h^*), \tag{3.12}$$

which can be defined with the isolated couplings as

$$\begin{aligned}|\mathcal{M}_{\text{total}}|^2(\xi_h^t, \kappa_\lambda, \xi_H^t \times \lambda_{hhH}, m_H, \Gamma_H) =& |\mathcal{M}_{\text{no res}}|^2 + |\mathcal{M}_{\text{res}}|^2 + (\xi_h^t)^2(\xi_H^t \times \lambda_{hhH})\mathcal{A}_5(m_H, \Gamma_H) \\ &+ \xi_h^t \kappa_\lambda(\xi_H^t \times \lambda_{hhH})\mathcal{A}_6(m_H, \Gamma_H).\end{aligned} \tag{3.13}$$

We show the new terms that have not been discussed so far in Fig. 3.7. The left plot shows the interference of the resonant diagram with the box, i.e. $(\xi_h^t)^2(\xi_H^t \times \lambda_{hhH})\mathcal{A}_5$, and the right plot shows the interference of the resonant diagram with the non-resonant continuum diagram, i.e. $\xi_h^t \kappa_\lambda(\xi_H^t \times \lambda_{hhH})\mathcal{A}_6$, for different values of κ_λ.

The behaviour around the resonance is dominated by the heavy Higgs propagator, which can be split into real and imaginary parts as follows

$$\mathcal{M}_{\Box} \propto \frac{1}{s - m_H^2 + im_H\Gamma_H} = \frac{(s - m_H^2) - im_H\Gamma_H}{(s - m_H^2)^2 + (m_H\Gamma_H)^2}, \tag{3.14}$$

so the $\text{Re}(\mathcal{M}_H \mathcal{M}_{\text{no res}}^*)$ piece of the interference terms $\mathcal{A}_5$ and $\mathcal{A}_6$ can be rewritten as a sum of these two terms

$$\sigma_{\text{interf}} \propto \text{Re}(\mathcal{M}_{\text{no res}})\frac{(s - m_H^2)}{(s - m_H^2)^2 + (m_H\Gamma_H)^2} + \text{Im}(\mathcal{M}_{\text{no res}})\frac{m_H\Gamma_H}{(s - m_H^2)^2 + (m_H\Gamma_H)^2}, \tag{3.15}$$

where $\mathcal{M}_{\text{no res}}$ refers only to the box on the left plot of Fig. 3.7 and only to the h triangle diagram in the right plot of Fig. 3.7. The interference term becomes zero roughly at

$$0 = s - m_H^2 - \frac{\text{Im}(\mathcal{M}_{\text{no res}})}{\text{Re}(\mathcal{M}_{\text{no res}})}m_H\Gamma_H, \tag{3.16}$$
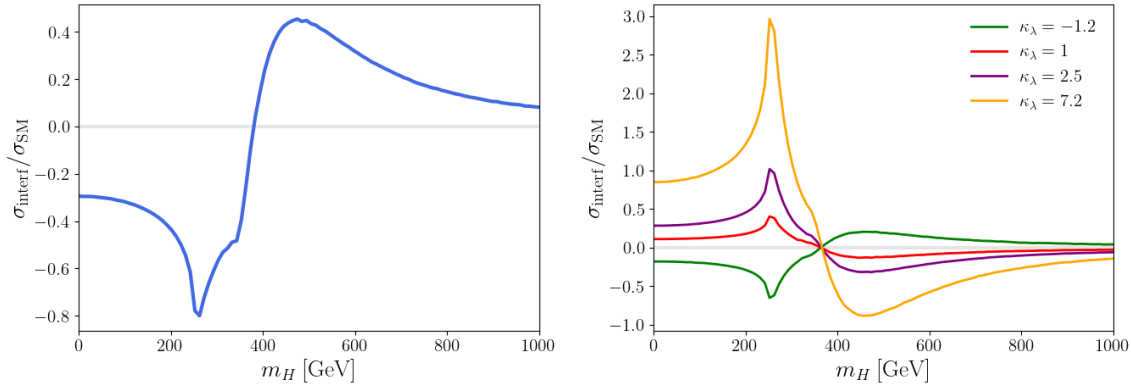
Figure 3.7
Interference patterns between the resonant diagram and the SM box (left) and
the SM triangle (right) diagram, shown as a function of m_H.

We can see where this happens in both plots of Fig. 3.7, the exact value of m_H differs in
the two cases because in the left plot the coefficient in front of the width-dependent term
is $\mathrm{Im}(\mathcal{M}_\square)/\mathrm{Re}(\mathcal{M}_\square)$ and in the right plot it is $\mathrm{Im}(\mathcal{M}_\mathrm{h})/\mathrm{Re}(\mathcal{M}_\mathrm{h})$. In the second case the
result is independent of the value of κ_λ, as this cancels out in the aforementioned coefficient.
In the second case we also see clearly that the interference pattern changes with the sign of
the couplings, in particular with the sign of κ_λ which is varied here: for a negative κ_λ the
interference is destructive at low m_{hh} and constructive for high m_{hh} values. Conversely, if
κ_λ is positive it becomes constructive for low m_{hh} values and destructive for higher m_{hh}.
As expected, the interference also becomes larger with larger values of κ_λ.

We proceed now to discuss the interference contributions in the context of the differential
cross sections. In Fig. 3.8 we show the interference contribution of the resonant diagram
with the continuum contribution in the differential invariant mass cross section assuming a
resonance of 400 GeV. We show the patterns for different parameters of the resonance, in
particular the sign of the trilinear coupling λ_{hhH} and the resonant scalar width Γ_H. This
means we show the last two terms in Eq. (3.13), fixing $\kappa_\lambda = \xi_h^t = \xi_H^t = 1$, i.e.

$$\lambda_{hhH}\mathcal{A}_5(400, \Gamma_H) + \lambda_{hhH}\mathcal{A}_6(m_H, \Gamma_H). \tag{3.17}$$

Clearly the sign of λ_{hhH} (in fact $\xi_H^t \times \lambda_{hhH}$) alters the interference pattern around
the resonance at $m_H = m_{hh}$. A positive sign leads to a constructive interference before
the resonance and a destructive interference after the resonance, i.e. a peak-dip structure
as in the blue curve of Fig. 3.8. In the opposite case, a negative sign in λ_{hhH} leads to
a destructive interference before the resonance and a destructive after it, which shows up
in the distribution as a dip-peak structure, as shown with the red curve in Fig. 3.8. We
also show what happens if the resonant width is increased, in that case the cross section is
smaller, as already discussed, but additionally the crossing of the zero happens slightly to
the right of the identity $m_H \sim m_{hh}$, this is really capturing the contribution of the second,
width-dependent term in Eq. (3.15) or the last term in Eq. (3.16), where now $s - m_H^2 = 0$
as this is the differential cross section. This effect is even more pronounced if we artificially

increase the width to higher values. The fact that for the chosen values of the width this effect is so small, suggests that the interference can be effectively described by the piece

$$\sigma_{\text{interf}} \propto \frac{(s - m_H^2)}{(s - m_H^2)^2 + (m_H \Gamma_H)^2}.$$ (3.18)
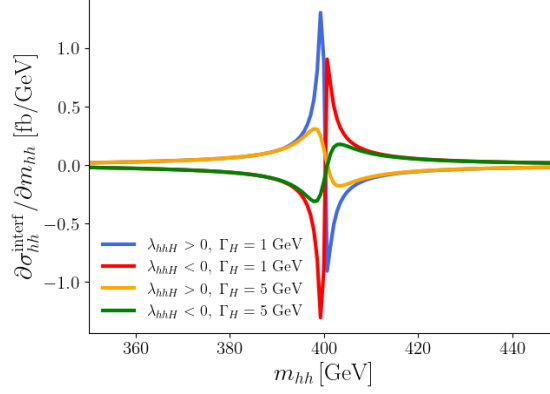
Figure 3.8
Interference patterns between the resonant diagram and the SM non-resonant contribution in the differential cross section.

3.1.4   Full process

The full process will be a sum of all the effects discussed above. In Fig. 3.9 we show these effects on the total cross section in the left plot and on the invariant mass distributions on the right. On the left we plot the prediction in terms of the value of the resonant mass m_H. We see that the process is only SM-like in the regions where the resonant production is negligible, i.e. below the kinematical threshold and for very heavy resonance. The effect of the change in κ_λ is added on top of the resonance. The variations in κ_λ contribute to enhance or decrease the total result throughout the range of possible values of m_H.

Looking at the differential distributions in the right plot of Fig. 3.9, we can see the richness of the possibilities even in this simple toy model. In all the cases we assume a resonant scalar of 400 GeV, which manifests as a resonant peak located at $m_{hh} \sim m_H$, which will be the only noticeable difference if κ_λ is SM-like, as in the red curve. In case κ_λ deviates from the SM prediction, we can expect to see a dip-peak structure as in the purple curve for $\kappa_\lambda = 2.5$, the dip arising from the cancellation of the form factors of the box and SM-like triangle diagrams and the peak from the resonance. The distribution to the sides of the resonant peak can look rather flat if $\kappa_\lambda = -1.2$ as in the green curve, or enhances at the threshold if $\kappa_\lambda = 7.2$ as in the yellow curve.

In this section we have explained in detail the contributions of the different parameters to the di-Higgs production cross section, focusing on the full inclusive and the differential cross sections. We have shown that the effects of the resonant and non-resonant contributions cannot be disentangled, and should be considered at the same time. In particular, we have
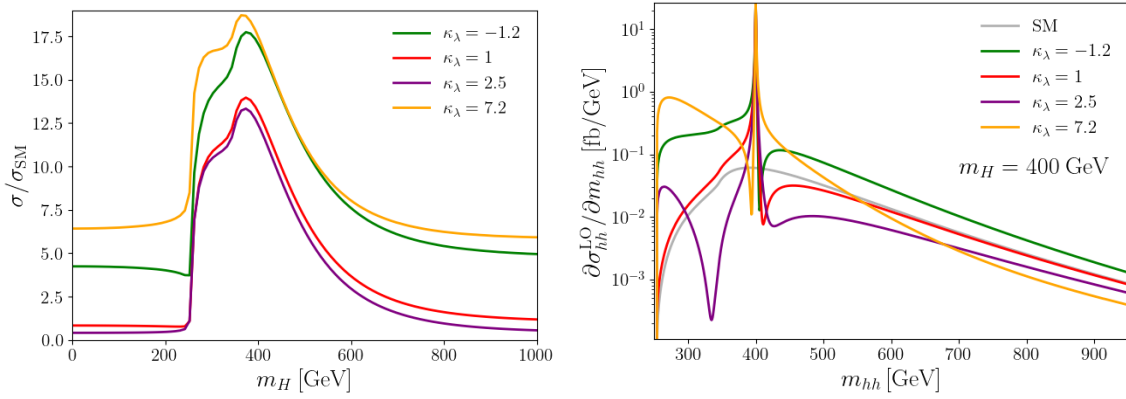
Figure 3.9
Full $gg \rightarrow hh$ total cross section (left) for different values of κ_λ as a function of the resonant mass m_H and invariant mass distributions (right) for that same values of κ_λ for a resonance at 400 GeV.

shown that the following ingredients significantly enhance the value of the cross section w.r.t the SM prediction:

1) large deviations in the trilinear coupling κ_λ,

2) a resonant scalar contribution with masses 250 GeV $< m_H \lesssim 800$ GeV,

3) sizeable BSM couplings $\xi_H^t \times \lambda_{hhH}$ and relatively small widths of the scalar resonance.

In the following we will show examples in a complete model, such as the 2HDM, where these effects arise naturally. We will additionally demonstrate that the presence of the heavy resonance that participates in di-Higgs production can automatically induce large loop corrections to κ_λ that will shift it away from the SM value, in the presence of mass splitting effects.

3.1.5   Higgs pair production in the 2HDM

In this section we will concentrate on the 2HDM as an example model in which the effects discussed above can be realised. In particular, the 2HDM features one scalar that can contribute to the resonant di-Higgs production, the CP-even scalar H. For the numerical evaluation we will use the code HPAIR [221, 241, 244, 250], adapted to the 2HDM, which also includes the possibility to specify an effective trilinear Higgs coupling that accounts for its radiative corrections. Originally, HPAIR was developed for the calculation of Higgs pair production in the SM and the MSSM at LO [241] and at NLO QCD in the HTL limit [221].

At LO, both top and bottom full mass dependence are included. The calculation is equivalent to the MSSM, which shares the Higgs sector of the 2HDM. The Yukawa interactions are adapted to each Type of the 2HDM. Since the coloured sector is equivalent in both models, the NLO QCD corrections can be taken over from the MSSM. At NLO QCD,

the HTL is used and the contributions of the bottom quark are neglected. This is the most accurate prediction publicly available.

Recently, for the 2HDM the full NLO QCD corrections have been provided for the production of a mixed Higgs pair Hh and for a pair of pseudoscalars, AA, in Ref. [251]. The invariant mass distributions were found to increase with large invariant mass reaching -30% (-20%) in hH (AA) production at an invariant mass of 1.5 TeV. The mass effects hence not only change the absolute value of the cross section but also the shape of the distribution, so that the heavy top-mass approximation does not work as good as for the inclusive cross section (see also [252]). So far, however, there is no public code available that allows to compute the top-quark mass effects on the distributions for 2HDM Higgs pair production, in particular not for the interesting case of intermediate resonant heavy Higgs production, which we investigate here. Therefore, for our analysis we take the best prediction available at the moment and resort to the NLO QCD corrections in the heavy-top limit with the here mentioned caveats.[5] Since we will investigate several distinct benchmark cases and analyse what issues in general can arise in the measurement of trilinear Higgs self-couplings, this will still give us new insights despite the used approximations. The overall conclusions will remain the same: They will represent the best case scenario, assuming the distributions are changed uniformly at NLO. In this way, they show what at least can be expected in the QCD sector.

In this work, we include for the first time in the 2HDM[6] the one-loop corrections to the trilinear Higgs couplings in the computation of Higgs pair production and analyse their effects. In the following sections we will include an effective one-loop-corrected coupling in an effective potential approach, as discussed in Sec. 2.6, which means that we will assume vanishing external momenta for the coupling. Taking into account the appropriate momentum dependence for the Higgs pair production process would be expected to modify the predictions for the total di-Higgs production cross section only at the percent level in the 2HDM Type I [131]. We will however elaborate in Sec. 3.6.

Our analysis is accurate in the regions where the loop-corrected effective trilinear couplings constitute the leading contributions to the full EW corrections for scenarios in which the loop corrections to λ_{hhh} and/or λ_{hhH} are very large. In this case, contributions beyond the trilinear Higgs self-couplings, e.g. including additional powers of the top Yukawa couplings, can be shown to be sub-dominant [126]. Therefore, for the case of sizeable loop corrections to the THCs our results should provide a good approximation to the full electroweak loop corrections to the inclusive process at this order. It is also in this limit where momentum effects are smallest in relative size.

In regions where loop corrections to the THCs are relatively small, which for the non-resonant case implies that the predicted cross sections are significantly below the current experimental sensitivity, this approach becomes less accurate and a complete next-to-leading-order (NLO) electroweak (EW) calculation of the cross section would be required, which is

---

[5]Our benchmarks also contain heavy Higgs bosons with masses above the top mass value which questions the applicability of the heavy-top limit in the QCD corrections. The finite top-mass effects can be roughly estimated from the NLO QCD results in the SM including the full top-quass dependence. They amount to about 20% for heavy Higgs masses around 500 GeV, increasing to about 30% for Higgs mass values of 1 TeV.

[6]For investigations of the effect in the SM, see Ref. [237], and in the next-to-minimal supersymmetric extension of the SM (NMSSM), see Refs. [242, 243].

beyond the scope of this work.[7] The aim of our work is an analysis of possible implications of large loop contributions and interference effects, in particular regarding the interpretation of the experimental results. For this purpose the approximate approach pursued here should be sufficiently accurate.

3.2   Sensitivity to trilinear Higgs couplings in the 2HDM

In this section we discuss the current sensitivity to the trilinear couplings in the 2HDM. Without loss of generality we focus on the Type I, where the largest deviations of κ_λ at the tree level were found [253]. As a starting point we have performed a general scan of the parameter space of the 2HDM setting the free parameters of the model in Eq. (2.69) within the limits specified in Tab. 3.1 and applying all the constraints in Sec. 2.7.2 with `thdmTools`. In particular we have set the more stringent bound of 8π for perturbative unitarity, a global minimum condition for the EW vacuum, 2σ agreement with the fit of S and T for the electroweak precision data and 2σ agreement with he SM χ^2 value for the Higgs rate measurements (for more details see Sec. 2.7.2).

	$\tan\beta$	$c_{\beta-\alpha}$	m_H	$m_A, m_H^\pm$	m_{12}^2	m_h
2HDM	[0.1 30]	[-0.3 0.3]	[130 1500]	[10 1500]	[0 $4\cdot10^6$]	125.25

Table 3.1: Regions of the parameter scan in the 2HDM-I used in Fig. 3.10

In Fig. 3.10 we show the scan of the allowed points in the multidimensional free parameters organised in a matrix-type projections of the relations between each pair of parameters. In the diagonal we show the distribution of points in the particular variable, in those cases the Y axis is the number of points. We show this information only to signal the limits of our scan, the density of points does not carry any meaningful physical information. The colour coding represents the magnitude of the one-loop effective trilinear coupling computed diagrammatically with `anyH3` in a fully OS scheme (for details see Sec. 3.6.1).

We use the scatter plot to find the regions of parameter space and the relations between the parameters that will lead to large corrections in κ_λ. We find that large deviations are possible in the alignment limit, which was not the case in a tree-level analysis where trivially $\kappa_\lambda^{(0)} = 1$. This will have an impact on the strength of the electroweak phase transition that will be discussed in Sec. 5.2.3. The overall values of $\kappa_\lambda^{(1)}$ range from 0 to 6, which lies within the experimentally allowed region. We also observe that the largest corrections appear precisely at the regions of largest mass splittings between $M \sim m_H$ and $m_A \sim m_H^\pm$. These observations will serve as an inspiration for defining benchmark scenarios that will help us understand the dynamics of the loop-corrected couplings and of the Higgs pair production.

We define three benchmark scenarios to analyse the impact of the loop-corrected trilinear couplings in the Higgs pair production:

1. $t_\beta = 10$, m_{12}^2 fixed via Eq. (2.95),
    free parameters: $c_{\beta-\alpha}$, $m_{H^\pm} = m_H = m_A$
    Expected features: variation of the relevance of the H exchange contribution, variation of top Yukawa couplings and λ_{hhH}.

---

[7]For results on the NLO EW corrections to SM Higgs pair production, see Refs. [235, 237–239].
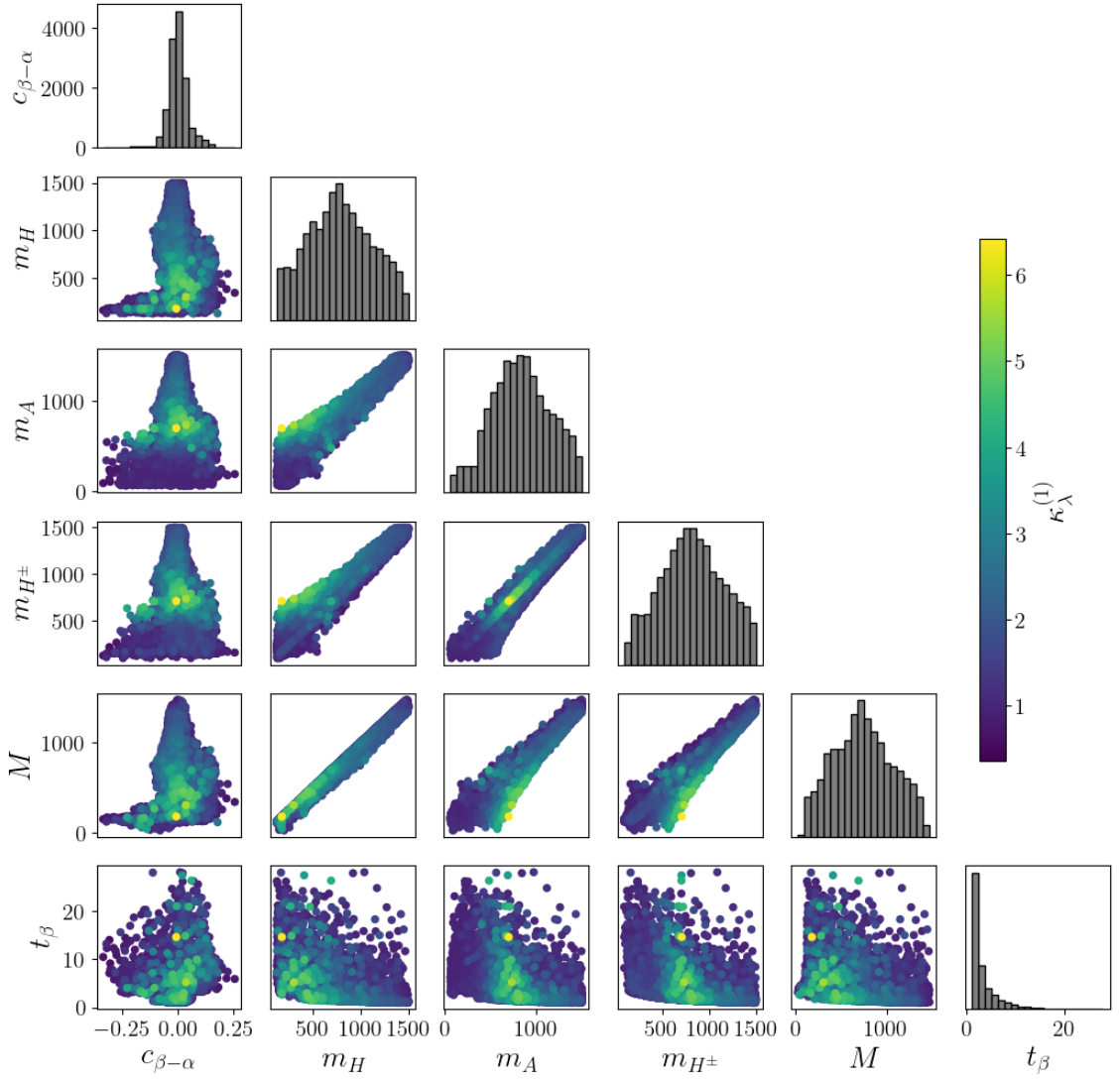
Figure 3.10
Values of $\kappa_\lambda^{(1)}$ in the 2HDM in a general scan with ranges defined in Tab. 3.1.

2. $t_\beta = 10$, $c_{\beta-\alpha} = 0.2$, m_{12}^2 fixed via Eq. (2.95)
   free parameters: m_H, $m_A = m_{H^\pm}$
   Expected features: variation of the relevance of the H exchange contribution, variation
   of top Yukawa couplings and λ_{hhH}.

3. $m_{H^\pm} = m_H = m_A = 450$ GeV, m_{12}^2 fixed via Eq. (2.95),
   free parameters: $c_{\beta-\alpha}$, t_β,
   Expected features: very large H contribution, variation of top Yukawa couplings and
   of λ_{hhh} and λ_{hhH}.

Our results for the trilinear couplings in the three benchmark planes are presented in Figs. 3.11, 3.14, and 3.17. We show as a colour coding the value of the relevant to us THCs: κ_λ (upper row) and λ_{hhH} (middle row) at tree-level (left) and at one-loop (right). The tree-level values are computed using the expressions in Eq. (2.75) . The one-loop values are calculated using `BSMPT v.2.` [141], i.e. from the one-loop effective potential. Additionally, we show in the lower row the top Yukawa couplings of the light (left) and heavy (right) CP-even Higgs bsoson, ξ_h^t and ξ_H^t, according to the expressions in Eq. (2.72). As a black contour we show the region of allowed parameter space, i.e. everything outside the black contour is disallowed by theoretical or experimental constraints. In the allowed region ξ_H^t varies from about -0.5 to roughly $+0.1$, ξ_h^t stays within a 2% deviation from the SM, where $\xi_h^t = 1$.

The **benchmark scenario 1** depicted in Fig. 3.11 features a non-resonant scenario since the mass of the heavy Higgs is $m_H = 1000$ GeV. This implies that the Higgs pair production cross section will overall feature the behaviour of the Higgs self-coupling κ_λ, as the resonant contribution will be subdominant. Large corrections due to the contribution of heavy scalars in the loop of the hhh vertex significantly modify the value of this coupling. Following the colours within the black countour[8] of the upper plots in Fig. 3.11 we observe that loop corrections to κ_λ shift the value $\kappa_\lambda = 1$ (indicated by a red line) away from the alignment limit, $c_{\beta-\alpha} = 0$. We observe that the tree level κ_λ decreases for larger values of $c_{\beta-\alpha}$ up to the 'tip' of the allowed region at $(c_{\beta-\alpha}, t_\beta) \approx (0.1, 8)$ where $\kappa_\lambda^{(0)} \approx 0$. At one-loop, however, it increases up to values of $\kappa_\lambda \approx 10$ that are realised in the borderline of the region excluded by perturbative unitarity. Note that a value of $\kappa_\lambda \approx 2.5$ is realised in the light orange region in upper right plot. On the other side, smaller values of κ_λ are reached for the slightly negative $c_{\beta-\alpha}$ values allowed (the exclusion of negative $c_{\beta-\alpha}$ in this scenario comes from vacuum stability constraints) and are barely modified when including loop corrections, being located roughy at $(c_{\beta-\alpha}, t_\beta) \approx (-0.02, 1.3)$ and reaching values of $\kappa_\lambda^{(0)} \approx 0.9$ and $\kappa_\lambda^{(1)} \approx 0.87$, respectively.

Switching the discussion to the λ_{hhH} coupling, we observe that it has no significant modification from the one-loop contributions inside the allowed region but is greatly enhanced in the upper right corner of the middle right plot. The largest one-loop effect is a strong modification of the prediction for this coupling found at larger (positive) values of $c_{\beta-\alpha}$ once the t_β is higher than 10. For a fixed $t_\beta \gtrsim 10$ for increasing $c_{\beta-\alpha}$ we first find a string increase, reaching its maximum. For even larger $c_{\beta-\alpha}$, λ_{hhH} is then decreasing and eventually turning negative. However, it should be noted that these features are found outside the region allowed by theoretical and experimental constraints.

Since this scenario features very large one-loop deviations of κ_λ together with very low deviations of ξ_h^t within the allowed region and very heavy resonant Higgs, which barely contributes to the di-Higgs production process, we regard this scenario as a non-resonant and will study it further in the context of the application of experimental non-resonant limits in Sec. 3.5.1.

In the upper row of Fig. 3.12 we show the decay width of the heavy Higgs boson to hh with λ_{hhH} at tree-level (left) and at one-loop (right). The behaviour follows largely the

---

[8]We show the predictions outside of the allowed parameter space to see the overall dependence of the parameters, but no physical conclusions should be drawn from this region, in particular in Fig. 3.11 the large corrections of the trilinear Higgs couplings up to 50 times the SM prediction appear in a region that does not fulfill constraints from perturbative unitarity and therefore should be taken into consideration.
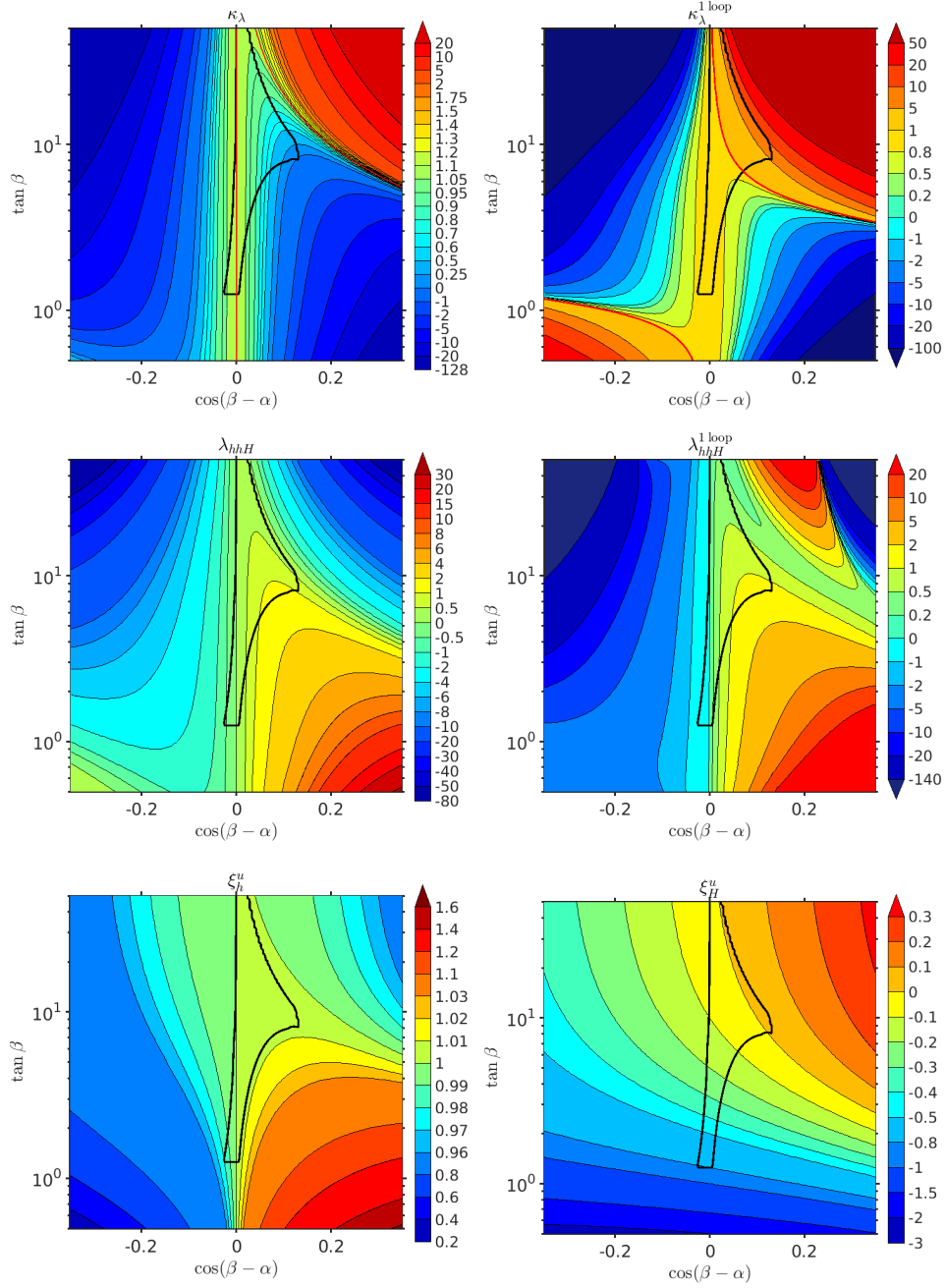
Figure 3.11
Plane 1. Tree-level predictions of κ_λ (upper left) and λ_{hhH} (middle left). Loop-level predictions of κ_λ (upper right) and λ_{hhH} (middle right) computed with `BSMPT`. The allowed region by theoretical and experimental constraints is within the black contour. The red line in the upper plots indicates $\kappa_\lambda = 1$. Predictions of the light (heavy) Higgs - top Yukawa modifier in the lower left (right).
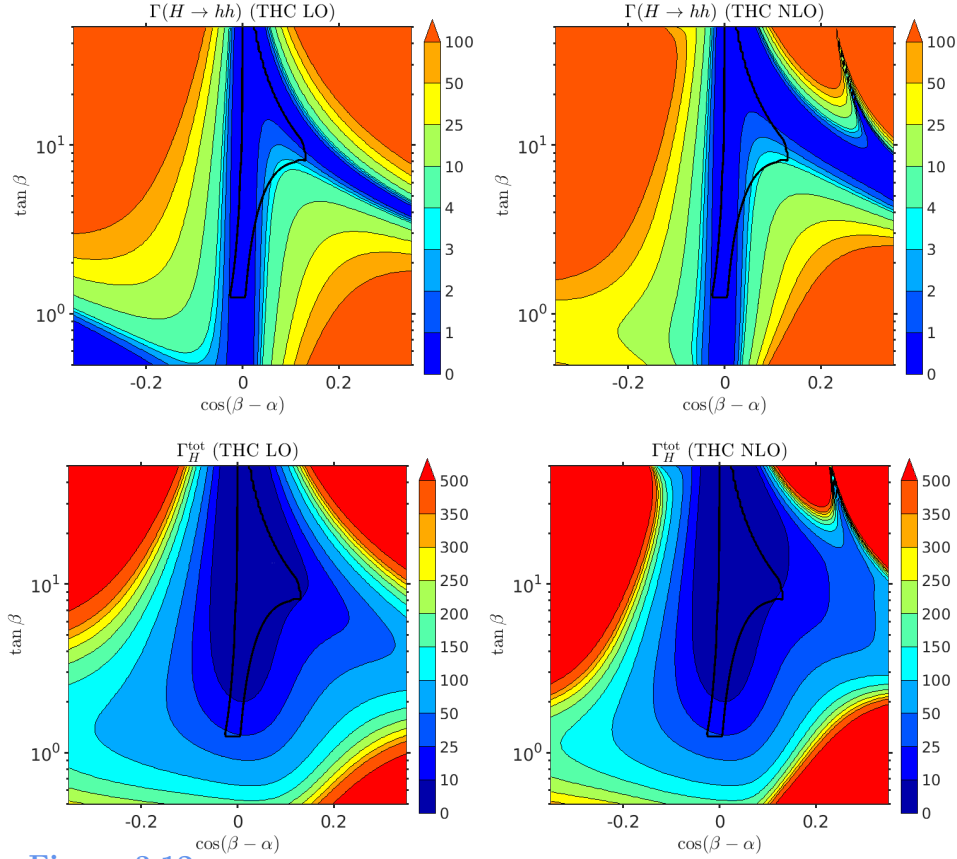
Figure 3.12

Plane 1. Decay width of the heavy Higgs boson H decaying into a pair of light
Higgs bosons h with a λ_{hhH} at tree-level (upper left) and at one-loop (upper
right). Total decay width of H, $\Gamma_H^{\rm tot}$ with a tree-level λ_{hhH} coupling (lower left)
and with the one-loop λ_{hhH} coupling (lower right).

THC λ_{hhH}, as discussed above, In particular, at the NLO level for large $c_{\beta-\alpha}$ and large
t_β a very small (and even vanishing) decay width can be found. This happens where the
coupling λ_{hhH} at one-loop crosses zero when the loop corrections introduced by the mass
scale M overpower the tree-level prediction. The dominant decay mode of H in the regions
where decay to hh is disallowed or cancelled is to $\bar{t}t$ and it remains unperturbed due to
the corrections on the THCs. The value of the heavy Higgs top Yukawa is close to 0.25 in
this region, as can be seen in the upper left plot. We conclude that in region of large t_β
and positive $c_{\beta-\alpha}$ almost the whole decay rate was given by the $H \to hh$ decay mode, but
at the parameter space where the loop corrections to λ_{hhH} are ~ 0 this decay mode does
not exist and the total decay width depicted in Fig. 3.11 presents a very large suppression
because of the absence of the hh decay mode. The decay to gauge bosons is 0 even when
the trilinear Higgs couplings are at one-loop.

In the lower row of Fig. 3.12 the values for $\Gamma_H^{\rm tot}$ are shown with the tree-level (one-
loop effective) λ_{hhH} coupling in the left (right). Since the correction to the trilinear Higgs
couplings does not enter in the rest of the decay channels entering in the total decay width,

the effect from the NLO corrections can only be observed in disallowed region with large $c_{\beta-\alpha}$ and $t_\beta \gtrsim 10$. Where λ_{hhH} changes from large positive to large negative values and pronounced minimum of $\Gamma_H^{\rm tot}$ can be observed, following the behaviour of $\Gamma(H \to hh)$.

A significant modification of the total decay width w.r.t. the tree-level value would have an impact on the contribution of the resonant diagram, since a suppression of $\Gamma_H^{\rm tot}$ could lead to an enhanced resonant contribution. Since this is not the case, we expect that indeed this scenario remains non-resonant even with the loop corrections to the THCs.
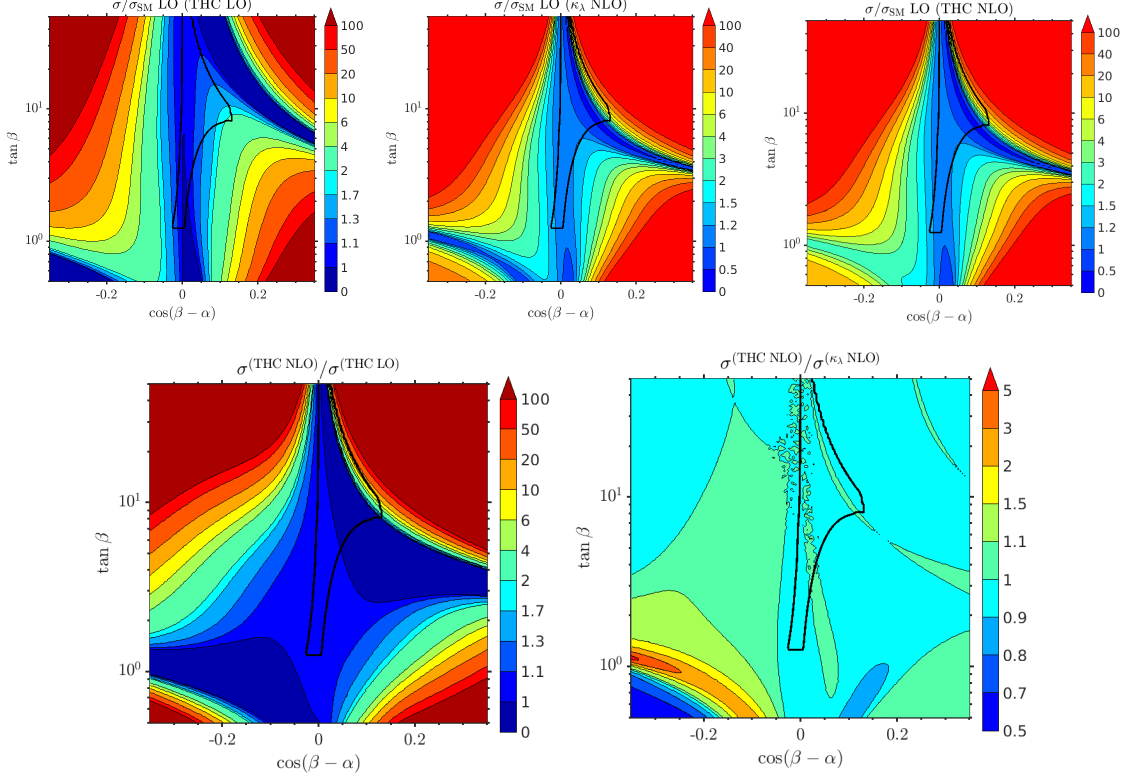

Figure 3.13
Plane 1. Di-Higgs production prediction in the 2HDM w.r.t. the SM computed at leading order including tree-level trilinear Higgs couplings (upper left), one-loop κ_λ and tree-level λ_{hhH} (upper middle), and both κ_λ and λ_{hhH} at loop level (upper right). Ratio of the cross section with both trilinear couplings at one-loop with respect to the cross section with both trilinear couplings at tree-level (lower left) and ratio of the cross section with both trilinear couplings at one-loop with respect to the cross section with only κ_λ at one-loop (lower right).

In Fig. 3.13 we present the results for the di-Higgs production cross section in the 2HDM. The upper row shows the 2HDM cross section normalised to the SM prediction, $\sigma_{\rm 2HDM}/\sigma_{\rm SM}$, where $\sigma_{\rm SM}$ does not receive loop corrections to the $\lambda_{\rm SM}$ (which are expected to be small). We show the results for $\sigma_{\rm 2HDM}$ using $\kappa_\lambda^{(0)}, \lambda_{hhH}^{(0)}$ ($\sigma^{\rm THC\ LO}$, left plot), $\kappa_\lambda^{(1)}, \lambda_{hhH}^{(0)}$ ($\sigma^{\kappa_\lambda\ \rm NLO}$, middle plot) and $\kappa_\lambda^{(1)}, \lambda_{hhH}^{(1)}$ ($\sigma^{\rm THC\ NLO}$, right plot). The lower row depicts $\sigma^{\rm THC\ NLO}/\sigma^{\rm THC\ LO}$ (left) and $\sigma^{\rm THC\ NLO}/\sigma^{\kappa_\lambda\ \rm NLO}$ (right). We find that the maximum value of $\sigma^{\rm 2HDM}/\sigma_{\rm SM} \approx 3$
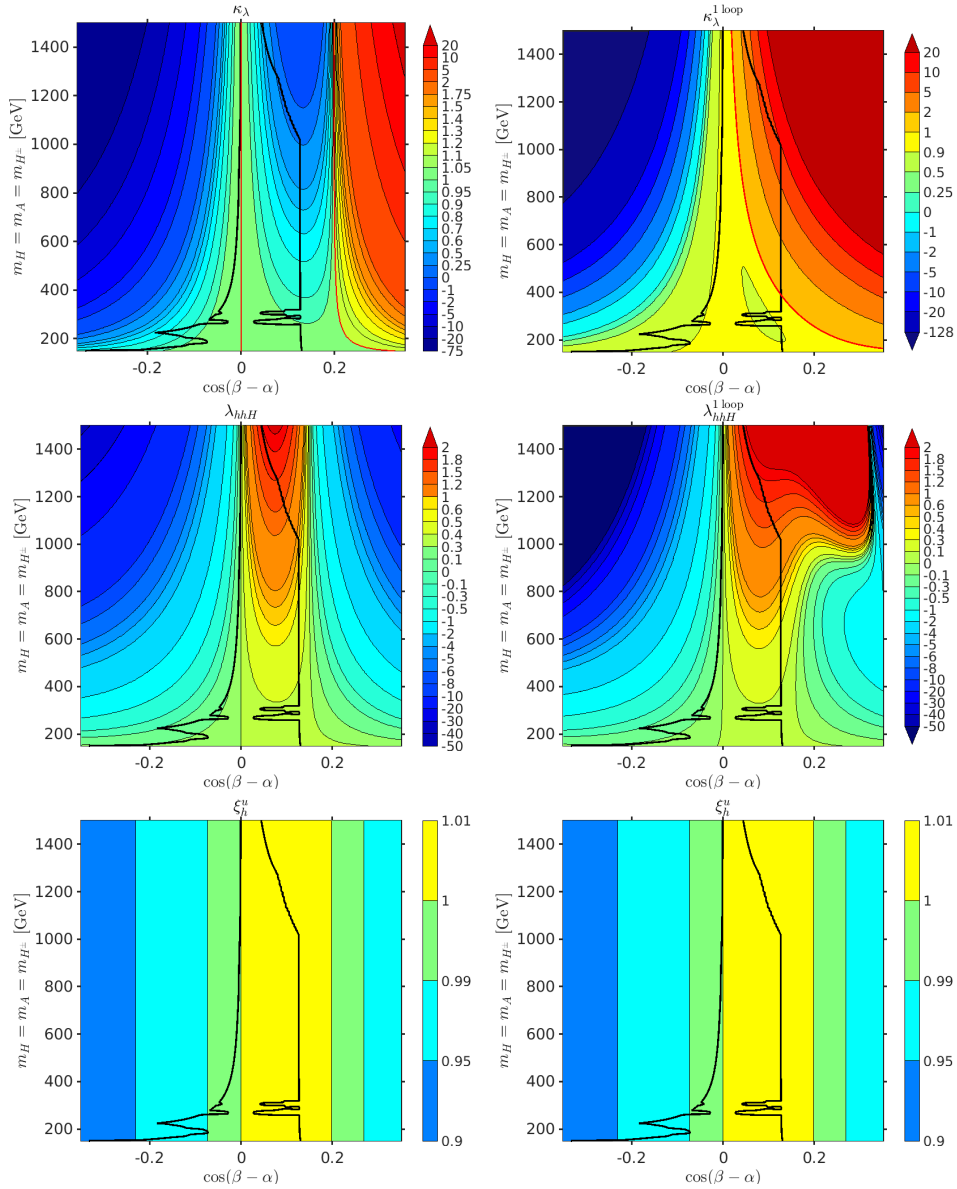
Figure 3.14

Same as Fig. 3.11 but for **Plane 2**.

is reached at the tip of the triangle where the value of the trilinear Higgs coupling λ_{hhH} is minimal Fig. 3.11. The middle plot shows the same ratio of the cross sections but incorporating the loop-corrected value of κ_λ. We observe a dramatic change in the prediction of this observable that mimics the behaviour of the trilinear. As discussed in Sec. 3.1, the cross section of Higgs pair production with κ_λ features a minimum at $\kappa_\lambda \approx 2.5$, due to an enhancement of the cancellation between the box and triangle diagrams in this process. We observe this feature in our scenario as well, in particular the 2HDM cross section is
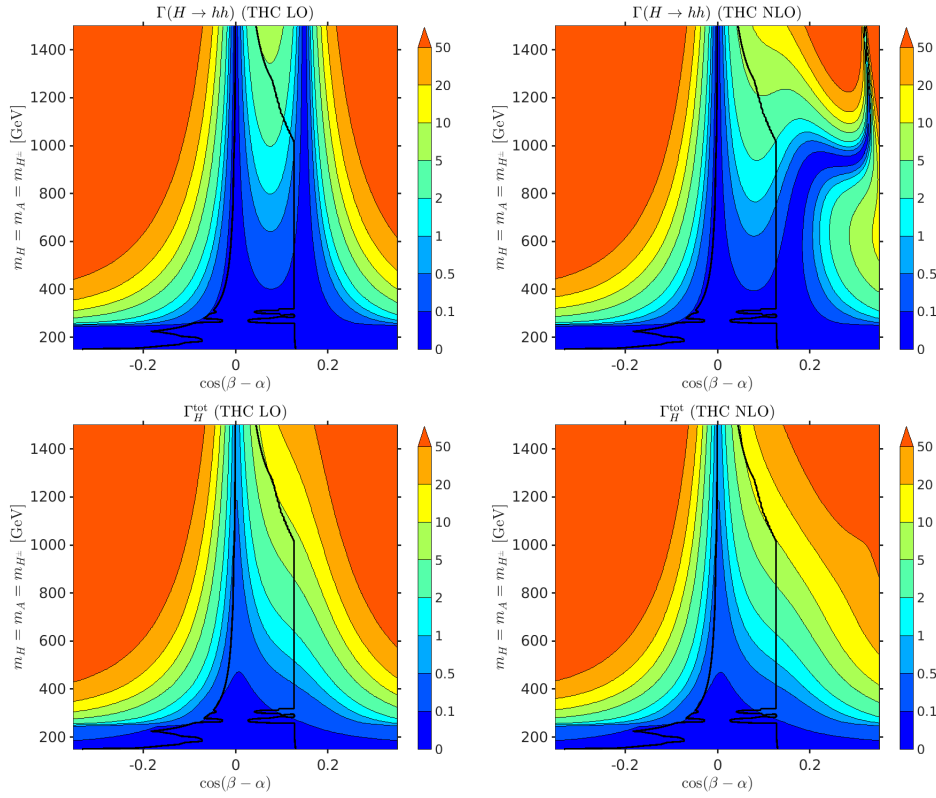
Figure 3.15
Same as Fig. 3.12 but for **Plane 2**.

diminished w.r.t the SM in the blue band within the allowed region for positive $c_{\beta-\alpha}$ and $t_\beta > 4$, where κ_λ at one-loop had a value of 2.5.

For a fixed value of t_β, if one follows the line of larger $c_{\beta-\alpha}$, after the decrease in the cross section, one encounters a steep rise that peaks for values of $\sigma_{\text{2HDM}}/\sigma_{\text{SM}} \approx 10$ at the border of what is allowed by perturbative unitarity. This reassures that in some benchmark scenarios, the loop correction to the trilinear Higgs couplings totally dominate over the Higgs pair production, and should not be disregarded in precise calculations that aim at comparing to the experimental data. For completeness we show in the lower left corner of Fig. 3.13 the ratio of the $\sigma_{\text{2HDM}}/\sigma_{\text{SM}}$ with κ_λ at NLO and LO. The significance of the loop corrections to the trilinear Higgs couplings is striking in the region close to the perturbative unitarity exclusion bound. We finally show in the upper right plot the prediction for the cross section with both trilinear Higgs couplings at NLO and we confirm that in this non-resonant scenario the coupling λ_{hhH} plays a minor role, which is also evident when one sees the ratio of the cross section with the both trilinear Higgs couplings at NLO and only κ_λ at NLO, as within the allowed region deviations of barely 10% are accomplished.

We proceed to analyse the **benchmark scenario 2**, the results are depicted in a same fashion as the scenario 1 in Fig. 3.14, Fig. 3.15 and Fig. 3.16. In Fig. 3.14 we show the predictions for the trilinear Higgs couplings and top Yukawas. The loop corrections to κ_λ in the region of $c_{\beta-\alpha} \approx 0.13$ and $m_H \approx 1000$ GeV reach 30. This corresponds to the slice
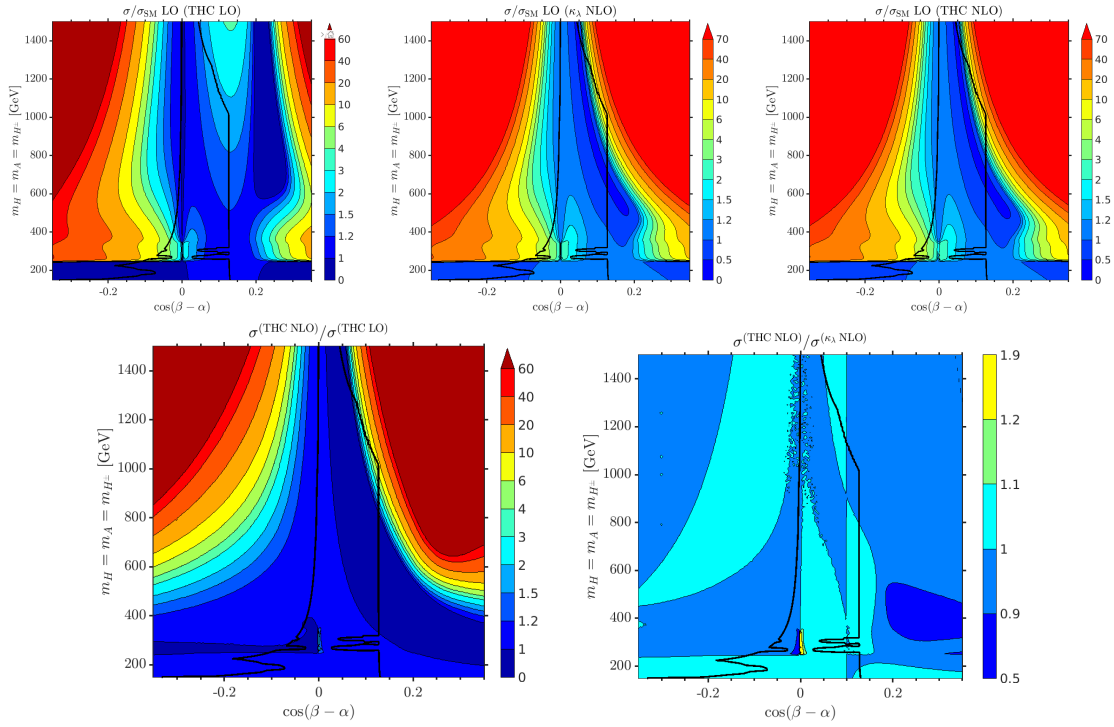
Figure 3.16
Same as Fig. 3.13 but for **Plane 2**.

of the benchmark scenario 1 with $t_\beta = 10$ and therefore the same discussion is applicable. Loop corrections to λ_{hhH} in the allowed region are not significant, which translates also into the very small changes in the total decay width of the heavy Higgs once those are taken into account (see Fig. 3.15). Since in this scenario the mass of the heavy Higgs is allowed to change, we observe a clear enhancement of the resonant production in the region $m_H \approx 400$ GeV, which is close to the top pair production threshold. We therefore expect an enhancement in the cross section in this region, which was already present at tree-level but we also expect large modifications of the prediction due to the impact of the loop corrections to κ_λ.

In Fig. 3.15 we show the prediction for the decay width of the heavy Higgs (without) including the loop corrections to λ_{hhH} in the upper row (left) right. We again see that within the allowed region the predictions are not significantly modified, which is translated to the total decay width of H shown in the lower row for tree (loop) level λ_{hhH} in the lower left (right) figure. Despite the smallness of these changes, we consistently use the prediction of Γ_H^{tot} (and Γ_h^{tot}) at tree-level for the LO THC cross section and at one-loop for NLO THC one.

The results for the cross section in this scenario are shown in Fig. 3.16. As expected, the production is resonantly enhanced at $m_H \approx 400$ GeV regardless of the loop corrections to λ_{hhH} up to a 10% of the SM prediction for $c_{\beta-\alpha} \approx -0.1$. The largest imact of the corrections to κ_λ is observed for $c_{\beta-\alpha} \approx 0.13$ and $m_H = 800$ GeV, where the cross section is enhanced up to 20 times w.r.t. the SM prediction and up to 10 w.r.t. the 2HDM prediction
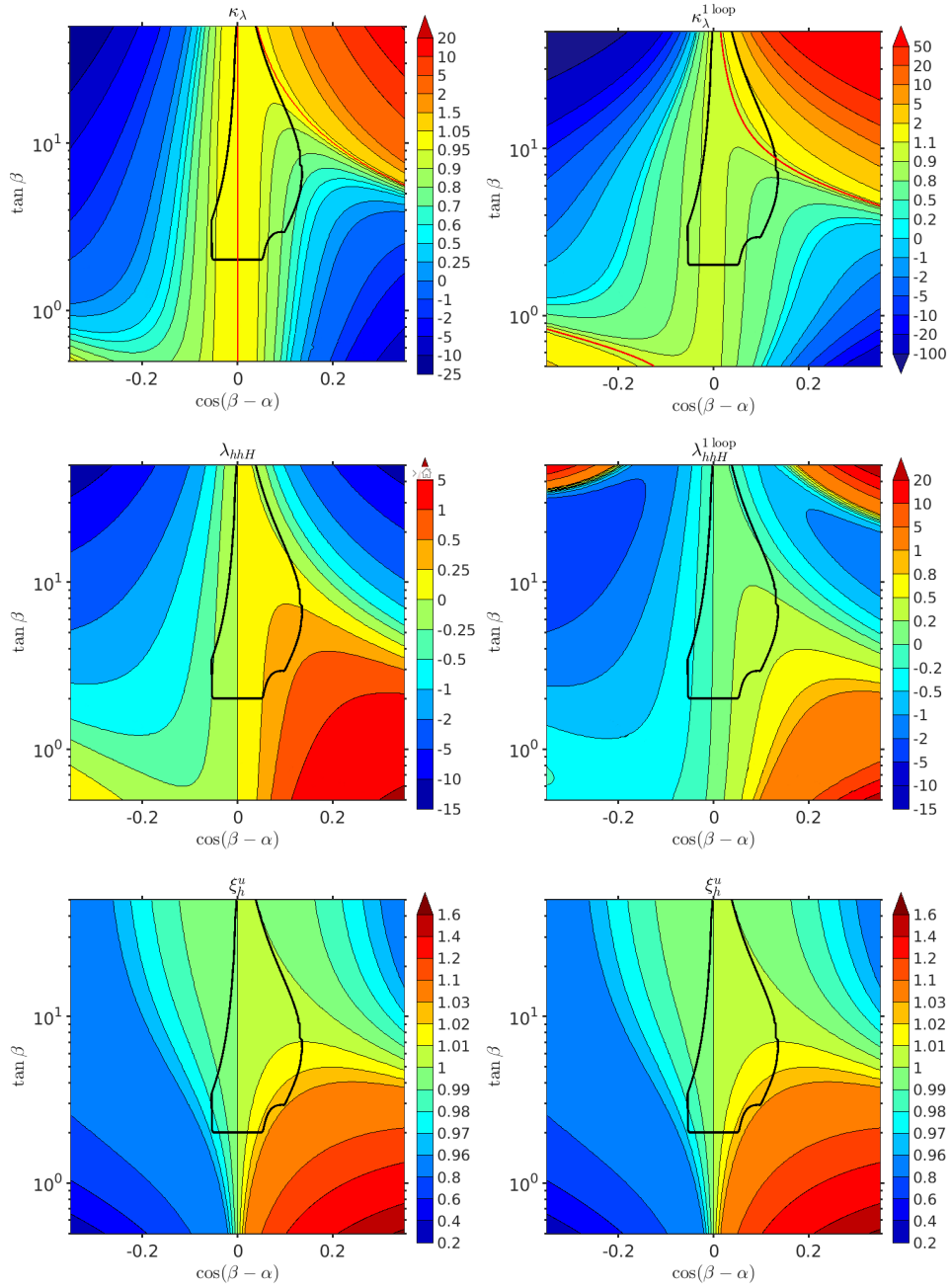
Figure 3.17

Same as Fig. 3.11 but for **Plane 3**.

with tree-level κ_λ. We note that the sharp cut off in the allowed region for larger values of $c_{\beta-\alpha}$ is originated in the signal strength of the 125 GeV Higgs whose signal strengths are checked with `HiggsSignals`. We also note that the loop corrections to κ_λ make the cross section decrease for values of $c_{\beta-\alpha} \approx 0.1$ and $m_H > 300$ GeV and $m_H < 800$ GeV.
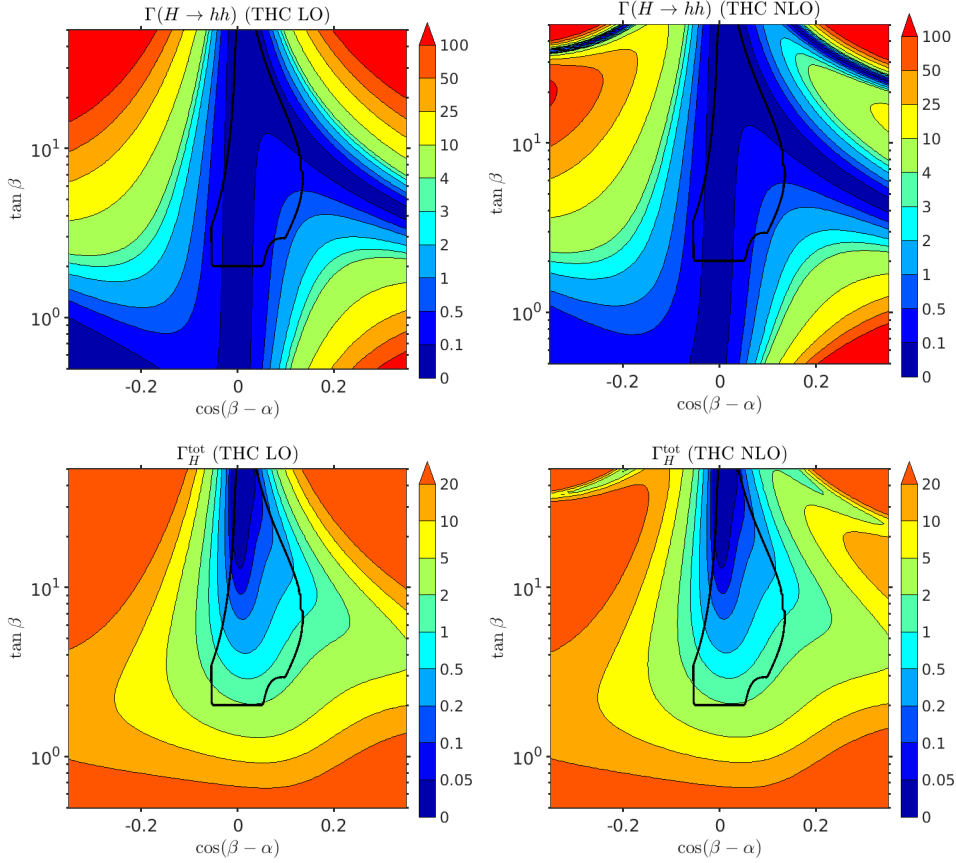
Figure 3.18
Same as Fig. 3.12 but for **Plane 3**.

The lowest value is reached at the darkest blue region and is close to 45% of the tree-level SM prediction. This shows that depending on $c_{\beta-\alpha}$ we could observe a very SM-like signal in the hh channel even in scenarios that are targeted at resonant production and with a mass of a heavy Higgs that would in principle favour a resonant enhancement. The largest corrections to λ_{hhH} are realised for values very close to the alignment limit and around $m_H \approx 300$ GeV.

Finally, we analyse the **benchmark scenario 3**, where the heavy Higgs has a mass of $m_H = 450$ GeV and therefore features a resonant production. In Fig. 3.17 we show the loop corrections to the trilinear Higgs couplings and the top Yukawas. Since the Yukawas for a given type of 2HDM only depend on $c_{\beta-\alpha}$ and t_β, we see the same behaviour as in the benchmark plane 1, although larger deviations from the SM are allowed because of the modified allowed region, especially in the regions further away from the tree-level alignment limit. The behaviour of the one-loop corrections resembles those of the benchmark plane 1, however the one-loop corrections to κ_λ are not as large in this case as the mass of the heavy scalars that run in the loop is less than half. Therefore, in the allowed region deviations in κ_λ up to a 100% in the region of positive $c_{\beta-\alpha}$ and large t_β. The corrections to λ_{hhH} in the
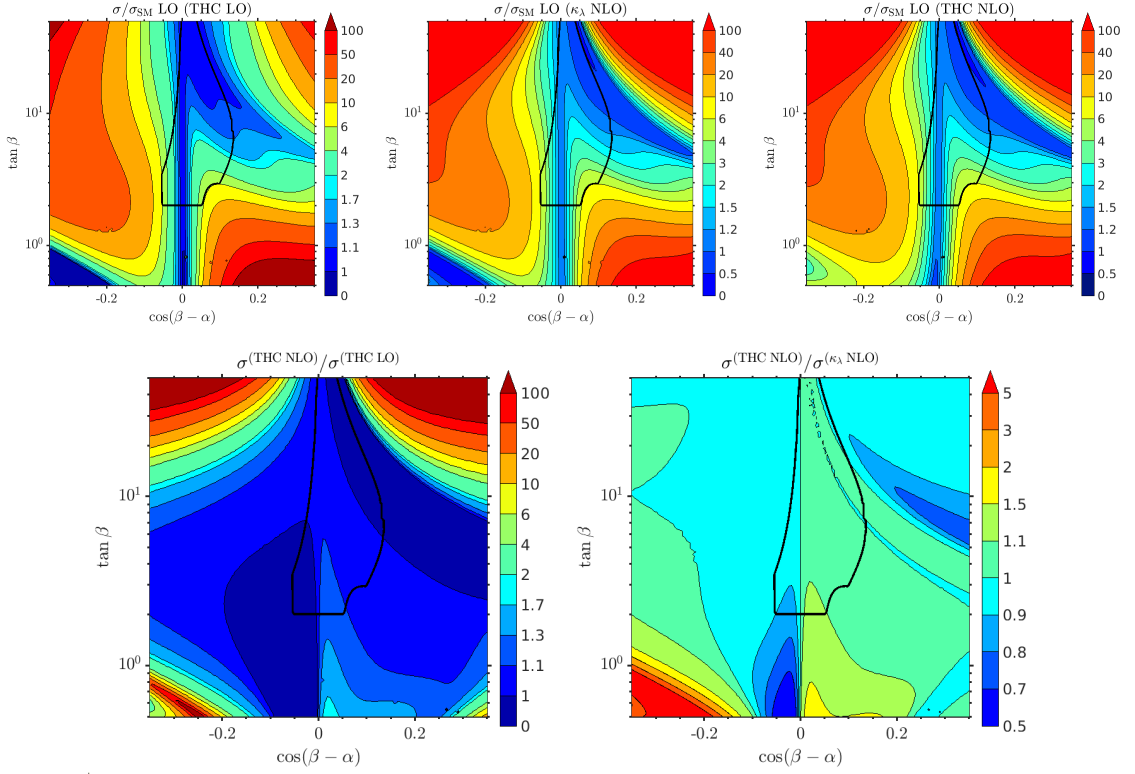
Figure 3.19
Same as Fig. 3.13 but for **Plane 3**.

allowed region are negligible and therefore there are no visible changes induced in Γ_H^{TOT}, as shown in Fig. 3.18.

In Fig. 3.17 we show the impact of the corrections in the Higgs pair production cross section. In this scenario, since the heavy scalars are all at masses of 450 GeV their contributions in the corrections to the trilinear Higgs couplings are not so large and therefore the impact in the cross section due to the deviation of the couplings is milder 30% deviations in the case of κ_λ corrections, and 10% deviations for λ_{hhH}. At tree-level, the largest enhancement of the cross section is observed at the region of $c_{\beta-\alpha} \approx 0.1$ and $t_\beta \approx 2$, where $\sigma_{\mathrm{2HDM}}/\sigma_{\mathrm{SM}} \approx 6$ this behaviour appears in the regions further away from the alignment (for negative, $c_{\beta-\alpha}$ $\sigma_{\mathrm{2HDM}}/\sigma_{\mathrm{SM}} \approx 5$) due to the rising importance of the resonant contribution and since m_H is closer to the top pair production threshold than in the benchmark scenario 1. The effect of the loop corrections in the allowed region is milder due to the lighter BSM scalars, the main feature of the corrections to κ_λ is visible in the region of large t_β and positive $c_{\beta-\alpha}$, where loop corrections shoft the values of κ_λ from roughly 1 to 2, shrinking the prediction of the cross section from a 10% enhancement with the tree-level trilinear couplings up to a 30% suppression w.r.t the SM cross section once the loop corrections to κ_λ are included, this corresponds to the black blue region that we see in the upper right corner of the allowed region in the lower left plot. The corrections to λ_{hhH} in this scenarios are again mild due to the lack of mass degeneracy between the heavy scalars, however, they

do account for up to a 20% enhancement (suppression) in the cross section in the region of small t_β visible in the lower right (left) part of the allowed region of the lower left plot.

To conclude this section we pick up some of the main phenomenological features that we learned from the inclusion of the corrections to the trilinear Higgs couplings in the Higgs pair production cross section:

1: The larger corrections arise for large masses of the heavy scalars and impact heavily on the value of κ_λ that can be directly translated to the cross section.

2: Mass splitting between the heavy scalars can introduce large radiative corrections, inducing a sign flip in λ_{hhH}.

3: In the benchmark scenarios analysed there was small interplay between the enhancement produced by a large correction to κ_λ and the one produced by the resonant production.

3.3   Impact of experimental uncertainties

This section is based on the following publication:

[1] F. Arco, S. Heinemeyer, M. Mühlleitner, and K. Radchenko, *Sensitivity to triple Higgs couplings via di-Higgs production in the 2HDM at the (HL-) LHC*, Eur. Phys. J. C 83 (2023) 1019 [2212.11242]

Before moving to the invariant mass distribution of hh-production, we will analyse the impact of experimental uncertainties on this observable, which will in turn impact the sensitivity to the trilinear couplings. These effects are the experimental smearing, i.e. the uncertainty in the m_{hh} measurement, and the experimental resolution, i.e. the size of the bin as well as its arbitrary location. We neglect any "background" from other SM processes, which would require a dedicated experimental analysis. Since both these effects will have a larger impact on the resonant structure, we will focus on the relative difference of the number of events around the resonance after the application of these uncertainties. To give a numeric estimate we define a variable R, following Ref. [254], as

$$R := \frac{\sum_i |N_i^R - N_i^C|}{\sqrt{\sum_i N_i^C}},$$ (3.19)

where N^R is the number of events of the resonant contribution, and N^C is the number of events of the continuum. The window in which the events are counted is defined by

$$|N^R - N^C| > \text{bin size} \times 20 \text{ GeV} .$$ (3.20)

The sum over i in Eq. (3.19) runs over all the bins that fulfill this condition. The chosen condition in Eq. (3.20) starts with a minimum of 1000 excess events due to the resonance

when the bin size is 50 GeV and 200 events when the bin size is 10 GeV, i.e. smaller bin sizes are not "punished". Using the absolute value in the definition of R in Eq. (3.19), as well as in the definition of the window in Eq. (3.20) effectively makes use of both the dip and the peak of the smeared distribution. This constitutes a simplified theory definition, where in a realistic experimental analysis the dip-peak structure would be taken into account via a template fitting, see e.g. the analysis in Ref. [255]. The numbers of events are in turn obtained using the relation between the cross section and the integrated luminosity of the collider,

$$N = \sigma \cdot \mathcal{L}, \tag{3.21}$$

where we have used $\mathcal{L} = 6000$ fb^{-1}, i.e. the sum of the anticipated luminosity of ATLAS and CMS combined at the end of the HL-LHC run. This constitutes the most optimistic case.

3.3.1 Smearing

Differential cross section measurements are affected by the finite resolution of the detectors. This translates into a blurred or "smeared" spectrum that can be observed in such experiments. We try to mimic this effect by artificially smearing the theoretical prediction for the invariant mass distributions of the chosen benchmark points. To do this we introduce a statistical error to our prediction of the invariant mass. We apply the uncertainties in m_{hh} by allowing the value of an event to shift to the left or to the right in the spectrum according to a Gaussian probability distribution. The amount of smearing is defined in terms of a percentage of smearing p that indicates the deviation from the m_{hh} value contained in the full width at half maximum (FWHM) of a Gaussian distribution cantered at that value of m_{hh}, i.e. the FWHM $= 2\sqrt{2\log 2}\sigma$, where σ is the standard deviation.

We illustrate this effect in Fig. 3.20 for one particular example of a benchmark point with the masses fixed to $m_A = m_{H^\pm} = 544.72$ GeV and $m_H = 515.5$ GeV, $c_{\beta-\alpha} = 0.12$, $t_\beta = 10$ and m_{12}^2 as in Eq. (2.95). In this figure we show in blue the m_{hh} distribution without smearing (the ideal case). The solid line depicts the full distribution, whereas the dashed line shows the result for the continuum (non-resonant) diagrams. The red lines demonstrate the effect of applying a 10% (left plot) and 15% (right plot) smearing on the theoretical prediction of the m_{hh} distributions, where the solid (dashed) lines indicates the full (continuum) result. While a 15% smearing was given as a realistic future estimate, the 10% smearing indicates a potential optimistic improvement. One can observe that from the original dip-peak structure as seen in the solid blue line effectively only a peak or bump around the original peak remains. The original dip is visible only as a very small reduction of the unsmeared distribution, as the relative weight of the points below the continuum is smaller than those above the continuum (note the logarithmic scale). Furthermore it should be noted that on the edges of the m_{hh} values there is a slight bump in the smeared distribution. This is an artefact of the method that we used for the smearing and should be neglected. Since we do not generate the number of events but rather a theoretical prediction for a specific value of $d\sigma/dm_{hh}$, we cannot redistribute the events according to some uncertainty. What we do is an approach that is independent of the number of events but should be equivalent. We generate a Gaussian probability distribution function centered at each of the predicted points and a standard deviation according to the percentage of smearing as explained above. Afterwards at each point in m_{hh} the Gaussians of the full

distribution are summed and finally normalised to the original value of the integrated total cross section. This corresponds to taking the limit of the number of events N → ∞. At the edges only events from one side contribute to the sum of the Gaussians and are not lowered by a smaller counterpart on the other side. If the distribution would continue down to infinite values, there would be no bumps at the edges.
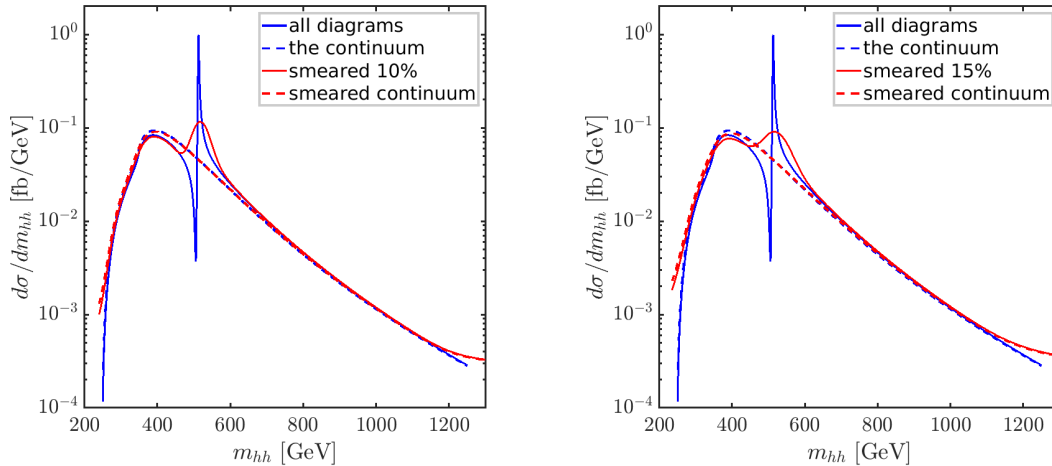

Figure 3.20
Theoretical (blue) and smeared (red) invariant mass distributions for the selected benchmark point (see text). Solid (dashed) lines show the contribution of the total (continuum) differential cross section. Left (right) plot has a 10% (15%) smearing.

3.3.2   Binning

As a further step in the evaluation of the experimental challenges, we analyse the effect of the bin width. The binning means that the data in a particular interval in m_{hh} is presented as the mean value of the differential cross section of all the points that fall in that interval. Assuming that at least one of the Higgs bosons analysed will decay in a $b\bar{b}$ pair, the bin size will eventually be determined by the b-jet mass resolution from the reconstruction of the $h \to b\bar{b}$ decay mode. This affects the visualisation of the results in a realistic experimental set up, but also the counting of events for the evaluation of the experimental sensitivity, see Eq. (3.19). The binning is applied after the smearing discussed in the previous subsection.

In Figs. 3.21 and 3.22 we show the same spectrum but for a different bin size in the m_{hh} variable: 10 GeV (upper left), 20 GeV (upper right), 40 GeV (lower left) and 50 GeV (lower right). Fig. 3.21 assumes a 10% smearing, whereas in Fig. 3.22 we show the more realistic result with 15% smearing. The red lines show the true (smeared and binned) prediction, whereas the other colours indicate the unsmeared, but binned results for comparison. One can observe that the effect of the smearing becomes less significant in the region of resonant production for a larger bin size. The resonance is already partially diluted by the smearing, and the effect of the binning becomes less visible, as can be observed best in the lower right plots of Figs. 3.21 and 3.22. The effect of the binning is less important once the smearing
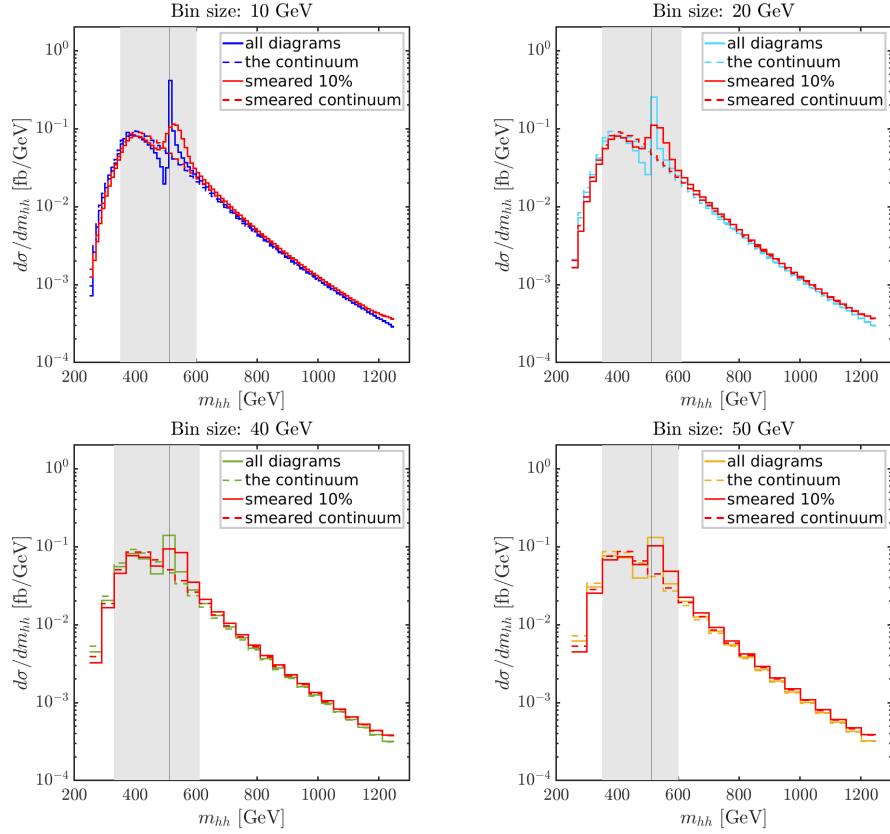
Figure 3.21

Different bin sizes for a 10% smeared distribution in the example benchmark point (10, 20, 40 and 50 GeV). The red lines correspond to the true (smeared and binned) prediction of the m_{hh} distribution. The other colour indicates the corresponding binned, but unsmeared distribution. Solid (dashed) lines represent the total (continuum) contribution to the cross section. The grey region represents the region that falls into the window defined to compute the variable R. The black vertical line indicates the value of the resonant mass, i.e. 512.5 GeV.

of the experimental data is taken into account. After the binning the "dip" is effectively indistinguishable from the continuum contribution. The peak is still persistent and for larger bin size approaches the same height as the bump at ~ 400 GeV before binning.

In the most conservative result, the expected experimental resolution should have a bin size of 50 GeV and a smearing of $\sim 15\%$. The expected results in this case would possibly give access to the location of the resonance (the mass of the CP-even H should be know via single production by the time the di-Higgs cross section is measured) and partially to the height, and thus possibly to the size of λ_{hhH}. In order to make a quantitative estimate of the sensitivity of the signal produced by the resonant diagram we have calculated the value of the variable R defined in Eq. (3.19) that is obtained from Figs. 3.21 - 3.22, shown in Tab. 3.2. The grey region represents the region that falls into the window defined to compute the variable R. Overall, one can see that the values of R are significant, i.e. the
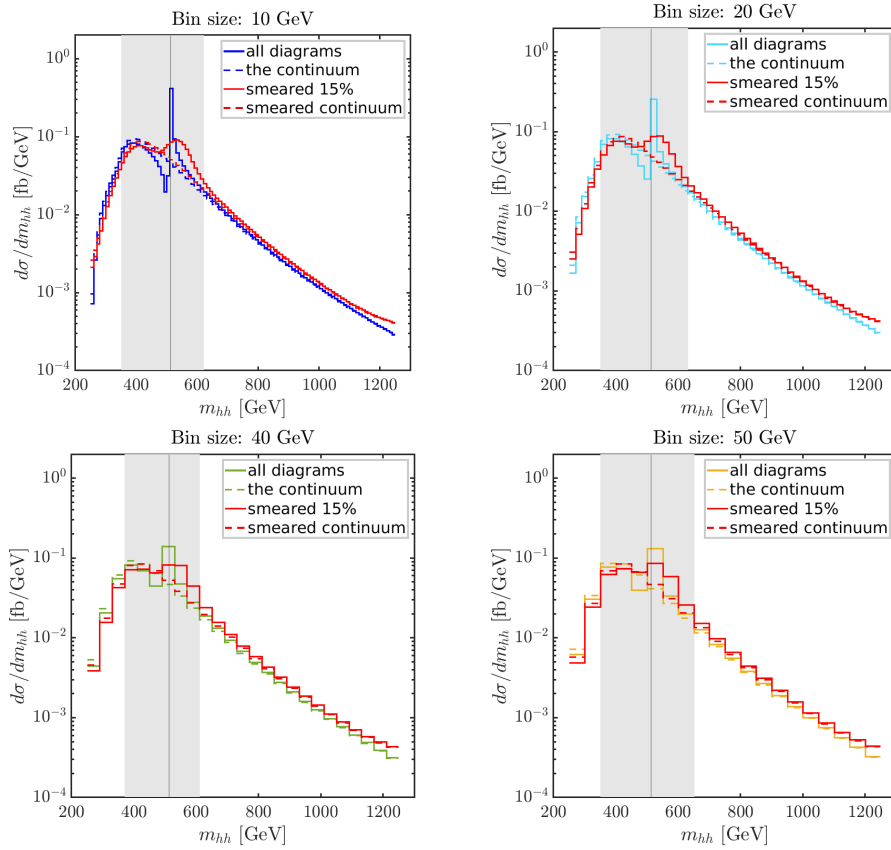
Figure 3.22
Same as Fig. 3.21 but for 15% smearing.

signal could possibly be distinguished at the HL-LHC if our assumptions on the experimental uncertainties are met. It should be noted that we are not taking into account the efficiency of the particle detectors, which could reduce significantly the estimate of R (see also the discussion in Sec. 4.2). Comparing the two columns in Tab. 3.2 one observes R is roughly 10% worse as the assumed percentage of smearing increases by 5%. However, R is is somewhat more stable w.r.t. the bin size, where deviations within $\sim 5\%$ are found. This would constitute a rather positive feature for an experimental set-up.

Bin size	R(10% smear)	R(15% smear)
10 GeV (blue)	108.8	98.0
20 GeV (light blue)	107.6	98.3
40 GeV (green)	106.5	101.0
50 GeV (yellow)	103.0	98.9

Table 3.2: Values of the variable R for the significance of the signal for different bin sizes for a 10% and 15% smeared distribution, see Figs. 3.21-3.22.

The next part of the analysis concerns the arbitrary choice of the location of the bin. This choice can also affect the pattern of the invariant mass distribution. The concrete value of $m_{hh}^{\min}$ (the value of m_{hh} at the bin start) and $m_{hh}^{\max}$ (the value of m_{hh} at the bin end) affects the number of events that fall into that bin and thus can have an impact on the evaluation of the sensitivity R. For the previously used benchmark point we change the location of the bin for a 10% and 15% smeared distribution and a 50 GeV bin size.
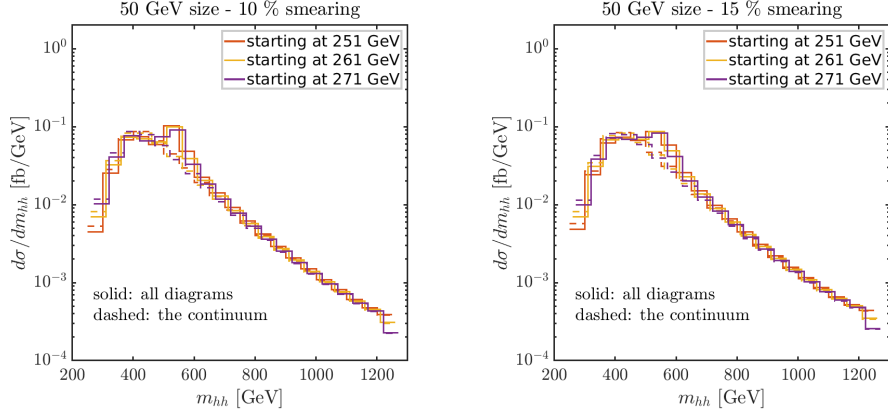

Figure 3.23
Invariant mass distributions for different bin locations assuming a bin size of 50 GeV and a smearing of 10% (left) and 15% (right). Solid (dashed) curves show the full (continuum) result.

In Fig. 3.23 we show the difference in the invariant mass distribution created by a change in the location of the first bin by 10 or 20 GeV, i.e. we start the distribution at $251, 261, 271$ GeV as orange, yellow and purple lines, respectively. In both plots we show the difference between the total differential cross section (solid lines) and the continuum contribution (dashed lines). The left (right) plot uses a smearing of 10% (15%). One can observe that for all three choices of bin locations the peak structure remains similarly visible (the dip is strongly diluted from the smearing and the binning as discussed in the previous subsections). To quantitatively evaluate the significance of the signal of the resonant enhancement we list the values of R for the two plots discussed above in Tab. 3.3.

Bin location	R(10% smear)	R(15% smear)
start at 251 GeV (orange)	103.0	98.9
start at 261 GeV (yellow)	104.6	90.4
start at 271 GeV (purple)	102.8	95.1

Table 3.3: Values of the variable R for the sensitivity of the signal for different bin locations for a 10% and 15% smeared distribution and a bin size of 50 GeV.

In Tab. 3.3 one can observe that the variation in R stays within 5% when we modify the location of the bins. That means that the uncertainties associated to the location of the bin are smaller than the ones associated to the smearing and about the same as for the bin size. Therefore, overall we find that the experimental resolution of the particle detector,

which we tried to mimic by smearing the data, has a larger impact on the resonance, and the width and location of the binning has a smaller effect in diluting the resonance.

We conclude this section saying that the smearing of experimental data partially blurs the dip-peak structure around the resonance and mostly a bump survives, with a very small reduction due to the dip w.r.t. the unsmeared result. While the smearing has a visible effect on R, the binning hardly reduces its value. Similarly, the location of the bin, which is partially arbitrary, has a smaller impact on R once we take into account the finite resolution of the detector (smearing), thus it is crucial for experimental analysis to reduce the smearing as much as possible, while the binning playing a smaller impact according to our analysis. We will investigate further experimental uncertainties and the expected sensitivity to the BSM $\xi_H^t \times \lambda_{hhH}$ couplings in greater detail in Sec. 4.2.

3.4   Loops and Interference

This section and Sec. 3.5 are based on the following publication:

[3] S. Heinemeyer, M. Mühlleitner, K. Radchenko, and G. Weiglein, *Higgs Pair Production in the 2HDM: Impact of Loop Corrections to the Trilinear Higgs Couplings and Interference Effects on Experimental Limits*, Eur. Phys. J. C. 85 (2025) 437 [2403.14776]

In this section, we explore the behaviour of the invariant mass distribution of the di-Higgs final state when incorporating loop corrections to the trilinear couplings involved in Higgs pair production. We start our analysis discussing the effects on two benchmark scenarios defined in Tab. 3.4.

	t_β	$c_{\beta-\alpha}$	m_H	m_A	m_{12}^2	$\kappa_\lambda^{(1)}$	$\lambda_{hhH}^{(1)}$
BP1	10	0.13	465	660	$m_H^2 s_\beta c_\beta$	3.65	0.25
BP2	15	0.12	400	660	$m_H^2 s_\beta c_\beta$	5.31	0.2

	$\kappa_\lambda^{(0)}$	$\lambda_{hhH}^{(0)}$	$\lambda_{hHH}^{(0)}$	$\lambda_{HHH}^{(0)}$	$\lambda_{hAA}^{(0)}$	$\lambda_{HAA}^{(0)}$	
BP1	0.84	0.1	-2.31	0.07	-5.83	0.54	
BP2	0.97	-0.07	-2.27	0.12	-6.77	0.67	

Table 3.4: Benchmark points for the analysis of the impact of trilinear Higgs couplings in the invariant mass distributions. Masses are given in GeV. For both points $s_{\beta-\alpha} > 0$ and $m_{H^\pm} = m_A$, which in particular means $\lambda_{hAA}^{(0)} = \lambda_{hH^\pm H^\pm}^{(0)}$ and $\lambda_{HAA}^{(0)} = \lambda_{HH^\pm H^\pm}^{(0)}$. These benchmarks are allowed by the applied constraints in 2HDM Type I, altough the quantities shown are independent of the type.

The invariant mass distributions shown in our analysis are calculated at leading order in QCD. It would be possible to compute the invariant mass spectrum with `HPAIR` at NLO QCD in the Born improved heavy-top limit. However, it has been shown that mass effects may significantly distort the NLO distributions [222–224, 226, 227]. While, for the 2HDM, the full mass effects at NLO QCD have been considered in Ref. [251], there exists no public code that allows us to obtain results for our benchmark scenarios, in particular including resonances. In Ref. [256] a parametrisation has been given for the total cross section and the m_{hh} distribution in the framework of a non-linear effective field theory as a function of the anomalous Higgs couplings that includes NLO corrections. While this framework considers deviations from the SM Higgs sector, it however does not include the possibility of additional Higgs bosons. Consequently, one has the choice between a LO distribution ignoring NLO effects and an approximate NLO distribution ignoring finite top-mass effects at NLO, where we chose to adopt the LO case. While this approach obviously cannot capture the full NLO mass effects, it does provide information regarding the possible impact of a BSM Higgs boson resonance and of NLO electroweak corrections to THCs on the m_{hh} distribution, which is the main goal of our analysis. The inclusive cross section, on the other hand, is rather well approximated at NLO QCD by applying a K-factor, obtained from the ratio of the NLO to the LO cross section, of $K(\text{NLO}) \approx 2$.
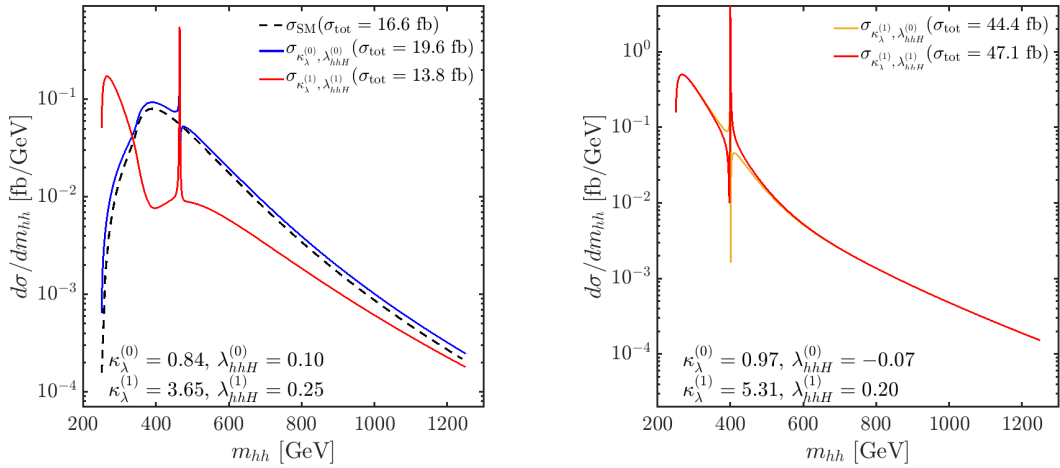
Figure 3.24

Left: Invariant mass distribution for the benchmark point BP1 in the 2HDM Type I defined in Tab. 3.4. The SM prediction (dashed black line) is shown together with the 2HDM results with (solid red line) and without (solid blue line) loop corrections to the THCs, see text. Right: Impact of the loop corrections to λ_{hhH} on the resonance shape for the benchmark point BP2 defined in Tab. 3.4. The red (orange) line shows the result with (without) loop corrections to λ_{hhH}.

In Fig. 3.24 we present the m_{hh} distributions for the points in the 2HDM Type I defined in Tab. 3.4, BP1 on the left and BP2 on the right. The blue curve in the left plot of Fig. 3.24 is the invariant mass distribution for BP1 with both THCs taken at tree-level, whereas the red line displays the result for the distribution for the case where both THCs are incorporated at the one-loop level. The dashed black line indicates the SM prediction.

Starting our discussion with the tree-level distribution (blue line), we can see the features discussed in the toy model in Sec. 3.1: (1) the small values of the differential cross section just above the threshold as a consequence of a cancellation of the form factors involved in the continuum diagrams and (2) the maximum at $m_{hh} \approx 400$ GeV, which is related to the di-top on-shell production. In this case, the resonance is located at $m_{hh} \approx m_H$ showing a peak-dip structure. Apart from the resonant contribution, the shape of the tree-level distribution resembles the SM prediction (dashed black line), taking into account the relatively SM-like value of $\lambda_{hhh}^{(0)}$.

Turning to the red line, incorporating one-loop corrections to both THCs, one can observe that the shape of the distribution changes drastically. In particular the cancellation close to the kinematical threshold in the leading order distribution is lifted.[9] This cancellation now happens at values of $m_{hh} \approx 400$ GeV and leads to a large reduction of the differential cross section in the region where at leading order a maximum occurred. Furthermore, close to the kinematical threshold the distribution is largely enhanced, leading to the appearance of a structure resembling a peak at $m_{hh} \approx 250$ GeV. We also investigated the impact of the one-loop corrections to the two THCs individually (not shown in the plot) and found that in this scenario the corrections to λ_{hhH} play a minor role, while the biggest changes are caused by the large one-loop corrections to κ_λ.

Also shown in the figure are the total cross section values.[10] Here it is interesting to note that the decrease in the tree-level value of κ_λ of about 15% w.r.t. the SM[11] leads to an increase of roughly 20% of the tree-level cross section, whereas the inclusion of the one-loop corrections to the THCs results in a reduction of the 2HDM cross section by about 30%, i.e. 20% smaller than the SM result.

On the right plot of Fig. 3.24 we show an example where the loop corrections to λ_{hhH} play a crucial role. The input parameters are defined in the BP2 of Tab. 3.4.

The result including NLO corrections only to κ_λ is shown as orange solid line, and corresponds to a total LO QCD cross section of 44.4 fb. The m_{hh} distribution shows a pronounced peak–dip structure at $m_{hh} \sim m_H$. The result including the one-loop corrections to both THCs is shown as solid red line. The incorporation of the higher-order corrections results in a larger $\lambda_{hhH}^{(1)}$ value with opposite sign compared to the tree-level value. Its inclusion gives rise to a dip–peak structure, i.e. the opposite behaviour compared to the tree-level case. This effect is caused by a change in the overall sign of the couplings involved in the resonant diagram, $\lambda_{hhH} \times \xi_H^t$, see the discussion in Sec. 3.1. In the present example we demonstrate that such a change can arise solely from one-loop corrections to λ_{hhH}, i.e. the incorporation of electroweak loop corrections is crucial in this case for a reliable prediction of the experimental signature (experimental effects like smearing due to a limited detector resolution will be discussed in the next section). This effect is clearly visible even in the case of large one-loop corrections to κ_λ, as it is the case in this example. Our discussion highlights the relevance of higher-order corrections also in the THCs involving BSM Higgs bosons, as they can have a drastic effect on the invariant mass distributions.

---

[9]This effect has already been observed in the context of the SM in Ref. [237].

[10]The total cross section values are given at LO QCD in accordance with the distributions given at LO. As stated above, including the NLO QCD corrections obtained with HPAIR, the cross section values would increase by about a factor of 2 [1].

[11]Here we use the LO SM total cross section.

3.5 Confrontation with experimental data

In view of the significant improvements in the experimental sensitivity to the di-Higgs production cross section that have occurred recently and are expected to be achieved in the future, it is crucial that the experimental limits (and of course eventually also the experimental measurements) are presented in such a way that they can be confronted with theoretical predictions in different scenarios of electroweak symmetry breaking in a well-defined way. Up to now the experimental limits presented by ATLAS and CMS are given either for non-resonant production, taking into account only SM-like contributions, or for purely resonant production, where SM-like non-resonant contributions are omitted. We discuss both types of limits in the following.

3.5.1 Non-resonant production

We start our discussion with the analysis of the non-resonant limits. In this case the experimental limits are obtained under the assumption that there is no contribution from an s-channel exchange of an additional Higgs boson, i.e. only the contributions of the first and second diagrams in Fig. 3.2 are taken into account. The most recent results from ATLAS [218] and CMS [193] report a limit on the cross section of $gg \to hh$, which depends on the value of κ_λ, and a bound on κ_λ is extracted. This is done by comparing the experimental limit with the SM prediction for a varied κ_λ. We show in Fig. 3.25 an example of the application of these limits for one particular benchmark scenario in the 2HDM, where we vary $c_{\beta-\alpha}$. The chosen input parameters are

$$
\begin{aligned}
t_\beta = 10, \ c_{\beta-\alpha} \in \{0 \ \dots \ 0.16\} \ (s_{\beta-\alpha} > 0), \\
m_H = m_A = m_{H^\pm} = 1000 \text{ GeV}, \ m_{12}^2 = m_H^2 c_\alpha^2 / t_\beta \ .
\end{aligned}
\tag{3.22}
$$

The large m_H value ensures that the resonant contribution from the s-channel H exchange is negligible (we do not discuss effects of varying λ_{hhH} in this context), as seen in Sec. 3.1. The variation of $c_{\beta-\alpha}$ results in a variation of κ_λ as indicated in the left plot of Fig. 3.25. The blue dashed line shows the prediction for κ_λ at lowest order, while the blue solid line shows the one-loop prediction for κ_λ. The gray line indicates the value of $\kappa_\lambda = 1$, which corresponds to a coupling value of $\lambda_{hhh} = \lambda_{\text{SM}}^{(0)}$. The parameter spaces that are excluded by theoretical constraints are indicated by the yellow (vacuum stability), dark green (perturbative unitarity at LO) and light green (perturbative unitarity at NLO) shaded areas. For the application of these limits we used the public package `thdmTools` [2]. The constraints from vacuum stability exclude the displayed yellow region with negative values of $c_{\beta-\alpha}$. For the largest positive values of $c_{\beta-\alpha}$ the tightest bound arises from perturbative unitarity (for the constraints at LO and NLO we require that the eigenvalues of the $2 \to 2$ scattering matrix satisfy $|a_0| < 1$, where a_0 denotes the s-wave amplitude of the scattering process). Demanding that the measured properties of the Higgs boson at 125 GeV should be satisfied poses a bound that is weaker than the one from NLO perturbative unitarity and therefore this bound is not explicitly shown in the plot. It can be observed that at tree level the variation of $c_{\beta-\alpha}$ towards larger values results in a decrease of $\kappa_\lambda^{(0)}$, which reaches values close to zero for $c_{\beta-\alpha} \gtrsim 0.1$. Including the one-loop corrections, as shown by the blue solid line, yields a strong increase of $\kappa_\lambda^{(1)}$, with $\kappa_\lambda^{(1)} \gtrsim 5$ for $c_{\beta-\alpha} \gtrsim 0.1$ in this example.
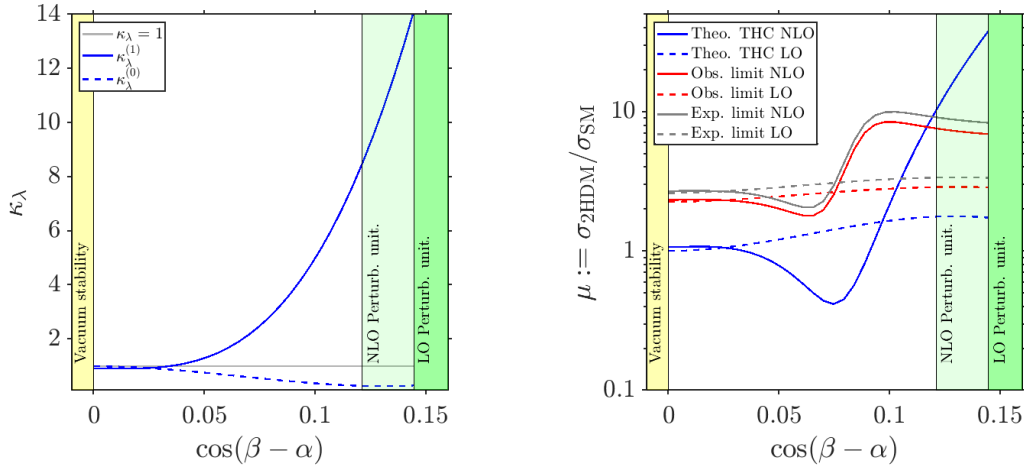
Figure 3.25

2HDM Type I scenario described in Eq. (3.22). Left: κ_λ as a function of $c_{\beta-\alpha}$. The gray (blue dashed, blue solid) line shows the result for $\lambda_{SM}^{(0)}$ ($\lambda_{hhh}^{(0)}$, $\lambda_{hhh}^{(1)}$), normalised to $\lambda_{SM}^{(0)}$. Right: Limits on $\mu \equiv \sigma_{2HDM}/\sigma_{SM}$ (each cross section calculated at LO QCD) as function of $c_{\beta-\alpha}$. Red, gray and blue: expected, observed experimental limits and theory predictions with κ_λ taken at LO (dashed) and NLO (full). In both plots the parameter space excluded by theoretical constraints is indicated by the yellow (vacuum stability), dark green (perturbative unitarity at LO) and light green (perturbative unitarity at NLO) shaded areas.

In the right plot we present the corresponding experimental limits and theoretical predictions for the ratio between the 2HDM and SM di-Higgs cross sections, $\mu \equiv \sigma_{2HDM}/\sigma_{SM}$, both calculated at LO QCD. The solid (dashed) blue line shows the theory prediction using the one-loop (tree-level) value for κ_λ. The dark red line shows the latest experimental observed limit from non-resonant searches reported by ATLAS [218]. The solid (dashed) line indicates the observed limit for the value of κ_λ that we have calculated at NLO (LO). The corresponding gray line represents the expected limit for κ_λ at NLO (LO), in this case the calculation is done using `BSMPT`. Confronting the experimental limits with the theoretical predictions, a value of $c_{\beta-\alpha}$ is regarded as excluded if the predicted cross section is larger than the experimentally excluded one. One can see that non-resonant di-Higgs searches would not exclude any value of $c_{\beta-\alpha}$ for the case where $\kappa_\lambda^{(0)}$ is used. As a consequence of the large loop corrections to κ_λ this changes once the one-loop corrections are taken into account. One can see that in this case for the considered example the non-resonant searches exclude a region for large $c_{\beta-\alpha}$ values that is allowed by all other constraints. This underlines the fact that the search for di-Higgs production at the LHC already provides sensitivity to parameter regions of the 2HDM that were unconstrained so far, see also Ref. [126], where scenarios with $c_{\beta-\alpha} = 0$ have been considered.

3.5.2 Resonant production

We now turn to the interpretation of experimental limits for resonant di-Higgs production in the 2HDM. The resonant limits that have been presented by ATLAS and CMS so far were obtained assuming that only one heavy resonance is realised, neglecting the contributions of the continuum diagrams. This approach is potentially problematic since in any realistic scenario the contributions of the non-resonant diagrams one and two in Fig. 3.2 will of course always be present in addition to the possible resonant contribution of an additional Higgs boson. The limits obtained by ATLAS and CMS can therefore only be directly applied to scenarios where the impact of the non-resonant diagrams is negligible compared to the contribution of the resonant diagram. Using the 2HDM as a test case for scenarios that have been claimed to be excluded or non-excluded by ATLAS and CMS we will investigate in the following to what extent the assumption made in obtaining the experimental limits is justified.

We note that the assumption of restricting to the resonant contribution implies that the m_{hh} distribution corresponding to the assumed signal will have a peak structure located at $m_{hh} \approx m_H$. This peak structure can potentially be modified by the continuum contributions and by interference effects, where the latter in particular can give rise to peak–dip or dip–peak structures. In the context of assessing the non-resonant contribution arising from the exchange of the detected Higgs boson at 125 GeV (second diagram in Fig. 3.2) we will analyse the impact of loop corrections to κ_λ.
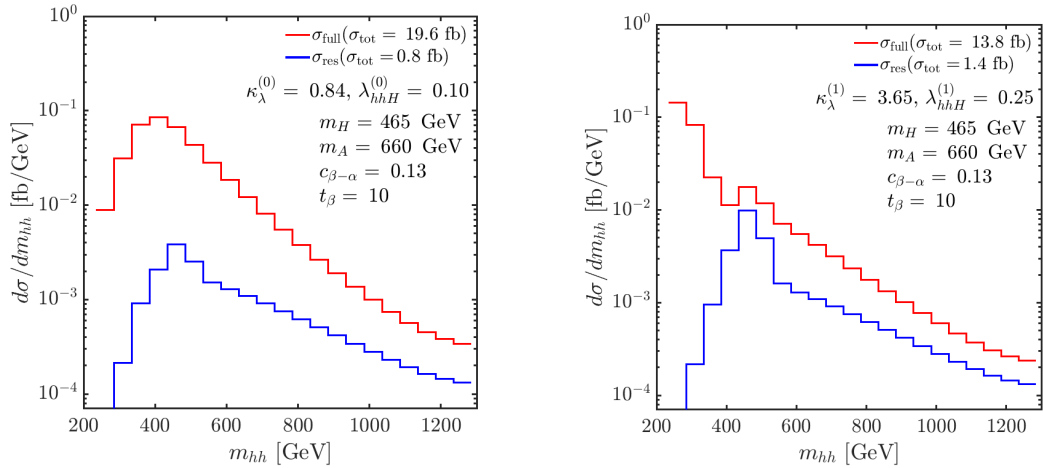
Figure 3.26

Invariant mass distribution for the 2HDM Type I benchmark point BP1 defined in Tab. 3.4. Left (right) plot: using $\kappa_\lambda^{(0)}$, $\lambda_{hhH}^{(0)}$ ($\kappa_\lambda^{(1)}$, $\lambda_{hhH}^{(1)}$). Red (blue): Complete $\sigma(gg \to hh)$ prediction (resonance contribution only).

As a first step, to demonstrate the various possible interference and higher-order effects, we show in Fig. 3.26 the invariant mass distributions for the benchmark point used on the left plot of Fig. 3.24, which is defined in Tab. 3.4. This benchmark point is allowed by all theoretical and experimental constraints. The blue curves show the pure resonant result, while the red curves correspond to the complete model calculation, including also the non-

resonant diagrams and the interference contributions. The left (right) plot uses the THCs at LO (NLO). Their values and those of the corresponding total cross sections are specified in the plots. Contrary to the plots in the previous subsections, here we apply a smearing of 15% and a binning in m_{hh} of 50 GeV in order to take into account the limited detector resolution in the experimental analyses, see Sec. 3.3 for details.

For the case where the tree-level THCs are used, as shown in the left plot of Fig. 3.26, one can observe that the peak in the m_{hh} distribution given by the pure resonant distribution is broadened substantially over several m_{hh} bins as a consequence of the inclusion of the non-resonant contributions. The effect of the resonance itself is very small, since its contribution to the full result is only about 4%. Furthermore, the "resonance-like" structure of the full result is caused dominantly by the contribution of the continuum diagrams, which peaks slightly above the di-top production threshold ($\sim$ 400 GeV), while the resonant contribution (at $\sim$ 465 GeV) in this case is minor and does not appear as a clear resonant structure above the continuum distribution. As can be inferred from the right plot, the inclusion of the NLO contributions to the THCs enhances the pure resonant distribution in this example due to the increased absolute size of $\lambda_{hhH}^{(1)}$ in comparison with $\lambda_{hhH}^{(0)}$, which is also reflected in the result for the total cross section. As indicated by the red curve in the right plot, the combined effect of taking into account non-resonant contributions, interference effects and the NLO corrections to the THCs has a drastic effect on the predicted m_{hh} distribution. Instead of a pronounced peak as it would be expected from the pure resonant contribution, the full result incorporating all relevant contributions gives rise to an m_{hh} distribution that is overall smoothly falling with just a small modulation near $m_{hh} \approx m_H$. Resolving this structure experimentally will clearly be much more challenging than it would be the case if the distribution had the form obtained from restricting to the pure resonant contribution. A striking feature that can be inferred from the plot is the large effect of the non-resonant contributions on the m_{hh} distribution just above the threshold at $m_{hh} \sim$ 250 GeV. In this region the differential cross section for the full result differs by several orders of magnitude from the one for the pure resonant contribution. The shape of the differential cross section in this region is also very significantly modified in comparison to the prediction using the THCs at lowest order (red curve in the left plot). As discussed above, the latter large enhancement happens as a result of a the change in κ_λ which affects the cancellation between the triangle and box form factors of the continuum diagrams that is present at the m_{hh} threshold at leading order. For $\kappa_\lambda \neq 1$ this cancellation does not take place, giving rise to a large enhancement just above the threshold.

While the benchmark point that we have discussed in Fig. 3.26 is unexcluded by the non-resonant and resonant searches, we now turn to two benchmark points that are claimed to be excluded by the existing resonant searches. In Fig. 3.27 we show the results for the two benchmark points in the 2HDM Type I whose input parameters and couplings are given in Tab. 3.5. For each case we compare the m_{hh} distributions based purely on the resonant diagram, shown in blue, with the one based on the full calculation, shown in red. In the displayed results the NLO results for the THCs have been used (with the values given in the respective plots). Like in the previous plots, all results are shown at LO in QCD. By comparing the predicted distributions based on the full result with the ones based on only the pure resonant contribution we will investigate to what extent the assumption of taking into account only the pure resonant contributions is justified.

	t_β	$c_{\beta-\alpha}$	m_H	m_A	m_{12}^2	$\kappa_\lambda^{(1)}$	$\lambda_{hhH}^{(1)}$
BP3	4.0	0.05	450	800	$m_H^2 c_\alpha^2/t_\beta$	5.01	0.23
BP4	2.2	0.04	450	800	$m_H^2 c_\alpha^2/t_\beta$	0.86	0.24

	$\kappa_\lambda^{(0)}$	$\lambda_{hhH}^{(0)}$	$\lambda_{hHH}^{(0)}$	$\lambda_{HHH}^{(0)}$	$\lambda_{hAA}^{(0)}$	$\lambda_{HAA}^{(0)}$
BP3	0.94	0.21	0.37	-0.06	7.56	0.3
BP4	0.96	0.20	0.15	-0.05	0.12	-0.05

Table 3.5: Benchmark points for the analysis of the applicability of resonant limits. Masses are given in GeV. For both points $s_{\beta-\alpha} > 0$ and $m_{H^\pm} = m_A$, which in particular means $\lambda_{hAA}^{(0)} = \lambda_{hH^\pm H^\pm}^{(0)}$ and $\lambda_{HAA}^{(0)} = \lambda_{HH^\pm H^\pm}^{(0)}$.

We also give the total cross section values calculated with `HPAIR` for the two benchmark points in Tab. 3.6. In column 2 and 3 we show the results of the full calculation at LO and NLO QCD in the HTL, respectively (confirming the factor of about 2 between them, as mentioned above). In column 4 and 5 we give the corresponding results taking into account only the resonant diagram. The cross section values at LO QCD quoted in the legends of the figures correspond to the integrated curves of Fig. 3.27. Column 6 shows the "obs. ratio", calculated with `HiggsTools` [187–191, 195–197, 257]. The obs. ratio in this case defined (see Eq. (2.105)) as

$$\text{obs. ratio} \equiv \frac{\sigma^{\text{model}}(ggH) \times \text{BR}^{\text{model}}(H \to hh)}{\sigma^{\text{obs}}(ggH) \times \text{BR}^{\text{obs}}(H \to hh)} \ , \tag{3.23}$$

where the superscript "obs." refers to the observed experimental limit and "model" refers to the 2HDM. Here, the model cross sections have been calculated at NLO QCD in the Born improved heavy-top limit, using `HPAIR`. The model branching ratios have been obtained with `HDECAY` [199, 200], which we modified to include the effective NLO coupling $\lambda_{hhH}^{(1)}$ in the decay width of the heavy Higgs boson into the SM-like Higgs boson pair. These calculated 2HDM cross section and branching ratio values are then provided as inputs for `HiggsTools`. The definition Eq. (3.23) implies that the points with an observed ratio larger than 1 are excluded by experimental searches. In view of the assumptions made in the experimental analyses we apply this limit only to the resonant contribution σ^{res}. The benchmark points BP3 and BP4 (left and right plots of Fig. 3.27) are both excluded by the resonant search $pp \to hh \to b\bar{b}\tau^+\tau^-$ [258].[12]

	σ (LO QCD)	σ (NLO QCD)	σ^{res} (LO QCD)	σ^{res} (NLO QCD)	obs. ratio
BP3	82.53	165.89	45.06	89.23	1.8
BP4	85.95	169.03	71.51	140.77	2.9

Table 3.6: Higgs pair production cross sections $\sigma(gg \to hh)$ [fb] and the resonant contribution only (σ^{res}), computed with `HPAIR` at LO and NLO QCD in the Born improved heavy-top limit for the total cross section, respectively; "obs. ratio" obtained with `HiggsTools` (see text).

---

[12]This search is included in `HiggsTools` dataset since version `v1.6`.

The left plot of Fig. 3.27 shows the result for the benchmark point BP3, which is claimed to be excluded by resonant di-Higgs searches, but not by non-resonant searches. This point is characterised by significant corrections to κ_λ, corresponding to a parameter region where the one-loop effective coupling approximation is well justified, the explicit values are given in Tab. 3.5.
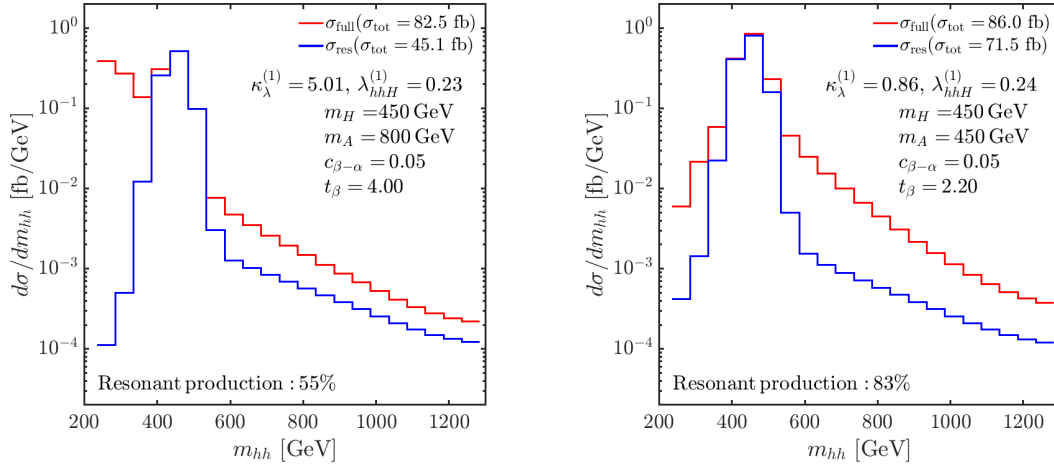
Figure 3.27

Invariant mass distribution versus the invariant mass for the full result (red) and the result based on the pure resonant contribution (blue). Both BP3 (left) and BP4 (right) are examples of scenarios allowed by non-resonant searches but excluded by resonant searches.

The results for the total cross sections indicate that the pure resonant contribution amounts to about half of the full result (both at LO and NLO QCD), this is indicated with the percentage of the resonant production contribution in the full process, displayed in the bottom of the plots in Fig. 3.27. Concerning the m_{hh} distributions, one can see that the qualitative features are similar to the right plot of Fig. 3.26. While the pure resonant contribution shows a pronounced peak, this peak-like structure appears only as a rather small modulation of a smoothly falling distribution in the full result. As in Fig. 3.26 the cross section just above the hh threshold is enhanced by several orders of magnitude compared to the expectation based on the pure resonant contribution. The peak-like structure in the full result will clearly be much more difficult to resolve experimentally than it would seem to be the case based on the pure resonant contribution. We therefore conclude that the exclusion limits obtained for the resonant di-Higgs searches by ATLAS and CMS may be too optimistic in view of the modifications that occur in the invariant m_{hh} mass distribution upon the inclusion of the SM-like non-resonant contributions that are present in all realistic scenarios and of the relevant interference contributions.

Our second example, BP4, is shown on the right plot of Fig. 3.27, and defined by the input values in the second row of Tab. 3.5. As BP3, it is claimed to be excluded by resonant di-Higgs searches, but not by the non-resonant ones. Contrary to BP3, the higher-order corrections to the THCs are substantially smaller, as shown in Tab. 3.5. For this parameter

point the m_{hh} distribution based on the pure resonant contribution and on the full result are more similar than in the previous example, and the pure resonant contribution amounts to about 83% of the full cross section. However, still a substantial broadening of the peak by the inclusion of the non-resonant diagrams can be observed. Similarly to BP1, we therefore conclude that the exclusion limits obtained for the resonant di-Higgs searches by ATLAS and CMS are possibly too optimistic in view of the m_{hh} modifications due to the inclusion of all the relevant contributions in a realistic scenario.

Our discussion shows that the sensitivity of the resonant di-Higgs searches by ATLAS and CMS has already reached a level of sensitivity that strongly motivates to go beyond the assumption of restricting to the pure resonant contribution in deriving the experimental limits. A dedicated joint effort of experiment and theory would be desirable to define an appropriate framework in which the experimental limits should be presented in the future. In particular, the non-resonant contributions should be included in the signal model, and the possibility of interference effects between the resonant and non-resonant contributions should be incorporated. This will require an extension of the analysis setup involving additional parameters.

3.6 Generalisation to any model: `anyH3` and `anyHH`

The introduction of this chapter provided a general overview of the leading order effects in the Higgs pair production. We then explored these effects in depth within the framework of the 2HDM, highlighting their implications for collider phenomenology and ongoing experimental searches. In addition, we incorporated the dominant source of electroweak corrections arising from mass-splitting effects through an effective trilinear coupling, which captures the one-loop contributions of the Coleman-Weinberg potential.

In this section, we compare the 2HDM results with those obtained using a diagrammatic approach to loop-corrected trilinear couplings. We complete the picture by extending our analysis to arbitrary renormalisable models with extended scalar sectors. This generalisation led to the development of an automated tool, `anyHH`, yet to be published.

The first public version of the tool, coined `anyH3` [131], was limited to the SM-like trilinear coupling λ_{hhh}. As part of this thesis, we contributed to extending the capabilities of `anyH3` to the calculation of generic trilinear coupling $\lambda_{h_i h_j h_k}$ in arbitrary renormalisable scalar sectors at one-loop order. Such corrections can be included in the LO QCD Higgs pair production cross section predictions within the `anyHH` framework. This approach enables the inclusion of the dominant corrections to hh while maintaining full control over both the corrections to the effective couplings and their momentum dependence.

3.6.1 One-loop corrections to λ_{ijk}

We begin by implementing a full OS scheme for the calculation of the trilinear scalar couplings λ_{ijk}. The generic one-loop coupling is given in Eq. (2.63). Here we provide the explicit form of the counterterm contribution which was not described in Sec. 2.6.2 and can be expressed as

$$\delta_{\mathrm{CT}}^{(1)}\lambda_{ijk} = \frac{\partial \lambda_{ijk}^{(0)}}{\partial v} \cdot \delta_{\mathrm{CT}}^{(1)}v + \sum_i \frac{\partial \lambda_{ijk}^{(0)}}{\partial t_i} \cdot \delta_{\mathrm{CT}}^{(1)}t_i + \sum_i \frac{\partial \lambda_{ijk}^{(0)}}{\partial m_i^2} \cdot \delta_{\mathrm{CT}}^{(1)}m_i^2 + \sum_{\alpha_i} \frac{\partial \lambda_{ijk}^{(0)}}{\partial \alpha_i} \cdot \delta_{\mathrm{CT}}^{(1)}\alpha_i, \quad (3.24)$$

in terms of the counterterms of the **vev**, $\delta_{\mathrm{CT}}^{(1)}v$, the **tadpoles** and **mass parameters** present in $\lambda_{ijk}^{(0)}$, $\delta_{\mathrm{CT}}^{(1)}t_i$ and $\delta_{\mathrm{CT}}^{(1)}m_i^2$ respectively (the index i runs over the different scalar states), and of the different **BSM-specific parameters** $\delta_{\mathrm{CT}}^{(1)}\alpha_i$, such as mixing angles, independent couplings or others. The coefficients in front of these counterterms are the partial derivatives of the corresponding parameters in the tree-level expressions of the trilinear coupling (including the tadpole contribution).

To guide the discussion of the necessary counterterms, let us start by defining the scalar self energy[13] as the 1-particle irreducible diagrams (1PI) two-point correlation function of a scalar [14]

$$i\Sigma_\phi(p^2) \equiv \text{-----}\left(\!\text{1PI}\!\right)\text{------} \quad (3.25)$$

The full propagator to all perturbative orders in the coupling can then be expressed as the tree-level contribution defined in Eq. (3.1.1) plus a series sum of 1PI diagrams

$$\Delta_\phi(p^2) = \text{-------------} + \text{------}\left(\!\text{1PI}\!\right)\text{------} + \text{---}\left(\!\text{1PI}\!\right)\text{---}\left(\!\text{1PI}\!\right)\text{---} + \dots$$

$$= \frac{i}{p^2 - m_\phi^2} + \frac{i}{p^2 - m_\phi^2} i\Sigma_\phi(p^2) \frac{i}{p^2 - m_\phi^2} + \frac{i}{p^2 - m_\phi^2}\left(i\Sigma_\phi(p^2)\frac{i}{p^2 - m_\phi^2}\right)^2 + \dots$$

$$= \frac{i}{p^2 - m_\phi^2}\left[1 + \frac{-\Sigma_\phi(p^2)}{p^2 - m_\phi^2} + \left(\frac{-\Sigma_\phi(p^2)}{p^2 - m_\phi^2}\right)^2 + \dots\right] = \frac{i}{p^2 - m_\phi^2 + \Sigma_\phi(p^2)},$$
$$(3.26)$$

where in the last step we used the geometric series resummation. This shows that the leading order mass parameter m_ϕ is *dressed* with the self energy contribution containing virtual particles. Applying the renormalisation conditions in Eq. (2.27) to the mass and to the scalar field we obtain the renormalised propagator

---

[13]This discussion is based on my personal notes from the course Renormalisation of spontaneously broken gauge theories and related phenomenological aspects by Prof. Dr. Georg Weiglein

[14]This means that the diagrams cannot be split into two distinct diagrams by cutting one internal line that carries a non vanishing momentum.

$$\hat{\Delta}_\phi(p^2) = \frac{i}{\sqrt{Z_\phi}^*\left(p^2 - m_\phi^2 + \Sigma_\phi(p^2) - \delta m_\phi^2\right)\sqrt{Z_\phi}} \simeq \frac{i}{p^2 - m_\phi^2 + \hat{\Sigma}_\phi(p^2)}, \quad (3.27)$$

where the hat indicates that the corresponding function is renormalised. In the last step we did not use a strict equality because approximate the renormalised self energy at one-loop as in Eq. (2.27). Correspondingly, the definition of the renormalised self energy is given by

$$\hat{\Sigma}_\phi(p^2) = \Sigma_\phi(p^2) - \delta m_\phi^2 + \frac{\delta Z_\phi^*}{2}(p^2 - m_\phi^2) + (p^2 - m_\phi^2)\frac{\delta Z_\phi}{2}, \quad (3.28)$$

which consists of the unrenormalised self energy plus the one-loop counterterm contributions. If we were to go beyond one-loop order in the perturbative expansion, we would need to include the second term in the square root of Z_ϕ expansion from Eq. (3.27) and the expression for the renormalised self energy would become more involved (involving also a subloop renormalisation). We see that the pole of the propagator occurs at m_P, which in general is a complex quantity,

$$m_P^2 - m_\phi^2 + \hat{\Sigma}_\phi(m_P^2) = 0. \quad (3.29)$$

In particular, $m_P^2 = m_\phi^2 - im_p\Gamma$, where m_p is the physical mass of the particle and Γ is its total width. If $\hat{\Sigma}(m_P^2) \neq 0$ it means that the pole is shifted by the higher order contributions. The Goldstone theorem ensures that this term is zero for the massless gauge bosons that arise from a SSB ($\hat{\Sigma}_\gamma(0) = 0$) for the photon, as it is protected by the $U(1)_{\text{EM}}$ symmetry.

In an **on-shell scheme** the counterterms are fixed in a way such that the loop-corrected quantities correspond to the physically measured quantities. This means in particular that the physical mass of the particle m_p coincides with its tree-level mass m_ϕ (from now on we will use only m_ϕ notation for simplicity, and because we define an OS scheme), and that the renormalised one-loop self energy at the real part of the complex pole vanishes:

$$\text{Re}\hat{\Sigma}_\phi(p^2 = m_\phi^2) \overset{!}{=} 0, \quad (3.30)$$

Additionally, the mixing between the different mass eigenstates also needs to vanish, for two particles i, j with $i \neq j$, the off-diagonal self energies must fulfil

$$\hat{\Sigma}_{ij}(p^2 = m_i^2) \overset{!}{=} 0 \quad \text{and} \quad \hat{\Sigma}_{ij}(p^2 = m_j^2) \overset{!}{=} 0. \quad (3.31)$$

These conditions ensure that the pole of the propagator remains at $p^2 = m_\phi^2$ at higher orders.

We proceed now to apply these conditions to all the parameters involved in the tree-level expressions of the trilinear couplings defined in Eq. (3.24). Starting from the **vev**, we define the OS scheme analogously to the SM definition in Ref. [63]. For this purpose we express the vev in terms of physically measured quantities, namely the masses of the $W^\pm$ and Z bosons, and the electric charge, e [15],

$$v = \frac{2m_W}{e}\sqrt{1 - \frac{m_W^2}{m_Z^2}} \rightarrow \frac{\delta_{\text{CT}}^{\text{OS}} v}{v} = \frac{\delta_{\text{CT}}^{\text{OS}} m_W^2}{2m_W^2} + \frac{c_\theta^2}{2s_\theta^2}\left(\frac{\delta_{\text{CT}}^{\text{OS}} m_Z^2}{m_Z^2} - \frac{\delta_{\text{CT}}^{\text{OS}} m_W^2}{m_W^2}\right) - \frac{\delta^{\text{OS}} e}{e}, \quad (3.32)$$

---

[15]From now we will omit the superindex (1) in all the counterterms for simplicity.

where θ is the weak mixing angle and the counterterms for the physical masses and electric charge are

$$
\begin{aligned}
\delta_{\text{CT}}^{\text{OS}} m_Z^2 &= \Sigma_Z^T\left(m_Z^2\right), \\
\delta_{\text{CT}}^{\text{OS}} m_W^2 &= \Sigma_W^T\left(m_W^2\right), \\
\delta_{\text{CT}}^{\text{OS}} e &= -\frac{1}{2}\delta_{\text{CT}}^{\text{OS}} Z_\gamma - \frac{s_\theta}{c_\theta}\frac{1}{2}\delta_{\text{CT}}^{\text{OS}} Z_{\gamma Z} = \frac{1}{2}\left.\frac{\partial \Sigma_\gamma^T\left(p^2\right)}{\partial p^2}\right|_{p^2=0} - \frac{s_\theta}{c_\theta}\frac{\Sigma_{\gamma Z}^T(0)}{m_Z^2},
\end{aligned}
\tag{3.33}
$$

where the upper index T stands for the transversal component of the corresponding self energy, which can be computed using the projector

$$
\mathcal{P}_T \equiv \frac{-1}{(D-1)}\left(g_{\mu\nu} - \frac{k_\mu k_\nu}{k^2}\right),
\tag{3.34}
$$

where D is the dimension (using dimensional regularisation), $g_{\mu\nu}$ is the metric tensor and k is the momentum. With this projector we compute the transversal part of a general vector boson self energy defined as

$$
\Sigma_{ab}^{\mu\nu}(k) = \quad \overset{a,\mu}{\underset{k}{\wavy}}\bigcirc\overset{b,\nu}{\underset{k}{\wavy}},
\tag{3.35}
$$

simply by applying the projector to the full result

$$
\Sigma_{ab}^{T\,\mu\nu}(k^2) = \mathcal{P}_T \Sigma_{ab}^{\mu\nu}(k).
\tag{3.36}
$$

The on-shell **tadpole counterterms** are defined to cancel exactly the tadpole diagrams

$$
\delta t_i^{\text{OS}} = -T_i, \quad \text{where} \quad T_i = \overset{\bigcirc}{\underset{h_i}{\vdots}},
\tag{3.37}
$$

note that there will be as many tadpole renormalisation conditions as vevs.

The conditions for the on-shell scalar **mass counterterms** arise from imposing the condition in Eq. (3.30) in the definition of the renormalised self energy in Eq. (3.28), which for the diagonal case reads

$$
\hat{\Sigma}_i(p^2) = \Sigma_i(p^2) - \delta m_i^2 + (p^2 - m_i^2)\delta Z_i,
\tag{3.38}
$$

and the unrenormalised scalar self energy is defined as

$$
\Sigma_i(p) = \quad \overset{h_i}{\underset{p}{\text{-----}}}\bigcirc\overset{h_i}{\underset{p}{\text{-----}}}.
\tag{3.39}
$$

Thus applying the condition in Eq. (3.30) leads to

$$
\delta m_i^{\text{OS}} = \text{Re}\Sigma_i(m_i^2).
\tag{3.40}
$$

From Eq. (3.38) an additional on-shell condition can be derived for the δZ counterterms that governs the **WFR corrections** that enter in Eq. (2.64). This condition is the vanishing of the derivative of the renormalised diagonal self energy w.r.t the momentum squared evaluated on shell

$$\left.\frac{\partial \Sigma_i(p^2)}{\partial p^2}\right|_{p^2=m_i^2} \overset{!}{=} 0. \tag{3.41}$$

Applying this condition leads to the following diagonal WFR conterterm definition

$$\delta Z_i^{\text{OS}} = \left.\frac{-\partial \Sigma_i(p^2)}{\partial p^2}\right|_{p^2=m_i^2}. \tag{3.42}$$

On the other hand the off-diagonal renormalised self energy can be written as

$$\hat{\Sigma}_{ij}(p^2) = \Sigma_{ij}(p^2) + (p^2 - m_i^2)\frac{\delta Z_{ij}}{2} + (p^2 - m_j^2)\frac{\delta Z{ji}}{2}, \tag{3.43}$$

where $i \neq j$ and the unrenormalised self energy diagramatically is

$$\Sigma_{ij}(p) = \quad \overset{h_i}{\underset{p}{\text{-----}}} \bigcirc \overset{h_j}{\underset{p}{\text{-----}}} . \tag{3.44}$$

The OS renormalisation conditions are imposed to cancel out the contributions of the renormalised self energies at the two on-shell momenta, $p^2 = m_i^2$ and $p^2 = m_j^2$. This will introduce equations for the counterterms that depend on the mixing parameters of the theory, such as for instance the **mixing angles** in the 2HDM. We will focus on this specific model from now on for concreteness, bu the above discussion remains general. For convenience, we can define the off diagonal Z-factors as

$$\frac{\delta Z_{Hh}}{2} := \delta C_h + \delta\alpha, \quad \frac{\delta Z_{hH}}{2} := \delta C_h - \delta\alpha. \tag{3.45}$$

And applying the renormalisation conditions

$$\hat{\Sigma}_{hH}(p^2 = m_h^2) \overset{!}{=} 0 \quad \text{and} \quad \hat{\Sigma}_{hH}(p^2 = m_H^2) \overset{!}{=} 0, \tag{3.46}$$

we get the counterterms for the mixing angle and the off-diagonal WFR that is included in the WFR contribution to λ_{ijk} defined in Eq. (2.64). Their explicit forms are

$$\begin{aligned}
\delta\alpha &= \frac{\Sigma_{Hh}(m_h^2) + \Sigma_{Hh}(m_H^2)}{2(m_h^2 - m_H^2)}, \\
\delta Z_{Hh} &= \frac{\Sigma_{Hh}(m_h^2)}{(m_h^2 - m_H^2)}, \\
\delta Z_{hH} &= \frac{\Sigma_{hH}(m_H^2)}{(m_H^2 - m_h^2)}.
\end{aligned} \tag{3.47}$$

Analogously for the CP-odd mixing angle we get

$$\delta\beta = \frac{\Sigma_{G^\pm H^\pm}(m_W^2) + \Sigma_{G^\pm H^\pm}(m_{H^\pm}^2)}{2(m_W^2 - m_{H^\pm}^2)}. \tag{3.48}$$

For our purposes, i.e. the trilinear couplings entering Higgs pair production, we do not need the WFR constants for the CP-odd fields. Note that there is an equivalence between calculating the β-counterterm with the charged $G^\pm H^\pm$ self energy and the neutral ZA self energy.

With this we have exploited all possible OS conditions. However, one counterterm remains to be fixed, the conterterm for the **BSM mass parameter** M:

$$M_0 \rightarrow M_R + \delta M.$$

We chose to define the counterterm of δM such that it cancels all the remaining UV divergence in λ_{hhh}. To also make it renormalisation scale independent, the counterterm δM was derived by integrating the one-loop RGE of M, fixing all the other parameters OS, i.e. not running. We define the input parameter $M^{\overline{\text{MS}}}$ at a reference scale $\mu_{\text{inp}} = M^{\overline{\text{MS}}}$, while the scale used in the calculation is renormalisation scale μ_{ren}. The resulting expression for δM thus effectively converts $M^{\overline{\text{MS}}}(\mu = M^{\overline{\text{MS}}})$ to $M^{\overline{\text{MS}}}(\mu = \mu_{\text{ren}})$, truncating at the one-loop order and retaining only the logarithmic dependence. The counterterm reads

$$\begin{aligned}
\delta M = \frac{M}{32\pi^2 v^2} &\left\{ -3\left(2m_W^2 + m_Z^2\right) + 6\left[\frac{m_u^2 + m_c^2 + m_t^2}{t_\beta^2} + \left(m_d^2 + m_s^2 + m_b^2\right)t_\beta^2\right] \right. \\
&+ 2t_\beta^2\left(m_e^2 + m_\mu^2 + m_\tau^2\right) + 4M^2 - 2m_{H^\pm}^2 - m_A^2 \\
&\left. - \frac{s_{2\alpha}}{s_{2\beta}}\left(m_h^2 - m_H^2\right)\right\}\frac{1}{\Delta}.
\end{aligned} \tag{3.49}$$

where $\Delta = 1/\epsilon + \ln(\mu^2/M^2)$ This scheme is known in the literature as KOSY scheme [125] (see also [259]). In our results we have explicitly verified that the results for the trilinear scalar couplings in this scheme are renormalisation scale independent and UV-finite. We will use the KOSY scheme to define the effective one-loop-corrected trilinear couplings that will be included in the calculation of the double Higgs production. Therefore we will focus on the two couplings involved in the di-Higgs production, λ_{hhh} and λ_{hhH}. To be more specific and to follow the discussion so far we will maintain the discussion in the 2HDM, even though `anyH3 v.2.` can be used for any trilinear scalar coupling in any renormalisable model with an extended scalar sector.

In Fig. 3.28, we compare the one-loop trilinear Higgs couplings computed with `anyH3` using the OS scheme described above with the results of the public code `BSMPT` [140–142], which uses the Coleman Weinberg one-loop effective potential [137, 138] as discussed in Sec. 2.6.2.[16] As said before, we concentrate on the two couplings involved in hh-production in the 2HDM, i.e. λ_{hhh} (left column) and λ_{hhH} (right column). The different rows show different benchmark scenarios, in particular

row 1: $m_H = m_A = m_H^\pm = 450$ GeV, $t_\beta = 10$ and $m_{12}^2 = m_H^2 c_\alpha^2/t_\beta$,

---

[16]Additionally, the diagrams contributing to the one-loop result of `anyH3` have been tested independently with the `FeynCalc` [260, 261] and `FeynArts` [262] `Mathematica` packages. The loop integrals were evaluated using `LoopTools` [263, 264].
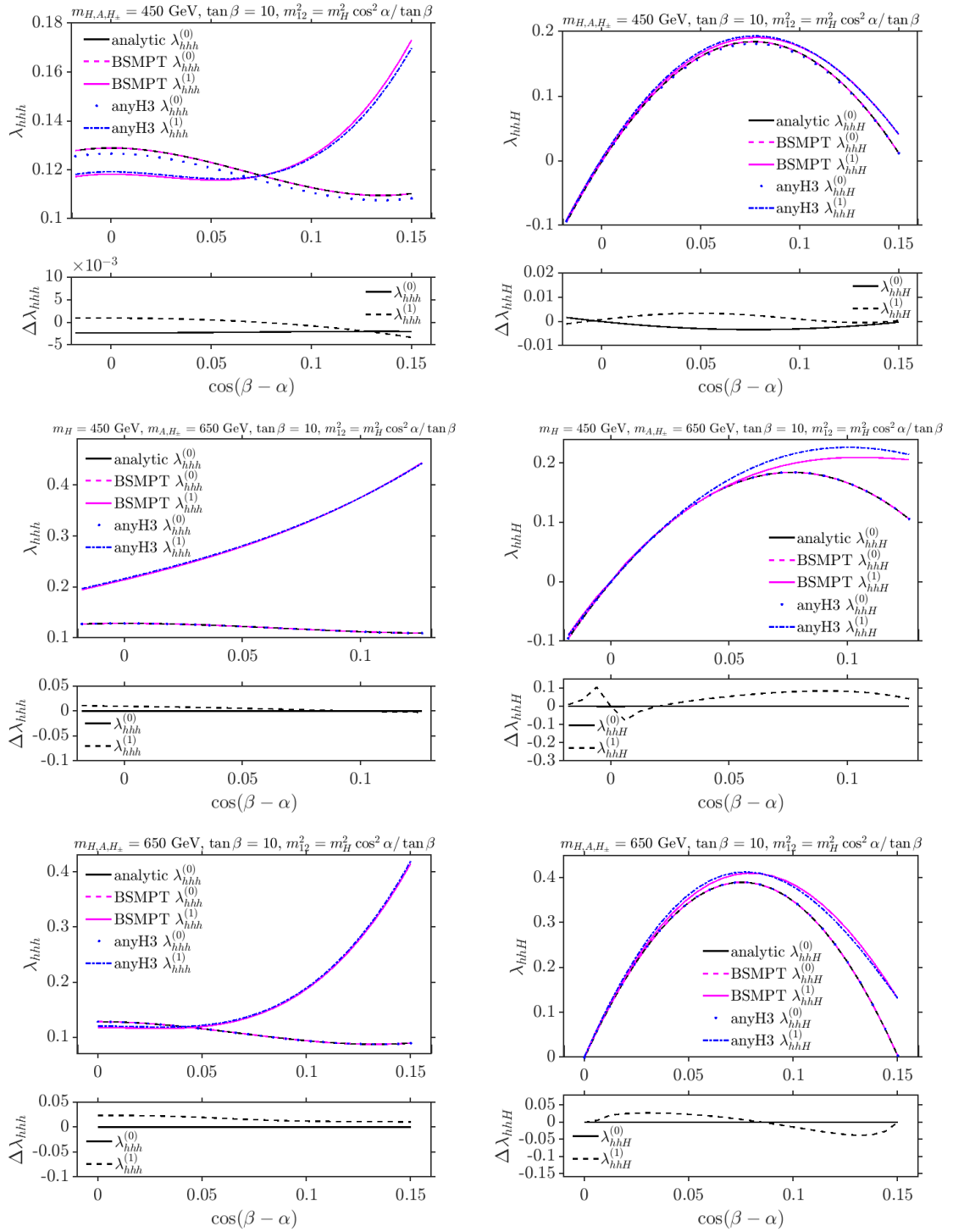
Figure 3.28

Comparison of the tree-level and one-loop trilinear Higgs couplings in the 2HDM Type I computed using the diagrammatic approach implemented in `anyH3` and the effective potential approach implemented in `BSMPT`. The left column shows the λ_{hhh} coupling and the right column shows the λ_{hhH} coupling, both involved in Higgs pair production in the 2HDM. The three rows represent three different benchmark scenarios. The lower panel represents the absolute difference between both approaches $\Delta\lambda_{ijk} := \lambda_{ijk}(\texttt{anyH3}) - \lambda_{ijk}(\texttt{BSMPT})$ for the tree-level (solid) and one-loop (dashed) results.

row 2: $m_H = 450$ GeV, $m_A = m_H^\pm = 650$ GeV, $t_\beta = 10$ and $m_{12}^2 = m_H^2 c_\alpha^2 / t_\beta$,

row 3: $m_H = m_A = m_H^\pm = 650$ GeV, $t_\beta = 10$ and $m_{12}^2 = m_H^2 c_\alpha^2 / t_\beta$.

The results from `anyH3` are shown in blue while the results from `BSMPT` are shown in pink. The tree-level result is a dashed line in the `BSMPT` case and a dotted line in `anyH3`. The difference at tree-level arises from a difference in the vev. On one hand, `BSMPT` uses the v as an input with a default value of $v = 246.2197$ GeV (extracted experimentally from G_F). On the other hand, `anyH3` extracts it from $m_W, \alpha := e^2/(4\pi)$ and m_Z (according to Eq. (3.32)), which leads to a numerical value of $v = 250.6919$ GeV. If we set them to equal values, the two results agree exactly. However, we chose to keep the `anyH3` approach both at tree-level and at one-loop in order to consistently define a renormalisation scheme with a proper treatment of the vev. The solid line shows the analytic result according to Eq. (2.75) with the value of the vev obtained from the value of G_F, therefore it matches the `BSMPT` result.

The one-loop results are depicted with a solid line for `BSMPT` and as a dot-dashed line for `anyH3`. The differences at one-loop order are in all the analysed scenarios below 10% of the one loop correction. For the benchmark scenario in row 1 displayed in Fig. 3.28 it is below 2% (4%) for λ_{hhh} (λ_{hhH}), for the scenario in row 2 it remains below 5% (10%) for λ_{hhh} (λ_{hhH}) and for the scenario in row 3 below 4% (7%) for λ_{hhh} (λ_{hhH}). Since the two results are not in the same renormalisation scheme we do not expect perfect agreement but deviations that are formally of higher order. In total, we find an overall relatively good agreement of both results which reassures the consistency of both approaches.

To conclude, we emphasise that our results show that there is in general a good agreement between the two codes at the zero momentum approximation and that our implementation is robust. It is also interesting to note how large these corrections are in both approaches and to note that their inclusion is always taken into account in the cosmological analysis by means of the CW potential but were up to now not included in collider phenomenology studies. The steps for obtaining these results were described in the previous sections of this chapter. In the following we will only present the capabilities of `anyHH` as a flexible tool for the collider phenomenology side of the loop-corrected trilinear Higgs couplings through Higgs pair production.

3.6.2   Higgs pair production

We have mentioned that `anyHH` is an extremely powerful tool that can perform calculations of the leading order QCD Higgs pair production cross section in arbitrary renormalisable models with extended scalar sectors. We incorporate the loop-corrected couplings in order to account for the leading higher-order electroweak effects, while for the higher-order QCD corrections K-factors ~ 2 are used. For simplicity and coherence, we will stick to the 2HDM in the examples shown here and will refer the interested reader to the forthcoming publication, where also scenarios with more than one heavy resonance (e.g. in models with doublets + singlets) are realised.

First we compare the performance of `anyHH` with the existing tools in the literature such as `HPAIR`. Although the public version of `HPAIR` does not include EW corrections, we use here the privately implemented version that was used in the analysis in Sec. 3.2 which includes the effective one-loop-corrected trilinear scalar couplings. In the THDM Type I, we

perform a comparison between `HPAIR` and `anyBSM` for several benchmark points with $t_\beta = 2$ and $M = 400\,\text{GeV}$, shown in Fig. 3.29. In the left plot we compare four benchmark points with $c_{\beta-\alpha} = 0.04$ and $c_{\beta-\alpha} = -0.04$, and $m_H = m_A = m_{H^\pm} = 500$ and $600\,\text{GeV}$, all of which are allowed by experimental and theoretical constraints (checked with `thdmTools` [2]). For completeness we show in Tab. 3.7 the values of their tree-level and one-loop couplings, where we also define the three benchmark points used in the right plot of Fig. 3.29, all of which are in the alignment limit. We show here the same normalisation as throughout this work, as defined in Eq. (2.57).

	m_H [GeV]	$c_{\beta-\alpha}$ [17]	$\kappa_\lambda^{(0)}$	$\kappa_\lambda^{(1)}$	$\lambda_{hhH}^{(0)}$	$\lambda_{hhH}^{(1)}$
BP1	500	-0.04	0.97	1.03	-0.11	-0.05
BP2	500	0.04	0.97	1.03	0.11	0.22
BP3	600	-0.04	0.97	1.76	-0.08	0.25
BP4	600	0.04	0.97	1.76	0.08	0.5
BP5	500	0	1	1.07	0	0.08
BP6	550	0	1	1.32	0	0.19
BP7	600	0	1	1.79	0	0.38

Table 3.7: Benchmark points chosen for the Higgs pair production comparison between `anyHH` and `HPAIR` with their κ_λ and λ_{hhH} trilinear couplings at tree-level and one-loop (at zero external momenta).

For the points outside the alignment limitshown in the right plot of Fig. 3.29 we implement the tree-level value of the trilinear couplings. The same input parameters were used in both codes, in particular the decay width for the involved scalars was obtained setting the automatic width mode of `anyHH`, which uses the optical theorem, namely $\Gamma_i = -\text{Im}\left(\Sigma_i(p^2 = m_i^2)\right)/m_i$, and implementing the same numerical value in `HPAIR`, where the width is an external parameter. We show the `anyHH` results with dashed lines and the `HPAIR` ones with solid lines, adopting a different colour for each scenario.

It can be seen that the four explored scenarios show very good agreement, the absolute difference between the two codes is very small as shown in the lower panel of Fig. 3.29, where $\Delta = |\partial\sigma_{hh}^{\text{LO}}/\partial m_{hh}(\text{HPAIR}) - \partial\sigma_{hh}^{\text{LO}}/\partial m_{hh}(\text{anyHH})|$. The largest difference arises close to the resonant peak, which has been checked to be an artefact of the numerical integration. Overall the curves of both codes are very similar to the SM curve, shown in black, as their κ_λ value at tree level (the one used for this plot) is very close to 1. Their main difference from the SM curve is the resonance located at the corresponding heavy Higgs mass, the dip-peak and peak-dip structure is determined by the sign of λ_{hhH} which in turn depends on the value of $c_{\beta-\alpha}$ according to the Eq. (2.75).

On the right plot of Fig. 3.29 we show the prediction for the differential hh-production cross section with loop corrections to the trilinear couplings, with solid lines we show the result using `anyHH`, and with dashed lines the results from the modified `HPAIR` code. The agreement between both codes is remarkable, with less than 1% deviations in the total cross section and, as shown in the lower panel, less than 1/1000 deviations in the absolute differential cross sections. Again the largest differences arise at the highest points of the resonant peak, where the numerical integration has the largest impact.

In this scenario we can see additionally that we are in the tree-level alignment limit. Still, the mass splitting between m_H and M induces sizeable loop corrections to the trilinear
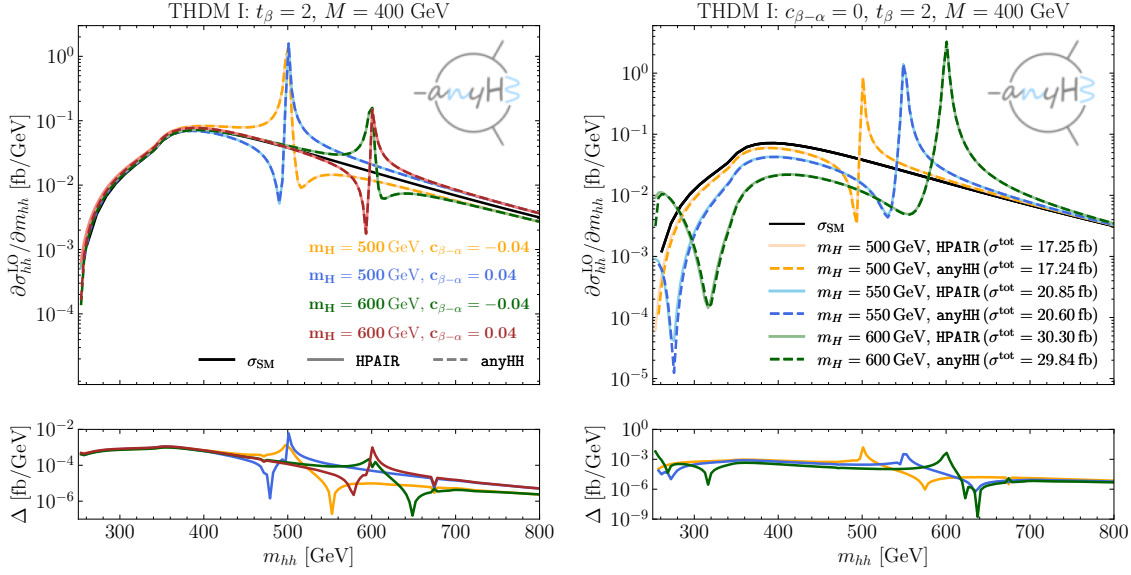
Figure 3.29

Comparison between the Higgs pair production cross section results by `anyHH` and `HPAIR`
in the 2HDM-I. Left: four benchmark scenarios with tree-level trilinear Higgs couplings
away from the alignment limit . Right: three scenarios with loop trilinear Higgs couplings,
all of them in the alignment limit, therefore the prediction with tree-level trilinear Higgs
couplings coincides with the SM prediction depicted by a solid black line.

scalar couplings, which in turn alter dramatically the invariant mass distribution. This can
also be seen in the values of the trilinear couplings provided in Tab. 3.7, were both κ_λ
and λ_{hhH} grow as the splitting between $M = 400$ GeV and the resonant mass rises. As
discussed in the previous section, a dip arises close to the di-top threshold as a consequence of
a deviation of κ_λ from the alignment limit, and, additionally, a resonance peak is developed
due to the loop corrections to λ_{hhH} which is absent at tree-level. Consequently, the results
underline the importance of precision calculations for BSM hh phenomenology.

Finally, we want to briefly study the momentum effects, as those can be included in
the `anyHH` setup. These were initially studied in the λ_{hhh} coupling in Ref. [131]. These
findings suggest that a sizeable momentum dependence is found for larger values of external
momentum, and therefore the impact on the SM-like hh-production is mild, as the cross
section becomes small in the high-momentum region. It was also found that the momentum
effects are relatively smaller than the one-loop corrections to κ_λ.

Here we study these effects for the hh invariant mass distribution. In particular we
include effective couplings of the type $\lambda_{hhh}(m_{hh}^2, m_h^2, m_h^2)$ and $\lambda_{hhH}(m_{hh}^2, m_h^2, m_h^2)$ where
the internal propagator is set to the energy of the invariant mass system in the final state,
i.e. m_{hh}, and the external legs are set to the on shell light Higgs masses m_h. In Fig. 3.30 we
show our results in the same benchmark scenarios as before, i.e. the four points out of the
alignment limit on the left plot and the three points in the alignment limit on the right. The
difference is that now we show the predictions with loop-corrected trilinear Higgs couplings
in both plots. With dashed lines we show the results with the effective couplings at zero

momenta $p^2 = 0$, while solid lines show the result with full momentum dependence in the couplings. Therefore the dashed lines in the right plot are the same results in Fig. 3.29 and Fig. 3.30. Again in the lower panel we show the absolute difference between the solid and dashed curves, which in this case means the difference between the zero-momentum effective couplings and the full momentum dependent ones.
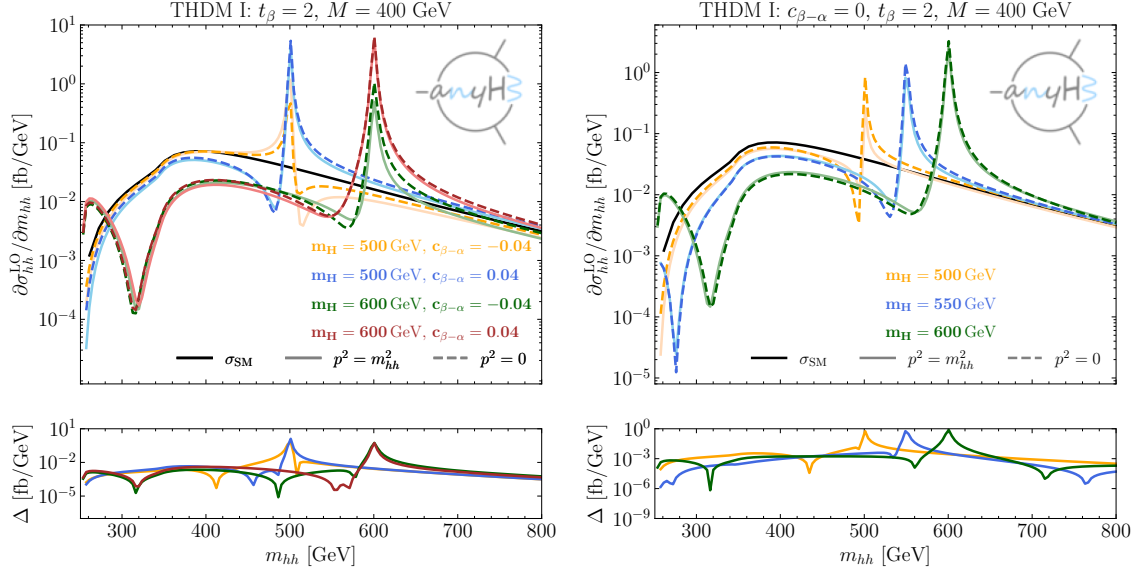

Figure 3.30

Higgs pair production invariant mass distribution for different scenarios in the THDM Type I. Same scenarios as in Fig. 3.30 are used, on the left outside of the alignment limit and on the right in the alignment limit. Solid lines depict the predictions including momentum dependence in the trilinear couplings and dashed lines show the results with the zero momentum approximation for the trilinear Higgs couplings.

We observe that the corrections in general are minor, in particular for the case of higher resonance masses ($m_H = 600$ GeV), ans become slightly more significant for smaller resonant masses ($m_H = 500$ GeV). The momentum dependence in λ_{hhH} is of smaller importance than the corrections to λ_{hhH}, which slightly alter the shape around the resonance, while maintaining the overall structure (peak/dip or dip/peak). In view of these results we conclude that the zero momentum approximation is a reasonable one, especially if the mass splittings become larger and the dominant source of corrections are captured by the large couplings. In that case, which is the scenario of highest interest to us, the momentum dependence is subdominant.

Chapter 4

Bridging the gap between theory and experiment

Contents

In this chapter, we address the challenge of bridging the gap between the theoretical predictions presented in the previous chapter and experimental measurements. To do so, we pursue two complementary approaches. First, we constrain the BSM parameter space of theoretically motivated models using the latest experimental limits, focusing on recent di-Higgs searches. To this end, we extended the capabilities of the public `HiggsTools` package by (*i*) incorporating resonant and non-resonant Higgs pair production cross section predictions into the `HiggsPredictions` module, (*ii*) implementing a coupling-dependent treatment for non-resonant searches that allows κ_λ to be used as an input parameter when testing against experimental constraints, and (*iii*) updating `HiggsBounds` with the most recent resonant ($gg \to H \to hh$) search results. Second, we explore how experimental data can be used to extract model parameters, using the BSM trilinear coupling λ_{hhH} in the 2HDM as a case study. Motivated by the goal of reconstructing the shape of the scalar potential, we analyse the sensitivity to this parameter through the measurable invariant mass distributions of Higgs pair production. We compare the performance of classical statistics and modern machine learning techniques.

4.1 Application of experimental data for testing BSM: HiggsTools

Our objective is to ensure that experimental data can be meaningfully interpreted within the framework of extended scalar sectors. To this end, the most effective approach is to develop an automated software framework that not only integrates the most recent experimental results but also facilitates direct comparisons with theoretical predictions from a broad class of models.

In the context of this thesis, we have extended the capabilities of `HiggsTools` [191] to incorporate recent di-Higgs searches, which are expected to play a central role in the Run 3 and High-Luminosity phases of the LHC programme. In particular, we have implemented predictions for both resonant and non-resonant Higgs-boson pair production cross sections using an effective coupling approach within the `HiggsPredictions` framework. Additionally, we have improved the `HiggsBounds` dataset by enabling the inclusion of coupling-dependent non-resonant searches, which depend on the value of κ_λ, and by integrating the latest experimental limits from resonant di-Higgs searches.

4.1.1 HiggsPredictions

The `HiggsPredictions` package serves to provide the necessary theoretical input to the other components of `HiggsTools`, `HiggsBounds` and `HiggsSignals`, in the form of production and decay rates for all relevant particle processes. As part of this thesis, the package was extended to include predictions for resonant, non-resonant, and combined resonant/non-resonant Higgs-boson pair production. The current implementation supports scenarios involving a single BSM resonance decaying into a Higgs-boson pair.

The LHCHWG [229, 234, 265, 266] provides a recommended parametrisation of the non-resonant Higgs pair production cross section as a function of κ_λ, effectively specifying the coefficients $\mathcal{A}_{1,2,3}$ in Eq. (3.7). For a c.m. energy of $\sqrt{s} = 13$ TeV, the cross section is given by:

$$\sigma_{\text{no res}}^{13\text{TeV}}(\kappa_\lambda)/\text{fb} = 68.5624 - 48.3673\,\kappa_\lambda + 10.5635\,\kappa_\lambda^2\,, \tag{4.1}$$

and for $\sqrt{s} = 13.6$ TeV:

$$\sigma_{\text{no res}}^{13.6\text{TeV}}(\kappa_\lambda)/\text{fb} = 75.7617 - 53.2855\,\kappa_\lambda + 11.6126\,\kappa_\lambda^2\,. \tag{4.2}$$

We have implemented both functions, as well as the prediction for 14 TeV c.m. energy, which is not explicitly provided but can be extracted by applying K-factors to the LO-prediction from `anyHH`. These K-factors were determined by comparing the LO predictions from `anyHH` to the LHCHWG recommendations, yielding agreement at the percent level for both 13 TeV and 13.6 TeV. The resulting non-resonant predictions for all three energies are now part of the `HiggsPredictions` output. These cross sections, plotted as a function of κ_λ, are shown in the left plot of Fig. 4.1, where the LHCHWG expressions are overlaid as dashed lines for comparison.

In order to capture additional BSM effects, we generalise the above κ_λ-dependent equations to also account for modifications to the top Yukawa coupling via the parameter ξ_h^t, in accordance to the more general equation Eq. (3.7). For 13 TeV, we implement:

$$\sigma_{\text{no res}}^{13\text{TeV}}(\xi_h^t \kappa_\lambda)/\text{fb} = 68.5624\,(\xi_h^t)^4 - 48.3673\,(\xi_h^t)^3\,\kappa_\lambda + 10.5635\,(\xi_h^t)^2\,\kappa_\lambda^2\,, \tag{4.3}$$

and analogously for the higher c.m. energies with the appropriate coefficients. The powers of ξ_h^t reflect the number of $ht\bar{t}$-vertices in the diagrams contributing to the cross section at leading order. As discussed in Sec. 3.1, the first term corresponds to the box diagram, which does not involve the trilinear Higgs coupling. The third term arises from the triangle diagram with an internal h propagator, and the second (negative) term reflects the destructive interference between the two.

The functional dependence of $\sigma_{\mathrm{no\,res}}$ on ξ_h^t has also been investigated in an (H)EFT approach in Ref. [267], where the dependence on further effective couplings in addition beyond ξ_h^t and κ_λ are considered. A fit formula for the cross section in terms of the Wilson coefficients in the HEFT is provided (see Eq. (4.1) in Ref. [267]), which can be mapped onto LHCHWG expression in Eq. (4.1).

However, the coefficients in Ref. [267] differ from the LHCHWG recommendations, as the former includes only NLO QCD corrections, whereas the latter is rescaled using the $\mathrm{FT}_{\mathrm{approx}}$ (see Sec. 3 for details) approximation for $\kappa_\lambda = 1$. Consequently, we adopt the LHCHWG parameterisation and extend it to include ξ_h^t dependence, as given by Eq. (4.3).
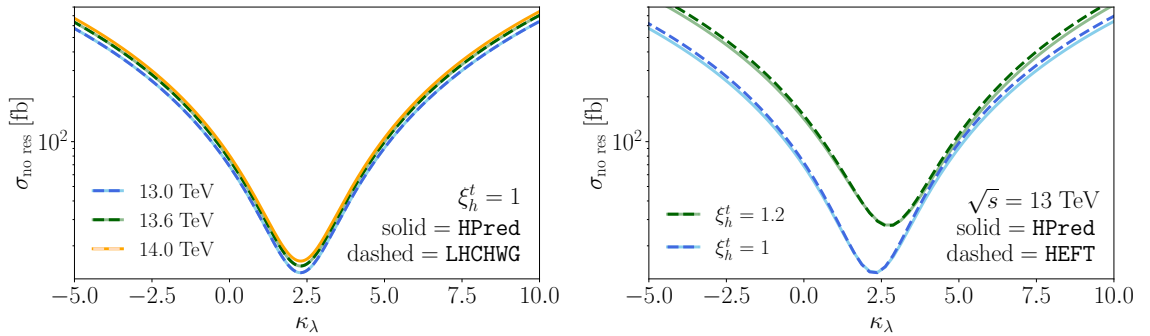

Figure 4.1

Prediction of the non-resonant Higgs pair production cross section as a function of κ_λ implemented in `HiggsPredictions`. Left: Comparison with the LHCHWG recommendations for different c.m. energies and $\xi_h^t = 1$. Right: Comparison with the NLO HEFT fit formula in Ref. [267] for different values of the light Higgs top Yukawa coupling modifier $\xi_h^t = 1$ and $\xi_h^t = 1.2$ and $\sqrt{s} = 13$ TeV.

In the right plot of Fig. 4.1, we show the difference between the two approaches at 13 TeV c.m. energy. The LHCHWG recommendation, valid only for $\xi_h^t = 1$, aligns with the implementation in `HiggsTools`, which is shown as a solid blue line in both plots in Fig. 4.1. The prediction from Ref. [267] for $\xi_h^t = 1$ appears as a dashed light blue curve and lies slightly above our implementation. For $\xi_h^t = 1.2$, the `HiggsTools` implementation (solid light green curve) shows reasonable agreement but remains slightly below the result of Ref. [267], as expected due to the difference in the coefficients. The expression from Ref. [267] is also implemented in `HiggsPredictions` and may be used if preferred, although we recommend to use the modified LHCHWG formula as the default.

The function for the non-resonant hh production cross section can be called in `python` simply by typing

```
import Higgs.predictions as HP

pred = HP.Predictions() # create the model predictions object

ggHH_XS_nores = HP.EffectiveCouplingCxns.ggHHnores(
    'LHC13',
    lam = 1,
    tt = 1)
```

which yields a result of the non-resonant di-Higgs production cross section in femtobarns, in this case $\sigma_{\text{no res}}^{13\text{TeV}}(1,1) = 30.76$ fb. The HEFT formula can be called with

```
ggHH_XS_nores = HP.EffectiveCouplingCxns.hhggh(
    'LHC13',
    mH = 125,
    lam = 1,
    tt = 1,
    bb = 1)
```

where additionally the mass of the SM-like Higgs and the bottom Yukawa coupling modifier, `bb`, need to be provided. This yields a cross section of $\sigma_{\text{HEFT}}^{13\text{TeV}} = 31.66$ fb.

We also provide a prediction for the resonant Higgs pair gluon fusion production cross section. In order to get the highest level of precision in the resonant production we apply the narrow width approximation (NWA), i.e. we split the full process into the gluon fusion production of a heavy resonance and subsequent decay into a $h-$pair

$$\sigma(gg \to H \to hh) \sim \sigma(gg \to H) \times \text{BR}(H \to hh). \tag{4.4}$$

The $\sigma(gg \to H)$ is obtained from the already existing `HiggsPredictions` implementation of single Higgs production, which in turn uses tabulated results from `SusHi 1.7.0` [268, 269] rescaled to the LHCHWG recommendations, which capture the N³LO corrections to the process. The branching ratio is computed as

$$\text{BR}(H \to hh) = \frac{\lambda_{hhH}^2}{32\pi m_H}\sqrt{1 - \frac{4m_h^2}{m_H^2}}\frac{1}{\Gamma_H}. \tag{4.5}$$

Our implementation assumes that the BSM resonance H is dominantly produced via gluon fusion production and that only the contribution from the top-quark loop is relevant. In particular, we do not include the effects of the bottom loop, which contribute at the per-cent-level [226]. Thus we effectively implement Eq. (3.10) from Sec. 3.1, where the coefficient $\mathcal{A}_4$ present in that equation has been computed as a function of m_H and Γ_H in a two dimensional grid and stored in the form of data tables in `HiggsPredictions` to speed up the calculation. An internal interpolation is performed to predict the result at arbitrary values of m_H and Γ_H. The validation plot of the implemented resonant hh production for different c.m. energies is shown in Fig. 4.2. With dashed lines we show the result using the NWA, since both agree we conclude that our interpolation function is robust. The resonant Higgs pair production cross section for an example resonant particle with a 400 GeV mass and 4 GeV width can be called in python by typing
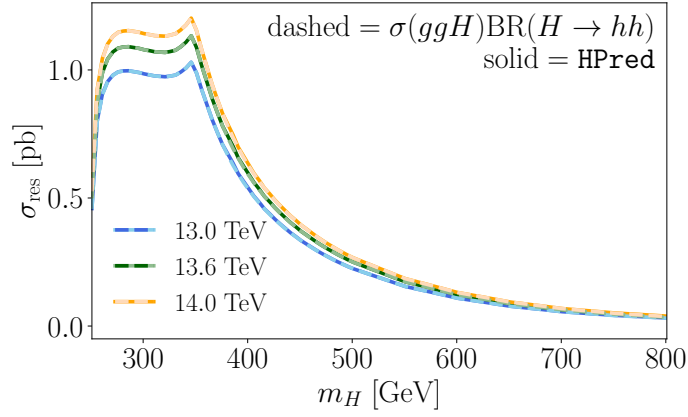
Figure 4.2

Prediction of the resonant Higgs pair production cross section as a function of m_H for different c.m. energies.

```
# set mass and width of the resonant particle
mH = 400
widthH = 4


# add the resonant particle with the above properties
H = pred.addParticle(HP.BsmParticle("H", "neutral", "even"))
H.setMass(mH)
H.setTotalWidth(widthH)


# compute only the resonant contribution
ggHH_XS_res = HP.EffectiveCouplingCxns.ggHHres(
    'LHC13',
    mH = mH,
    totalWidth = widthH,
    la112 = -0.1)
```

where the symbol `la112` refers to $\xi_H^t \times \lambda_{hhH}$.

Our prediction for the total di-Higgs cross section is defined as in Eq. (3.13). We have already described the $|\mathcal{M}_{\text{no res}}|^2$ and the $|\mathcal{M}_{\text{res}}|^2$ contributions entering in this equation. Now we concentrate on the interference terms proportional to the coefficients $\mathcal{A}_5$ and $\mathcal{A}_6$. To compute them we have used the framework of `anyHH`, which provides the LO gluon fusion Higgs pair production cross section $\sigma(gg \to hh)$ based on a user-defined `UFO` model file. We have implemented a toy model that contains an additional resonant scalar that is produced via gluon fusion. The additional terms in the SM Lagrangian that will generate such a resonant contribution are the ones that contain ttH and hhH interactions:

$$\mathcal{L}_H = \frac{1}{2}\partial_\mu H \partial^\mu H - \frac{1}{2}M_H^2 H^2 - \lambda_{hhH} v hhH - \xi_H^t \frac{m_t}{v}\bar{t}tH, \tag{4.6}$$

where λ_{hhH} and ξ_H^t are the aforementioned dimensionless parameters. We note that for the Feynman rules of the trilinear BSM coupling defined in such a way, a symmetry factor of 2 would appear, which needs to be taken into account to map the couplings to a particular model.

Since `anyHH` can only compute a LO QCD prediction, we defined K-factors to account for the NLO contributions in the interference terms that are already included in the resonant and non-resonant pieces as described above. These K-factors are multiplicative and depend on the value of m_H. The interference between the box and the triangle diagrams, $\Box - h$, is already captured by the negative coefficient of Eq. (4.3). For the interference between the triangle and the resonant diagram, $h - H$, and between the box and the resonant diagram, $\Box - H$, we approximate the K-factors of the interference terms as

$$K_{\mathrm{no\,res}-H} = \sqrt{K_{\mathrm{no\,res}}K_H}, \tag{4.7}$$

where $K_{\mathrm{no\,res}}$ is the K-factor accounting for the contributions of either the box $\Box$ or the h triangle diagram and K_H is the K-factor of the resonant contribution. The total cross section then becomes,

$$\sigma_{\mathrm{tot}}(\xi_h^t, \kappa_\lambda, \xi_H^t \times \lambda_{hhH}, m_H, \Gamma_H) = \sigma_{\mathrm{no\,res}} + \sigma_{\mathrm{res}} +$$
$$(\xi_h^t)^2(\xi_H^t \times \lambda_{hhH})\,K_{\Box-H}(m_H)\mathcal{A}_5(m_H, \Gamma_H) + \tag{4.8}$$
$$\xi_h^t \kappa_\lambda(\xi_H^t \times \lambda_{hhH})\,K_{h-H}(m_H)\mathcal{A}_6(m_H, \Gamma_H).$$

In practice, we compute the K-factor for interference between the resonant and non-resonant contributions using Eq. (4.7) as

$$K_{\mathrm{interf}} = \sqrt{K_{\mathrm{res}}\,K_{\mathrm{no\,res}}} =$$
$$= \left(\frac{[\sigma(ggH)\,\mathrm{BR}(H \to hh)]_{\texttt{HiggsPredictions}}}{[\sigma_{\mathrm{res}}(gg \to hh)]_{\texttt{anyBSM}}} \cdot \frac{[\sigma_{\mathrm{no\,res}}(gg \to hh)]_{\mathrm{LHCHWG}}}{[\sigma_{\mathrm{no\,res}}(gg \to hh)]_{\texttt{anyBSM}}}\right)^{1/2}. \tag{4.9}$$

In this way, we obtain all the terms in Eq. (4.8) and save them in the form of grids in `HiggsPredictions`. Analogously to the resonant cross section, this data is linearly interpolated to obtain values at non-grid points.

An example usage of the described full di-Higgs production cross section, after loading the `HiggsPredictions` package is shown below:

```
ggHH_XS = HP.EffectiveCouplingCxns.ggHH(
    'LHC13',
    mH = 400,
    totalWidth = 4,
    lam = 0.8,
    la112 = -0.1,
    tt = 1
)

# set the internal 'pair' cross section to apply experimental bounds
H.setCxn('LHC13', 'pair', ggHH_XS)
```

Where we set the collider to `LHC13`, refering to the 13 TeV c.m. energy, the resonant mass to 400 GeV, the total width of the resonance to 4 GeV, $\kappa_\lambda = 0.8$, $\xi_H^t \times \lambda_{hhH} = -0.1$ and $\xi_h^t = 1$. In the final command, the Higgs pair production cross section is set to the value calculated above for later application of the limits from experimental searches. Prior to the implementation of di-Higgs production predictions developed in this work, this value had to be supplied manually by the user based on an independent cross section calculation.

In Fig. 4.3 we show an example application of the implemented function to predict the Higgs pair production cross section in the 2HDM Type II. We set $t_\beta = 2$, $c_{\beta-\alpha} = 0.1$, $m_H = m_A = m_{H^\pm} = M$ and plot the prediction of `HiggsPredictions` for a variable resonant mass m_H. We use `thdmTools` [2] to compute the total decay width of the resonant Higgs, Γ_H. We use the tree level formulas for the Yukawa coupling modifiers of h and H in Eq. (2.72) and we use the tree level trilinear λ_{hhh} and λ_{hhH} as in Eq. (2.75).
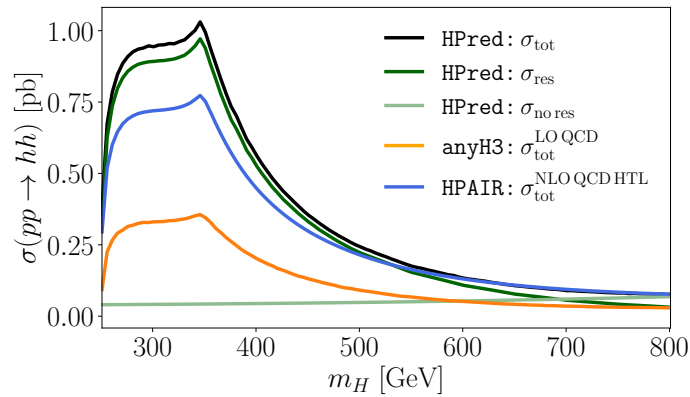

Figure 4.3

Contributions to the Higgs pair production cross section in the 2HDM Type II ($t_\beta = 2$, $c_{\beta-\alpha} = 0.1$, $m_H = m_A = m_{H^\pm} = M$) done with `HiggsPredictions`: full cross section (black), resonant only contribution (dark green) and non-resonant contribution (light green). The LO result in `anyHH` is shown in orange and the NLO QCD in the heavy top limit result of `HPAIR` in blue. No constraints applied.

The full Higgs pair production cross section prediction is shown as a solid black line in Fig. 4.3. [1] The non-resonant contribution is indicated in light green, while the resonant only contribution is shown in dark green. A significant enhancement of the cross section is observed for values of the heavy scalar mass m_H near the di-top mass threshold, where the resonant contribution overwhelmingly dominates the total production cross section. For BSM masses above approximately 700 GeV, the non-resonant contribution becomes the dominant, causing the total cross section to plateau.

We also display the LO prediction from `anyHH` in orange, alongside the NLO prediction from `HPAIR` in the heavy top limit. A discrepancy of roughly a factor of two is observed between these two predictions, due to the well known $K \sim 2$ factor for NLO contributions. The inclusion of the N^{3}LO corrections in the resonant single Higgs gluon fusion production,

---

[1]No experimental constraints are applied in this plot.

as detailed above, further raises the K-factor of the LO prediction to approximately a factor of 3.

4.1.2 `HiggsBounds`

In this section, we describe how experimental constraints from non-resonant and resonant di-Higgs searches were incorporated into `HiggsBounds`, enabling their application to BSM models once the corresponding cross section predictions have been provided.

4.1.2.1 Non-resonant searches

The new version of `HiggsBounds` supports the implementation of coupling-dependent exclusion limits. This feature is particularly important for Higgs pair production, where the experimental bounds depend the value of the trilinear Higgs coupling κ_λ, as shown in Fig. 2.5. The implementation is based on an additional acceptance factor that captures this dependence of the cross section when defining the exclusion limit. To determine the acceptance factor, we approximate the observed exclusion limit (solid black line in Fig. 2.5) as a function of κ_λ using the rational expression:

$$\sigma_{\text{obs}} = \frac{A\kappa_\lambda^2 + B\kappa_\lambda + C}{D\kappa_\lambda^2 + E\kappa_\lambda + F}\sigma_{\text{SM}}. \tag{4.10}$$

The coefficients A, B, C, D, E, and F are obtained via a fit to the observed experimental exclusion limit using FindFit in `Mathematica`. These coefficients along with the value of the limit at $\sigma_{\text{obs}}(\kappa_\lambda = 1)$, are implemented in the limit definition files for each non-resonant search. Because combinations of multiple decay channels yield significantly stronger constraints than individual channels (represented as coloured lines in Fig. 2.5), we only include the two non-resonant combinations from ATLAS [121] and CMS [193] in the current implementation.
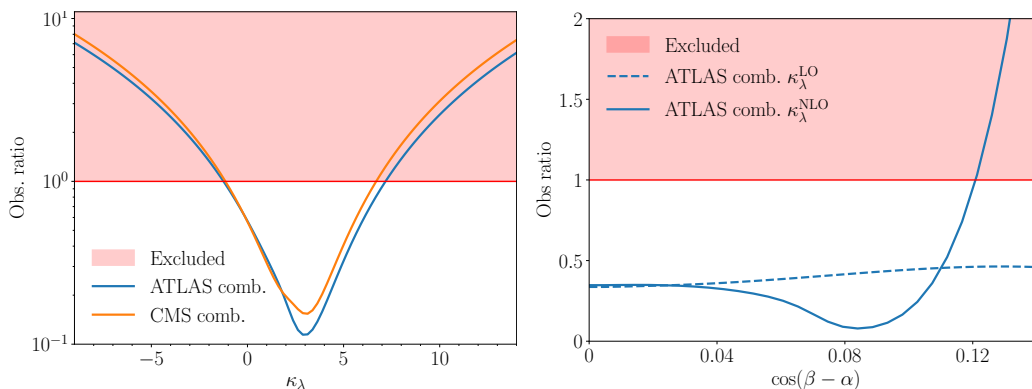

Figure 4.4

Coupling-dependent non-resonant di-Higgs limits. Left: observed ratio for an effective value of κ_λ. Right: observed ratio for different values of $c_{\beta-\alpha}$ for the benchmark plane defined in Eq. (3.22) for the Type I 2HDM depending on the value of κ_λ, taken at tree-level (dashed) or one-loop (solid).

In practice, this feature enables the automated application of exclusion limits to BSM parameter space, as demonstrated in Fig. 4.4. The left plot shows the observed exclusion ratio for different values of κ_λ based on the ATLAS and CMS combinations. The red shaded region denotes the excluded parameter space where the predicted cross section exceeds the experimental limit, i.e. the observed ratio defined in Eq. (2.105) is larger than one. The allowed range for κ_λ corresponds to the values at which the exclusion lines enter this region, with a slight difference from the experimental values due to the different contributions to the result.

The right plot illustrates the application of the coupling dependent limits in a concrete BSM scenario, for convenience we chose the 2HDM Type I, though this procedure is general and can be used for any model that predicts a deviation κ_λ from the SM. For simplicity, we use as an example the same scenario as in Fig. 3.25, defined in Eq. (3.22) as: $t_\beta = 10$, $m_H = m_A = m_{H^\pm} = 1000$ GeV and $m_{12}^2 = m_H^2 c_\alpha/t_\beta$. In this case the limits are automatically applied by adding κ_λ to the `effectiveCouplingInput` feature of `HiggsPredictions`, either at tree-level (dashed line) or including full one-loop corrections (solid line), the latter computed using `anyH3` [131]. The applied limit corresponds to the most sensitive channel, i.e. the one that maximises the ratio between the model prediction and the expected 95% C.L. exclusion bound on the cross section. In this case, that channel is the ATLAS combination.

Since κ_λ is now part of the effective coupling input, `HiggsTools` can automatically evaluate whether a given parameter point is excluded by the implemented limits. In this example, including loop-level corrections to κ_λ leads to exclusion for $c_{\beta-\alpha} \gtrsim 0.12$ from the ATLAS combination (we do not show the limits from the CMS combination as they are weaker).

This implementation benefits from the flexibility of the `HiggsTools` framework: once the effective couplings of a BSM point are specified, all relevant limits are automatically applied. As a result, non-resonant di-Higgs searches are now integrated into global analyses of BSM scenarios.

4.1.2.2   Resonant searches

A number of resonant di-Higgs searches have been incorporated into the `HiggsBounds` dataset. In keeping with the philosophy of `HiggsBounds`, we did not differentiate between the experimental searches. In particular, we chose not to exclude the most sensitive di-Higgs searches discussed in Sec. 3.5.2, despite concerns about their potentially optimistic applicability. Thus although they are applied by default, the user must be cautious in the regions where large trilinear couplings or interference effects are realised. The complete list of newly added searches is as follows:

- $pp \to hh \to b\bar{b}\gamma\gamma$ at 13 TeV including 35.9 fb^{-1} [1806.00408] [270]

- $pp \to hh \to b\bar{b}\gamma\gamma$ at 13 TeV including 139 fb^{-1} [2112.11876] [271]

- $pp \to hh \to b\bar{b}b\bar{b}$ at 13 TeV including $126 - 139$ fb^{-1} [2202.07288] [272]

- $pp \to hh \to b\bar{b}\tau^+\tau^-$ at 13 TeV including 139 fb^{-1} [2209.10910] [258]

- $pp \to H \to hh$ ATLAS combination at 13 TeV including up to 139 fb^{-1} [2311.15956] [273]

- $pp \to H \to hh$ CMS combination at 13 TeV including up to 138 fb^{-1} [2403.16926] [274]

- $pp \to hh \to b\bar{b}b\bar{b}$ at 13 TeV including 138 fb^{-1} [2407.13872] [275]

In Fig. 4.5, we present a comprehensive overview of all the currently implemented limits on the resonant Higgs pair production cross section, $\sigma_{\text{res}}(pp \to H \to hh)$, as a function of the resonant scalar mass m_H. This includes both the newly incorporated searches discussed above and those implemented in previous releases of `HiggsTools`. For the purpose of this plot, we assume a gluon fusion production cross section of 1 pb and a that H only decays into hh, i.e. a branching ratio of 1.

The searches implemented as part of this thesis currently impose the most stringent constraints on the resonant cross section. In particular, the combined analyses by ATLAS and CMS across different h-pair decay channels, depicted as solid pink and green lines, respectively, set the strongest bounds. Notably, the search in the $b\bar{b}\tau^+\tau^-$ final state, shown as a solid dark orange line, is also highly competitive and provides a dominant contribution to the combined limit, as discussed in Sec. 3.5.2.
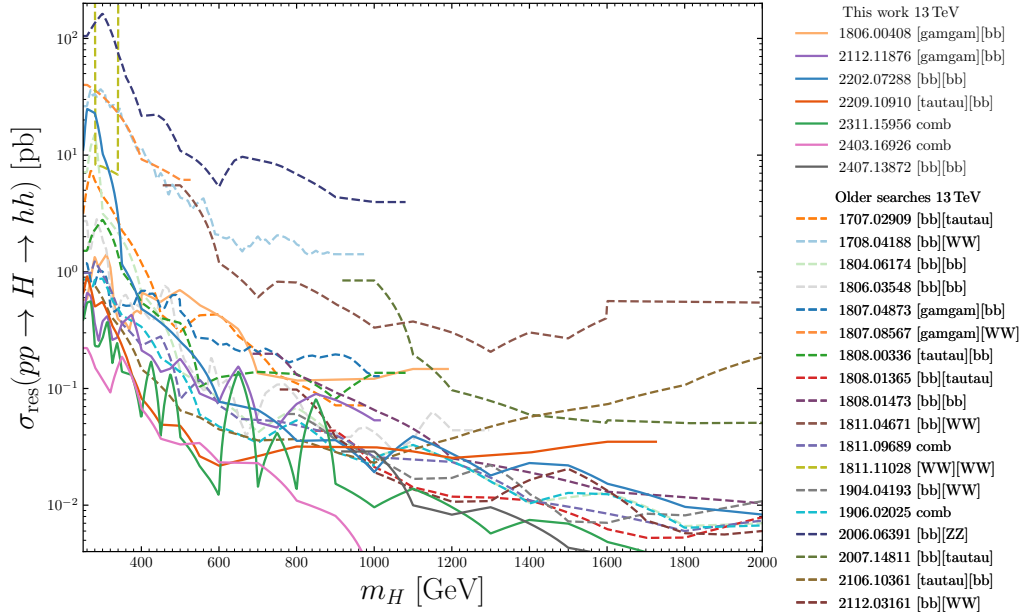
Figure 4.5
Included resonant di-Higgs searches in `HiggsBounds`. 95% confidence-level cross section limits on the process $pp \to H \to hh$ from the experimental searches in various final states. Solid lines show the searches implemented in the context of this thesis and dashed lines represent previously implemented searches.

We proceed now to illustrate some applications in the context of BSM scenarios of these newly implemented searches and their impact in the allowed regions. In Fig. 4.6 we present four benchmark scenarios in the 2HDM, these scenarios are defined by the parameters:

upper left: Type I, $c_{\beta-\alpha} = 0.1$, $m_H = m_A = m_{H^\pm}$ and $m_{12}^2 = m_H^2 c_\beta s_\beta$,

upper right: Type II, $c_{\beta-\alpha} = 0.03$, $m_H = m_A = m_{H^\pm}$ and $m_{12}^2 = m_H^2 c_\beta s_\beta$,

lower left: Type I, $m_H = 450$ GeV, $m_A = m_{H^\pm} = 650$ GeV and $m_{12}^2 = m_H^2 c_\beta s_\beta$,

lower right: Type II, $m_H = 450$ GeV, $m_A = m_{H^\pm} = 650$ GeV and $m_{12}^2 = m_H^2 c_\beta s_\beta$.
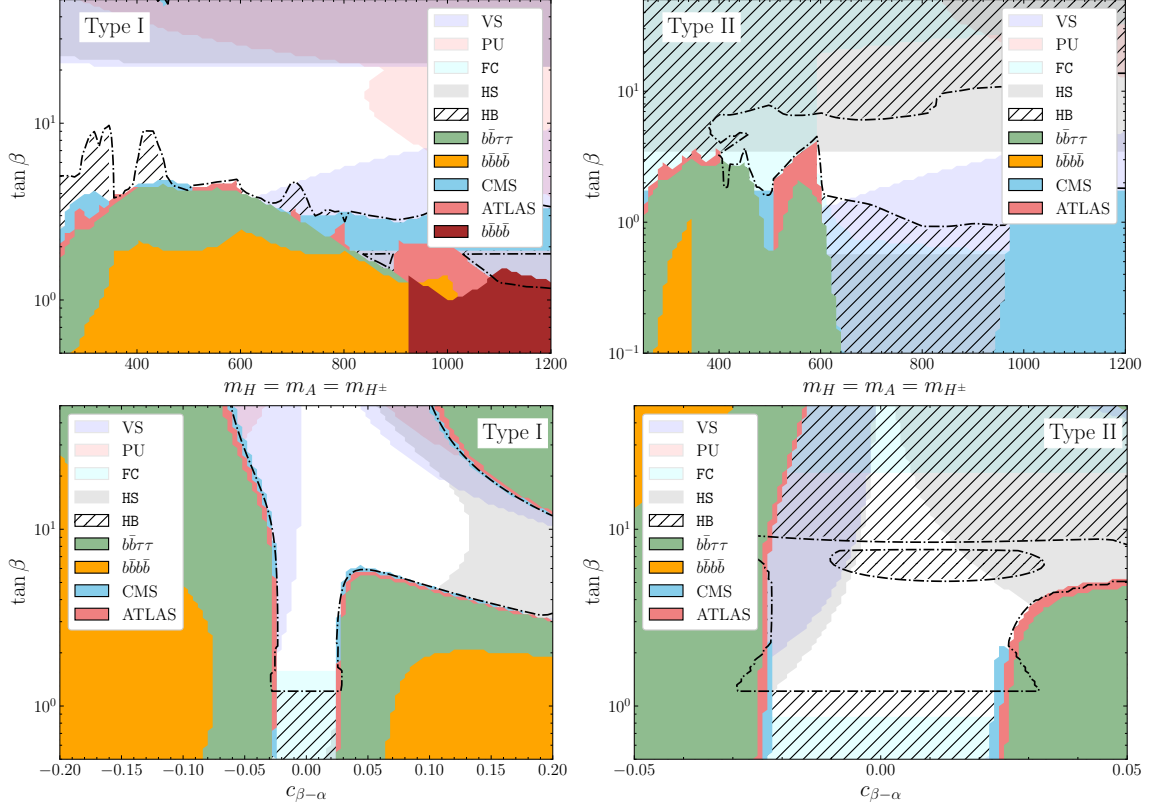
Figure 4.6

Impact of resonant di-Higgs searches in selected 2HDM benchmark planes. Colored regions show exclusion bounds, while white regions are allowed (see text for details).

In all plots, coloured and hatched regions are excluded by theoretical or experimental constraints, verified using `thdmTools`, while white regions are allowed. The region excluded by vacuum stability (VS in the legend) constraints at tree level appears in light purple. The perturbative unitarity (PU) exclusion at leading order—based on the bound $|a_0| \leq 1$ for $2 \to 2$ partial wave amplitudes—is shown in shaded pink. The region disfavoured by flavour constraints (FC) is depicted in light blue and is mostly relevant for low t_β and charged Higgs masses below 600 GeV in Type II. The region disfavoured by `HiggsSignals` (HS) is shown in grey, using the definition from Sec. 2.7.2, where points with a χ^2 value within 2σ, corresponding to $\Delta\chi^2 \leq 6.18$, of the SM best fit (assuming a Gaussian distribution) are considered allowed.

To determine exclusions at 95% C.L. in the 2HDM scenarios considered, we use `Higgs Bounds` (HB), which applies only the observed limit with the highest expected sensitivity per parameter point, ensuring a statistically consistent interpretation. Requiring all individual 95% C.L. limits to be satisfied simultaneously would lead to overly conservative exclusions. For comparison, we also show in solid colours the parameter regions that would be excluded if each resonant search were applied individually, highlighting the impact of newly implemented resonant hh-searches across different final states and how they probe previously unconstrained regions. The exclusion from the rest of the searches implemented in `HiggsTools` is marked by a hatched black region, while the overall exclusion is represented by the dot-dashed contours.

Due to statistical fluctuations, this approach can sometimes yield weaker exclusions than those suggested by individual limits. For instance, in the lower right plot, the resonant searches provide stronger bounds than the combined `HiggsTools` result for $t_\beta \sim 1.5$ and $t_\beta \sim 10$. However, their expected sensitivity is lower than that of the $A \to ZH$ channel (see Sec. 5.2 for a detailed discussion of these searches), which has an observed limit ratio below 1 in that region of parameter space, therefore leaving it viable.

Whenever the dot-dashed line coincides with the coloured regions from the different searches, it means the strongest limit is the resonant hh bound. In the upper plot we can see that in both types these searches have the highest sensitivity for $m_H \sim 400$–600 GeV, where the ATLAS and CMS combinations dominate over the individual channels (it is also seen that $b\bar{b}\tau^+\tau^-$ dominates the combination, as discussed in Sec. 3.5.2).

In Type I (upper left), the most sensitive searches besides the hh-resonant ones show up as three hatched peaks for masses $m_H = m_A = m_{H^\pm} \lesssim 300$, around 450 GeV, and 700 GeV. These are all excluded by searches for a pseudoscalar decaying into a SM-like Higgs and a Z boson [276, 277].

In Type II (upper right), the only competing search with the resonant di-Higgs searches is $pp \to tbH^\pm \to tbtb$ [278], which dominates the region of charged Higgs masses between 600–900 GeV. For masses below 400 GeV, the searches into $\tau^+\tau^-$ dominate over the whole range of t_β [279]. They also dominate in the region with large t_β [279, 280]. The searches in the $\tau^+\tau^-$ final state are very relevant in Type II due to the enhancement in the lepton Yukawa coupling modifier with t_β^2 (see Tab. 2.2 and also the discussion in Sec. 5.2). Although the regions covered by these searches are also in tension with other constraints, in particular flavour physics for $m_{H^\pm} \lesssim 400$ GeV and `HiggsSignals` for $t_\beta > 10$.

In the lower left plot in Type I, the resonant hh-searches are more sensitive than the others, except in the alignment limit for $t_\beta \lesssim 1$, which is excluded by $pp \to tbH^\pm \to tbtb$ [278] in this mass range of the charged Higgs boson. This region is also in tension with the bounds from flavour observables precisely because of the charged scalar mass. The large impact on the exclusion region from the resonant di-Higgs searches further emphasises the need to improve the resonant Higgs pair analysis by taking into account the non-resonant contribution and the interference effects, so that they can be interpreted within complete models (see the discussion in Sec. 3.5.2).

The lower left plot is similar to the lower right but in Type II. In this case, `HiggsSignals` and `HiggsBounds` constrain regions with $c_{\beta-\alpha} \gtrsim |0.03|$. The resonant di-Higgs searches are the most restrictive ones for $1 \lesssim t_\beta \lesssim 4$ for positive values of $c_{\beta-\alpha}$ and $1 \lesssim t_\beta \lesssim 6$ for negative values. Around $t_\beta \sim 1$ and $t_\beta \sim 10$, the $A \to ZH$ search becomes the most sensitive one and therefore the allowed region is larger than for individual resonant hh-

searches, as discussed above. This is also the search giving rise to the exclusion "island" at $5 \lesssim t_\beta \lesssim 9$, in the $\ell^+\ell^- b\bar{b}$ and $\ell^+\ell^- W^+W^-$ final states [281]. For values of $t_\beta > 10$, searches for heavy Higgs into τ-pairs [280] become the most sensitive and dominate the region at any value of $c_{\beta-\alpha}$ in the analysed region. The region for $t_\beta < 1$ is in tension with the search $pp \to tbH^\pm \to tbtb$ [278], as in Type I.

While hh-searches provide leading constraints in many parts of the parameter space, they are ineffective in the alignment limit, where the $H \to hh$ decay is zero at tree level.

4.2   Parameter estimation using neural networks

In this section, we describe the second approach for bridging theory and experiment, related to a reliable parameter estimation analysis. An ever-increasing availability of experimental data in particle physics poses a challenge on conventional statistical methods. In response, a broad selection of modern data analysis tools, particularly machine learning (ML) techniques, have been adopted by the high-energy physics community in recent years [282, 283]. In particular, in experimental particle physics, ML techniques have proven to be extremely useful for tasks such as the event selection. More recently, phenomenological studies have begun exploiting the capabilities of neural networks (NN) and related techniques to explore the underlying structure of physical theories (for a brief review see e.g. Ref. [284]).

In this work, we study the possibility of inferring the magnitude of $\xi_H^t \times \lambda_{hhH}$ from the invariant mass distribution of the di-Higgs pair in gluon fusion, m_{hh}, all computed at leading order QCD and with tree level THCs with our version of the code HPAIR, introduced in Chapter 3. To this end, we evaluate the performance of machine learning techniques, specifically, a NN, in determining this coupling from anticipated HL-LHC data of di-Higgs production, as opposed to conventional statistical approaches. To our knowledge, this work constitutes the first analysis of the feasibility of extracting BSM THCs from (HL-)LHC data.

We note that loop corrections to the THC are not included in this analysis, although they can be relevant in di-Higgs production, as discussed in Chapter 3. Our focus lies on the broader question of whether, assuming a theoretical prediction for m_{hh}, the underlying coupling can be inferred. In the hypothetical case of a future detection of a heavy Higgs resonance in the di-Higgs production, the framework we present here should be extended to include higher order corrections in the trilinear couplings, as well as in the QCD part. However, such refinements are not expected to significantly affect the performance of the NN analysis.

Our numerical study is carried out for a specific benchmark scenario within the Type I 2HDM, chosen without loss of generality. The results are identical in all 2HDM Types, where the $\xi_H^t \times \lambda_{hhH}$ couplings are the same, although the possible realisable values of $\xi_H^t \times \lambda_{hhH}$ depend on the experimental constraints that change in the different types. We assume mass degeneracy $m_\phi := m_A = m_H = m_{H^\pm}$ for simplicity and because EWPO favour either $m_{H^\pm} \approx m_H$ or $m_A \approx m_H$. The example is chosen to be representative of a scenario with resonant di-Higgs production: we set $m_\phi = 450$ GeV, assuming this mass to be determined independently through a different, experimentally cleaner process. The mixing angles t_β and $c_{\beta-\alpha}$ are taken as free parameters, under the assumption that their determination in the future will be more complicated. m_{12}^2 is either fixed via Eq. (2.95) or left as a free parameter. The experimental prospects of determining m_{12}^2 at the HL-

LHC are unclear [285], therefore the variation of m_{12}^2 as a third free parameter is the most conservative approach. Additionally, we explore the possibility of the measured m_H value to differ from the one in reality due to limited detector efficiency. In such a scenario we train the net on datasets with a different value of m_H within some uncertainty, in particular $m_H \pm 15$ GeV. In all these cases we will only include parameter points that are in agreement with the constraints after checking with `thdmTools`.

In Fig. 4.7 we show our original benchmark plane for m_{12}^2 fixed according to Eq. (2.95) and $m_H = 450$ GeV. The coloured region is allowed by all the applied constraints (while the white region is excluded by either of them), and the colour coding indicates the product of the couplings $\xi_H^t \times \lambda_{hhH}$ that we aim to extract. The black lines indicate the regions where $\xi_H^t \times \lambda_{hhH} = 0$. It can be observed that $\xi_H^t \times \lambda_{hhH} = 0$ for $c_{\beta-\alpha} = 0$, i.e. the alignment limit, as expected. However, the value of $\xi_H^t \times \lambda_{hhH} = 0$ is also found along a curve for $\lambda_{hhH} = 0$ at $c_{\beta-\alpha} = 0.02 - 0.12$ and $t_\beta = 8 - 50$, as well as for $\xi_H^t = 0$ at $c_{\beta-\alpha} = 0.03 - 0.10$ and $t_\beta = 15 - 50$. The coloured crosses are benchmark points that will be discussed in more detail further on.
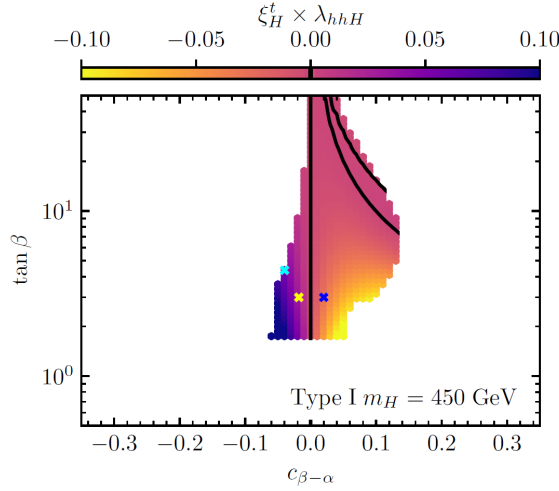
Figure 4.7

$\xi_H^t \times \lambda_{hhH}$ in the example benchmark plane in Type I 2HDM with $m_\phi = 450$ GeV and m_{12}^2 fixed via Eq. (2.95). Black lines located at $\xi_H^t \times \lambda_{hhH} = 0$, either because $\lambda_{hhH} = 0$ (in the alignment limit and the lower curved line on the right upper corner) or $\xi_H^t = 0$ (the upper line on the right corner). The blue cross indicates an example point whose m_{hh} distribution is displayed later in Fig. 4.9. The yellow cross features an example with roughly the opposite sign value of $\xi_H^t \times \lambda_{hhH}$ and its distribution is displayed in Fig. 4.8. The cyan cross is an example point for which different predictions of the NN will be analysed further in Fig. 4.14.

The core of our analysis will be the connection between the value of $\xi_H^t \times \lambda_{hhH}$ and the shape of the corresponding m_{hh} distribution. The shape of the invariant mass distribution of di-Higgs production has been analysed with great detail in the past. In Ref. [252], the possibility of classifying different kinds of distributions with a NN was investigated. The projected shapes were classified in the region of the coupling parameters space in an EFT

approach, allowing for the identification of deviations in the coupling involved in the SM gluon fusion di-Higgs production trough the invariant mass shape analysis. However, since no further BSM state was assumed, there was no investigation of the role of a BSM THC.

In Sec. 3.3 we have shown that di-Higgs invariant mass distributions at the HL-LHC could possibly provide access to the BSM THC λ_{hhH}. In particular, assuming that a resonant scenario is realised, i.e. the contribution of H is sizeable, the sign of the product $\xi_H^t \times \lambda_{hhH}$ would determine the resonant structure at $m_{hh} \approx m_H$. More precisely, the structure would be dip-peak for an overall negative sign and peak-dip for an overall positive sign, assuming no further BSM effects arise from e.g. large loop corrections to the λ_{hhh} trilinear Higgs coupling. However, the structure around the resonant peak is partially washed out by experimental uncertainties, as we have seen in Chapter 3.

After smearing and binning the theoretical prediction for the m_{hh} distributions with different signs of $\xi_H^t \times \lambda_{hhH}$, the peak–dip / dip–peak structure cannot be resolved optically anymore, as a concrete example see Fig. 4.8. These curves represent the smeared and binned prediction of an invariant mass distribution for the points marked with the yellow and blue crosses in Fig. 4.7. The yellow point has $t_\beta = 3$ and $c_{\beta-\alpha} = -0.018$, which yields a value of $\xi_H^t \times \lambda_{hhH} = 0.0304$ and corresponds to the red m_{hh} distribution. It is roughly the same magnitude but opposite sign as the blue point, giving rise to the blue curve. The loss of the clear peak-dip/dip-peack structure poses a challenge on the experimental access to $\xi_H^t \times \lambda_{hhH}$ that we address below.
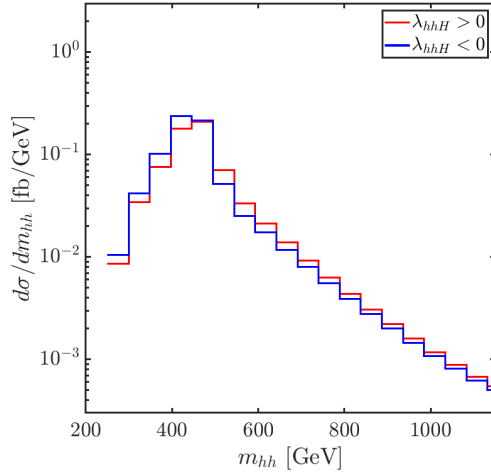
Figure 4.8

Comparison of two benchmark points yielding a positive (blue) and negative (red) value of $\xi_H^t \times \lambda_{hhH}$ with $\xi_H^t \times \lambda_{hhH} \approx \pm 0.03$. The blue (red) curve corresponds to the point marked by a blue (yellow) cross in Fig. 4.7.

The location of data points in an experimental distribution is inevitably subject to uncertainties. These uncertainties can generally be categorised into three components: statistical, theoretical, and systematic. In this work, we focus exclusively on the statistical component, as the theoretical and systematic uncertainties are more difficult to estimate and, in an optimistic scenario, are expected to be subdominant.

To determine the statistical uncertainty, we compute the expected number of events in each bin of the m_{hh} distribution. However, experimental efficiencies are only available for specific final states that include the decay products of the Higgs-boson pair. A combination of various final states, on the other hand, is an experimental analysis on its own and thus goes far beyond the scope of our NN focused work. We restrict our analysis to a single decay channel, the most promising option (i.e. the one producing the largest number of events taking into account experimental efficiencies) being $gg \to hh \to b\bar{b}\,b\bar{b}$.

We have calculated the expected number of events in this channel in each bin as:

$$N_i \;=\; \sigma_i(gg \to hh) \;\times\; \mathcal{L} \;\times\; \mathrm{BR}^2(h \to b\bar{b}) \;\times\; \epsilon, \tag{4.11}$$

where $\sigma_i(gg \to hh)$ is the differential production cross section in each m_{hh} bin, i, times the size of the bin (in our case 50 GeV), $\mathcal{L} = 3000\,\mathrm{fb}^{-1}$ is the integrated luminosity expected at the end of the HL-LHC, $\mathrm{BR}(h \to b\bar{b}) = 0.5841$ is the branching ratio of the decay of a SM Higgs boson to a pair of bottom quarks. Finally, $\epsilon = \epsilon_{\mathrm{TOT}}\,\epsilon_{\mathrm{SR}}$ is the detector efficiency, ϵ_{TOT} is the preselection efficiency, in this case it is the number of events with ≤ 2 b-tagged jets over the total number of events ($N = \sigma \times \mathrm{BR} \times \mathcal{L}$), and ϵ_{SR} is the efficiency of the signal region, i.e. the number of di-Higgs events out of the preselected events. For the $b\bar{b}\,b\bar{b}$ channel we took the efficiencies from Fig. 3 (right plot for $s = 0$) in Ref. [272] for $m_H = 450$ GeV. They are 17.3% and 1% for the total and the signal region efficiencies, respectively. The statistical uncertainty in bin i is then given by $\sqrt{N_i}$, where N_i is defined in Eq. (4.11).
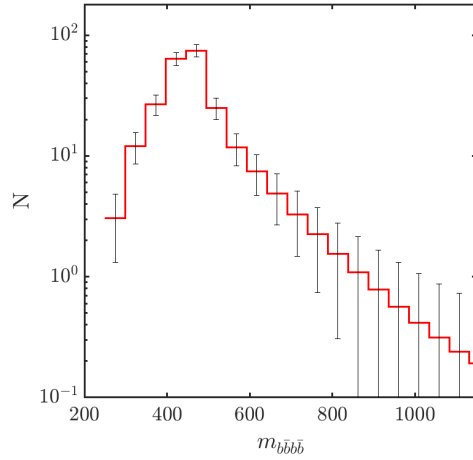
Figure 4.9
Example number of events in the $b\bar{b}\,b\bar{b}$ channel with statistical errorbars (see text) for the point marked by the blue cross in Fig. 4.7.

In Fig. 4.9, we show an example of the expected number of events in the $b\bar{b}\,b\bar{b}$ channel for the parameter point in the benchmark scenario with $m_H = 450$ GeV, indicated by the blue cross in Fig. 4.7. The statistical uncertainties are shown by black error bars in each m_{hh} bin. These uncertainties are interpreted as one standard deviation of a Poisson distribution centered around the theoretical prediction, which serves as the mean of the distribution.

The input data will therefore consist of the event counts in each bin, and the output is the value of $\xi_H^t \times \lambda_{hhH}$ for each distribution.

4.2.1 Classical statistical analysis

Our setup is as follows: we have a predicted mean count of the number of events in each bin from our theory, m_i, and an observed count from experimental data n_i. For hypothesis testing we want to check whether the null hypothesis H_0 can be rejected, H_0: *the observed counts n_i come from Poisson distributions with means m_i*, in our case the null hypothesis is the distribution with $\xi_H^t \times \lambda_{hhH} = 0$. Our alternative hypothesis is the opposite H_1: *The observed counts n_i do not come from Poisson distributions with means m_i*. The Poisson probability mass function (PMF) provides the probability of observing exactly n_i events in bin i, if the true mean number of events is m_i

$$P(n_i|m_i) = \frac{m_i^{n_i} e^{-m_i}}{n_i!}. \tag{4.12}$$

When the PMF is viewed as a likelihood function, we treat m_i as a variable and evaluate how well different values of m_i explain the observed data n_i. In the first case we can compute the likelihood under the null hypothesis as:

$$L(H_0) = \prod_{i=0}^{N_i} \frac{m_i^{n_i} e^{-m_i}}{n_i!}, \tag{4.13}$$

where we have multiplied the likelihoods in each of the N_i bin because they are independent. In the second case we compute the likelihood under the alternative hypothesis H_1 as

$$L(H_1) = \prod_{i=0}^{N_i} \frac{n_i^{n_i} e^{-n_i}}{n_i!}, \tag{4.14}$$

where we do not assume a specific mean value m_i but we allow each bin to have its own most likely mean. For a Poisson distribution, the maximum likelihood estimate (MLE) of the mean is simply equal to the observed count, n_i.

With this we can compute the standard likelihood ratio test statistic, λ_{LR}, which is defined as:

$$\lambda_{\mathrm{LR}} = -2\ln\left(\frac{L(H_0)}{L(H_1)}\right) = 2\sum_{i=0}^{N_{\mathrm{bins}}} \left(n_i \ln\frac{n_i}{m_i} + m_i - n_i\right), \tag{4.15}$$

whose interpretation is: for small λ_{LR} the observed data is consistent with the model mean m_i, so H_0 cannot be rejected. Alternatively, if λ_{LR} is large then the data is inconsistent with the model predicted mean m_i, so we reject H_0 in favour of H_1.

λ_{LR} is by itself hard to interpret, but it is useful because it can be asymptotically[2] approximated by a χ-squared distribution under the null hypothesis. This result is known as Wilks' theorem, and it allows to directly compute a p-value as

---

[2]This means the sample size (each n_i and m_i) must be large enough, as a rule of thumb they should be larger than 5.

$$p = P(\chi^2 > \lambda_{\mathrm{LR}}).$$ (4.16)

The p-value is the probability of obtaining a result at least as extreme as the data, assuming the null hypothesis is true. Typically values of $p < 0.05$ (roughly corresponding to a 95% CL) suggest evidence against the null hypothesis. To summarise, we assumed a certain distribution of data to properly define a p-value, if our number of counts in each bin is large enough, we can make use of Wilks' theorem to assume such distribution to be a χ^2, if we could not use this theorem, we would have to estimate an empirical distribution of the data with e.g. a Montecarlo simulation, in order to statistically define a p-value for each parameter.

In order to correctly apply Wicks' theorem, we need to ensure that the number of events in each bin is "large enough", therefore we aggregate some bins together in order to have better statistics. We show an example of this aggregation in Fig. 4.10, where two sample distributions from Fig. 4.7 are shown, one with a small $\xi_H^t \times \lambda_{hhH}$ (orange) and one with a large $\xi_H^t \times \lambda_{hhH}$ (green), and compared to the SM distribution (blue), which is equivalent to a distribution in the alignment limit. On the left we show the distributions with the original 50 GeV binning and on the right the aggregated bins that lead to a particle count of at least 4 events, so that the statistical tests can be performed. In particular, the first and second bins are added up together, and correspond to the first bin on the right. The third, fourth, fifth and sixth bin are unchanged and correspond to the bins 2, 3, 4 and 5 on the right. All the other bins are combined in bin number 6 on the right.
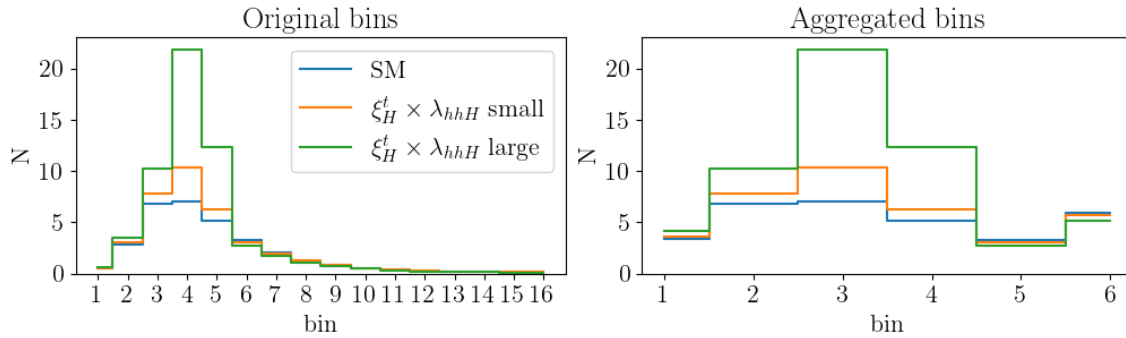
Figure 4.10

Example disributions for the number of events with the original 50 GeV binning (left) and the aggregated bins (right). Shown the distributions for the SM (blue), and two examples with small $\xi_H^t \times \lambda_{hhH}$ (orange) and large $\xi_H^t \times \lambda_{hhH}$ (green).

As a side note, the square root of a χ^2-distributed variable, in our case λ_{LR}, can be interpreted in terms of standard deviations or *sigmas* from the null hypothesis, which is a more common statistical variable in particle physics. In particular if $\sqrt{\lambda_{\mathrm{LR}}} > 1.96$, the conclusion would be the same as if $p < 0.05$, meaning such point is statistically far from the null hypothesis. However, this approach only works exactly for 1 degree of freedom, and gets worse for our case, where we have 6 degrees of freedom (N_{bins} after aggregation). Therefore in Fig. 4.11 we will only show p-values for the benchmark scenario defined in Fig. 4.7, and not the significance, which we however checked that yields a similar result. In Fig. 4.11

we have coloured in red the points in the parameter space with $p > 0.05$, i.e. compatible with the null hypothesis. Outside this region, we plot the values of $\xi_H^t \times \lambda_{hhH}$ that are incompatible with the null hypothesis, however with this approach we do not really have a way of estimating the value of $\xi_H^t \times \lambda_{hhH}$ from the data. For that we need to perform a parameter estimation.
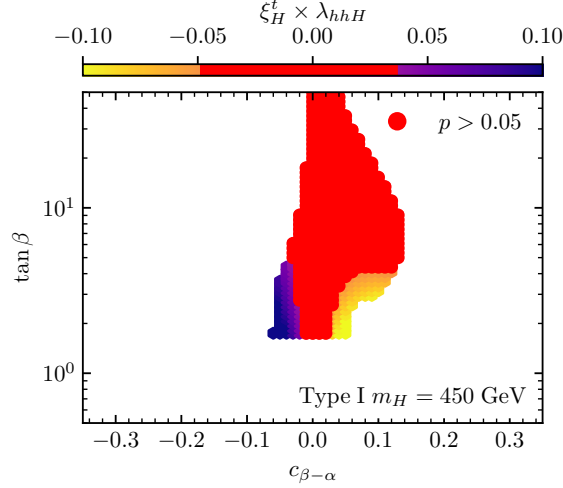
Figure 4.11

p-value in the example benchmark plane. The red region shows the parameters points where the p-value is larger than 0.05, i.e. the null hypothesis cannot be rejected. The colour coding indicates the value of $\xi_H^t \times \lambda_{hhH}$ in the regions where the null hypothesis is unlikely.

Classically, the most precise method for parameter estimation is maximum likelihood estimation (MLE). The likelihood of each BSM scenario is defined as in Eq. (4.13). We calculate L for every set of m_i (all the points in Fig. 4.7) and find the one that maximises L given the experimentally observed count n_i. This would be the most likely parameter point to produce the observed distribution. This method is only meaningful when we input Poisson distributed data according to the errorbars shown in Fig. 4.9, as otherwise the actual value of $\xi_H^t \times \lambda_{hhH}$ will trivially be the best fit.

Fig. 4.12 shows the predicted parameter $\xi_H^t \times \lambda_{hhH}$ with the MLE method versus the model parameter, where we used 2048 sample Poisson distributed m_{hh} distributions. We see that the method fails to correctly predict the sign of the $\xi_H^t \times \lambda_{hhH}$ couplings, as we expected from the invariant mass distributions, because the dip-peak structure becomes unresolvable.
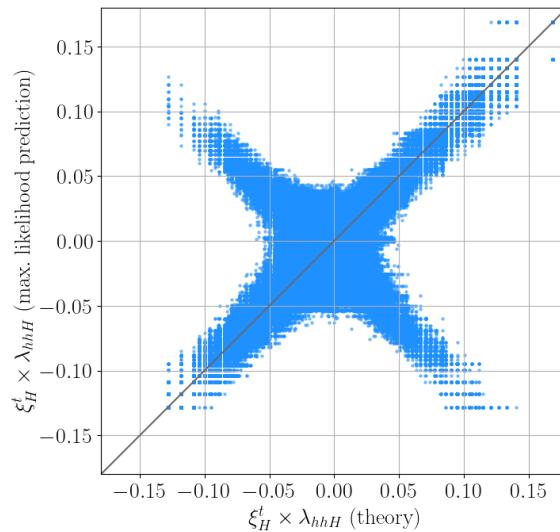
Figure 4.12
Predicted value of $\xi_H^t \times \lambda_{hhH}$ with classical maximum likelihood estimation
method versus the theoretical value of $\xi_H^t \times \lambda_{hhH}$.

4.2.2   Neural Network analysis

In this section we go beyond classical statistics to compare their performance with more
recent machine learning approaches. Our analysis can be essentially summarised as the use
of deep learning in statistical parameter estimation, which has already been proposed in
Ref. [286]. We will demonstrate that this method performs better in our example scenario,
which serves as a proof of concept for future use of such methods in the context of high
energy physics.

In this work, we focus on a technical question: the extraction of the value of $\xi_H^t \times \lambda_{hhH}$
from the m_{hh} distribution, as anticipated to be measured at the HL-LHC. We employ a
neural network that has been trained on "realistic" m_{hh} distributions, i.e. taking into ac-
count smearing, binning, and, most crucially, Poisson noise to reflect statistical fluctuations
in future measurements. This approach enables the simulation of the expected conditions
under which experimental data would be obtained, making our analysis as close to reality
as possible.

We employ a simple one layer network using `PyTorch` [287]. The network architecture
consists of an initial batch normalisation layer, followed by a single hidden layer with 64
neurons and ReLU activation, and a final output neuron with a linear activation to predict
the value of $\xi_H^t \times \lambda_{hhH}$. The Adam optimiser is used with mean squared error (MSE) as the
loss function. More complex architectures were tested but offered no significant performance
advantage, despite requiring substantially more computational resources.

As input, the model receives 16-bin histograms of the smeared m_{hh} distribution, with
each bin representing a width of 50 GeV. These inputs are modified during training by
applying Poisson noise, mimicking statistical uncertainties on the binned data. The train-
ing dataset consists of $\mathcal{O}(600 - 5000)$ distributions, depending on the scan settings of the

2HDM parameter space (i.e. wether we fix m_{12}^2 and m_H, or not). Each model is trained for a total of 32768 epochs, during which a new noisy version of the input is generated at each epoch. In the following we will refer to the value of $\xi_H^t \times \lambda_{hhH}$ obtained by theoretical calculation as "$\xi_H^t \times \lambda_{hhH}$(theory)", whereas the corresponding NN prediction is labeled as "$\xi_H^t \times \lambda_{hhH}$(NN predicted)".

We use three different datasets:

1) one corresponding to the benchmark scenario defined in Fig. 4.7,

2) one where we drop the condition on m_{12}^2 in Eq. (2.95), allowing m_{12}^2 to vary freely within the ranges of the allowed parameter space, and

3) one incorporating the potential future uncertainty in the measured m_H value. In this case, we employ a total of 9 datasets, each corresponding to the allowed regions of t_β and $c_{\beta-\alpha}$ for $m_H = \{435, 440, 445, 449, 450, 451, 455, 460, 460\}$ GeV. In this case, m_{12}^2 is fixed according to Eq. (2.95). We do not let m_{12}^2 as a free parameter as predicting distributions for such a large dataset would otherwise require the computation of 9 three-dimensional allowed parameter regions, which is computationally cumbersome. This choice is further motivated by the stability of our results when relaxing the m_{12}^2 condition applied in the benchmark scenario. Also in the third case, we test the network on a dataset with $m_H = 443$ GeV, which was part of the training set.

The result of the NN prediction, $\xi_H^t \times \lambda_{hhH}$(NN predicted), for the dataset (1) is shown as a function of the $\xi_H^t \times \lambda_{hhH}$(theory) value in the left plot of Fig. 4.13. We observe that most of the points lie in the diagonal, i.e. that overall the NN provides a good estimate of the value of $\xi_H^t \times \lambda_{hhH}$. Comparing to the result of the MLE in Fig. 4.12, the cross shape is much more subtle, with less faulty predictions of the net, that however cover all the space between the true value of $\xi_H^t \times \lambda_{hhH}$ and the same value with the opposite sign.

In order to clearly illustrate the distribution of the points, in the right plot of Fig. 4.13 we show the density distribution corresponding to the points in the left plot. The density is normalised to 100 in each bin of $\xi_H^t \times \lambda_{hhH}$(theory), meaning that the total density in one vertical strip, corresponding to a given value of $\xi_H^t \times \lambda_{hhH}$(theory), adds up to 100. The colour code indicates such density. One can see that the highest density of points in the prediction falls into the diagonal line of $\xi_H^t \times \lambda_{hhH}$(NN predicted) $= \xi_H^t \times \lambda_{hhH}$(theory). This indicates that, although there are some outliers, the neural network's main prediction is reasonably accurate.

We have analysed in detail the case of two different smeared distributions, both associated with the same benchmark point, marked by a cyan cross in Fig. 4.7. The $\xi_H^t \times \lambda_{hhH}$(NN predicted) values for each of them are shown as red and green points in the left panel of Fig. 4.14. The parameters of the benchmark point are provided in Tab. 4.1, along with the NN predictions of the two smeared distributions. These distributions are displayed in Fig. 4.14, where the red m_{hh} distribution is identical in both plots and was calculated with $\xi_H^t \times \lambda_{hhH}$(theory). As before, the vertical bars represent the statistical uncertainty for each bin. Based on these uncertainties, the two blue m_{hh} were randomly selected for this point and fed to the trained NN to evaluate $\xi_H^t \times \lambda_{hhH}$(NN predicted). In the left plot (refereed in the table as the "close" point), the $\xi_H^t \times \lambda_{hhH}$(NN predicted) value is very
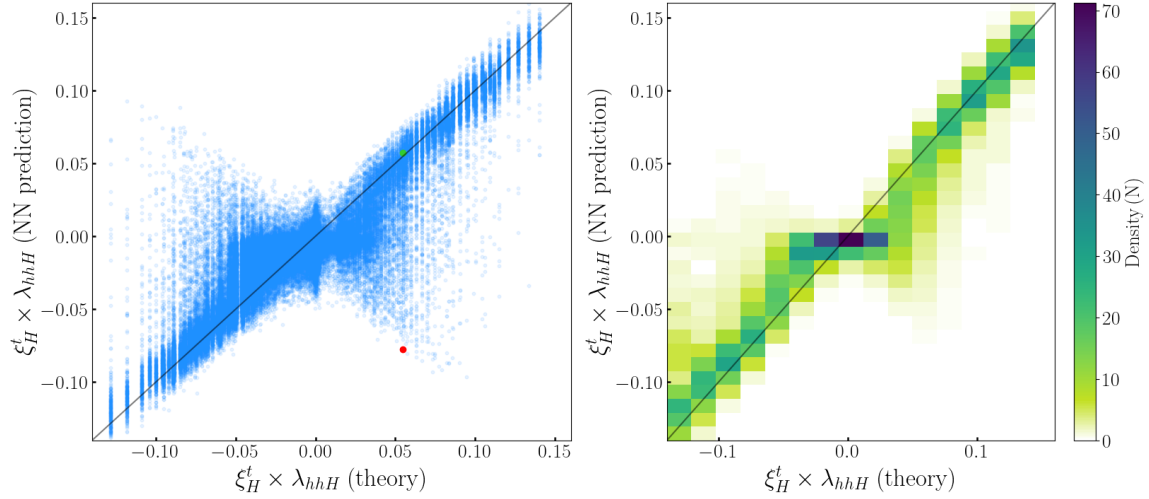
Figure 4.13

Prediction of $\xi_H^t \times \lambda_{hhH}$ for the dataset (1). We show the results in a scatter plot (left) and a density plot (right), where in the latter case the colour represents the density of points that falls into this grid. The green and red points in the left plot are example results discussed in the text.
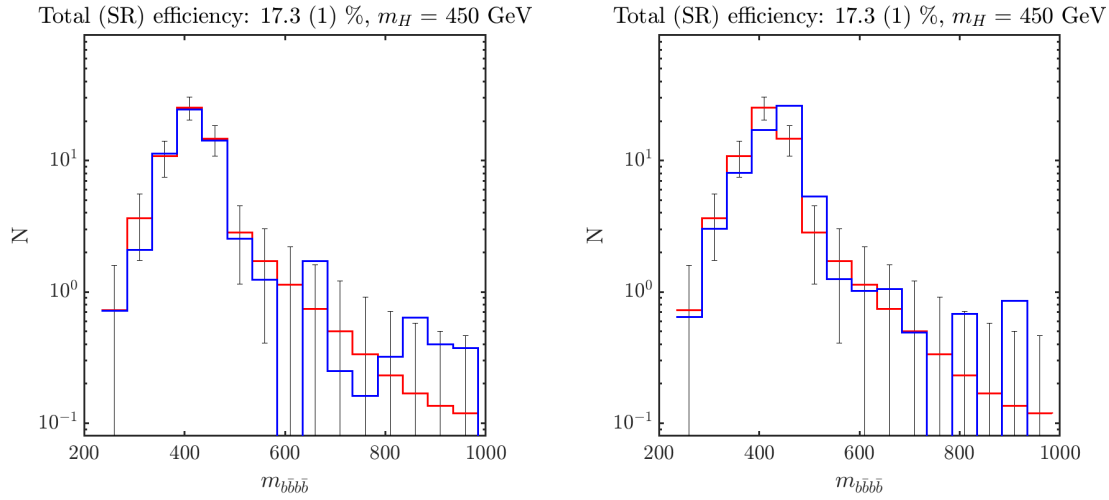
Figure 4.14

Examples of invariant mass distributions of the point marked by a cyan cross in Fig. 4.7 with the parameters given in Tab. 4.1. The red distributions are based on $\xi_H^t \times \lambda_{hhH}$(theory), and the vertical bars represent the statistical uncertainties. The blue distributions are randomly chosen based on these uncertainties (see text). They correspond to the green point on the left plot of Fig. 4.13 (left) and the red point of the left plot of Fig. 4.13(right).

close to $\xi_H^t \times \lambda_{hhH}$(theory). The key to achieving this good agreement in the NN prediction lies in the small deviation of the randomly chosen distribution from the one based on $\xi_H^t \times \lambda_{hhH}$(theory), particularly in the five bins around the resonance at $m_{hh} = 450$ GeV. This argument is further illustrated in the right plot (for the "far" point), where the five bins near the resonance show a shift in the relative height of the true distribution compared to the randomly chosen one, due to the statistical uncertainties. These shifts result in event numbers in three out of five bins around the resonance falling outside the 1σ range of their respective bin, leading to a large discrepancy between $\xi_H^t \times \lambda_{hhH}$(NN predicted) and $\xi_H^t \times \lambda_{hhH}$(theory). In this case, the NN predicts the wrong sign, indicated by a red point in the left plot of Fig. 4.13.

t_β	$c_{\beta-\alpha}$ $(s_{\beta-\alpha} > 0)$	$\xi_H^t \times \lambda_{hhH}$(th)	$\xi_H^t \times \lambda_{hhH}$(NN) "close"	$\xi_H^t \times \lambda_{hhH}$(NN) "far"
4.38	-0.04	0.0547	0.0572	-0.0775

Table 4.1: Parameters for the point marked by a cyan cross in Fig. 4.7. The value of $\xi_H^t \times \lambda_{hhH}$(NN predicted) "close" ("far") corresponds to the random distribution shown in blue in the left (right) plot of Fig. 4.14. ($\xi_H^t \times \lambda_{hhH}$(th) is short for $\xi_H^t \times \lambda_{hhH}$(theory), $\xi_H^t \times \lambda_{hhH}$(NN) is short for $\xi_H^t \times \lambda_{hhH}$(NN predicted).) The "close" point is marked in green in the left plot of Fig. 4.13, and the "far" point is marked in red.

Next, we switch to the analysis the dataset (2), where we have extended the dataset to add the allowed parameter points without fixing m_{12}^2 to Eq. (2.95). This lead to an increase in the dataset for the learning process from roughly 600 points of the original benchmark scenario to 4500 points. We show the results for Poisson smeared distributions in the scatter plot of the left side oF Fig. 4.15, with the corresponding density of points shown on the right side.
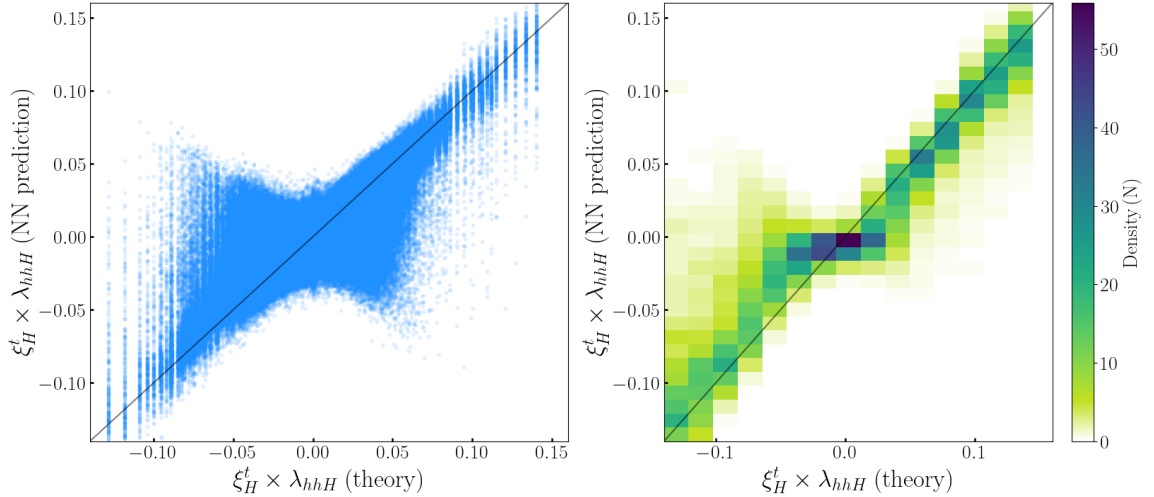

Figure 4.15
Predictions for the dataset (2), leaving m_{12}^2 as a free parameter.

We observe in Fig. 4.15 that the density of faulty points increases slightly w.r.t the dataset (1), specially in the regions around $\xi_H^t \times \lambda_{hhH}$(theory) $= \pm 0.05$, with less outliers in the most extreme values of $\xi_H^t \times \lambda_{hhH}$. We see that despite this, the largest density of points still lies in the diagonal $\xi_H^t \times \lambda_{hhH}$(theory) $= \xi_H^t \times \lambda_{hhH}$(NN predicted), with a density close to 70% in the three vertical bins around the diagonal for positive $\xi_H^t \times \lambda_{hhH}$(theory) values, and closer to 50% for negative values od $\xi_H^t \times \lambda_{hhH}$(theory).

Finally, the results for the dataset (3) are shown in Fig. 4.16 in the same fashion as before. In this case we observe a slight preference for the predicted data to lie above the diagonal for negative values of $\xi_H^t \times \lambda_{hhH}$(theory), and below for positive ones. We attribute this feature to the fact that the tested dataset has more trouble handling the uncertainty in m_H as it shifts the position of the peak-dip structure along the horizontal axis. Still, the overall prediction is within reasonable proximity of the true value of $\xi_H^t \times \lambda_{hhH}$.
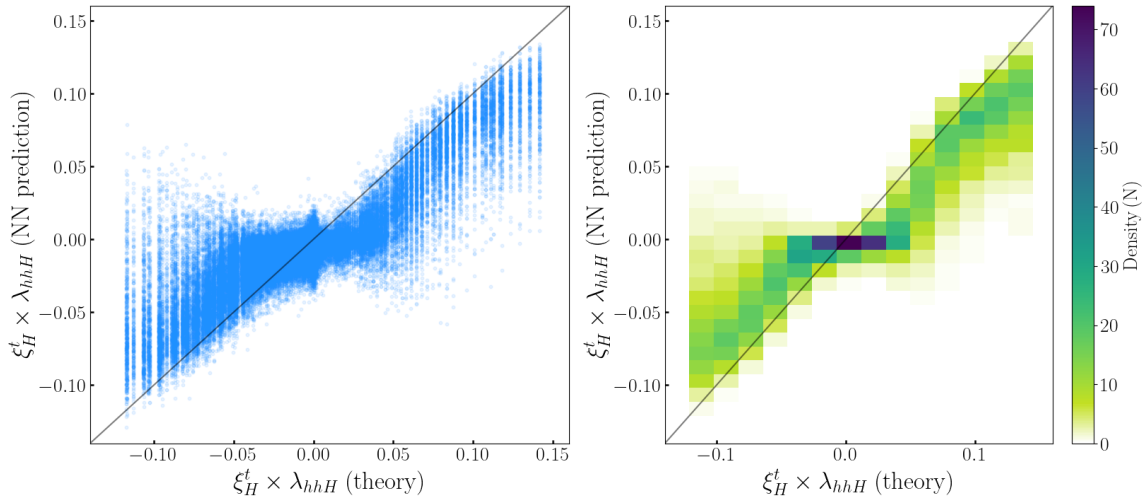
Figure 4.16
Predictions for the dataset (3), i.e. including uncertainties in the measured value of m_H in the training set and tested on statistically smeared values of a benchmark scenario with $m_H = 443$ GeV, which is not part of the training set.

Our conclusion from this analysis is that the determination of the variable $\xi_H^t \times \lambda_{hhH}$ with the correctly trained NN is possible, even taking into account all relevant experimental uncertainties (we did not take into account the systematic and theoretical uncertainties as they are harder to estimate). For this determination it is crucial to reduce the statistical uncertainties, and the result depends strongly on the experimental efficiencies. But even with the low acceptance of $\epsilon = 0.17 \times 0.01$, the results presented in this section demonstrate that an experimental determination of $\xi_H^t \times \lambda_{hhH}$ is possible.

4.2.3   Comparison between classical statistics and Neural Networks

In this section we compare the improvement in the performance of the NN relative to the classical MLE method on the original benchmark scenario. To quantify this we have used the 95% confidence interval for the absolute error of $\xi_H^t \times \lambda_{hhH}$ AE95. We trained on an equal number of samples the NN and the MLE. The interpretation of AE95 is that the error in the prediction of $\xi_H^t \times \lambda_{hhH}$ is at 95% CL smaller than AE95.

We find that the error is highly sensitive to the value of $\xi_H^t \times \lambda_{hhH}$ as illustrated in Fig. 4.17. The left plot shows the AE95 for $\xi_H^t \times \lambda_{hhH}$ computed using the MLE method, while the right plot displays the results from the NN analysis. Both approaches reveal a similar overall trend: the largest errors occur near $\xi_H^t \times \lambda_{hhH} = \pm 0.05$ and decrease for larger absolute values. Additionally, the minimum error appears near zero, with a slight preference for negative values.
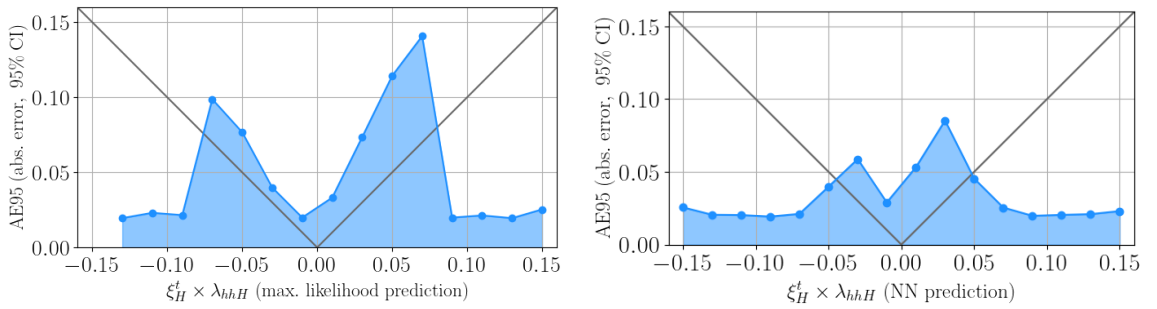
Figure 4.17
Comparison of the AE95 with MLE (left) and NN (right).

We can define the ranges where the 95% CL error is larger than the value itself as the crossing points between the blue and gray lines in Fig. 4.17, this comparison yields the $\xi_H^t \times \lambda_{hhH}$ intervals:

$$-0.0755 < \xi_H^t \times \lambda_{hhH} < 0.0799 \text{ for MLE,}$$
$$-0.0459 < \xi_H^t \times \lambda_{hhH} < 0.0450 \text{ for NN } (1\sigma). \tag{4.17}$$

These intervals can be interpreted as the sensitivity ranges of $\xi_H^t \times \lambda_{hhH}$ with each method. It is clearly visible that the NN method yields a larger sensitivity to the BSM couplings.

We can also use these intervals to compare the regions of the original plane that can be probed with both methods, this region is shown in Fig. 4.18. In this figure, we display the original benchmark plane with the colour coding indicating the magnitude of $\xi_H^t \times \lambda_{hhH}$. Inside the solid contour lines the determination of $\xi_H^t \times \lambda_{hhH}$ would not be conclusive with each respective method, i.e. compatible with zero. We point out several observations: (1) the MLE (red contour) is worse than the NN (cyan contour) for the determination of $\xi_H^t \times \lambda_{hhH}$, (2) the p-value (black contour) cannot do a parameter estimation, it can only exclude the null hypothesis of the SM, and in this it is competitive with the NN, and (3) the NN can do both, a hypothesis test and parameter estimation simultaneously, while being
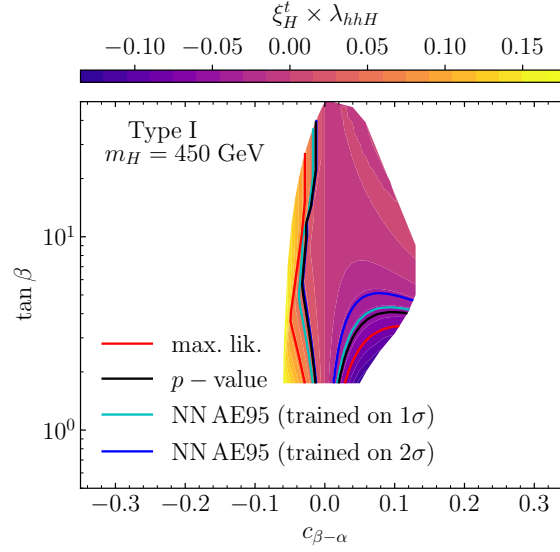
Figure 4.18
Comparison between classical methods and NN for the $\xi_H^t \times \lambda_{hhH}$ estimation
in the benchmark scenario of Fig. 4.7

comparable with the classical methods in the first case, it outperforms them in the second case.

Additionally, we trained the network on data with a larger uncertainty range (allowing 2σ errorbars with the means of the Poisson distribution at the the theoretical values of $\xi_H^t \times \lambda_{hhH}$) and validated it on data with a 1σ smaller uncertainty. In this way we provide to the net more information about the points that deviate the most from the prediction, so that it can learn more about them. The AE95 limits for $\xi_H^t \times \lambda_{hhH}$ in that case are

$$-0.0334 < \xi_H^t \times \lambda_{hhH} < 0.0341 \text{ for NN } (2\sigma), \tag{4.18}$$

shown with a solid blue line in Fig. 4.18. The results were better than with other methods, specially for negative values of $\xi_H^t \times \lambda_{hhH}$. However, training the net on points with a larger Poisson deviation from the mean values ($> 2\sigma$) proved to worsen the results, as the dataset became too noisy to extract any meaningful information. We therefore conclude that the NN is not only the best method for BSM parameter determination, as it can do both hypothesis testing and parameter estimation in a more efficient way, it also has the potential to be improved with a dedicated analysis of the data.

If we compare the different training datasets with the AE95 metric we obtain the following result

$$\begin{aligned}
-0.0459 &< \xi_H^t \times \lambda_{hhH} < 0.0450 \text{ for dataset } (1), \\
-0.0386 &< \xi_H^t \times \lambda_{hhH} < 0.0338 \text{ for dataset } (2), \\
-0.0503 &< \xi_H^t \times \lambda_{hhH} < 0.0712 \text{ for dataset } (3).
\end{aligned} \tag{4.19}$$

The respective AE95 for each value $\xi_H^t \times \lambda_{hhH}$ are shown in Fig. 4.19. The key features are: the net performs better for the dataset (2) than for dataset (1), i.e. more adding a free parameter of the model to the dataset improves its performance, and it performs worse for the dataset (3) than for the dataset (1), specially for positive $\xi_H^t \times \lambda_{hhH}$ values, which suggests that an uncertainty in the measurement might be a source of error in the NN approach, which however can be taken under control by including a larger training sample with more m_H values.
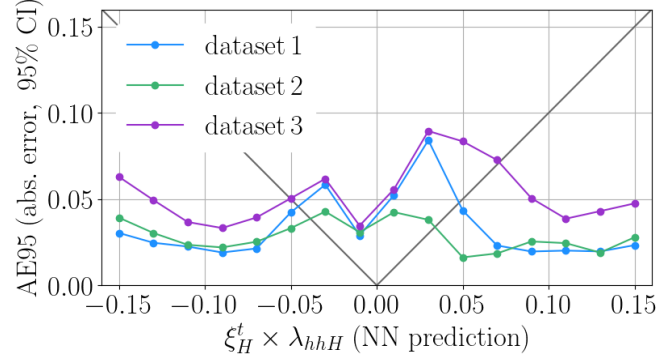
Figure 4.19
AE95 for the different datasets studied here.

Finally, we also mention here how we used the AE95 metric to decide on the network architecture. As shown in Fig. 4.20, there is no significant improvement in the ranges of $\xi_H^t \times \lambda_{hhH}$(NN predicted) when using a 2-hidden layer network with 128 neurons or even a 4 layer with 128 neurons each w.r.t the simple 1 layer with 64 neurons employed in the present analysis.

4.2.4 Future prospects

The results in the previous subsection have been obtained using the experimental efficiencies as given by ATLAS [272]. However, it is conceivable that the efficiencies during the HL run of the LHC might improve due to a better knowledge of the systematic uncertainties with increasing luminosity. As a hypothetical scenario we analyse here the level of improvement in the NN determination of $\xi_H^t \times \lambda_{hhH}$ in the case that each of the two efficiencies, ϵ_{TOT} and ϵ_{SR} are improved by a factor of two. This increase of the number of events by a factor of four would yield a factor of $1/2$ in the statistical uncertainty for each bin in the m_{hh} distribution.

In Fig. 4.21 we show the results of the NN analysis assuming this improvement of the combined efficiency by a factor of four, i.e. the same as in Figs. 4.13, 4.15, and 4.15 but with relative statistical uncertainties smaller by a factor of $1/2$. We evaluate the improvements on the initial benchmark plane (first row), on the plane with the free m_{12}^2 (middle row) and the uncertain m_H (lower row). We show the scatter plots on the left and the density plots on the right, in the same fashion as before. All the plots in Fig. 4.21 show a substantial improvement over the corresponding in Figs. 4.13, 4.15, and 4.15. The conclusion being
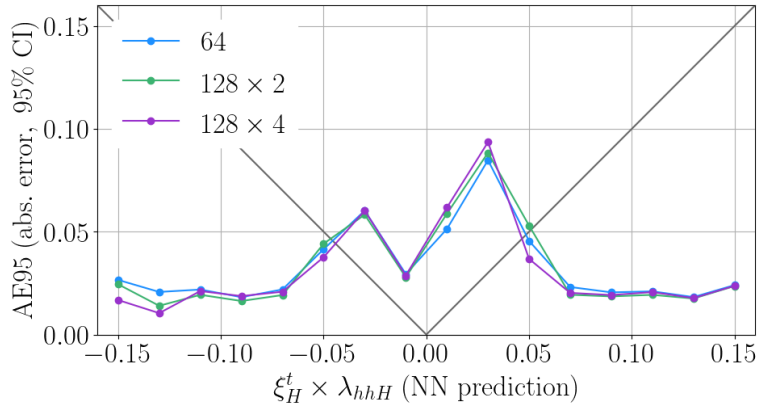
Figure 4.20
AE95 for different NN architectures. The one employed in this project
is the simplest 1 hidden layer with 64 neurons (blue), the more complex
architectures include a 2 and 4 hidden layers with 128 neurons each, shown
in green and purple respectively.

that a factor of two improvement in the efficiencies will lead to a NN determination of
$\xi_H^t \times \lambda_{hhH}$ at the level of 10-20%.

4.2.5 Outlook

As discussed in Chapter 2, the shape of the scalar potential remains undetermined exper-
imentally and is strongly influenced by deviations in the scalar sector from the minimal
electroweak sector of the SM. In particular, the presence of additional scalar fields would
induce new BSM scalar self-interactions, as for instance λ_{hhH}. Motivated by BSM theories
that suggest modifications of the "vanilla" SM-like scalar potential, we present an analysis
aimed at determining the access to one BSM parameter shaping its possible form.

   We presented the first sensitivity study of such a BSM trilinear scalar coupling using a
NN trained on the invariant mass distributions of Higgs pair production at the HL-LHC to
extract $\xi_H^t \times \lambda_{hhH}$, the product of the resonant scalar top Yukawa coupling and trilinear
coupling of H to the two SM-like Higgses in the final state, hh. Assuming a hypothetical H
mass of 450 GeV, we show that, depending on future experimental efficiencies and uncer-
tainties, a determination of $\xi_H^t \times \lambda_{hhH}$ at the 10–20% level may be achievable by the end of
the HL-LHC. We also present a simple and efficient alternative to classical statistical meth-
ods, demonstrating that basic NNs are effective for both hypothesis testing and parameter
estimation, outperforming conventional MLE methods in this context.

   If in the future data is available that confirms the existence of a BSM scalar particle
in nature, a NN model with a larger accuracy can be trained, by taking into account
the future mass uncertainty range and by including higher order loop corrections to the
process $gg \rightarrow hh$, and in particular to the involved THCs. We expect a more realistic and
sophisticated analysis based on this future knowledge to outperform our results. Despite the
fact that our analysis is model dependent, it is reasonable to assume that any model with
a similar experimental signature that may then be favoured by experimental data will have
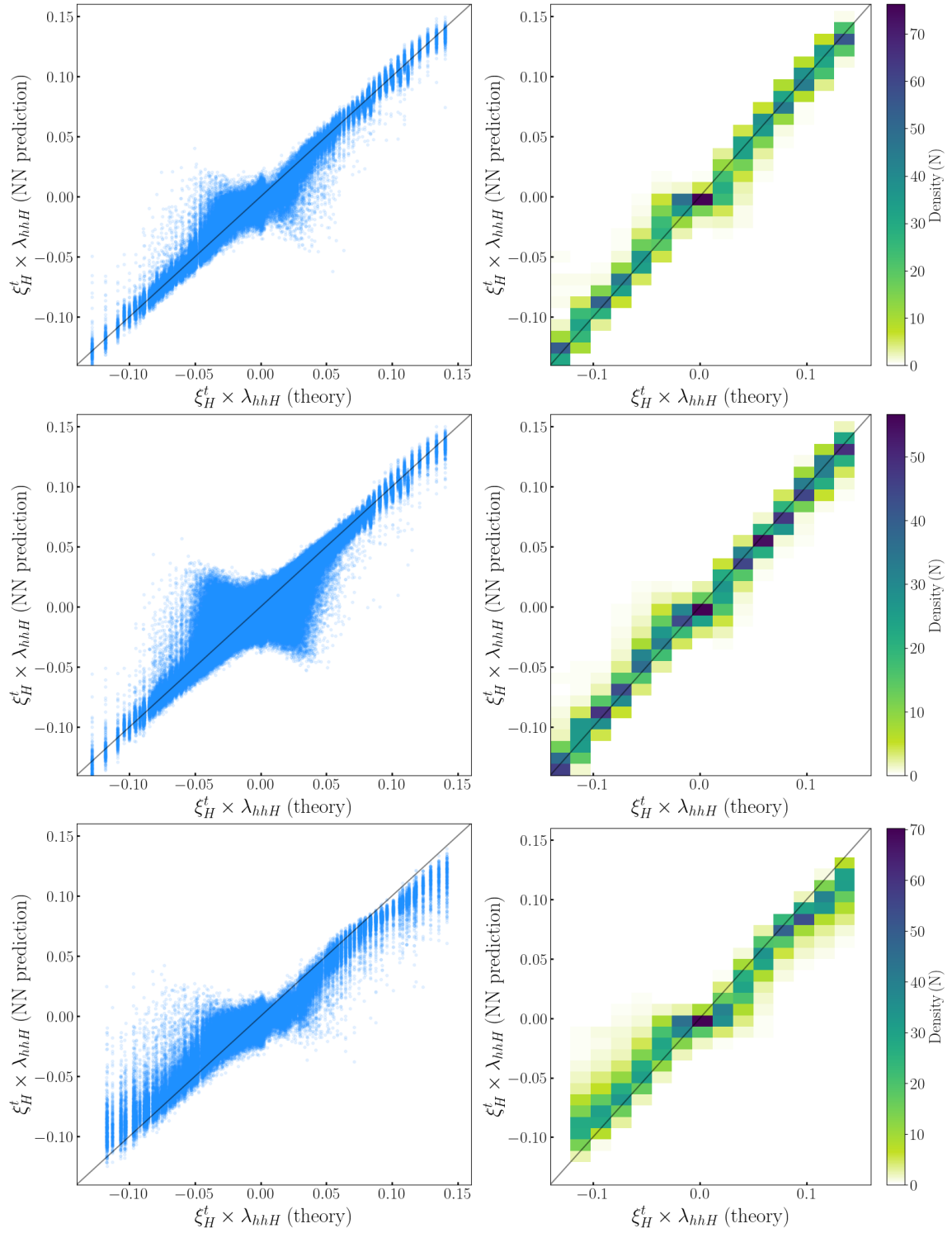
Figure 4.21
NN prediction of $\xi_H^t \times \lambda_{hhH}$ for the different datasets: (1) upper, (2) middle and (3) lower row. All with a factor 4 improvement in the total efficiency ϵ (see text).

good prospects for the determination of the couplings involved in the resonantly produced Higgs-boson pairs. In this way, NNs pave the way to determine the shape of the BSM Higgs potential.

Chapter 5

New probes of a strong first order electroweak phase transition

Contents

In this section we will explore the different phenomenological probes of a strong first order electroweak phase transition in the early Universe. We begin with collider probes, followed by cosmological ones. On the collider side, we focus on two main aspects: (1) searches for additional scalar particles, which, as we discussed, are a requirement for electroweak baryogenesis due to the absence of a first-order phase transition in the SM, highlighting in particular the *smoking gun* signature $A \to ZH$, and (2) deviations in the Higgs trilinear coupling, which are linked to the observation of Higgs pair production. On the cosmological side we explore the cosmological probes of a strong first order phase transition, where we will explore the gravitational wave stochastic background produced by such a transition.

5.1   General effects of a SFOEWPT in the 2HDM

In order to study the physics of the EW phase transition, we will use the finite-temperature effective potential formalism. The one-loop, daisy resummed, finite-temperature 2HDM effective potential is derived in App. A. It is given by

$$V_{\text{eff}} = V_{\text{tree}} + V_{\text{CW}} + V_{\text{CT}} + V_{\text{T}} + V_{\text{daisy}} \ . \tag{5.1}$$

The temperature-independent part of the potential comprises the first three terms, where V_{tree} is defined in Eq. (2.66), V_{CW} is the one-loop Coleman Weinberg potential [138] incorporating the radiative corrections, and V_{CT} is a UV-finite counterterm potential introduced in order to keep the physical masses and the vevs of the Higgs fields at their tree-level values at zero temperature [211]. The thermal corrections to the scalar potential are split into two terms. The first one, V_{T}, incorporates the one-loop thermal corrections in terms of the well-known J-functions (see e.g. Ref. [288]). The second term, V_{daisy}, is an additional piece accounting for the resummation of the so-called daisy diagrams. As resummation prescription, we follow the Arnold-Espinosa method [289], which resums the infrared-divergent contributions from the bosonic Matsubara zero-modes. We emphasize that the computation of the finite-temperature effective potential, at the order performed in this work, is affected by sizeable theoretical uncertainties, see Refs. [290–293] for a detailed discussion.

For the numerical evaluation of the effective potential at finite temperatures we use the public code `CosmoTransitions` [294], which was updated in Ref. [295]. Typically, the universe evolves starting from an EW symmetric vacuum configuration at the origin of field space.[1] We identify the regions of the 2HDM parameter space that, as the Universe cools down, develop an electroweak symmetry-breaking minimum in the Higgs potential, separated from the origin by a potential barrier. The universe reaches the critical temperature T_c when these two coexisting vacua are degenerate. At later times, when $T < T_c$, the minimum corresponding to the EW vacuum drops below the minimum in the origin, and thus becomes energetically more favourable. At this point, the onset of the first-order phase transition from the minimum at the origin to the EW vacuum depends on the transition rate per unit time and unit volume

$$\Gamma(T) = A(T)e^{-S_3(T)/T}, \tag{5.2}$$

where $A(T) \sim T^4(S_3/2\pi T)^{3/2}$ [296]. Here $S_3(T)$ is the temperature-dependent Euclidean bounce action of the (multi-)scalar field configurations, defined as

$$S_3 = 4\pi \int r^2 dr \left[\frac{1}{2} \left(\frac{d\phi_B}{dr} \right)^2 + V(\phi_B, T) \right], \tag{5.3}$$

where ϕ_B is the solution to the equation of motion defined by the Euclidean action $S_3(T)$. The onset of the phase transition occurs when (see e.g. Ref. [110])

$$S_3(T_n)/T_n \approx 140 \ , \tag{5.4}$$

---

[1]EW symmetry non-restoration in the high-temperature regime $T \gg m_A, m_{H^\pm}, m_H, M$ (with $M^2 \equiv m_{12}^2/(s_\beta c_\beta)$) is possible in the 2HDM [77].

which arises from the comparison of the transition rate and the expansion rate of the universe. T_n is the nucleation temperature, which very accurately corresponds to the temperature at which the transition takes place. If the condition (5.4) is not fulfilled at any temperature $T < T_c$, the phase transition cannot complete successfully, and the universe remains trapped in the false vacuum at the origin [77] (see also Refs. [295, 297]).

With this in mind, and following Ref. [77] (see also Ref. [298]), we can define several thermal histories in the 2HDM according to the temperature evolution of the vacuum configuration:

Global minimum at the origin: parameter points that fall in this category exhibit a global minimum at the origin of field space at $T = 0$. They can be divided into two subregions: region **A**, where the electroweak minimum existed at high temperature but the system never transitioned to it, resulting in electroweak symmetry non-restoration (see discussion below); and region **B**, where the global minimum remained at the origin throughout the thermal history, and no phase transition occurred either. In region **A**, the SSB required for the Higgs mechanism must have taken place at temperatures higher than the range considered in our analysis (valid up to $T_{\max} \sim 500$ GeV), thus beyond the reach of perturbative effective potential methods. For related work on high-scale baryogenesis, see Ref. [299–304]. Region **B** is unphysical, as the system remains in the symmetric phase at zero temperature.

Symmetry non-restoration (SnR): refers to scenarios where the EW symmetry remains broken even at high temperatures, contrary to the standard expectation of symmetry restoration. This phenomenon can occur due to large quartic couplings and resummed thermal corrections. Contrary to vacuum trapping, EW SnR is not necessarily an unphysical scenario. Even though in the presence of SnR an EWPT is not possible, high-scale GUT baryogenesis scenarios might happen due to the suppression sphaleron processes in the broken phase [305–309]. However care must be taken as SnR up to high scales alters the thermal history of the Universe, potentially affecting dark matter abundance, the Hubble rate, and the evolution of particle species through modified interactions with the thermal bath. These points belong to the category labelled **C**.

Vacuum trapping: refers to the unphysical situation where the Universe becomes stuck in a false vacuum during its thermal evolution, preventing it from reaching the EW vev at zero temperature at 246 GeV. Even if the EW vacuum is the global minimum at $T = 0$, a viable cosmological history requires that the Universe can evolve to it at an earlier stage. This means that zero-temperature analyses alone are insufficient to determine the physically allowed parameter space in BSM models. If a potential barrier prevents a first order phase transition, the Universe may remain trapped in a symmetric (false) vacuum. These points belong to the category labelled **D**, and same as for **B**, they are unphysical.

Strong first order electroweak phase transition: In this category we classify the parameter points that feature a phase transition strong enough to allow for electroweak bayogenesis. We label this region as **E**. For them the condition in Eq. (2.48) $\xi_n > 1$ is satisfied. The transition happens at a nucleation temperature T_n. The larger the

splitting between the nucleation and the critical temperature T_c, the stronger the transition and the better the prospects for GW observations.

Weak phase transition: here we classify the points that feature either a weak first-order transition that cannot lead to successful baryogenesis or a second order phase transition. In such cases the evolution of the vacuum with temperature is continuous and no vacuum tunnelling occurs, therefore no bubble nucleation takes place and the transition happens continuously and simultaneously throughout space.

In the context of this thesis we extended the analysis performed in Ref. [77] to further regions of the 2HDM parameter space. In Figs. 5.1 and 5.2 we show our results in the four 2HDM Types for $t_\beta = 2$ and $t_\beta = 10$, respectively. The x-axis represents the mass of the CP-even scalar, m_H, and the y-axis is the mass of the CP-odd scalar. All these scenarios are in the alignment limit, $c_{\beta-\alpha} = 0$, and furthermore satisfy $m_A = m_{H^\pm}$ in order to avoid constraints from EWPO, and $m_{12}^2 = m_H c_\beta s_\beta$ to enlarge the region allowed by perturbative unitarity. In the four upper plots we show as a colour coding the regions excluded by experimental constraints, using the same conventions as described in Sec. 2.7.2. The yellow regions are excluded by tree-level vacuum stability (VS), the green regions by perturbative unitarity (PU), the cyan regions by flavour constraints (FC), the pink by electroweak precision observables (EW), the red by `HiggsBounds` (HB) and the purple by `HiggsSignals` (HS). The allowed regions by all the constraints are white. We observe that the flavour constraints cut the parameter space of all $m_A < 600$ GeV. Regions with large mass-splittings between m_A and m_H are constrained by perturbative unitarity. In the analysed benchmark plane, the region with $m_H \lesssim 400$ GeV is excluded mostly by $A \to ZH$ searches analysed in greater detail in the following subsection. We note that in Type II the searches for BSM scalars in regions with $t_\beta = 10$ exclude most of the analysed parameter space, with masses of the scalar particles up to 800 GeV. This is mainly due to $H/A \to \tau^+\tau^-$ searches, as will be discussed in more detail in the next section.

The lower four plots show the thermal histories in the allowed parameter regions (i.e. the white regions in the four upper plots). We show the same scenario in the four 2HDM Types. In this case, the disallowed region by experimental constraints that was coloured in the plots above is represented by a gray region. In the allowed region we distinguish between the coloured regions **A** (light blue), **B** (green), **C** (dark blue), **D** (black), **E** (colour code indicating the nucleation temperature T_n) and **F** (light brown) explained above. In the white points the numerical calculation failed. In most of the cases this happens in the limits of the weakest transitions, as the numerical integration struggles to find a transition. We could have tuned the parameters of the numerical integration in these regions, but since this is a qualitative study of the effects we did not perform a detailed investigation of specific parameter points.

In general, we recover the results from Ref. [77], which was however restricted to Type II and $t_\beta = 3$. We observe that in the $m_H - m_A$ plane a weak phase transition takes place at the values along the diagonal. For a fixed m_H, the strength of the transition increases as m_A becomes larger, i.e. as the mass splitting between the scalars increases, which in turn implies larger quartic couplings and a larger barrier. When the phase transition becomes strong, thus entering in the region **E**, for which we show the bubble nucleation temperature as a colour coding. The strongest transitions happen at yellow values of the coloured region, which correspond to a nucleation temperature $T_n \sim 50$ GeV. When the mass splittings
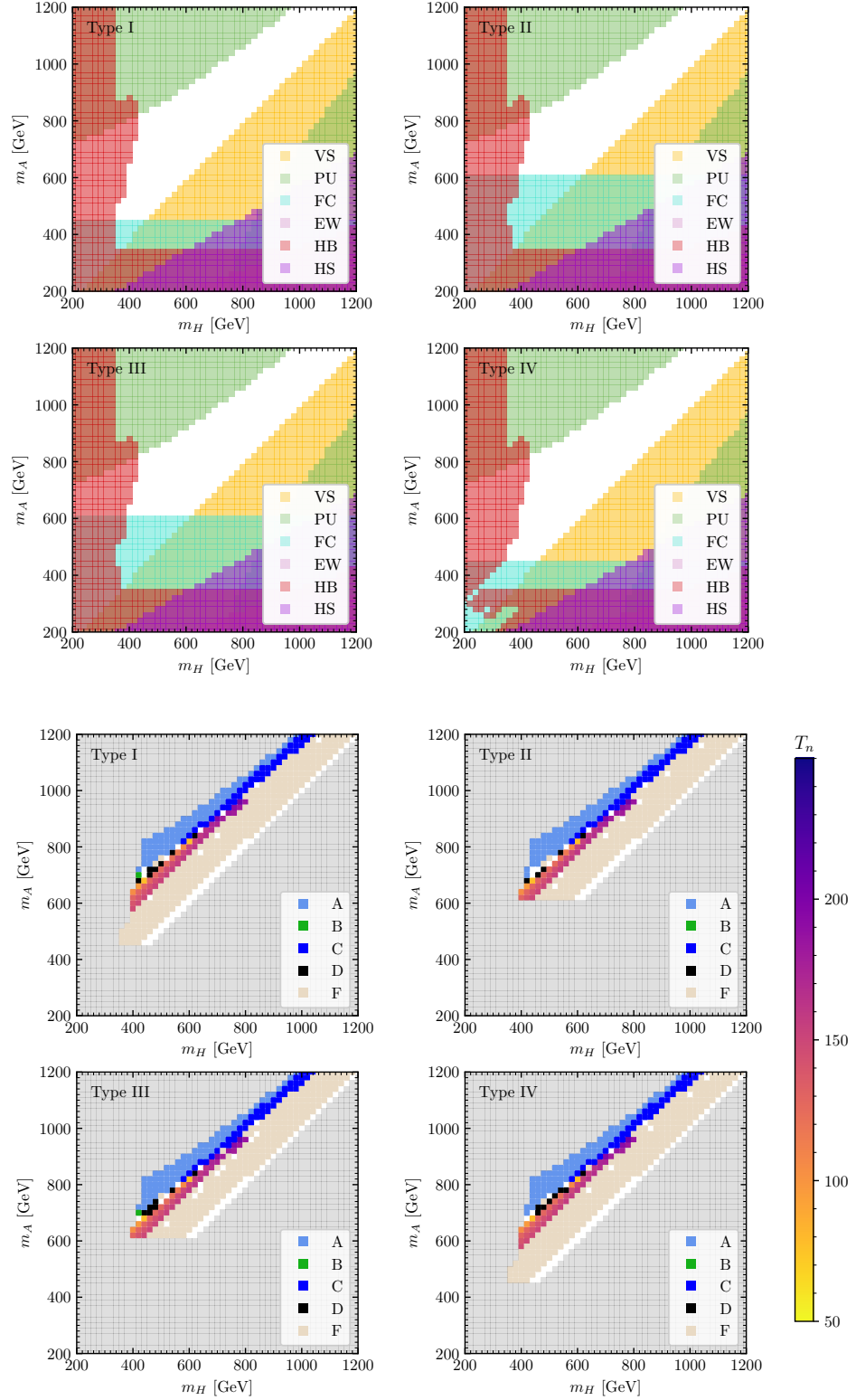
Figure 5.1

All 2HDM Types for $t_\beta = 2$, $c_{\beta-\alpha} = 0$. The four upper plots show the region constrained by the applied theoretical and experimental constraints. The four lower plots depict the different thermal histories in the allowed region. The colour coding indicates the nucleation temperature in the region compatible with a SFOEWPT. See text for details.
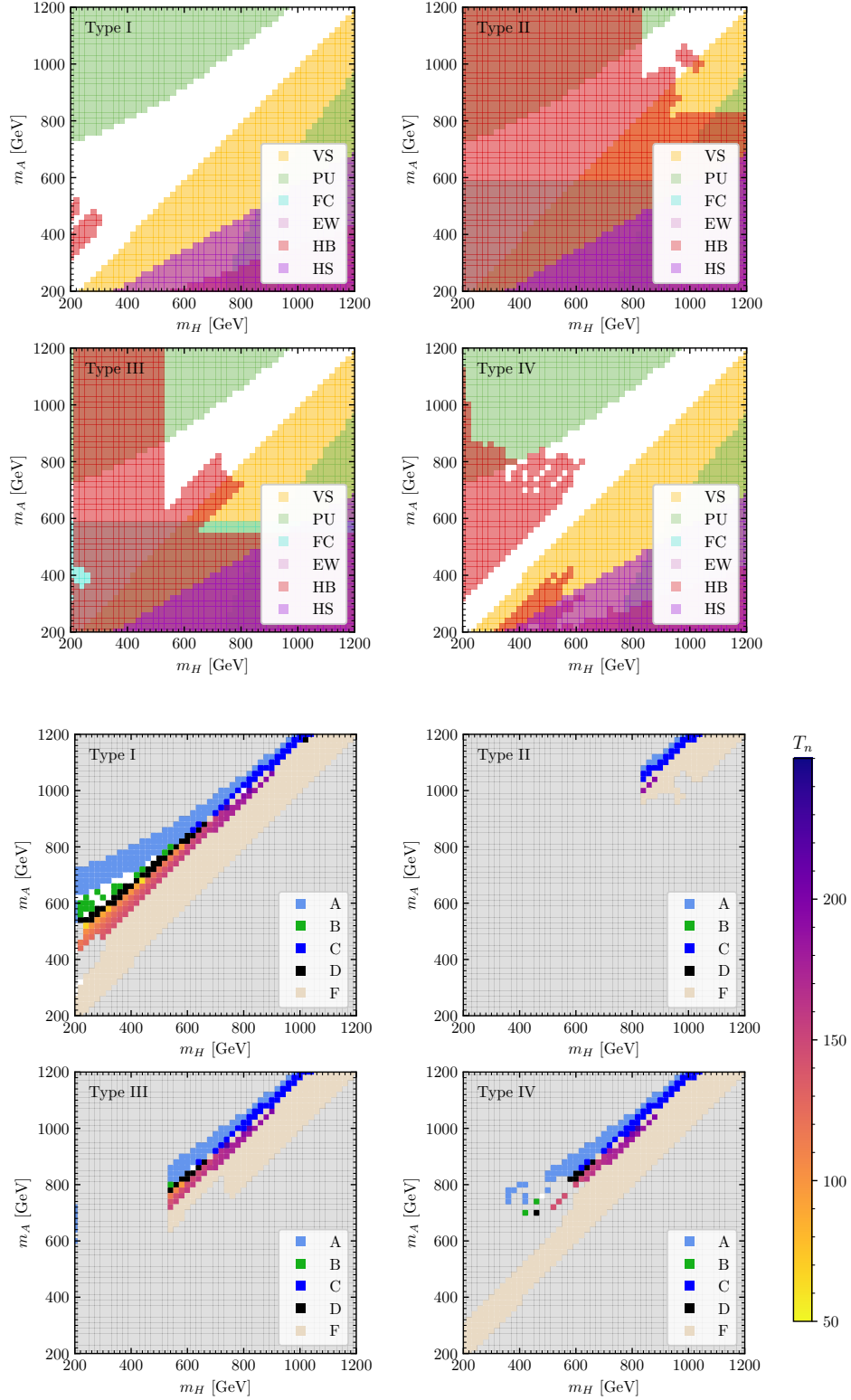
Figure 5.2
Same as in Fig. 5.1, but for $t_\beta = 10$, $c_{\beta-\alpha} = 0$.

become larger, the vacuum trapped region **D** emerges for masses roughly below $m_H \lesssim 600$ GeV. For higher masses, the EW symmetry remains unrestored at high temperatures.

The main conclusion that can be drawn from this analysis is that the Yukawa type does not play a major role in the phase transition. The differences in the type are differences among the light Yukawa couplings and therefore the contributions in the effective potential are minor, this was expected. A major difference between types arises once experimental constraints are taken into account, as they depend on the allowed production channels and decay rates and these depend significantly on the Yukawas of the light particles (see Sec. 5.2 for a detailed discussion).

Comparing the results for $t_\beta = 2$ and $t_\beta = 10$, we cannot see a major difference in the thermal histories. Turning to the region featuring a SFOEWPT, which is most relevant here, we can see that larger values of t_β seem to open the possibility for a strong transition at larger masses of the CP-even scalar, m_H, up to values of 1 TeV. The strongest transitions have a $T_n \sim 50$ GeV, as in the case for smaller t_β values.

5.2 Collider probes

We have seen that mass splitting effects in BSM theories induce large quartic couplings and these contribute to enhancing the energy barrier in the early Universe that opens up the possibility for a strong first order transition to take place. There are two phenomenological consequences of the above statement, one is the occurrence of BSM states, which is an active area of experimental searches, and the second one is the deviation in the measured trilinear Higgs coupling today.

5.2.1 Direct searches

Any BSM searches could *a priori* lead to the discovery of a particle that would favour a strong first order electroweak phase transition. In this thesis we will focus on one search in particular, which has been coined a *smoking gun signature* for a FOEWPT [310]. This process is the decay of a pseudoscalar particle into a Z boson and a heavy BSM CP-even particle, $A \rightarrow ZH$. This search requires a mass splitting between m_A and m_H at least of the order of the Z-boson mass ($m_Z \sim 91$ GeV) in order to be kinematically allowed and therefore enforces the necessary mass splittings that induce a SFOEWPT in BSM theories. It also contains two of the four BSM states present in the 2HDM, which is therefore a minimal complete theory that accommodates such a decay channel.

Our analysis will be based on the recent ATLAS $A \rightarrow ZH$ searches that were published during the course of this thesis in two A production modes (gluon fusion and $b\bar{b}$-associated production) and three decay channels ($\ell^+\ell^- t\bar{t}$, $\ell^+\ell^- b\bar{b}$ and $\nu\nu b\bar{b}$):

- $gg \rightarrow A \rightarrow ZH \rightarrow \ell^+\ell^- b\bar{b}$ at 13 TeV including 139 fb^{-1} from Ref. [281]

- $b\bar{b} \rightarrow A \rightarrow ZH \rightarrow \ell^+\ell^- b\bar{b}$ at 13 TeV including 139 fb^{-1} from Ref. [281]

- $gg \rightarrow A \rightarrow ZH \rightarrow \ell^+\ell^- t\bar{t}$ at 13 TeV including 140 fb^{-1} from Ref. [311]

- $gg \rightarrow A \rightarrow ZH \rightarrow \nu\nu b\bar{b}$ at 13 TeV including 140 fb^{-1} from Ref. [311]

- $b\bar{b} \rightarrow A \rightarrow ZH \rightarrow \nu\nu b\bar{b}$ at 13 TeV including 140 fb^{-1} from Ref. [311]

We note that the results from Ref. [281] update the previous ATLAS results based on 36.1 fb^{-1} collected during the first two years of Run 2 [312], which are contained in the public `HiggsBounds` dataset (and which will now be replaced by the full Run 2 results). The corresponding CMS results include first-year Run 2 data [313] and are also implemented in `HiggsBounds`, but since they are based on less data, the extracted limits are weaker than the limits from the new ATLAS analyses. More recently, CMS published the results in the $\ell^+\ell^- t\bar{t}$ final state [314], which were not available at the time of our analysis and are therefore not included here.

We focus on two distinct regions of the 2HDM parameter space: a low-t_β regime ($t_\beta \leq 3$) and a high-t_β regime ($t_\beta \geq 10$). In the **low-t_β regime**, the pseudoscalar Higgs boson A can be efficiently produced via gluon fusion. Similarly to the CP-even scalar production discussed so far, the dominant fermion loop is the top quark loop, whose Yukawa coupling is proportional to $1/t_\beta$ and therefore leads to a cross section scaling as $1/t_\beta^2$ for all 2HDM Types (see Eq. (2.72) and Tab. 2.2). The contributing diagram is shown on the left of Fig. 5.3. We find that searches in the $\ell^+\ell^- t\bar{t}$ final state exclude substantial regions of parameter space that were previously unconstrained. In contrast, searches in the $\nu\nu b\bar{b}$ final state primarily exclude regions already ruled out by other LHC analyses or theoretical constraints such as perturbative unitarity. Due to the aforementioned dependence on t_β, these searches quickly lose sensitivity in intermediate t_β regions, where also $b\bar{b}$-associated production remains inefficient, for which the corresponding Feynman diagram shown on the right of Fig. 5.3.
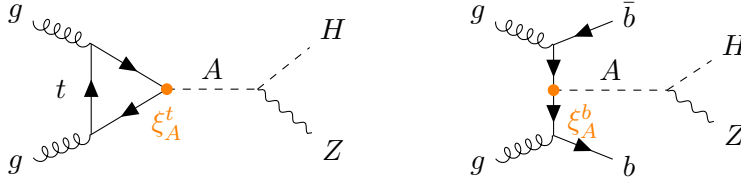
Figure 5.3
Diagrams with the main $A \to ZH$ production modes: gluon fusion on the left and $b\bar{b}$-associated production on the right. In orange the involved Yukawa coupling modifiers are indicated, the A-boson top-Yukawa on the left and the A-boson bottom-Yukawa on the right.

In the **high-t_β regime**, $b\bar{b}$-associated processes for A production become efficient in some 2HDM Types. In this case, the cross section is enhanced in Yukawa Types II and IV (scaling as t_β^2), and suppressed in Types I and III (scaling as $1/t_\beta^2$) (see Eq. (2.72) and Tab. 2.2). In this regime, the $\nu\nu b\bar{b}$ searches primarily probe regions already covered by previous $\ell^+\ell^- b\bar{b}$ analyses, we find however that in order for this production mode to have a sizeable sensitivity, the enhancement needs to be of $t_\beta^2 \approx 100$, which fixed the minimum value of our high-t_β regime at 10. The impact of the searches for even larger values of t_β can be extrapolated from the discussion of this scenario, as will be shown in detail in Sec. 5.2.1.2.

The 2HDM parameter region that we explore in this work is motivated by the possibility of realising a strong FOEWPT giving rise to EW baryogenesis in the early Universe. In this scenario the CP-odd scalar A and the charged scalars $H^\pm$ are assumed to be mass-degenerate, i.e. $m_A = m_{H^\pm}$, and the squared mass scale $M^2 = m_{12}^2/(s_\beta c_\beta)$ is set equal

to the mass of the heavy CP-even scalar H, i.e. $M = m_H$.[2] In addition, the alignment limit $\cos(\alpha - \beta) = 0$ is assumed, in which the properties of the (in this case) lightest Higgs boson h with mass $m_h = 125$ GeV are the same as for the SM Higgs boson at tree level. These conditions on the parameter space allow for sizeable $m_A - m_H$ mass splittings, driven by the quartic couplings in the 2HDM scalar potential Eq. (2.66), facilitating the presence of a FOEWPT [77, 310] while being in agreement with the LHC measurements of the properties of the detected Higgs boson at 125 GeV as well as with the results for the EW precision observables and further theoretical constraints. After imposing the above-mentioned conditions, the only remaining free parameters are the masses m_H and $m_A = m_{H^\pm}$ as well as t_β. In the following, we discuss our results in the (m_H, m_A)-plane for different values of t_β within the two regimes discussed above. We check the compatibility of the parameter space with experimental and theoretical constraints using `thdmTools`, although we do not explicitly apply the constraints from flavour physics, as we focus on the direct sensitivity of collider searches in the BSM parameter space.

5.2.1.1 Low t_β-regime

In this section we present our results for the low-t_β regime, which focuses on the range $1 \leq t_\beta \leq 3$. The lower bound on t_β was chosen because values of t_β below 1 are in strong tension with constraints from flavour physics observables. The indirect limits from flavour physics also constrain the 2HDM parameter space for slightly larger values of t_β depending on the 2HDM Yukawa Type and the mass of the charged Higgs boson. As discussed above, we do not carry out a detailed investigation of the indirect limits from flavour physics in the following.

In Fig. 5.4 we show the impact of the new $A \to ZH$ searches from ATLAS [281, 311] in the (m_H, m_A)-plane for $t_\beta = 1$ (upper left), $t_\beta = 1.5$ (upper right), $t_\beta = 2$ (lower left) and $t_\beta = 3$ (lower right). The upper left plot is valid independently of the chosen 2HDM Yukawa Type. However, for $t_\beta \neq 1$ the relevant cross sections and branching ratios depend on the Yukawa Type, and the specific choice of type that is specified in the upper right and the lower plots will be further discussed below.

In each plot we indicate the parts of the parameter space that are excluded by vacuum stability and perturbative unitarity with pink and cyan colours, respectively. The regions excluded by the new ATLAS search [311] for $gg \to A \to ZH$ in the $\ell^+\ell^- t\bar{t}$ and the $\nu\nu b\bar{b}$ final states are indicated with red and blue shaded contours, respectively, whereas regions excluded from previous LHC searches (including the recent ATLAS $gg \to A \to ZH \to \ell^+\ell^- b\bar{b}$ search [281]) are indicated in gray. In each case the search channel giving rise to the exclusion (under the assumption that this search is applied individually, see the discussion in Sec. 4.1.2.2) is stated in the plots. For the new ATLAS searches we show in addition the expected exclusion regions with dashed lines in the same colours. By comparing the gray shaded areas with the red and blue shaded areas, one can determine to what extent the new ATLAS searches probe previously unexplored parameter space regions.

---

[2]We note that in the 2HDM interpretation presented by ATLAS almost the same benchmark scenario was considered [311]. However, therein the condition $M = m_A$ was used instead of $M = m_H$ as applied here. We apply the latter condition in order to have a theoretically consistent form of the Higgs potential for $m_A = m_{H^\pm} \gg m_H$, whereas the condition used by ATLAS gives rise to an unbounded Higgs potential, and thus an unstable EW vacuum, in the parameter space regions in which the $A \to ZH$ decay is kinematically allowed.

Finally, we show in the plots in Fig. 5.4 the parameter regions that exhibit a strong FOEWPT as defined in Sec. 5.1 (based on the one-loop thermal effective potential with daisy resummation in the so-called Arnold-Espinosa scheme). As discussed above, we note the sizeable theoretical uncertainties in the predictions for a strong FOEWPT using this approach, and thus the regions shown should only be regarded as indicative for the presence of such strong transitions. The colour coding of the points indicates the ratio between the vev v_n in the broken phase at the onset of the transition and the nucleation temperature T_n.

The results for $t_\beta = 1$ (all Types) are shown in the upper-left plot of Fig. 5.4. One can see that the new $A \to ZH \to \ell^+\ell^- t\bar{t}$ ATLAS search (red) excludes the region 350 GeV $\lesssim$ $m_H \lesssim$ 450 GeV and 650 GeV $\lesssim m_A = m_{H^\pm} \lesssim$ 800 GeV, which was so far allowed. This demonstrates the exclusion power of such smoking gun signature for masses above the di-top threshold. In addition, when combined with searches for the charged scalars using the $H^\pm \to$ tb decay [278, 315], searches for neutral scalars decaying into top-quark pairs [255], and searches for the $A \to ZH$ decay in the $\ell^+\ell^- b\bar{b}$ final state [281], the mass range 300 GeV $\lesssim$ $m_H \lesssim$ 450 GeV and 450 GeV $\lesssim m_A = m_{H^\pm} \lesssim$ 700 GeV is now excluded. Fig. 5.4 also highlights that for $t_\beta = 1$ the parameter region with a strong FOEWPT to which the new ATLAS search is sensitive, assuming $m_A = m_{H^\pm}$, is already excluded by the charged Higgs-boson searches. Yet, we stress that if the condition $m_A = m_{H^\pm}$ were relaxed by allowing for an additional mass gap between these states, i.e. $m_{H^\pm} > m_A$ (which however would lead to a tension with the electroweak precision observables), the searches for the charged scalars would become less sensitive, such that the smoking gun search would have the highest sensitivity in an even larger region of parameter space.

The results for $t_\beta = 1.5$ (Type II) are shown in the upper right plot of Fig. 5.4. While for low t_β values the gluon-fusion production cross sections of A are dominantly mediated by the top-quark loop, making the cross sections still very much independent of the type, the branching ratios of A and H differ depending on the chosen type. However, for $t_\beta = 1.5$ the differences between the types are mild, and we focus on the Yukawa Type II for definiteness. Comparing to the results for $t_\beta = 1$ (upper left plot), one can see that the region excluded by the searches for the charged scalars via $pp \to H^\pm tb \to tb\,tb$, where the cross section times branching ratio roughly scales with $1/t_\beta^2$ in the low-t_β regime, is substantially smaller. This search loses even more sensitivity where the decay $H^\pm \to W^\pm H$ is kinematically allowed, giving rise to the slope of the corresponding excluded region for $m_H \lesssim$ 500 GeV (which is more pronounced than for $t_\beta = 1$ because of the reduced $H^\pm tb$ coupling). As a consequence, for $t_\beta = 1.5$ the $H^\pm \to tb$ searches are not sensitive anymore to the parameter space region indicative of a strong FOEWPT. Instead, this region is excluded up to masses of $m_H \approx 2\,m_t$ by searches for $H \to \tau^+\tau^-$ [279, 280] and by searches for the $A \to ZH$ decay using the $\ell^+\ell^- b\bar{b}$ final state [281]. Above the di-top threshold, the decay $H \to t\bar{t}$ very quickly dominates, and the new ATLAS search in the $\ell^+\ell^- t\bar{t}$ final state is the most sensitive one. In contrast to the $t_\beta = 1$ case, for $t_\beta = 1.5$ the new search is able to exclude a significant parameter region featuring a strong FOEWPT that was previously allowed. The new search substantially pushes the lower limit on the Higgs boson masses to larger values of about $m_H \gtrsim$ 400 GeV and $m_A = m_{H^\pm} \gtrsim$ 550 GeV. We also stress that, based on the expected cross section limits, an even larger mass region would be excluded, as indicated with the dashed red line. However, ATLAS observed a local 2.85σ excess for $m_A \approx$ 650 GeV and $m_H \approx$ 450 GeV, giving rise to a weaker observed cross section limit. The masses corresponding to the excess, indicated with a magenta star in the upper right
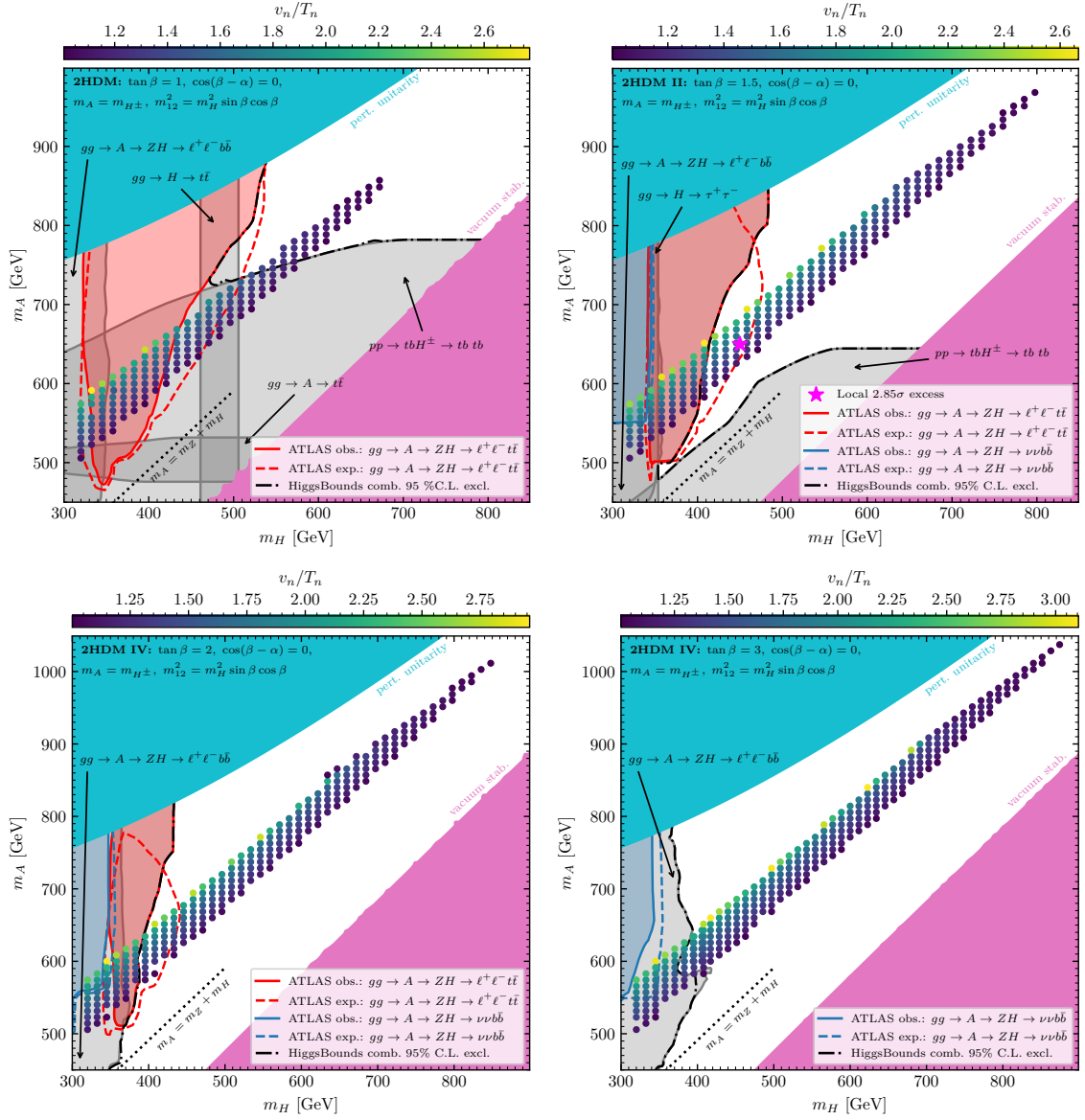
Figure 5.4

Impact of the new ATLAS searches for the $A \rightarrow ZH$ signature in the (m_H, m_A)-plane for $t_\beta = 1$ (upper left), $t_\beta = 1.5$ and Type II (upper right), $t_\beta = 2$ and Type IV (lower left), and $t_\beta = 3$ and Type IV (lower right). Parameter space regions excluded by vacuum stability or perturbative unitarity are indicated with pink and cyan colours, respectively. Regions excluded from previous LHC searches are indicated in gray, and regions excluded by the new $\ell^+\ell^- t\bar{t}$ and $\nu\nu b\bar{b}$ searches are indicated in red and blue, respectively, where the dashed lines indicate the corresponding expected exclusion limits. Parameter space regions featuring a FOEWPT with $v_n/T_n > 1$ are indicated with the scatter points, where the colour coding indicates the values of v_n/T_n. The mass values of the most significant excess ($2.85\,\sigma$ local significance) observed by ATLAS in the $\ell^+\ell^- t\bar{t}$ search are indicated with a magenta star in the upper right plot.

plot of Fig. 5.4, and the corresponding cross section are such that they fall into the strong FOEWPT region. This excess was however not confirmed by the later CMS search in the same parameter region [314].

As an important outcome of the above discussion, a promising complementary LHC search to target the strong FOEWPT region consists of charged scalar production followed by the decay $H^\pm \to W^\pm H \to \ell^\pm \nu t\bar{t}$, which so far has not been performed.[3] In particular, producing the charged scalar via $pp \to tbH^\pm$ would in this case lead to a 4-top-like (or 3-top-like, depending on the signal selection) signature, which has very recently been performed by CMS [317] and ATLAS [318] (but not interpreted in terms of the scenario discussed here), yielding a mild excess over the SM expectation.

Finally, it can be seen that for $t_\beta = 1.5$ the new smoking gun search using the $\nu\nu b\bar{b}$ final state starts to probe the considered parameter plane. An exclusion region is visible below the di-top threshold regarding m_H and for a minimum amount of mass splitting of $m_A - m_H \gtrsim 200$ GeV. However, in contrast to the searches using the $\ell^+\ell^- t\bar{t}$ final state indicated by the red shaded region, the blue shaded region indicating the new exclusion region resulting from the search using the $\nu\nu b\bar{b}$ final state is already excluded by previous LHC searches, namely searches for H decaying into tau-lepton pairs [279, 280] and searches for the smoking gun signature $A \to ZH$ with $Z \to \ell^+\ell^-$ and the decay of H into bottom-quark pairs [281]. One should note, however, that the new $A \to ZH$ search in the $\nu\nu b\bar{b}$ final state covers larger masses up to $m_H = 600$ GeV and $m_A = 1000$ GeV [311], extending the reach of previous ATLAS searches in $\ell^+\ell^- b\bar{b}$ and $\ell^+\ell^- W^+W^-$ final states [281] in the region with $m_H > 350$ GeV and $m_A > 800$ GeV. In the 2HDM constraints from perturbative unitarity (cyan area in Fig. 5.4) exclude large mass splittings between states from the same $SU(2)$ doublet. As a consequence, the extended mass reach of the new searches in the $\nu\nu b\bar{b}$ final state (not visible in the plot) does not give rise to new constraints on the 2HDM for $m_A > 800$ GeV. However, in other models allowing for larger mass splittings between the BSM states, the searches in the $\nu\nu b\bar{b}$ final state can potentially provide new constraints.

We show the results for $\boldsymbol{t_\beta = 2}$ **(Type IV)** in the lower left plot of Fig. 5.4. From here on, we focus our discussion on the Yukawa Type IV, in which the new ATLAS searches have the highest potential for probing parameter regions that were unconstrained so far. In particular, compared to Type I and III the decay width for $H \to b\bar{b}$ is enhanced in Type IV for $t_\beta > 1$, such that the searches in the $\nu\nu b\bar{b}$ final state become more important with increasing values of t_β. Moreover, in Type IV the decay width for $H \to \tau^+\tau^-$ is suppressed approximately by $1/t_\beta^2$, whereas it is enhanced by about a factor of t_β^2 in Type II. Hence, while in Type II the parameter region below the di-top threshold, i.e. $m_H < 2m_t$, is entirely excluded by the searches for di-tau resonances, in Type IV the $\nu\nu b\bar{b}$ search can potentially yield stronger constraints.

One can see in the lower left plot of Fig. 5.4 that in this case only three LHC searches give rise to excluded regions in the parameter plane. This is a manifestation of the fact that the so-called wedge-region of the 2HDM, with intermediate values of $2 \lesssim t_\beta \lesssim 8$, is difficult to probe at the LHC [319]. As an example, we note that the searches for the charged scalars via the signature $pp \to H^\pm tb \to tb\, tb$, suppressed by factors of about $1/t_\beta^2$ in the low-t_β regime, cannot probe the parameter plane in this case. Below the di-top threshold, we find that the $A \to ZH$ searches in the $\ell^+\ell^- b\bar{b}$ (gray) and the $\nu\nu b\bar{b}$ (blue)

---

[3]Searches targeting the $H^\pm \to W^\pm H$ decay have been performed by CMS assuming the decay $H \to \tau^+\tau^-$ and assuming a fixed mass of $m_H = 200$ GeV [316].

final states exclude the entire region allowed by the theoretical constraints. As discussed above, for $m_A < 800$ GeV searches for the decay $A \to ZH$ using the decay $Z \to \ell^+\ell^-$ have been performed by ATLAS [281], which are more powerful than the new searches using the $Z \to \nu\nu$ decay (the corresponding CMS search using the $Z \to \ell^+\ell^-$ decay covers masses up to $m_A = 1$ TeV, but is based on first-year Run 2 data only [320]). For $m_A > 800$ GeV ATLAS limits exist only from the new searches using the decay $Z \to \nu\nu$ (the resulting exclusion regions are not visible in our plots since in the 2HDM such large mass splittings are excluded by perturbative unitarity, indicated by the cyan area). Above the di-top threshold, the searches relying on the decay $H \to b\bar{b}$ quickly lose their sensitivity to the 2HDM parameter plane. Accordingly, for masses of H substantially larger than twice the top-quark mass the new smoking gun search for the decay $H \to t\bar{t}$ is in fact the only channel that can probe the parameter plane. As indicated with the red shaded area, the searches in the $\ell^+\ell^- t\bar{t}$ final state are able to exclude masses smaller than $m_H \approx 400$ GeV and $m_A \approx 750$ GeV for the lighter and the heavier BSM resonance, respectively. As it is also visible in the plots for $t_\beta = 1$, $t_\beta = 1.5$ and $t_\beta = 2$ of Fig. 5.4, the difference between the expected (red dashed line) and the observed (red solid line) exclusion region resulting from the searches using the $\ell^+\ell^- t\bar{t}$ final state arises from the excess observed in the ATLAS search (except for the upper right part of the red region in the plots for $t_\beta = 1.5$ and $t_\beta = 2$, where the observed limit is stronger than the expected one).

As a final step of the discussion of the low-t_β regime we consider a value of $\boldsymbol{t_\beta = 3}$, in **(Type IV)**. The results of our analysis are shown in the lower right plot of Fig. 5.4. Again, we focus on the Yukawa Type IV (see the discussion above).

One can see that in this case the smoking gun searches in the $\ell^+\ell^- t\bar{t}$ final state cannot probe the parameter space as a consequence of the suppression of the gluon-fusion production cross section of A. We will discuss in Sec. 5.2.2 the prospects for probing the benchmark plane for $t_\beta = 3$ in future runs of the LHC, in which roughly 20 times more integrated luminosity will be collected by both ATLAS and CMS.[4] At and below the di-top threshold $m_H \approx 2m_t$ the results are similar to the case of $t_\beta = 2$, where the smoking gun searches relying on the decay $H \to b\bar{b}$ essentially exclude the whole parameter region. One should note that in Type IV (and Type II) the partial widths for the decays $A, H \to t\bar{t}$ are suppressed approximately by $1/t_\beta^2$, and the partial width for the decay $H \to b\bar{b}$ is conversely enhanced by (approximately) t_β^2. As a result, the gray exclusion region from the searches in the $A \to ZH \to \ell^+\ell^- b\bar{b}$ channel extends to slightly larger masses for $t_\beta = 3$ compared to $t_\beta = 2$ (lower left plot).

5.2.1.2   High t_β-region

In the discussion above, we investigated the low-t_β regime where the CP-odd Higgs boson A can be produced with a sizeable cross section via gluon fusion. For $t_\beta \gtrsim 10$, this production mode is suppressed, and in Yukawa Types II and IV, A is instead produced more efficiently via $b\bar{b}$-associated production, which scales with t_β^2. Focusing now on this high-t_β regime, we consider the relevance of the new ATLAS searches for the $A \to ZH$ signature in this production mode. We focus on Type IV because the constraints from di-tau resonance searches are significantly weaker than in Type II (as discussed above).

---

[4]See Ref. [77] for an earlier projection based on expected cross section limits reported by CMS.

It should be noted that the new ATLAS searches reported in Ref. [311] only considered the $b\bar{b}$-associated production utilising the $\nu\nu b\bar{b}$ final state, whereas the smoking gun search utilising the $\ell^+\ell^- t\bar{t}$ final state was considered only assuming gluon-fusion production of the heavy BSM resonance. Thus, the only relevant searches for the $A \to ZH$ decay in the following discussion will be the previously reported searches utilising the $\ell^+\ell^- b\bar{b}$ final state [281,313] and the new searches utilising the $\nu\nu b\bar{b}$ final state [311].
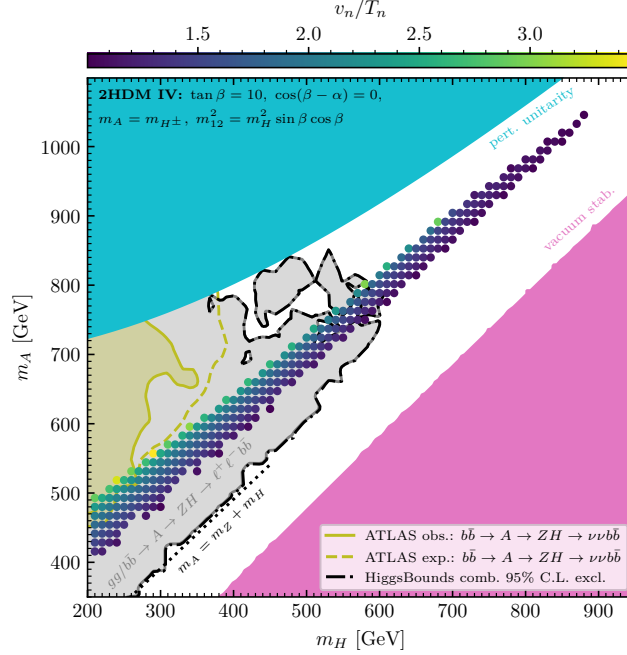
Figure 5.5

As in Fig. 5.4, but for $t_\beta = 10$ in Type IV. Parameter space regions excluded by the new $\nu\nu b\bar{b}$ searches in the $b\bar{b}$-associated production channel are indicated in yellow, while the yellow dashed line indicates the expected exclusion limit

In Fig. 5.5 we show our results for $t_\beta = 10$ as a representative benchmark scenario for the high-t_β regime. The colour coding of the exclusion regions and the scatter points is the same as in Fig. 5.4, except for the yellow dashed and solid lines indicating the expected and observed exclusion limits resulting from the recent ATLAS search for $b\bar{b} \to A \to ZH \to \nu\nu b\bar{b}$, respectively. One can see that the parameter space region excluded by this search (yellow shaded area) lies within the gray shaded area indicating the exclusion from the searches for $b\bar{b} \to A \to ZH \to \ell^+\ell^- b\bar{b}$ [281], which were published previously. Hence, although the new searches based on the decay of the Z boson into neutrinos are able to probe the 2HDM parameter space for values of $t_\beta \gtrsim 10$, these regions are already excluded by the searches making use of the decay of the Z boson into charged leptons. We stress, however, that the new searches using the $\nu\nu b\bar{b}$ final state cover a larger mass interval of up to 1.2 TeV for the heavy BSM resonance (not visible in the plot), whereas the corresponding upper limit in the ATLAS searches using the $\ell^+\ell^- b\bar{b}$ final state is about 800 GeV. Therefore, in other models in which larger mass splittings between the heavier and the lighter BSM

resonance are possible compared to the 2HDM (where perturbative unitarity implies an upper limit on such mass splittings, see the cyan region in Fig. 5.5), the new searches using the $\nu\nu b\bar{b}$ final state could potentially give rise to new constraints.

The two LHC searches relevant in Fig. 5.5 differ in the targeted decay mode of the Z boson, whose branching ratios are precisely measured. As a consequence, the relative importance of both searches is independent of the 2HDM parameters, especially of t_β. We can therefore extrapolate based on the results for $t_\beta = 10$ shown in Fig. 5.5 that also for larger values of t_β the searches making use of the $Z \to \ell^+\ell^-$ decay mode are more promising to probe the considered benchmark plane compared to the searches using the $Z \to \nu\nu$ decay mode. It should also be taken into account that for larger values of t_β other LHC searches become relevant in Type IV.[5] In particular, searches for new resonances produced in $b\bar{b}$-associated production with subsequent decay into bottom-quark pairs [322], giving rise to four b-jet final states, start to exclude sizeable parts of the benchmark plane for $t_\beta \gtrsim 15$. Moreover, for such values of t_β searches for new resonances produced in association with a photon and decaying into two jets [323] are able to exclude parameter regions especially in the mass-degenerate regime.

5.2.2 Future prospects for $\ell^+\ell^- t\bar{t}$ searches

In Sec. 5.2.1.1 we have demonstrated that the new ATLAS smoking gun searches targeting the $\ell^+\ell^- t\bar{t}$ final state exclude sizeable parts of previously allowed parameter space of the 2HDM assuming values of t_β not much larger than one. In particular, we have shown that for BSM scalar masses above the di-top threshold and values of $1.5 \lesssim t_\beta \lesssim 3$ the smoking gun searches arguably are the most promising of all LHC searches for probing so far unexplored parameter space regions, with the potential to discover additional Higgs bosons that are consistent with a 2HDM interpretation. Due to their exceptional importance, we briefly discuss here the projected sensitivity of the searches for the $A \to ZH$ decay in the $\ell^+\ell^- t\bar{t}$ final state during future runs of the LHC and HL-LHC. As input for our projections we use the expected limits from the ATLAS analysis for an integrated luminosity of 140 fb^{-1}. This improves upon the previous projections presented in Ref. [77] that were obtained based on an estimate of the expected sensitivities from the CMS collaboration.

The projected exclusion limits discussed in the following were obtained by re-scaling the expected cross section limits reported in Ref. [311] with future values for the integrated luminosity that will be collected during future runs of the (HL-)LHC, i.e.

$$\sigma_{\text{proj.}}^{\text{exp. 95\% CL}}(\mathcal{L}, m_H, m_A) = \sigma_{\text{Run 2}}^{\text{exp. 95\% CL}}(m_H, m_A) \sqrt{\frac{140 \text{ fb}^{-1}}{\mathcal{L}}} \ . \tag{5.5}$$

Here, $\sigma_{\text{Run 2}}^{\text{exp. 95\% CL}}$ is the expected cross section limit at 95% confidence level reported by ATLAS based on 140 fb^{-1} collected during Run 2 as a function of the masses of the probed BSM resonances, and $\sigma_{\text{proj.}}^{\text{exp. 95\% CL}}$ is the future projection of the expected cross section limits depending additionally on the assumed integrated luminosity $\mathcal{L}$. Accordingly, in the projections we only account for the reduction of statistical uncertainties, whereas no assumption is made on possible improvements of systematic theoretical or experimental

---

[5]In Type II, for $t_\beta \gtrsim 10$ the whole investigated parameter plane is excluded for masses up to about 1 TeV by searches for scalar resonances decaying into tau-lepton pairs [279, 280, 321].

uncertainties. Moreover, we do not account for the slight increase of the center-of-mass energy at future runs of the LHC and the HL-LHC, operating at 13.6 TeV and 14 TeV, respectively, compared to the Run 2 dataset collected at 13 TeV. Taking this into account, we consider our projections as fairly conservative estimates.
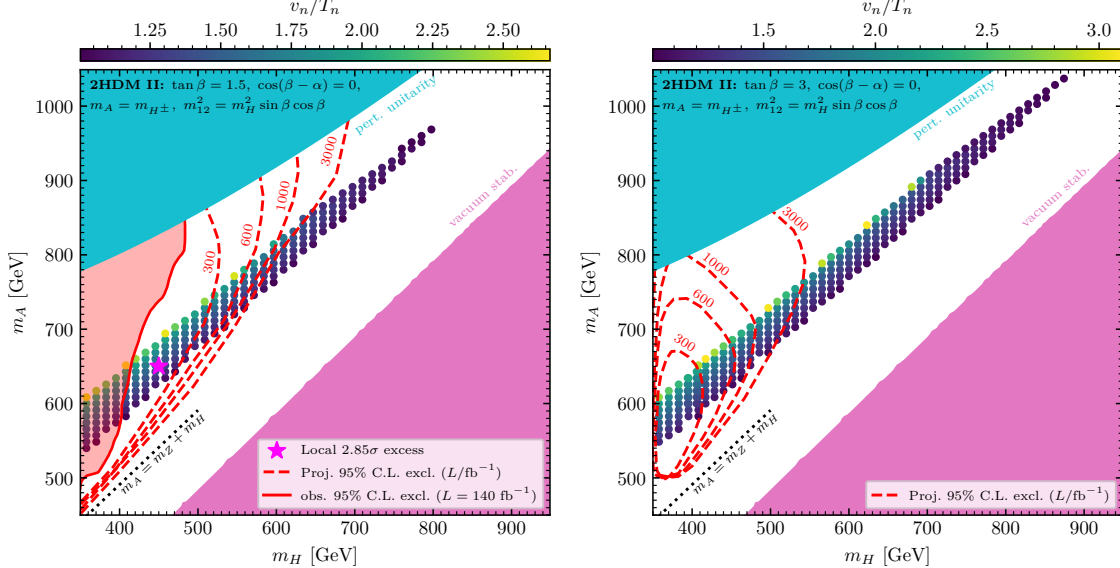
Figure 5.6
As in Fig. 5.4 for $t_\beta = 1.5$ (left) and $t_\beta = 3$ (right), shown here for Type II, but the red dashed lines indicate projected expected exclusion regions assuming integrated luminosities of $300, 600, 1000, 3000$ fb^{-1} from future runs of the LHC.

The projected expected cross section limits can be cast into projected exclusion regions in the 2HDM. In Fig. 5.6 we show our projections in the same 2HDM benchmark plane discussed so far for the Yukawa Type II with $t_\beta = 1.5$ in the left plot and $t_\beta = 3$ in the right plot.

In both plots, the colour coding of the scatter points and the definition of the pink and cyan regions is as in Fig. 5.4, and the red dashed lines indicate the expected exclusion regions for different values of the integrated luminosity, ranging from $\mathcal{L} = 300$ fb^{-1} (end of LHC Run 3) to $\mathcal{L} = 3000$ fb^{-1} (end of the LHC high-luminosity phase). Moreover, in the left plot the red shaded area indicates the currently excluded region based on the observed cross section limits obtained for $\mathcal{L} = 140$ fb^{-1}, and the magenta star indicates the masses for which ATLAS has observed the most pronounced local excess. As already discussed in Sec. 5.2.1.1, currently the smoking gun searches are not able to probe the benchmark plane for $t_\beta = 3$ (see the lower left plot of Fig. 5.4). Accordingly, no red shaded region is visible in the right plot of Fig. 5.6.

One can observe in the left plot of Fig. 5.6 that with the prospective improvements of the integrated luminosity it will be possible to increase very significantly the regions that can be probed in the considered benchmark plane for $t_\beta = 1.5$. While currently in the upper right part of the red shaded region the smoking gun searches are able to exclude masses up to values slightly below 500 GeV for the lighter and up to 850 GeV for the heavier BSM scalar,

in the future the LHC will be able to probe via this search masses up to about 700 GeV and 1 TeV for the lighter and the heavier BSM scalar, respectively. This improvement in sensitivity has a very important impact on the parameter region that is suitable for the realisation of a strong FOEWPT according to the thermal effective potential approach. In the case of the absence of a signal the exclusion within the region that is indicative for a strong FOEWPT would extend up to $m_H \lesssim 550$ GeV and $m_A \lesssim 700$ GeV. It should be noted in this context that the strength of the phase transition diminishes with increasing masses of the BSM scalars. As one can infer from the colour coding of the displayed points, the projected exclusion regions cover the parameter region for which the strongest phase transitions can be accommodated. As a result, and since in the 2HDM the generation of a sufficiently large BAU may be possible only for small values of t_β not much larger than one [40], the searches for the smoking gun signature will provide a stringent test of the possibility to explain the BAU by means of EW baryogenesis in the 2HDM.

In this context it is also important to note that in the 2HDM the primordial GW background generated during the phase transition is only potentially detectable with LISA for the largest possible values of v_n/T_n, which are only reached in a very restricted region of the 2HDM parameter space and have a very strong dependence on the details of the scalar spectrum [77]. We have verified using the approach that will be detailed in Sec. 5.3 that for the considered values of t_β all parameter points predicting a GW signal that is potentially detectable with LISA would be probed by the projected exclusion limits from the HL-LHC. Hence, in the 2HDM the HL-LHC results will have an enormous impact on the possibility for a detection of a GW background with LISA consistent with a FOEWPT. This exemplifies that the HL-LHC has the potential to probe large parts of the relevant parameter space before the LISA experiment will have started its operation. Here it should be noted, however, that the presence of a strong FOEWPT, without demanding a realisation of EW baryogenesis, is also possible for larger values of t_β, where the $gg \to A \to ZH \to \ell^+\ell^- t\bar{t}$ searches lose their sensitivity. A GW signal potentially detectable with LISA therefore cannot be fully probed with the searches in the $\ell^+\ell^- t\bar{t}$ final state.

Besides the analysis of the potential of future runs of the (HL-)LHC for probing the 2HDM parameter space in terms of projected exclusion limits, it is also of interest to investigate the possible interplay between the LHC and LISA for the case where a smoking gun signal would be detected. The detection of the smoking gun signal would allow for the determination of m_H and m_A, and possibly also of $m_{H^\pm}$ via the corresponding cross sections in combination with the application of other constraints. The experimentally determined values of the BSM scalar masses could then be used in dedicated analyses of the phase transition dynamics. For instance, the experimental information about the mass hierarchy of the scalar spectrum would allow an analysis of the thermal potential in an appropriately chosen dimensionally-reduced effective-field theory, in which the heavier scalars have been integrated out in a systematic way in order to facilitate the incorporation of relevant higher-order effects, as well as dedicated lattice simulations (see Refs. [324, 325] for recent efforts towards these directions in the 2HDM, and Refs. [292, 293, 326–328] for related investigations in other extended scalar sectors).

In the right plot of Fig. 5.6, in which we show the projections for $t_\beta = 3$, one can see that with more integrated luminosity the (HL)-LHC also in this case is able to probe substantial parts of the otherwise unconstrained parameter space regions. Interestingly, the red dashed lines indicating the expected reach of the LHC stretch out to the largest values

of m_H within the parameter regions which might be suitable for a realisation of a strong FOEWPT. Assuming an integrated luminosity of 3000 fb^{-1} collected by both ATLAS and CMS by the end of the LHC high-luminosity phase, masses of up to $m_H \approx 550$ GeV and $m_A \approx 800$ GeV can be probed. Here it should be taken into account that the parameter space region with m_H below the di-top threshold is already excluded by di-tau searches (only for Type II) and by searches for $gg \to A \to ZH \to \ell^+\ell^- b\bar{b}$ (both for Type II and Type IV), as was discussed in detail in Sec. 5.2.1.1 (see the lower right plot of Fig. 5.4). However, the sensitivity of these searches to the parameter space regions above the di-top threshold will not improve significantly with increasing data, because the branching ratio for the decay $H \to b\bar{b}$ is strongly suppressed for $m_H > 2m_t$.

Figure 5.7 provides a summary of the various searches discussed in this section, highlighting their sensitivity across different regions of the 2HDM parameter space. The x-axis represents t_β and the y-axis the mass of the heavy scalar states. As before, we divide the discussion into the low- and high-t_β regimes. Notably the low-t_β region is favourable for electroweak baryogenesis in the presence of CP-violating sources.

The most promising searches in each regime are marked with a red exclamation mark, and their regions of sensitivity are roughly indicated by their location in the $t_\beta - m_{H/A}$ coordinates. The new ATLAS searches discussed in this section are represented with the same color scheme used in previous figures. The $gg \to A \to ZH \to \ell^+\ell^- t\bar{t}$ search (shown in red) is particularly important in the low-t_β regime and above the di-top threshold: it covers large unconstrained region for $t_\beta = 1$, it is the only one to probe the SFOEWPT favoured region for $t_\beta = 1.5$ and the only one to probe the allowed parameter region for $t_\beta > 2$, with even better prospects for the future, when a higher luminosity will be available.

The $gg/b\bar{b} \to A \to ZH \to \nu\nu b\bar{b}$ searches (indicated in blue/yellow) are generally less sensitive in their respective regimes than the ones in the $\ell^+\ell^- b\bar{b}$ decay channel, which are quite sensitive specially below the $t\bar{t}$ threshold. However, the $\nu\nu b\bar{b}$ final state can access regions with large mass splittings, which, while excluded in 2HDM by perturbative unitarity, may remain viable in other BSM scenarios.

At $t_\beta = 1$, the $tbH^\pm \to tb, tb$ search already excludes a large portion of the SFOEWPT-favoured region, although its sensitivity decreases rapidly with increasing t_β. We propose a new search channel which so far has not been performed: $H^\pm \to W^\pm H \to \ell^\pm \nu t\bar{t}$. It becomes accessible for sizeable $m_H - m_{H^\pm}$ mass splittings and complements the reach of the smoking gun. We also show the sensitivity of the $H/A \to \tau^+\tau^-$ searches, which are particularly relevant in Type II at both low- and very high-t_β.

5.2.3   Deviations in the Triple Higgs Self-Coupling

A deviation in the trilinear Higgs self-coupling from the SM prediction offers a complementary collider probe of a SFOEWPT (see discussion in Sec. 2.6.3) and directly affects Higgs pair production. In this section, we quantify the impact of a SFOEWPT on di-Higgs production, highlighting the necessity of including loop-corrected trilinear couplings in both predictions. Since loop effects are essential for capturing the dynamics of the electroweak phase transition, we consistently include one-loop corrections to the Higgs trilinear interactions also in the calculation of the pair production cross section. Fig. 5.8 illustrates the correlation between the strength of the phase transition and the magnitude of loop corrections in the 2HDM. To produce it, we perform a general scan over the viable param-

Low t_β region   High t_β region

m_H, m_A

future

$gg \to A \to ZH \to \ell^+\ell^- t\bar{t}$ (!)$\longrightarrow$ $H/A \to \tau^+\tau^-$ **(in Type II)** (!)

$H^\pm \to W^\pm H \to \ell^\pm \nu t\bar{t}$ (!)

$tbH^\pm \to tb\,tb$ (!)

$2m_t$ $H \to t\bar{t}$ $gg \to A \to ZH \to \ell^+\ell^- b\bar{b}$ (!)

$gg \to A \to ZH \to \ell^+\ell^- b\bar{b}$ (!) $b\bar{b} \to A \to ZH \to \ell^+\ell^- b\bar{b}$ (!)

$gg \to A \to ZH \to \nu\bar{\nu}b\bar{b}$ $b\bar{b} \to A \to ZH \to \nu\bar{\nu}b\bar{b}$

(reaches larger mass splittings)   (reaches larger mass splittings)

$H/A \to \tau^+\tau^-$ **(in Type II)** (!)

0

1 1.5 2   3   *wedge region*   10

t_β

Favored for EW baryogenesis
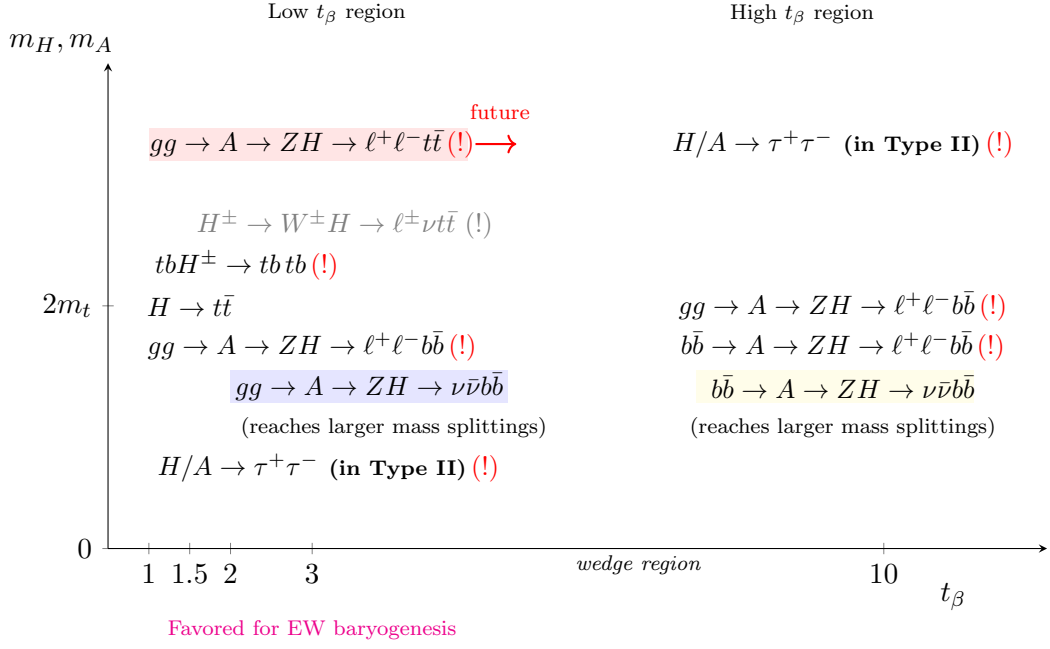
Figure 5.7
Summary of the most sensitive experimental searches in the EWPT favoured region depending on the t_β (x-axis) and the mass of the scalar particles (y-axis). Exclamation marks indicate the most sensitive searches in the corresponding region. The future arrow indicates that this search will be sensitive to higher values of t_β at future higher luminosity LHC runs. The searches implemented in this work are marked with red, blue and yellow, depending on the production and decay modes.

eter space of the 2HDM Type II, selecting only points with a strong first-order transition ($\xi_n > 1$). The x-axis, shows the hh-production cross section with loop-corrected trilinear Higgs couplings[6], while the y-axis shows the relative size of the loop corrections to the Higgs trilinear coupling in the leading order cross section, defined as

$$\Delta\sigma_{\lambda_{ijk}^{(1)}} \equiv 100 \cdot (\sigma_{\lambda_{ijk}^{(1)}} - \sigma_{\lambda_{ijk}^{(0)}})/\sigma_{\lambda_{ijk}^{(0)}}. \tag{5.6}$$

where $\sigma_{\lambda_{ijk}^{(1)}}$ is the cross section with the THC at tree level and $\sigma_{\lambda_{ijk}^{(0)}}$ includes one-loop corrections to the THC. We find loop-induced corrections ranging from –60% to +80%. The parameter points featuring positive corrections can have an enhancement of the total cross section value w.r.t. the SM up to a factor of 20. These large enhancements are driven by a resonant contribution with a mass located very close the on-shell top production threshold, which significantly enhances the cross section (see Sec. 3.1). In Fig. 5.8 we also show the SM value with a red star, which does not feature a SFOEWPT. The maximum values of the strength that we find are around 3. The general trend is to find the largest values at the negative corrections, which drive the cross section to be roughly a factor of 2 smaller

---

[6]We have computed the cross section at LO in QCD with `anyHH` and applied a K-factor of 2 to roughly account for higher order QCD corrections.
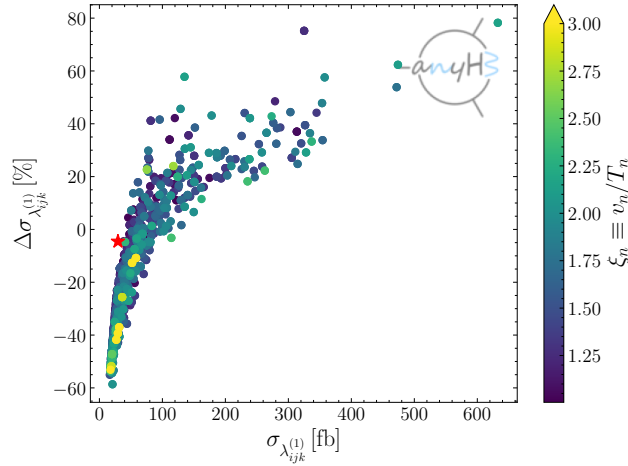
Figure 5.8

Impact of the loop corrections to the trilinear couplings in the Higgs pair production cross section and strength of the electroweak phase transition. The relative size of the loop correction to the trilinear Higgs couplings is defined as $\Delta\sigma_{\lambda^{(1)}_{ijk}}$ (see text). The red star shows the cross section with loop corrections to the trilinear Higgs couplings (including momentum dependence) in the SM.

than in the SM, leading to cross sections around 15 fb. These corrections are mainly driven by non-resonant production. We observe that in general, stronger transitions are correlated with larger κ_λ values, but this does not necessarily imply a smaller cross section, as resonant production can still lead to an enhancement in these scenarios.

These effects can be observed in Fig. 5.9, where we show $\kappa_\lambda^{(1)}$ (left) and the resonant scalar mass m_H (right) for the same benchmark points as in Fig. 5.8. For scenarios with negative corrections, a heavy resonance with $m_H > 500$ GeV suppresses the resonant contributions. Near the di-top threshold at 350 GeV, however, resonant enhancement becomes significant, enabling strong transitions even with positive corrections.

We confirm that a SFOEWPT in the 2HDM typically requires $\kappa_\lambda \in [1.3, 2.2]$, in agreement with Ref. [77]. Smaller values of κ_λ are generally correlated with a smaller energy barrier and lead to second order transitions or crossovers, while for larger values of κ_λ the barrier can be enhanced so much that the vacuum is trapped in the false minimum, leading to the phenomenon of vacuum trapping. These bounds are reflected in limits of the colour-coded points of the left plot in Fig. 5.9. Furthermore, we observe that the cross sections are minimised around $\kappa_\lambda \approx 2.5$, where destructive interference between the triangle and box form factors becomes maximal.

Our results indicate a tension between the values of κ_λ compatible with a SFOEWPT in the 2HDM and the sensitivity in non-resonant Higgs pair production that will be within the reach of the HL-LHC. Specifically, the largest trilinear couplings compatible with a SFOEWPT tend to lie precisely in regions where destructive interference in the di-Higgs production cross section suppresses its total magnitude. While some parameter points yield cross sections above this minimum, they often correspond to vacuum-trapped configurations, rendering them unphysical. This coincidence highlights a limitation in pp-collider sensitivity
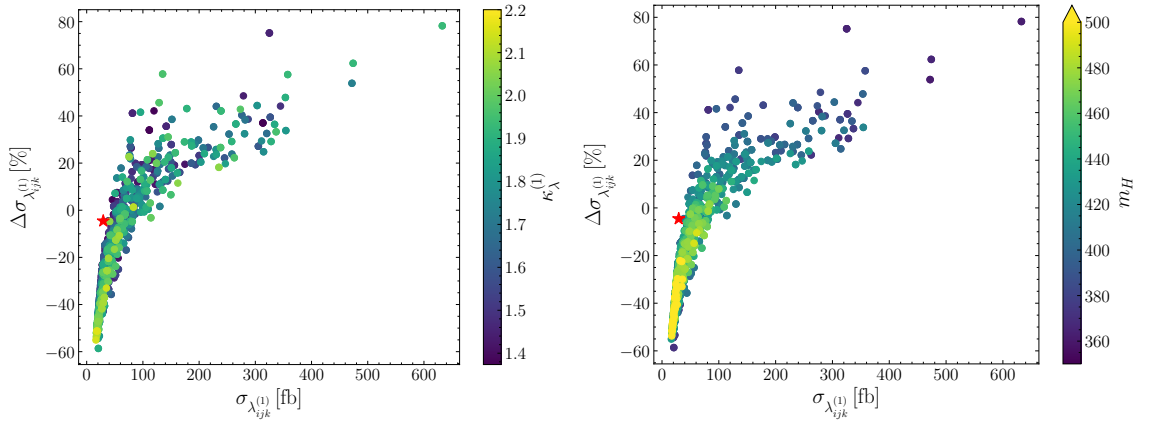
Left: values of the one-loop-corrected trilinear coupling $\kappa_\lambda^{(1)}$ for the parameter points depicted in Fig. 5.8. Right: value of the resonant scalar mass for the same parameter points.

via hh-production precisely in the parameter space most relevant for baryogenesis. In particular, if a value of $\kappa_\lambda \sim 1$ is realised, the expected sensitivity at the HL-LHC is around 30%, while if the true value of κ_λ is close to 2.5, which is favoured by the realisation of a SFOEWPT in the 2HDM, the sensitivity to κ_λ diminishes up to 60% at the HL-LHC [145]. An opposite situation happens at e^+e^- linear colliders such as the ILC (for a detailed analysis of the sensitivity to trilinear scalar couplings in future high-energy e^+e^- colliders see Ref. [329]), where for $\kappa_\lambda \sim 2$ the sensitivity is increased w.r.t. the SM value [330]. The total cross section can still be large due to large resonant production, in such case we expect resonant di-Higgs searches to capture such deviations. Overall, this result emphasises the need for complementary probes to fully access the physics of the electroweak phase transition. With this spirit in mind, we address the cosmological probes in the following section.

5.3 Cosmological probes

A cosmological first order phase transition gives rise to a stochastic gravitational wave signal [331, 332]. Since the EW phase transition would have happened at temperatures comparable to the EW scale, the GW signal spectrum would be largest around milli-Hz frequencies, thus in the best-sensitivity range of the planned LISA space-based GW interferometer [110, 333].

The GWs in a FOEWPT are sourced by the collision of bubbles and the surrounding plasma motions in the form of sound waves [334–337], as well as the turbulence generated after the collisions [338–342] (see Ref. [343] for a review). In the case of the 2HDM, the GW contribution from bubble collisions themselves can be neglected, and the GW power spectrum may be modelled with the sound waves as dominant source [210].

There are four phase transition parameters that characterise the corresponding GW signal [343]:

(i) the temperature T_* at which the phase transition occurs, which we identify here with the nucleation temperature T_n.[7] *(ii)* the phase transition strength α, defined as the difference of the trace of the energy-momentum tensor between the two vacua involved in the transition, normalised to the radiation background energy density. *(iii)* the inverse duration of the phase transition in Hubble units, β/H. *(iv)* the bubble wall velocity in the rest frame of the fluid (and far from the bubble), v_{w}.

To compute α we follow Refs. [110, 343],

$$\alpha = \frac{1}{\rho_R} \left(\Delta V(T_*) - \left(\frac{T}{4} \frac{\partial \Delta V(T)}{\partial T} \right) \bigg|_{T_*} \right), \tag{5.7}$$

where $\Delta V(T_*)$ is the potential difference between the two vacua evaluated at the temperature of the phase transition, and ρ_R is the radiation energy density of the Universe. The inverse duration of the phase transition β/H can be generally calculated as

$$\frac{\beta}{H} = T_* \left(\frac{d}{dT} \frac{S_3(T)}{T} \right) \bigg|_{T_*}, \tag{5.8}$$

where $S_3(T)$ is (as in Eq. Eq. (5.4)) the temperature-dependent (3-dimensional) Euclidean bounce action. Finally, based on recent results indicating that phase transition bubbles preferentially expand with either $v_{\mathrm{w}} \approx c_s$ (c_s being the speed of sound of the plasma)[8] or $v_{\mathrm{w}} \to 1$ [345, 346] (see also Ref. [347] for a further discussion of bubble wall velocity estimates in BSM theories) we choose to fix $v_{\mathrm{w}} = 0.6$ as a representative case.

Based on the four quantities introduced above, the primordial stochastic GW background produced during a cosmological phase transition can be computed using numerical power-law fits to results of GW production obtained in hydrodynamical simulations of the thermal plasma. In our numerical analysis, we include the contributions to the GW power spectrum from sound waves $h^2 \Omega_{\mathrm{sw}}$ and turbulence $h^2 \Omega_{\mathrm{turb}}$, where sound waves are the dominant GW source for the FOEWPTs considered here. The specific formulas used in our analysis for the computation of the GW spectral shapes, their amplitudes and the peak frequencies can be found in Ref. [77], which closely follows Refs. [342, 343].

Whether a stochastic GW signal is detectable at a GW observatory depends on the signal-to-noise ratio (SNR), which can be computed for a specific parameter point and a specific GW experiment as

$$\mathrm{SNR} = \sqrt{\mathcal{T} \int_{-\infty}^{+\infty} df \left[\frac{h^2 \Omega_{\mathrm{GW}}(f)}{h^2 \Omega_{\mathrm{Sens}}(f)} \right]^2}, \tag{5.9}$$

where $\mathcal{T}$ is the duration of the experiment, $h^2 \Omega_{\mathrm{Sens}}$ is the nominal sensitivity of the detector, computed according to the mission requirements [348], and $h^2 \Omega_{\mathrm{GW}} = h^2 \Omega_{\mathrm{sw}} + h^2 \Omega_{\mathrm{turb}}$ is the spectral shape of the GW signal. For the present analysis, we focus on the GW detectability with LISA, for which we will assume an operation time of $\mathcal{T} = 7$ years, and consider a GW signal to be detectable if $\mathrm{SNR} > 1$ (more stringent SNR detection criteria could also be considered [343]).

---

[7]We could instead consider T_* to be the percolation temperature [344], at which the phase transition completes from the percolation of bubbles, yet the numerical difference compared to T_n is very small.

[8]For a relativistic perfect fluid, $c_s = 1/\sqrt{3} \simeq 0.577$.

5.3.1 Gravitational waves in the 2HDM

To further illustrate the impact of the experimental mass resolution of BSM scalar searches at the LHC on the predicted GW signals, we show in Fig. 5.10 the spectral shape of the GW backgrounds produced during a FOEWPT for several parameter points with masses of the heavy scalars specified in Tab. 5.1 together with the parameters that characterise the phase transition. The remaining 2HDM parameters are kept fixed according to the previous discussion. We chose the point with the largest SNR found in the vicinity of the ATLAS excess marked with the pink star in Fig. 5.4 for $t_\beta = 1.5$. We take it as an example for analysis of a possible hint for a BSM particle in the smoking gun search, even though this particular point is disfavoured by the later CMS searches in this channel, as mentioned above. We allow for up to 10% deviations in the values of the masses m_H, m_A, which translates into deviations of the SNR of several orders of magnitude. In addition, we show in Tab. 5.1 the parameters for the point $(m_H, m_A) = (450, 650)$ GeV, although we omit its GW spectrum in Fig. 5.10 because of the smallness of the SNR. The spectral shapes of the GW backgrounds are computed as discussed above, where the solid curves depict the sound-wave contribution $h^2 \Omega_{\rm sw}$ only, whereas the dashed curves depict the sum of sound-wave and turbulence contributions, i.e. $h^2 \Omega_{\rm sw} + h^2 \Omega_{\rm turb}$.
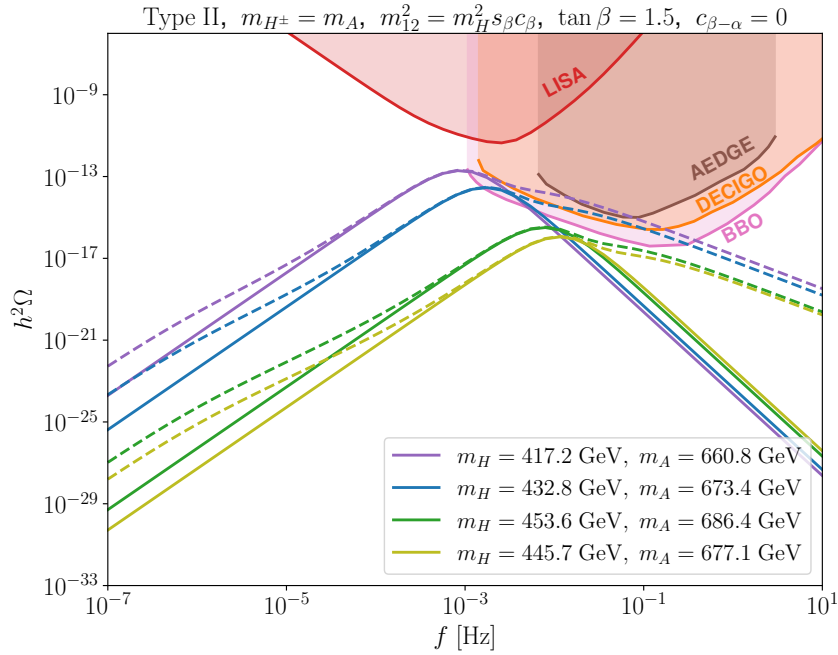

Figure 5.10

Gravitational wave spectra for parameter points specified in Tab. 5.1 that are compatible with the excess observed in the ATLAS search. The solid (dashed) lines show the prediction without (including) the turbulence contribution, using $v_{\rm w} = 0.6$. The coloured regions show the prospective sensitivities of future experiments.

m_H	m_A	$m_A - m_H$	T_n	v_n/T_n	α	β/H	SNR
417.2	660.8	243.6	79.44	3.10	0.0308	77	13.7
432.8	673.4	240.6	86.23	2.85	0.0206	134	3.8
453.6	686.4	232.8	110.89	2.19	0.0073	468	0.022
445.7	677.1	231.4	116.48	2.06	0.0062	674	0.004
450.0	650.0	200.0	145.08	1.42	0.0029	5399	< 0.001

Table 5.1: Results for parameters characterising the phase transition for example points of the 2HDM that are compatible with the excess observed in the ATLAS search. The corresponding GW spectra are shown in Fig. 5.10. Dimensionful parameters are given in GeV. The SNR values evaluated for LISA include the turbulence contribution.

We also show the sensitivity curves of LISA [110], AEDGE [349], DECIGO [350, 351] and BBO [352], where the latter three are planned, but not yet approved space-based GW detectors. One can see that only for the smallest value of $m_H = 417.2$ GeV, i.e. the largest mass splitting between H and A, the GW signal might be detectable with LISA, according to the predicted SNR. For values of m_H only a few percent larger, the peak amplitudes of the GW signals drastically decrease and quickly drop to values far below the experimental sensitivity of the proposed GW detectors. We emphasise again at this point that the detectability of the GW signal for a single parameter point cannot be determined definitively with the methods applied here due to the substantial theoretical uncertainties in the prediction of the GW signals [291]. However, the fact that in the case of a possible detection of BSM scalars at the LHC a mass resolution at the percent level would be required in order to draw conclusions about the detectability of a GW signal poses a challenge independently of the status of the remaining theoretical uncertainties at that time.

Of course, one can also turn this argument around. An LHC discovery, e.g. a signal in the smoking gun signature, in combination with a GW detection at LISA that is consistent with a SFOEWPT as interpreted in a UV-complete model, could be used for a more precise (but model-dependent) determination of the parameters of the considered BSM Higgs sector. In this way space-based GW astronomy could become a complementary tool to sharpen the precision of particle physics.[9]

To further illustrate the large spread in SNR over the particular BSM model parameters, we study the thermal histories away from the alignment limit. In Fig. 5.11 we show three benchmark points in the 2HDM Type I that feature a strong phase transition in the alignment limit. We select three points with masses very close to each other: $m_H = 404.7$ GeV, $m_H = 405.7$ GeV and $m_H = 406.7$ GeV. We evaluate the strength of the transition away from the alignment limit and therefore we show the variable $c_{\beta-\alpha}$ in the x-axis. In the the y-axis we show the temperatures on the left and the SNR on the right. The shaded regions represent the exclusions from experimental constraints, in particular the pale purple region is disfavoured by `HiggsSignals` constraints, the pale orange area is disfavoured by `HiggsBounds`, and the pale red region by both.

The types of the lines indicate the scenario, dashed for $m_H = 406.7$ GeV, solid for $m_H = 405.7$ GeV and dotted for $m_H = 406.7$ GeV. The red lines show the nucleation

---

[9]This would be similar in spirit to the present situation regarding the sum of neutrino masses, constrained most stringently using astrophysical observations, e.g. the measurement of the spectrum of the cosmic microwave background [353].

temperature and the orange-black show the critical temperature, the transition from orange to black represents the moment at which the minimum becomes trapped, i.e. there is no corresponding nucleation temperature for the given critical temperature. Additionally, the SNR of each benchmark scenario is shown with blue lines and its magnitude is represented in the right-y-axis. On the right plot of Fig. 5.11 we zoom in the relevant region of the left plot.
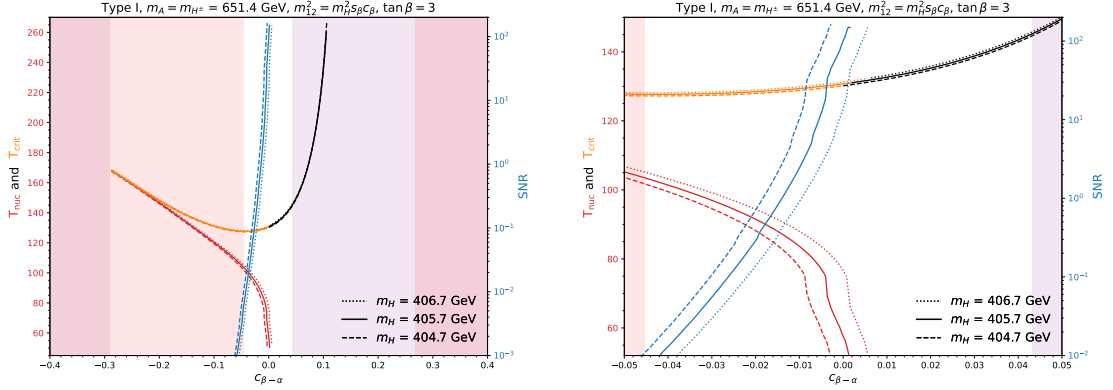
Figure 5.11

Analysis of the benchmark points away from the alignment limit in the 2HDM Type II. Each benchmark point is indicated with a different line style. The critical and nucleation temperatures are indicated with orange-black and red lines, respectively, in the left vertical axis (the critical temperature becomes black if the point with that scalar mass is vacuum trapped). The SNR is indicated in blue in the right vertical axis. The pale purple area is disallowed by `HiggsSignals`, the pale orange area is disallowed by `HiggsBounds` and the pale red is disallowed by both. On the right we zoom into the relevant region of the left plot.

In the 2HDM, we find that the strength of the electroweak phase transition increases near the alignment limit, especially for lighter m_H, with the strongest transitions occurring for values with very small and positive $c_{\beta-\alpha}$ alignment, prior to the onset of vacuum trapping. This is correlated with the stronger GW signal, reaching values of the SNR up to 100. Intuitively, this trend can be understood by analogy with the SM, where a light Higgs mass ($\lesssim 80$ GeV) allows for a thermally induced first-order transition via gauge boson loops, while the physical Higgs mass of 125 GeV suppresses the barrier due to the dominance of the quartic term. In contrast, the 2HDM introduces additional scalar fields that enhance the thermal cubic terms and deepen the barrier with a smaller impact on the quartic term. However, deviations from alignment cause the EW vev direction to be shared between h and H, weakening the transition similarly to how a heavier scalar does in the SM. Thus, the alignment limit in the 2HDM plays a double role: it ensures SM-like phenomenology for h, bringing it closer to the experimental data gathered at colliders, while also supporting a stronger first-order phase transition in the early Universe.

Chapter 6

Conclusions

In this thesis, we have explored complementary approaches to probing the shape of the scalar potential realised in nature. At zero temperature, we focus on collider observables, particularly Higgs pair production, which provide a unique window into the structure of the potential via its sensitivity to the trilinear Higgs self-couplings. At finite temperature, we have studied the implications of a strong first-order electroweak phase transition in the early universe, revealing insights into the dynamics of electroweak symmetry breaking and its potential cosmological consequences. We now return to the central questions posed in the introduction and address them in light of our findings.

Q1: *What are the phenomenological signatures of extra scalar particles in Higgs pair production at the HL-LHC?*

We have reviewed the effects of the leading order gluon fusion Higgs-boson pair production in BSM theories with additional scalar particles in Sec. 3.1. We concluded that the combination of the sizeable trilinear scalar self-interactions and resonant masses within 250-800 GeV can give rise to a wide range of phenomenological implications in both the total production cross section and the invariant mass distribution. The presence of both these effects in concrete UV-complete BSM models cannot be isolated from each other. As a result, the interference patterns between resonant and non-resonant Higgs pair production are widely different from the SM and can be substantially enhanced.

We have explored the possibility of realising such a scenario in the context of the 2HDM. In the first place, we have performed a general analysis of the effects in h-pair production in the allowed region of the 2HDM parameter space (Sec. 3.2), where we took into account the sizeable radiative corrections to the trilinear scalar-couplings. We included these corrections for the first time in the analysis of hh-production, showing that the impact on the phenomenology is dramatic. Even considering the experimental uncertainties that a future measurement would entail, such as smearing and binning (Sec. 3.3), we concluded that the impact on the measurable invariant mass of the hh-system can significantly alter the interpretations that can be derived from experimental data gathered with simplified assumptions.

In Sec. 3.4 we have seen that the increasing experimental sensitivity in hh-searches affects both non-resonant and resonant production modes. The former already puts constraints on the otherwise allowed region of the parameter space of BSM models, once the loop

corrections to the trilinear couplings are taken into account. The latter shows remarkable sensitivity in a vast region of parameter space which was unexplored by previous searches.

In Sec. 3.5 we outline the major consequences of the loop corrections to the trilinear couplings in the experimental resonant and non-resonant searches. We found that non-resonant searches can probe regions of otherwise unconstrained parameter space in the 2HDM. We have also shown that the contribution of the heavy states targeted in the resonant searches will inevitably enhance the loop corrections to the trilinear couplings in scenarios with mass splitting between the BSM states. In such scenarios, the signal model used by the experimental collaborations so far to target the resonance does not reproduce the predictions of a complete BSM theory.

Despite the fact that our results are illustrated for the 2HDM, they are quite general for BSM scenarios with extra scalars and mass-splitting effects. Therefore, an extension of the public tool `anyH3` is provided, which generalises the calculation of the one-loop effective trilinear scalar coupling to arbitrary renormalisable theories with extended scalar sectors. These results can be used in the prediction for the leading-order hh-production cross section in these models. We developed a full on-shell renormalisation scheme for such couplings and tested the robustness of the new version of the tool, which is implemented into the `anyHH` package.

A major conclusion of this section is that in view of the increasing experimental improvements in Higgs pair searches, loop corrections to THC need to be included in theory calculations in the BSM frameworks. Additionally, experimental analyses should be modified to take into account all resonant and non-resonant contributions as well as their interference terms simultaneously. Well-motivated BSM scenarios should be analysed in this context and reliably tested taking into account the effects outlined in Chapter 3.

Q2: *How can we use experimental data from the HL-LHC in theoretical developments?*

As a first step, a versatile framework was developed to accommodate new di-Higgs searches in the context of the existing `HiggsTools` framework. As a result, any BSM scenarios that accommodate deviations in the trilinear self-coupling can now be tested with experimental data, which is necessary, considering that non-resonant searches are narrowing the regions of allowed BSM parameter space. Resonant hh-searches were also implemented and are now part of the `HiggsTools` dataset. We have shown their importance in several selected benchmark scenarios in the 2HDM. In particular, they are the most sensitive searches to constrain deviations from the alignment limit in 2HDM Types I (for $t_\beta \gtrsim 1$) and II (for $1 \lesssim t_\beta \lesssim 10$) for resonant masses around $400 - 600$ GeV. This further exemplifies the need to improve the experimental analyses with the incorporation of the non-resonant contribution and the interference terms in order consistently interpret such limits in UV-complete models.

As a second step, we have studied the sensitivity to BSM trilinear scalar couplings in the di-Higgs invariant mass distributions. Assuming a heavy scalar mass of 450 GeV, we find that a precision of 10–20% on $\xi_H^t \times \lambda_{hhH}$ (the product of the BSM trilinear coupling between hhH and the heavy Higgs top Yukawa coupling) may be achievable, depending on experimental efficiencies, whose improvements can suppress the statistical uncertainties. Our results show that even simple neural networks can outperform traditional statistical methods like MLE for parameter estimation and hypothesis testing. While the analysis

is model-dependent, the methodology is adaptable and can be refined with future data and improved theoretical inputs, offering a promising path toward reconstructing the BSM scalar potential.

Q3: *If a strong first order electroweak phase transition occurred, what observable consequences would we detect today?*

After studying the possible thermal histories predicted for the parameter points in the 2HDM in Sec. 5.1, we proceeded to the analysis of different ways to probe the region compatible with a SFOEWPT. We have shown that mass splittings between scalars enhance the strength of the phase transition in the 2HDM. The CP-even state has to be ideally between 400-600 GeV, the lower bound being typically imposed by collider constraints and the higher bound by the Boltzmann suppression of the very heavy states in the thermal corrections that drive the energy barrier. The ideal mass splitting with m_A is around $100 - 200$ GeV, which enlarges the barrier with the right amount to prevent the vacuum trapping phenomenon. This mass hierarchy naturally leads to a scenario that can be probed by the $A \to ZH$ searches, which become kinematically open in the region preferred by a SFOEWPT and therefore were coined "smoking gun" searches.

The relative heaviness of the charged Higgs boson $H^{\pm}$ can further contribute to thermal corrections that strengthen the transition, provided its mass arises largely from the vev, so we set its mass to the heaviest scale $m_{H^{\pm}} = m_A$, in order to also accommodate constraints from EWPO. M cannot significantly deviate from m_H without hitting constraints from perturbative unitarity, therefore the splittings between m_H and M are quite constrained and cannot enhance the phase transition further, so for simplicity we chose to keep $M = m_H$. Additionally, in the alignment limit, the direction of the electroweak symmetry breaking is aligned with the direction of the lighter state. This allows the heavier scalars to enhance the thermal corrections that strengthen the transition without deviating from the EWSB direction, which would weaken the transition. Based on these considerations, we show that the transition is stronger closer to the alignment limit.

We have analysed in detail the impact of the smoking gun search in the 2HDM parameter space. We stress that because of the above considerations this search is interesting regardless of the dynamics of the phase transition because it would completely constrain the mass sector of the 2HDM. In particular, the search $gg \to A \to ZH \to \ell^+\ell^- t\bar{t}$ is the most promising one to probe masses of $m_H > 2m_t$ in the low t_β regime at present as well as future collider experiments. It is crucial for testing the 2HDM parameter space regions overlapping with a plausible explanation of the BAU via EW baryogenesis. It is the only search to target the so far unexplored regions for $t_\beta > 2$ and the regions featuring a SFOEWPT for $t_\beta \sim 1.5$.

A further well known probe of the SFOEWPT is a deviation of the trilinear Higgs self coupling from the SM prediction. In this regard we want to stress that despite the fact that sizeable loop corrections in the trilinear couplings have always been considered in the Coleman-Weinberg potential in the analysis of the phase transitions, up to now they had not been systematically included in the corrections to the collider signature of hh-production in the context of BSM models. Our results stress the importance of including them not only in the finite temperature observables, but also in the predictions at zero temperature.

We have explored the interplay between di-Higgs production at colliders and the nature of the electroweak phase transition in the 2HDM, focusing on the role of loop-corrected trilinear Higgs self-couplings. Our analysis shows that large deviations in these couplings can

significantly alter the Higgs pair production cross section. However, the parameter space regions that feature the largest trilinear couplings and could enhance the strength of the phase transition often lie near the destructive interference minimum in di-Higgs production. This reveals an important limitation: the hadron collider sensitivity to κ_λ is naturally suppressed precisely in the regions of parameter space that are most favourable for baryogenesis. As such, our results underscore the complementarity of collider and cosmological probes: while trilinear coupling measurements at the HL-LHC can provide valuable indirect insight into the scalar potential, they may have a low accuracy in key regions linked to a viable SFOEWPT. A complete understanding of the electroweak epoch therefore requires a synergy between hadron and e^+e^- at sufficiently high energies, gravitational wave observations, and theoretical modelling of the Higgs sector.

Turning to cosmological probes, we find that predictions for the GW spectrum are highly sensitive to the exact values of the BSM scalar masses. As a result, the expected signal-to-noise ratio at LISA can vary by several orders of magnitude within the parameter region compatible with potential collider signals. Therefore, if a BSM particle consistent with a SFOEWPT is discovered at colliders, a detectable GW background cannot be generally expected at LISA or other future space-based GW detectors. However, if LISA were to observe a stochastic GW signal alongside a corresponding collider signal, it would, in the context of the 2HDM, provide new and very precise information on the allowed values of the parameters.

In summary, this work has investigated the prospects for measurable deviations in the trilinear Higgs couplings within a simple BSM framework, guided by a pragmatic approach that merges precise theoretical predictions with realistic experimental signatures. It emphasizes the importance of complementarity between different observational strategies, spanning collider experiments and cosmological probes. More broadly, it underscores the essential role of collaboration between theory and experiment and across the high-energy physics and cosmology communities in advancing our understanding of fundamental physics.

Appendices

Appendix A

Effective potential at Finite Temperatures

We can split the potential into temperature-dependent and temperature-independent parts [38,288].[1] The $T = 0$ part includes the tree-level potential, the one-loop quantum corrections and a counterterm to cancel the UV-divergences, usually in the $\overline{\text{MS}}$ scheme. This potential has been derived by Coleman and Weinberg [138]. Explicitly, it is given by

$$V_{\text{CW}}(\phi, T = 0) = \sum_j \frac{(n_j)(-1)^{(2s_j)}}{64\pi^2} m_j^4(\phi) \left[\ln\left(\frac{m_j(\phi)^2}{\mu^2} \right) - c_j \right] \tag{A.1}$$

where s_j is the spin corresponding to the particle j with n_j degrees of freedom and mass $m_j(\phi)$, and c_j are renormalisation constants such that $c_j = 3/2$ for scalars and fermions and $c_j = 5/6$ for gauge bosons. It is evaluated in the Landau gauge to avoid ghost contributions. It is a gauge-dependent quantity, but these dependencies are smaller than other contributions [324, 355] and can be taken under control in the calculation of observables [356, 357] for instance using Nielsen identities [358].

At finite temperatures, QFT needs to be extended to incorporate thermal effects. In this regime, the vacuum energy is no longer sufficient to describe the system's equilibrium properties. Instead, these are governed by the free energy, which accounts for thermal excitations. In practice, this involves incorporating some tools employed in statistical mechanics into QFT, in particular the canonical ensemble. In the canonical ensemble, the central quantity is the partition function, which encodes all thermodynamic properties of the system. It is defined as a trace over the Hilbert space

$$Z = \text{Tr}\left[e^{-\beta H} \right] = \int \mathcal{D}\phi \, e^{-S_E}, \tag{A.2}$$

where H is the Hamiltonian, $\beta = 1/T$, and T is the temperature. After the second equality we expressed the partition function in the path integral formulation of QFT, in which the trace becomes a functional integral over all field configurations and S_E is the Euclidean action. The partition function is related to the free energy in the canonical ensemble by the expression:

---

[1]This section is based on [94, 288, 354]

$$F = -T \ln Z. \tag{A.3}$$

Therefore, the free energy of the system in quantum mechanics is the sum over microstates weighted by a Boltzmann factor, while in QFT it is the integral over fields in a functional integral weighted by the exponential of the Euclidean action.

To gain some intuition on the meaning of the effective potential, we will develop it from thermodynamic arguments in the following. Thermodynamically, the free energy is given by

$$F = E - TS, \tag{A.4}$$

where E is the energy, T is the temperature and S is the entropy. In terms of energy and entropy densities, the above relation becomes:

$$f = \rho - Ts = -P, \tag{A.5}$$

where f is the free energy density, ρ the energy density, s the entropy density and P is the pressure. The last equality follows from the thermodynamic identity $s = (\rho + P)/T$. The Eq. (A.5) shows the system prefers configurations that minimize the energy density, because those are the ones that maximize the pressure. In the context of cosmological phase transitions, this means that if a bubble of a lower-energy vacuum (the true electroweak vacuum) nucleates, it will tend to expand, since it has a higher pressure, displacing the surrounding phase (false vacuum at the origin of field space).

The free energy is more conveniently described by the temperature dependent scalar effective potential $V_{\text{eff}}(\phi, T)$. For a homogeneous scalar field ϕ, the total free energy is given by

$$F = \Omega V_{\text{eff}}(\phi, T), \tag{A.6}$$

where Ω is the spacial volume. Thus, the free energy density f is V_{eff}

$$f = V_{\text{eff}}(\phi, T). \tag{A.7}$$

The free energy depends non trivially on the vacuum expectation value of the scalar field, as it determines the masses of the particles and these contribute to the pressure. We can therefore derive the effective potential from its relation to the pressure in Eq. (A.5) by adding up the contributions to the pressure from the scalar field itself and the particles present in the medium.

The tree level contribution (or background field pressure) is simply the zero temperature potential:

$$P(\phi) = -V(\phi). \tag{A.8}$$

The thermal contribution from the particles assuming they form an ideal gas is given by

$$f_i = -p_i = -\frac{g_i}{6\pi^2} \int_0^\infty \frac{k^4 dk}{\sqrt{k^2 + m_i^2}} \frac{1}{e^{\sqrt{k^2 + m_i^2}/T} \pm 1}, \tag{A.9}$$

where g_i counts the degrees of freedom and the sign depends on the species, $+$ is for fermions and $-$ for bosons. This term captures the thermal pressure contribution of each species i.

Thus effective potential becomes simply

$$V_{\text{eff}} = V(\phi) + \sum_i f_i. \tag{A.10}$$

The equation in Eq. (A.9) does not have an analytical solution, but it can be approximated analytically in the high energy limit, where $T \gg m_i$. A general expression can be written as

$$V_{\text{eff}}(\phi) = V(\phi) + \frac{T^2}{24}\left(\sum_{i=\text{bosons}} g_i m_i^2(\phi) + \frac{1}{2}\sum_{i=\text{fermions}} g_i m_i^2(\phi)\right) - \frac{T^2}{12\pi}\sum_i g_i m_i^3(\phi)... \tag{A.11}$$

The quadratic term is the one that restores the symmetry at high temperatures. For a simple scalar potential at $T = 0$ such as the SM potential given in Eq. (2.29) the effective thermal mass of the scalar is given by the second derivative of the potential with respect to the field ϕ and therefore is

$$m_{\text{eff}}^2(\phi, T) = -\mu^2 + cT^2 \tag{A.12}$$

where $c \propto \sum_i g_i$ is constant. Since at high T $m_{\text{eff}} > 0$ the origin of field space becomes a local minimum and the electroweak symmetry is restored. The cubic term is the one that can induce a strong first order phase transition.

The thermal corrections can be expanded at one loop as

$$V_{\text{T}}(\phi, T) = \sum_{i=\text{boson}} n_i \frac{T^4}{2\pi^2} J_b\left(\frac{m_i^2}{T^2}\right) - \sum_{j=\text{fermion}} n_j \frac{T^4}{2\pi^2} J_f\left(\frac{m_j^2}{T^2}\right) \tag{A.13}$$

where J_b and J_f are loop functions, that in the high-temperature regime, $x \ll 1$ can be expanded as

$$\begin{aligned}
J_b(x^2) &= \frac{-\pi^4}{45} + \frac{\pi^2}{12}x^2 + \frac{\pi}{6}x^2 - \frac{1}{32}x^3\ln(x^2/a_b) + \mathcal{O}(x^3), \\
J_f(x^2) &= \frac{-7\pi^4}{360} - \frac{\pi^2}{24}x^2 - \frac{1}{32}x^4\ln(x^2/a_f) + \mathcal{O}(x^3).
\end{aligned} \tag{A.14}$$

where $\ln(a_b) \simeq 5.4076$ and $\ln(a_f) \simeq 2.6351$. In the opposite limit, when $m_i \gg T_i$, the J-functions take the form

$$J_b(x^2) \simeq J_f(x^2) = \left(\frac{x}{2\pi}\right)^{3/2} \mathrm{e}^{-x}\left(1 + \frac{15}{8\pi} + \mathcal{O}(x^{-2})\right), \tag{A.15}$$

showing that particles much heavier than the temperature get Boltzmann suppressed and do not participate framing the barriers in the effective potential.

In models where the masses of the particles are given by the vacuum expectation values of the scalar field, the expression of the full effective potential can be more conveniently written as

$$V_{\text{eff}}(\phi, T) \simeq D(T^2 - T_0^2)\phi^2 - ET\phi^3 + \frac{\tilde{\lambda}}{4}\phi^4, \tag{A.16}$$

where D and $\tilde{\lambda}$ are functions mildly depending on T. The cubic term $\propto E$ is what drives the barrier in the phase transition. The form of the J-functions in the high T limit given in Eq. (A.14) shows that fermions, notably the top due to the Yukawa hierarchy, do not contribute to a ϕ^3 term in the thermal masses and do not help enhancing a transition. In fact the opposite is the case, they weaken the transition by contributing to the ϕ^2 term.

In more formal derivations of these quantities in QFT, the Matsubara formalism is usually used. This formalism consists in performing a Wick rotation on time $t \to i\tau$, and compactifying the time direction into a finite interval with periodic boundary conditions $\tau \in [0, \ \beta]$. This leads to periodic boundary conditions for fermions and bosons: fermionic fields are antiperiodic in imaginary time while bosonic fields are periodic. This in turn leads to a discrete spectrum of frequencies for these particles, namely $\omega_n = 2\pi n/\beta$ for bosons and $\omega_n = (2n + 1)\pi/\beta$ for fermions. The fields can then be Fourier expanded in these Matsubara frequencies, and thermal observables can be computed using path integrals over these periodic fields. We do not derive the equations above using this formalism here but we refer to the literature [288, 359].

The above perturbative treatment of the finite temperature potential is known to break down at very high temperatures when the expansion parameter T^2/m^2 becomes large. This situation can be amended by adding the largest thermal corrections. This is done by incorporating the thermal masses in the propagators and resumming the resulting diagrams, named *daisy diagrams* due to their flower-like (or also bubble-like) shape. There are several methods available to perform such resummation. The Parwani method [360] consists in *dressing* the Matsubara modes of the bosonic fields by replacing their tree-level masses with thermally corrected, resummed masses in the one-loop potential, which avoids the IR divergencies, this shift is given by,

$$m_i^2(\phi, T) \to m_i^2(\phi) + \Pi_i(T), \tag{A.17}$$

where $\Pi_i(T)$ is the leading-order thermal mass correction, obtained from the one-loop self-energy (1PI diagram) of the field i in the high-temperature limit. The main issue with this approach it over-counts contributions which do not contribute to the IR divergences. To fix this, the Arnorld-Espinosa method was proposed [289], where only the zero modes of the bosonic propagators are dressed. A review of other resummation methods can be found in Ref. [361, 362].

These diagrams can be written as

$$V_{\text{daisy}}(\phi, T) = -\sum_i \frac{T}{12\pi} \text{Tr} \left[(m_i^2(\phi_i) + \Pi_i^2)^{3/2} - (m_i^2(\phi_i))^{3/2} \right] \tag{A.18}$$

The daisy terms are crucial for a first order phase transition analysis because they contain cubic terms that alter the energy barrier.

Therefore, the full effective finite temperature potential is

$$V_{\text{eff}} = V_{\text{tree}} + V_{\text{CW}} + V_{\text{CT}} + V_{\text{T}} + V_{\text{daisy}} . \tag{A.19}$$

Appendix B

Form factors for ggHH production

For the definition of the form LO QCD form factors in gluon fusion Higgs pair production, $g_a g_b \to h_c h_d$, we follow [241]. The triangle form factor for the top-loop is defined as:

$$F_\triangle = \tau_t \left[1 + (1 - \tau_t) f(\tau_t) \right] \tag{B.1}$$

where $\tau_t = 4m_t^2/(p_a + p_b)^2$, m_t is the mass of the top quark, and p_a, p_b are the momenta of the incoming gluons, and

$$f(\tau_t) = \begin{cases} \arcsin^2 \frac{1}{\sqrt{\tau_t}} & \text{if } \tau_t \geq 1, \\ -\frac{1}{4} \left[\log \frac{1+\sqrt{1-\tau_t}}{1-\sqrt{1-\tau_t}} - i\pi \right]^2 & \text{if } \tau_t < 1. \end{cases} \tag{B.2}$$

The top-quark from factor of the box diagram can be decomposed into contributions corresponding to different total angular momentum states of the initial gluon pair, specifically the spin can be either $s = 0$ or $s = 2$. This reflects the fact that two massless gluons can couple to form either a scalar ($J = 0$) or a tensor ($J = 2$) state, and each component gives rise to a distinct Lorentz structure in the form factor decomposition. The two form factors are:

$$
\begin{aligned}
F_\Box &= \frac{1}{S^2} \Big\{ 4S + 8S m_t^2 C_{ab} - 2S(S + \rho_c + \rho_d - 8) m_t^4 (D_{abc} + D_{bac} + D_{acb}) \\
&\quad + (\rho_c + \rho_d - 8) m_t^2 \left[T_1 C_{ac} + U_1 C_{bc} + U_2 C_{ad} + T_2 C_{bd} - (TU - \rho_c \rho_d) m_t^2 D_{acb} \right] \Big\}, \\
G_\Box &= \frac{1}{S(TU - \rho_c \rho_d)} \Big\{ (T^2 + \rho_c \rho_d - 8T) m_t^2 \left[S C_{ab} + T_1 C_{ac} + T_2 C_{bd} - ST m_t^2 D_{bac} \right] \\
&\quad + (U^2 + \rho_c \rho_d - 8U) m_t^2 \left[S C_{ab} + U_1 C_{bc} + U_2 C_{ad} - SU m_t^2 D_{abc} \right] \\
&\quad - (T^2 + U^2 - 2\rho_c \rho_d)(T + U - 8) m_t^2 C_{cd} \\
&\quad - 2(T + U - 8)(TU - \rho_c \rho_d) m_t^4 (D_{abc} + D_{bac} + D_{acb}) \Big\},
\end{aligned} \tag{B.3}
$$

where $\rho_c = \rho_d = m_h^2/m_t^2$, $T_1 = T - \rho_c$, $U_1 = U - \rho_c$, $T_2 = T - \rho_d$, $U_2 = U - \rho_d$,

$$S = \frac{(p_a + p_b)^2}{m_t^2}, \quad T = \frac{(p_c - p_a)^2}{m_t^2} \quad \text{and} \quad U = \frac{(p_c - p_b)^2}{m_t^2}, \tag{B.4}$$

and C_{ij}, D_{ij} are the scalar Passarino-Veltman integrals [139]

$$C_{ij} = \int \frac{d^4q}{i\pi^2} \frac{1}{(q^2 - m_t^2)\left[(q+p_i)^2 - m_t^2\right]\left[(q+p_i+p_j)^2 - m_t^2\right]}$$
$$D_{ijk} = \int \frac{d^4q}{i\pi^2} \frac{1}{(q^2 - m_t^2)\left[(q+p_i)^2 - m_t^2\right]\left[(q+p_i+p_j)^2 - m_t^2\right]\left[(q+p_i+p_j+p_k)^2 - m_t^2\right]}$$
$$(B.5)$$

The full matrix element will be

$$\mathcal{M}(gg \to hh) = \mathcal{M}_\triangle^h + \mathcal{M}_\triangle^H + \mathcal{M}_\square, \tag{B.6}$$

where

$$\mathcal{M}_\triangle^{h/H} = K \frac{\lambda_{hh(h/H)} v \, \xi_t^{h/H}}{s - m_{h/H}^2 + i m_{h/H}\Gamma_{h/H}} F_\triangle A_{\mu\nu}^{s=0} \epsilon_a^\mu \epsilon_b^\nu \delta_{ab}$$
$$\mathcal{M}_\square = K \xi_t^h (F_\square A_{\mu\nu}^{s=0} + G_\square A_{\mu\nu}^{s=2}) \epsilon_a^\mu \epsilon_b^\nu \delta_{ab}, \tag{B.7}$$

where $K = G_F \alpha_s s/(2\sqrt{2}\pi)$, G_F is the Fermi constant, α_s is the strong coupling constant, v is the vev, $\xi_t^{h/H}$ are the Yukawa couplings modifiers of the Higgs in the s-channel in units of the SM Yukawa couplings, $\lambda_{hh(h/H)}$ are the dimensionful trilinear Higgs couplings (e.g. $\lambda_{hhh} = 3m_h^2/v$), $\epsilon_{a,b}$ are the gluon polarisation vectors.

The helicity projectors are

$$A_{s=0}^{\mu\nu} = g^{\mu\nu} - \frac{p_a^\nu p_b^\mu}{p_a \cdot p_b}, \tag{B.8}$$

$$A_{s=2}^{\mu\nu} = g^{\mu\nu} + \frac{p_h^2 p_a^\nu p_b^\mu}{p_T^2(p_a \cdot p_b)} - \frac{2(p_b \cdot p_h)p_a^\nu p_h^\mu}{p_T^2(p_a \cdot p_b)} - \frac{2(p_a \cdot p_h)p_b^\mu p_h^\nu}{p_T^2(p_a \cdot p_b)} + \frac{2p_h^\mu p_h^\nu}{p_T^2}, \tag{B.9}$$

with

$$p_T^2 = 2\frac{(p_a \cdot p_c)(p_b \cdot p_c)}{p_a \cdot p_b} - p_c^2 \,. \tag{B.10}$$

In the large top quark mass limit, $m_t^2 \gg m_h^2$, the form factors simplify to

$$F_\triangle = \frac{2}{3} + \mathcal{O}(s/m_t^2),$$
$$F_\square = -\frac{2}{3} + \mathcal{O}(s/m_t^2), \tag{B.11}$$
$$G_\square = \mathcal{O}(s/m_t^2),$$

where s is the Mandelstam variable $s = (p_a + p_b)^2$. Notably, the triangle and box form factors cancel exactly at threshold, which plays a key role in the double Higgs production invariant mass distributions. In a BSM scenario with a modified κ_λ, this cancellation is shifted due to the change in the trilinear coupling. If it happens closer to the mass of the top quark, this approximation is less exact ad the corresponding cancellation is smaller than in the SM.

Appendix C

NN loss functions

In Fig. C.1 we show the loss functions and the AE95 evolutions over the training epochs for the different datasets used in 4.2. The upper row corresponds to the dataset (1), the middle row to the dataset (2) and the lower row to the dataset (3). These correspond to datasets with the original benchmark plane, with free m_{12}^2, and with an uncertainty in m_H, respectively.

Clearly, the training and validation losses closely track each other throughout the entire training process. There is no visible gap between them, and the decrease steadily over the epochs, which suggests that there is no overfitting. We could consider an early stopping, as the MSE does not decrease significantly after ~ 20k epochs. However, we prefer to keep a longer learning rate to include further data, as each epoch learns from new Poisson smeared data.
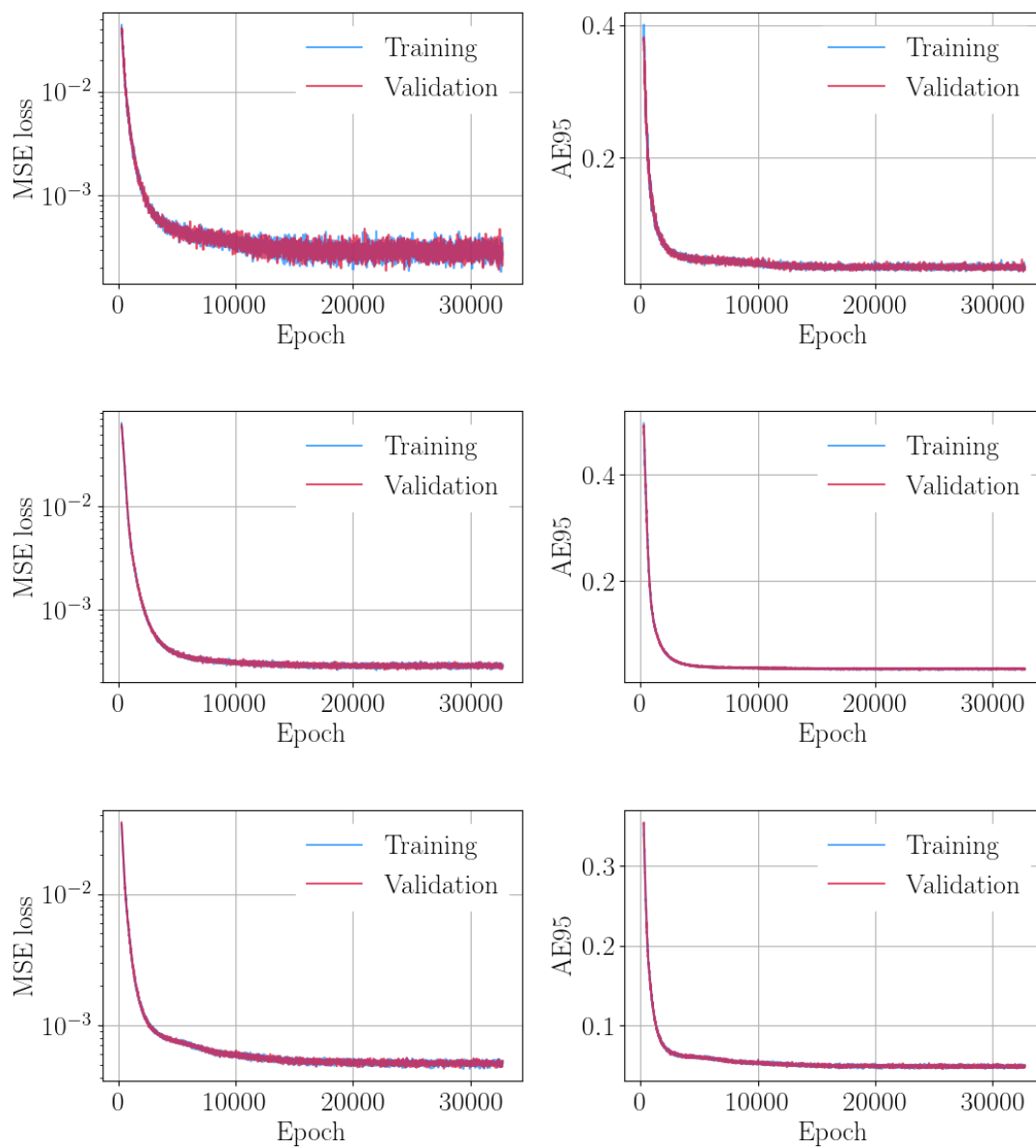
Figure C.1

NN prediction of $\xi_H^t \times \lambda_{hhH}$ for the different datasets: (1) upper, (2) middle and (3) lower row.

Bibliography

[1] F. Arco, S. Heinemeyer, M. Mühlleitner and K. Radchenko, *Sensitivity to triple Higgs couplings via di-Higgs production in the 2HDM at the (HL-)LHC*, *Eur. Phys. J. C* **83** (2023) 1019 [2212.11242].

[2] T. Biekötter, S. Heinemeyer, J.M. No, K. Radchenko, M.O. Olea Romacho and G. Weiglein, *First shot of the smoking gun: probing the electroweak phase transition in the 2HDM with novel searches for $A \to ZH$ in $\ell^+\ell^- t\bar{t}$ and $\nu\nu b\bar{b}$ final states*, *JHEP* **01** (2024) 107 [2309.17431].

[3] S. Heinemeyer, M. Mühlleitner, K. Radchenko and G. Weiglein, *Higgs pair production in the 2HDM: impact of loop corrections to the trilinear Higgs couplings and interference effects on experimental limits*, *Eur. Phys. J. C* **85** (2025) 437 [2403.14776].

[4] H. Bahl, J. Braathen, M. Gabelmann, K. Radchenko and G. Weiglein, "`anyh3` and `anyhh`: *precise predictions for trilinear higgs couplings and double higgs production in extended scalar sectors*."

[5] H. Bahl, T. Biekötter, S. Heinemeyer, K. Radchenko and G. Weiglein, "*New developments in* `HiggsTools`."

[6] M. Frank, S. Heinemeyer, M. Mühlleitner and K. Radchenko, "*Experimental determination of BSM Triple Higgs Couplings at the HL-LHC with Neural Networks*."

[7] E. Wigner, *The unreasonable effectiveness of mathematics in the natural sciences*, *Commun. Pure Appl. Math.* **13** (1960) 1.

[8] M.E. Peskin and D.V. Schroeder, *An Introduction to quantum field theory*, Addison-Wesley, Reading, USA (1995), 10.1201/9780429503559.

[9] S. Weinberg, *The Quantum theory of fields. Vol. 1: Foundations*, Cambridge University Press (6, 2005), 10.1017/CBO9781139644167.

[10] M.D. Schwartz, *Quantum Field Theory and the Standard Model*, Cambridge University Press (3, 2014).

[11] P.A.M. Dirac, *The quantum theory of the electron*, *Proc. Roy. Soc. Lond. A* **117** (1928) 610.

[12] C.D. Anderson, *The Positive Electron*, *Phys. Rev.* **43** (1933) 491.

[13] R.P. Feynman, *Space - time approach to quantum electrodynamics*, *Phys. Rev.* **76** (1949) 769.

[14] R.P. Feynman, *A Relativistic cutoff for classical electrodynamics*, *Phys. Rev.* **74** (1948) 939.

[15] J.S. Schwinger, *On Quantum electrodynamics and the magnetic moment of the electron*, *Phys. Rev.* **73** (1948) 416.

[16] J. Schwinger, *Quantum Electrodynamics. I. A Covariant Formulation*, *Phys. Rev.* **74** (1948) 1439.

[17] J. Schwinger, *Quantum Electrodynamics. II. Vacuum Polarization and Self-Energy*, *Phys. Rev.* **75** (1949) 651.

[18] J. Schwinger, *Quantum Electrodynamics. III. The Electromagnetic Properties of the Electron—Radiative Corrections to Scattering*, *Phys. Rev.* **76** (1949) 790.

[19] S. Tomonaga, *On a relativistically invariant formulation of the quantum theory of wave fields*, *Prog. Theor. Phys.* **1** (1946) 27.

[20] F.J. Dyson, *The Radiation theories of Tomonaga, Schwinger, and Feynman*, *Phys. Rev.* **75** (1949) 486.

[21] C.-N. Yang and R.L. Mills, *Conservation of Isotopic Spin and Isotopic Gauge Invariance*, *Phys. Rev.* **96** (1954) 191.

[22] F. Englert and R. Brout, *Broken Symmetry and the Mass of Gauge Vector Mesons*, *Phys. Rev. Lett.* **13** (1964) 321.

[23] P.W. Higgs, *Broken symmetries, massless particles and gauge fields*, *Phys. Lett.* **12** (1964) 132.

[24] S.L. Glashow, *Partial-symmetries of weak interactions*, *Nuclear Physics* **22** (1961) 579.

[25] S. Weinberg, *A Model of Leptons*, *Phys. Rev. Lett.* **19** (1967) 1264.

[26] A. Salam, *Weak and Electromagnetic Interactions*, *Conf. Proc. C* **680519** (1968) 367.

[27] ATLAS collaboration, *Observation of a new particle in the search for the Standard Model Higgs boson with the ATLAS detector at the LHC*, *Phys. Lett. B* **716** (2012) 1 [1207.7214].

[28] CMS collaboration, *Observation of a New Boson at a Mass of 125 GeV with the CMS Experiment at the LHC*, *Phys. Lett. B* **716** (2012) 30 [1207.7235].

[29] R. Boyd, P. Gasper and J.D. Trout, eds., *The Philosophy of Science*, MIT Press (1991).

[30] J.F. Gunion, H.E. Haber, G.L. Kane and S. Dawson, *The Higgs Hunter's Guide*, vol. 80 (2000).

[31] J. McDonald, *Gauge singlet scalars as cold dark matter*, *Phys. Rev. D* **50** (1994) 3637 [`hep-ph/0702143`].

[32] M.C. Bento, O. Bertolami, R. Rosenfeld and L. Teodoro, *Selfinteracting dark matter and invisibly decaying Higgs*, *Phys. Rev. D* **62** (2000) 041302 [`astro-ph/0003350`].

[33] C.P. Burgess, M. Pospelov and T. ter Veldhuis, *The Minimal model of nonbaryonic dark matter: A Singlet scalar*, *Nucl. Phys. B* **619** (2001) 709 [`hep-ph/0011335`].

[34] N.G. Deshpande and E. Ma, *Pattern of Symmetry Breaking with Two Higgs Doublets*, *Phys. Rev. D* **18** (1978) 2574.

[35] Q.-H. Cao, E. Ma and G. Rajasekaran, *Observing the Dark Scalar Doublet and its Impact on the Standard-Model Higgs Boson at Colliders*, *Phys. Rev. D* **76** (2007) 095011 [`0708.2939`].

[36] L. Lopez Honorez, E. Nezri, J.F. Oliver and M.H.G. Tytgat, *The Inert Doublet Model: An Archetype for Dark Matter*, *JCAP* **02** (2007) 028 [`hep-ph/0612275`].

[37] A.G. Cohen, D.B. Kaplan and A.E. Nelson, *Progress in electroweak baryogenesis*, *Ann. Rev. Nucl. Part. Sci.* **43** (1993) 27 [`hep-ph/9302210`].

[38] D.E. Morrissey and M.J. Ramsey-Musolf, *Electroweak baryogenesis*, *New J. Phys.* **14** (2012) 125003 [`1206.2942`].

[39] J.M. Cline and P.-A. Lemieux, *Electroweak phase transition in two Higgs doublet models*, *Phys. Rev. D* **55** (1997) 3873 [`hep-ph/9609240`].

[40] L. Fromme, S.J. Huber and M. Seniuch, *Baryogenesis in the two-Higgs doublet model*, *JHEP* **11** (2006) 038 [`hep-ph/0605242`].

[41] W.G. Hollik, G. Weiglein and J. Wittbrodt, *Impact of Vacuum Stability Constraints on the Phenomenology of Supersymmetric Models*, *JHEP* **03** (2019) 109 [`1812.04644`].

[42] T. Lee, *A theory of spontaneous t violation*, Phys. Rev. D **8** (1973) 1226.

[43] M. Aoki, S. Kanemura, K. Tsumura and K. Yagyu, *Models of Yukawa interaction in the two Higgs doublet model, and their collider phenomenology*, *Phys. Rev. D* **80** (2009) 015017 [`0902.4665`].

[44] G.C. Branco, P.M. Ferreira, L. Lavoura, M.N. Rebelo, M. Sher and J.P. Silva, *Theory and phenomenology of two-Higgs-doublet models*, *Phys. Rept.* **516** (2012) 1 [`1106.0034`].

[45] J.M. Moreno, M. Quiros and M. Seco, *Bubbles in the supersymmetric standard model*, *Nucl. Phys. B* **526** (1998) 489 [`hep-ph/9801272`].

[46] D. Bodeker, P. John, M. Laine and M.G. Schmidt, *The Two loop MSSM finite temperature effective potential with stop condensation*, *Nucl. Phys. B* **497** (1997) 387 [`hep-ph/9612364`].

[47] M. Laine and K. Rummukainen, *The MSSM electroweak phase transition on the lattice*, *Nucl. Phys. B* **535** (1998) 423 [`hep-lat/9804019`].

[48] A.D. Sakharov, *Violation of CP Invariance, C asymmetry, and baryon asymmetry of the universe*, *Pisma Zh. Eksp. Teor. Fiz.* **5** (1967) 32.

[49] PLANCK collaboration, *Planck 2018 results. VI. Cosmological parameters*, *Astron. Astrophys.* **641** (2020) A6 [`1807.06209`].

[50] S. Dodelson, *Modern Cosmology*, Academic Press, Amsterdam (2003).

[51] LIGO SCIENTIFIC, VIRGO collaboration, *Observation of Gravitational Waves from a Binary Black Hole Merger*, *Phys. Rev. Lett.* **116** (2016) 061102 [`1602.03837`].

[52] NANOGRAV collaboration, *The NANOGrav 15 yr Data Set: Evidence for a Gravitational-wave Background*, *Astrophys. J. Lett.* **951** (2023) L8 [`2306.16213`].

[53] A. Dainese, M. Mangano, A.B. Meyer, A. Nisati, G. Salam and M.A. Vesterinen, eds., *Report on the Physics at the HL-LHC,and Perspectives for the HE-LHC*, vol. 7/2019 of *CERN Yellow Reports: Monographs*, CERN, Geneva, Switzerland (2019), 10.23731/CYRM-2019-007.

[54] ATLAS, CMS collaboration, *Addendum to the report on the physics at the HL-LHC, and perspectives for the HE-LHC: Collection of notes from ATLAS and CMS*, *CERN Yellow Rep. Monogr.* **7** (2019) Addendum [`1902.10229`].

[55] LISA collaboration, *LISA Definition Study Report*, `2402.07571`.

[56] R.P. Feynman, R.B. Leighton and M. Sands, *The Feynman lectures on physics; New millennium ed.*, Basic Books, New York, NY (2010).

[57] M. Thomson, *Modern particle physics*, Cambridge University Press, New York (10, 2013), 10.1017/CBO9781139525367.

[58] E. Noether, *Invariant Variation Problems*, *Gott. Nachr.* (1918) 235.

[59] C.S. Wu, E. Ambler, R.W. Hayward, D.D. Hoppes and R.P. Hudson, *Experimental Test of Parity Conservation in β Decay*, *Phys. Rev.* **105** (1957) 1413.

[60] M. Gell-Mann, *Isotopic Spin and New Unstable Particles*, *Phys. Rev.* **92** (1953) 833.

[61] C.N. Yang and R.L. Mills, *Conservation of Isotopic Spin and Isotopic Gauge Invariance*, *Physical Review* **96** (1954) 191.

[62] R. Haag, J.T. Lopuszanski and M. Sohnius, *All Possible Generators of Supersymmetries of the s Matrix*, *Nucl. Phys. B* **88** (1975) 257.

[63] A. Denner, *Techniques for calculation of electroweak radiative corrections at the one loop level and results for W physics at LEP-200*, *Fortsch. Phys.* **41** (1993) 307 [`0709.1075`].

[64] H. Fritzsch, M. Gell-Mann and H. Leutwyler, *Advantages of the Color Octet Gluon Picture*, *Phys. Lett. B* **47** (1973) 365.

[65] PLUTO collaboration, *Evidence for Gluon Bremsstrahlung in e+ e- Annihilations at High-Energies*, *Phys. Lett. B* **86** (1979) 418.

[66] L. Di Lella and C. Rubbia, *The Discovery of the W and Z Particles*, *Adv. Ser. Direct. High Energy Phys.* **23** (2015) 137.

[67] G.S. Guralnik, C.R. Hagen and T.W.B. Kibble, *Global Conservation Laws and Massless Particles*, *Phys. Rev. Lett.* **13** (1964) 585.

[68] L. Morel, Z. Yao, P. Cladé and S. Guellati-Khélifa, *Determination of the fine-structure constant with an accuracy of 81 parts per trillion*, *Nature* **588** (2020) 61.

[69] M. Herrero, *The Standard model*, *NATO Sci. Ser. C* **534** (1999) 1 [`hep-ph/9812242`].

[70] V.L. Ginzburg and L.D. Landau, *On the Theory of superconductivity*, *Zh. Eksp. Teor. Fiz.* **20** (1950) 1064.

[71] Y. Nambu, *Axial vector current conservation in weak interactions*, *Phys. Rev. Lett.* **4** (1960) 380.

[72] J. Goldstone, *Field Theories with Superconductor Solutions*, *Nuovo Cim.* **19** (1961) 154.

[73] J. Goldstone, A. Salam and S. Weinberg, *Broken Symmetries*, *Phys. Rev.* **127** (1962) 965.

[74] D. Baumann, *Primordial Cosmology*, *PoS* **TASI2017** (2018) 009 [`1807.03098`].

[75] D.o.T.P. Universidad Autónoma de Madrid, "Cosmology and the Early Universe, lectures by Prof. Alexander Knebe and Dr. Savvas Nesseris."

[76] DESI collaboration, *DESI DR2 Results II: Measurements of Baryon Acoustic Oscillations and Cosmological Constraints*, `2503.14738`.

[77] T. Biekötter, S. Heinemeyer, J.M. No, M.O. Olea-Romacho and G. Weiglein, *The trap in the early Universe: impact on the interplay between gravitational waves and LHC physics in the 2HDM*, *JCAP* **03** (2023) 031 [`2208.14466`].

[78] N. Craig, *Naturalness: past, present, and future*, *Eur. Phys. J. C* **83** (2023) 825 [`2205.05708`].

[79] P.A.M. Dirac, *New basis for cosmology*, *Proc. Roy. Soc. Lond. A* **165** (1938) 199.

[80] G. 't Hooft, *Naturalness, chiral symmetry, and spontaneous chiral symmetry breaking*, *NATO Sci. Ser. B* **59** (1980) 135.

[81] M. Dine, *TASI lectures on the strong CP problem*, in *Theoretical Advanced Study Institute in Elementary Particle Physics (TASI 2000): Flavor Physics for the Millennium*, pp. 349–369, 6, 2000 [`hep-ph/0011376`].

[82] A. Hook, *TASI Lectures on the Strong CP Problem and Axions*, *PoS* **TASI2018** (2019) 004 [1812.02669].

[83] J.M. Pendlebury et al., *Revised experimental upper limit on the electric dipole moment of the neutron*, *Phys. Rev. D* **92** (2015) 092003 [1509.04411].

[84] J. Huston, K. Rabbertz and G. Zanderighi, *Quantum Chromodynamics*, 2312.14015.

[85] R.D. Peccei and H.R. Quinn, *CP Conservation in the Presence of Instantons*, *Phys. Rev. Lett.* **38** (1977) 1440.

[86] R.D. Peccei, *The Strong CP problem and axions*, *Lect. Notes Phys.* **741** (2008) 3 [hep-ph/0607268].

[87] S. Weinberg, *The Cosmological Constant Problem*, *Rev. Mod. Phys.* **61** (1989) 1.

[88] R. Bousso, *TASI Lectures on the Cosmological Constant*, *Gen. Rel. Grav.* **40** (2008) 607 [0708.4231].

[89] Muon g-2 collaboration, *Measurement of the Positive Muon Anomalous Magnetic Moment to 0.20 ppm*, *Phys. Rev. Lett.* **131** (2023) 161802 [2308.06230].

[90] T. Aoyama et al., *The anomalous magnetic moment of the muon in the Standard Model*, *Phys. Rept.* **887** (2020) 1 [2006.04822].

[91] S. Borsanyi et al., *Leading hadronic contribution to the muon magnetic moment from lattice QCD*, *Nature* **593** (2021) 51 [2002.12347].

[92] C. Davies, *Muon g-2*, *PoS* **LATTICE2024** (2025) 019 [2503.03364].

[93] J.M. Cline, *Baryogenesis*, in *Les Houches Summer School - Session 86: Particle Physics and Cosmology: The Fabric of Spacetime*, 9, 2006 [hep-ph/0609145].

[94] V.A. Rubakov and D.S. Gorbunov, *Introduction to the Theory of the Early Universe: Hot big bang theory*, World Scientific, Singapore (2017), 10.1142/10447.

[95] G. 't Hooft, *Symmetry Breaking Through Bell-Jackiw Anomalies*, *Phys. Rev. Lett.* **37** (1976) 8.

[96] V.A. Rubakov, *Classical theory of gauge fields*, Princeton University Press, Princeton, New Jersey (5, 2002).

[97] V.A. Kuzmin, V.A. Rubakov and M.E. Shaposhnikov, *On the Anomalous Electroweak Baryon Number Nonconservation in the Early Universe*, *Phys. Lett. B* **155** (1985) 36.

[98] P.B. Arnold, *The Electroweak phase transition: Part 1. Review of perturbative methods*, in *8th International Seminar on High-energy Physics*, 10, 1994 [hep-ph/9410294].

[99] Particle Data Group collaboration, *Review of particle physics*, *Phys. Rev. D* **110** (2024) 030001.

[100] G.C. Branco, R.G. Felipe and F.R. Joaquim, *Leptonic CP Violation*, *Rev. Mod. Phys.* **84** (2012) 515 [`1111.5332`].

[101] M.B. Gavela, P. Hernandez, J. Orloff, O. Pene and C. Quimbay, *Standard model CP violation and baryon asymmetry. Part 2: Finite temperature*, *Nucl. Phys. B* **430** (1994) 382 [`hep-ph/9406289`].

[102] G. Servant, *Baryogenesis from Strong CP Violation and the QCD Axion*, *Phys. Rev. Lett.* **113** (2014) 171803 [`1407.0030`].

[103] B. von Harling and G. Servant, *QCD-induced Electroweak Phase Transition*, *JHEP* **01** (2018) 159 [`1711.11554`].

[104] K. Kajantie, M. Laine, K. Rummukainen and M.E. Shaposhnikov, *Is there a hot electroweak phase transition at $m_H \gtrsim m_W$?*, *Phys. Rev. Lett.* **77** (1996) 2887 [`hep-ph/9605288`].

[105] K. Rummukainen, M. Tsypin, K. Kajantie, M. Laine and M.E. Shaposhnikov, *The Universality class of the electroweak theory*, *Nucl. Phys. B* **532** (1998) 283 [`hep-lat/9805013`].

[106] A.D. Dolgov, *NonGUT baryogenesis*, *Phys. Rept.* **222** (1992) 309.

[107] S. Davidson, E. Nardi and Y. Nir, *Leptogenesis*, *Phys. Rept.* **466** (2008) 105 [`0802.2962`].

[108] I. Affleck and M. Dine, *A New Mechanism for Baryogenesis*, *Nucl. Phys. B* **249** (1985) 361.

[109] C. Grojean and G. Servant, *Gravitational Waves from Phase Transitions at the Electroweak Scale and Beyond*, *Phys. Rev. D* **75** (2007) 043507 [`hep-ph/0607107`].

[110] LISA Cosmology Working Group collaboration, *Cosmology with the Laser Interferometer Space Antenna*, *Living Rev. Rel.* **26** (2023) 5 [`2204.05434`].

[111] J. Steggemann, *Extended Scalar Sectors*, *Ann. Rev. Nucl. Part. Sci.* **70** (2020) 197.

[112] D. Curtin, P. Jaiswal and P. Meade, *Excluding Electroweak Baryogenesis in the MSSM*, *JHEP* **08** (2012) 005 [`1203.2932`].

[113] T. Biekötter, D. Fontes, M. Mühlleitner, J.C. Romão, R. Santos and J.a.P. Silva, *Impact of new experimental data on the C2HDM: the strong interdependence between LHC Higgs data and the electron EDM*, *JHEP* **05** (2024) 127 [`2403.02425`].

[114] D. O'Connell, M.J. Ramsey-Musolf and M.B. Wise, *Minimal Extension of the Standard Model Scalar Sector*, *Phys. Rev. D* **75** (2007) 037701 [`hep-ph/0611014`].

[115] G.W. Anderson and L.J. Hall, *Electroweak phase transition and baryogenesis*, *Phys. Rev. D* **45** (1992) 2685.

[116] J.R. Espinosa and M. Quiros, *The Electroweak phase transition with a singlet*, *Phys. Lett. B* **305** (1993) 98 [`hep-ph/9301285`].

[117] J.R. Espinosa, T. Konstandin and F. Riva, *Strong Electroweak Phase Transitions in the Standard Model with a Singlet*, *Nucl. Phys. B* **854** (2012) 592 [1107.5441].

[118] T. Robens, T. Stefaniak and J. Wittbrodt, *Two-real-scalar-singlet extension of the SM: LHC phenomenology and benchmark scenarios*, *Eur. Phys. J. C* **80** (2020) 151 [1908.08554].

[119] S. Weinberg, *Gauge Theory of* CP *Nonconservation*, *Phys. Rev. Lett.* **37** (1976) 657.

[120] H. Bahl, W.H. Chiu, C. Gao, L.-T. Wang and Y.-M. Zhong, *Tripling down on the W boson mass*, *Eur. Phys. J. C* **82** (2022) 944 [2207.04059].

[121] ATLAS collaboration, *Combination of Searches for Higgs Boson Pair Production in pp Collisions at s=13 TeV with the ATLAS Detector*, *Phys. Rev. Lett.* **133** (2024) 101801 [2406.09971].

[122] CMS collaboration, *Constraints on the Higgs boson self-coupling from the combination of single and double Higgs boson production in proton-proton collisions at s=13TeV*, *Phys. Lett. B* **861** (2025) 139210 [2407.13554].

[123] O. Brüning and L. Rossi, eds., *The High Luminosity Large Hadron Collider: the new machine for illuminating the mysteries of Universe*, vol. 24 (2015), 10.1142/9581.

[124] S. Kanemura, S. Kiyoura, Y. Okada, E. Senaha and C.P. Yuan, *New physics effect on the Higgs selfcoupling*, *Phys. Lett. B* **558** (2003) 157 [hep-ph/0211308].

[125] S. Kanemura, Y. Okada, E. Senaha and C.P. Yuan, *Higgs coupling constants as a probe of new physics*, *Phys. Rev. D* **70** (2004) 115002 [hep-ph/0408364].

[126] H. Bahl, J. Braathen and G. Weiglein, *New Constraints on Extended Higgs Sectors from the Trilinear Higgs Coupling*, *Phys. Rev. Lett.* **129** (2022) 231802 [2202.03453].

[127] M. Aoki, S. Kanemura, M. Kikuchi and K. Yagyu, *Radiative corrections to the Higgs boson couplings in the triplet model*, *Phys. Rev. D* **87** (2013) 015012 [1211.6029].

[128] A. Arhrib, R. Benbrik, J. El Falaki and A. Jueid, *Radiative corrections to the Triple Higgs Coupling in the Inert Higgs Doublet Model*, *JHEP* **12** (2015) 007 [1507.03630].

[129] S. Kanemura, M. Kikuchi and K. Yagyu, *One-loop corrections to the Higgs self-couplings in the singlet extension*, *Nucl. Phys. B* **917** (2017) 154 [1608.01582].

[130] M. Krause, M. Muhlleitner, R. Santos and H. Ziesche, *Higgs-to-Higgs boson decays in a 2HDM at next-to-leading order*, *Phys. Rev. D* **95** (2017) 075019 [1609.04185].

[131] H. Bahl, J. Braathen, M. Gabelmann and G. Weiglein, *anyH3: precise predictions for the trilinear Higgs coupling in the Standard Model and beyond*, *Eur. Phys. J. C* **83** (2023) 1156 [2305.03015].

[132] W. Hollik and S. Penaranda, *Yukawa coupling quantum corrections to the selfcouplings of the lightest MSSM Higgs boson*, *Eur. Phys. J. C* **23** (2002) 163 [hep-ph/0108245].

[133] M. Brucherseifer, R. Gavin and M. Spira, *Minimal supersymmetric Higgs boson self-couplings: Two-loop $O(\alpha_t\alpha_s)$ corrections*, *Phys. Rev. D* **90** (2014) 117701 [1309.3140].

[134] J. Braathen and S. Kanemura, *On two-loop corrections to the Higgs trilinear coupling in models with extended scalar sectors*, *Phys. Lett. B* **796** (2019) 38 [1903.05417].

[135] J. Braathen and S. Kanemura, *Leading two-loop corrections to the Higgs boson self-couplings in models with extended scalar sectors*, *Eur. Phys. J. C* **80** (2020) 227 [1911.11507].

[136] H. Bahl, J. Braathen, M. Gabelmann and S. Paßehr, *Generic two-loop results for trilinear and quartic scalar self-interactions*, 2503.15645.

[137] E.J. Weinberg, *Radiative corrections as the origin of spontaneous symmetry breaking*, Ph.D. thesis, Harvard U., 1973. hep-th/0507214.

[138] S.R. Coleman and E.J. Weinberg, *Radiative Corrections as the Origin of Spontaneous Symmetry Breaking*, *Phys. Rev. D* **7** (1973) 1888.

[139] G. Passarino and M. Veltman, *One loop corrections for e^+e^- annihilation into $\mu^+\mu^-$ in the weinberg model*, *Nucl. Phys. B* **160** (1979) 151.

[140] P. Basler and M. Mühlleitner, *BSMPT (Beyond the Standard Model Phase Transitions): A tool for the electroweak phase transition in extended Higgs sectors*, *Comput. Phys. Commun.* **237** (2019) 62 [1803.02846].

[141] P. Basler, M. Mühlleitner and J. Müller, *BSMPT v2 a tool for the electroweak phase transition and the baryon asymmetry of the universe in extended Higgs Sectors*, *Comput. Phys. Commun.* **269** (2021) 108124 [2007.01725].

[142] P. Basler, L. Biermann, M. Mühlleitner, J. Müller, R. Santos and J.a. Viana, *BSMPT v3 A Tool for Phase Transitions and Primordial Gravitational Waves in Extended Higgs Sectors*, 2404.19037.

[143] A. Noble and M. Perelstein, *Higgs self-coupling as a probe of electroweak phase transition*, *Phys. Rev. D* **78** (2008) 063518 [0711.3018].

[144] M. Reichert, A. Eichhorn, H. Gies, J.M. Pawlowski, T. Plehn and M.M. Scherer, *Probing baryogenesis through the Higgs boson self-coupling*, *Phys. Rev. D* **97** (2018) 075008 [1711.00019].

[145] CMS collaboration, *Highlights of the HL-LHC physics projections by ATLAS and CMS*, 2504.00672.

[146] S. Kanemura, Y. Okada and E. Senaha, *Electroweak baryogenesis and quantum corrections to the triple Higgs boson coupling*, *Phys. Lett. B* **606** (2005) 361 [hep-ph/0411354].

[147] W. Buchmuller and D. Wyler, *Effective Lagrangian Analysis of New Interactions and Flavor Conservation*, *Nucl. Phys. B* **268** (1986) 621.

[148] B. Grzadkowski, M. Iskrzynski, M. Misiak and J. Rosiek, *Dimension-Six Terms in the Standard Model Lagrangian*, *JHEP* **10** (2010) 085 [1008.4884].

[149] I. Brivio and M. Trott, *The Standard Model as an Effective Field Theory*, *Phys. Rept.* **793** (2019) 1 [1706.08945].

[150] C. Grojean, G. Servant and J.D. Wells, *First-order electroweak phase transition in the standard model with a low cutoff*, *Phys. Rev. D* **71** (2005) 036001 [hep-ph/0407019].

[151] E. Camargo-Molina, R. Enberg and J. Löfgren, *A Catalog of First-Order Electroweak Phase Transitions in the Standard Model Effective Field Theory*, 2410.23210.

[152] I. Banta, *A strongly first-order electroweak phase transition from Loryons*, *JHEP* **06** (2022) 099 [2202.04608].

[153] R. Alonso, J.C. Criado, R. Houtz and M. West, *Walls, bubbles and doom — the cosmology of HEFT*, *JHEP* **05** (2024) 049 [2312.00881].

[154] R.R. Florentino, S. Kanemura and M. Tanaka, *Exploring loop-induced first-order electroweak phase transition in the Higgs effective field theory*, *Phys. Lett. B* **856** (2024) 138940 [2406.03957].

[155] P.N. Bhattiprolu and J.D. Wells, *A sensitivity target for an impactful Higgs boson self coupling measurement*, *Phys. Lett. B* **861** (2025) 139263 [2407.11847].

[156] S. Profumo, M.J. Ramsey-Musolf and G. Shaughnessy, *Singlet Higgs phenomenology and the electroweak phase transition*, *JHEP* **08** (2007) 010 [0705.2425].

[157] A. Ashoorioon and T. Konstandin, *Strong electroweak phase transitions without collider traces*, *JHEP* **07** (2009) 086 [0904.0353].

[158] S.L. Glashow and S. Weinberg, *Natural Conservation Laws for Neutral Currents*, *Phys. Rev. D* **15** (1977) 1958.

[159] E.A. Paschos, *Diagonal Neutral Currents*, *Phys. Rev. D* **15** (1977) 1966.

[160] T. Appelquist and J. Carazzone, *Infrared Singularities and Massive Fields*, *Phys. Rev. D* **11** (1975) 2856.

[161] J.F. Gunion and H.E. Haber, *The CP conserving two Higgs doublet model: The Approach to the decoupling limit*, *Phys. Rev. D* **67** (2003) 075019 [hep-ph/0207010].

[162] F.M. Arco García, *Searching for Triple Higgs Couplings: a phenomenological analysis in the Two Higgs Doublet Model*, Ph.D. thesis, Madrid, Autonoma U., 2023.

[163] T. Plehn, *Lectures on LHC Physics*, Springer Berlin Heidelberg (2012), 10.1007/978-3-642-24040-9.

[164] H.E. Logan, *Lectures on perturbative unitarity and decoupling in Higgs physics*, 2207.01064.

[165] B.W. Lee, C. Quigg and H.B. Thacker, *The Strength of Weak Interactions at Very High-Energies and the Higgs Boson Mass*, *Phys. Rev. Lett.* **38** (1977) 883.

[166] B.W. Lee, C. Quigg and H.B. Thacker, *Weak Interactions at Very High-Energies: The Role of the Higgs Boson Mass*, *Phys. Rev. D* **16** (1977) 1519.

[167] S. Kanemura, T. Kubota and E. Takasugi, *Lee-Quigg-Thacker bounds for Higgs boson masses in a two doublet model*, *Phys. Lett. B* **313** (1993) 155 [hep-ph/9303263].

[168] I.F. Ginzburg and I.P. Ivanov, *Tree-level unitarity constraints in the most general 2HDM*, *Phys. Rev. D* **72** (2005) 115010 [hep-ph/0508020].

[169] A.G. Akeroyd, A. Arhrib and E.-M. Naimi, *Note on tree level unitarity in the general two Higgs doublet model*, *Phys. Lett. B* **490** (2000) 119 [hep-ph/0006035].

[170] B. Grinstein, C.W. Murphy and P. Uttayarat, *One-loop corrections to the perturbative unitarity bounds in the CP-conserving two-Higgs doublet model with a softly broken $\mathbb{Z}_2$ symmetry*, *JHEP* **06** (2016) 070 [1512.04567].

[171] V. Cacchio, D. Chowdhury, O. Eberhardt and C.W. Murphy, *Next-to-leading order unitarity fits in Two-Higgs-Doublet models with soft $\mathbb{Z}_2$ breaking*, *JHEP* **11** (2016) 026 [1609.01290].

[172] J. Ren, R.-Q. Xiao, M. Zhou, Y. Fang, H.-J. He and W. Yao, *LHC Search of New Higgs Boson via Resonant Di-Higgs Production with Decays into 4W*, *JHEP* **06** (2018) 090 [1706.05980].

[173] M. Maniatis, A. von Manteuffel, O. Nachtmann and F. Nagel, *Stability and symmetry breaking in the general two-Higgs-doublet model*, *Eur. Phys. J. C* **48** (2006) 805 [hep-ph/0605184].

[174] D. Buttazzo, G. Degrassi, P.P. Giardino, G.F. Giudice, F. Sala, A. Salvio et al., *Investigating the near-criticality of the Higgs boson*, *JHEP* **12** (2013) 089 [1307.3536].

[175] S. Chigusa, T. Moroi and Y. Shoji, *Decay Rate of Electroweak Vacuum in the Standard Model and Beyond*, *Phys. Rev. D* **97** (2018) 116012 [1803.03902].

[176] J. Wittbrodt, *Exploring Models of Electroweak Symmetry Breaking at the LHC and Beyond*, Ph.D. thesis, Hamburg U., Hamburg, 2019. 10.3204/PUBDB-2019-03809.

[177] A. Barroso, P.M. Ferreira, I.P. Ivanov and R. Santos, *Metastability bounds on the two Higgs doublet model*, *JHEP* **06** (2013) 045 [1303.5098].

[178] M.E. Peskin and T. Takeuchi, *A New constraint on a strongly interacting Higgs sector*, *Phys. Rev. Lett.* **65** (1990) 964.

[179] M.E. Peskin and T. Takeuchi, *Estimation of oblique electroweak corrections*, *Phys. Rev. D* **46** (1992) 381.

[180] J. Erler and P. Langacker, *Electroweak model and constraints on new physics*, hep-ph/0407097.

[181] S. Hessenberger and W. Hollik, *Two-loop corrections to the ρ parameter in Two-Higgs-Doublet Models*, *Eur. Phys. J. C* **77** (2017) 178 [1607.04610].

[182] S.Hessenberger, *Two-loop corrections to electroweak precision observables in two-higgs-doublet-models*, Ph.D. thesis, Munich, Tech. U., 2018.

[183] S. Hessenberger and W. Hollik, *Two-loop improved predictions for M_W and $\sin^2 \theta_{\text{eff}}$ in Two-Higgs-Doublet models*, *Eur. Phys. J. C* **82** (2022) 970 [2207.03845].

[184] S. Amoroso et al., *Compatibility and combination of world W-boson mass measurements*, 2308.09417.

[185] W. Grimus, L. Lavoura, O. Ogreid and P. Osland, *A Precision constraint on multi-Higgs-doublet models*, *J. Phys. G* **35** (2008) 075001 [0711.4022].

[186] J. Haller, A. Hoecker, R. Kogler, K. Mönig, T. Peiffer and J. Stelzer, *Update of the global electroweak fit and constraints on two-Higgs-doublet models*, *Eur. Phys. J. C* **78** (2018) 675 [1803.01853].

[187] P. Bechtle, O. Brein, S. Heinemeyer, G. Weiglein and K.E. Williams, *HiggsBounds: Confronting Arbitrary Higgs Sectors with Exclusion Bounds from LEP and the Tevatron*, *Comput. Phys. Commun.* **181** (2010) 138 [0811.4169].

[188] P. Bechtle, O. Brein, S. Heinemeyer, G. Weiglein and K.E. Williams, *HiggsBounds 2.0.0: Confronting Neutral and Charged Higgs Sector Predictions with Exclusion Bounds from LEP and the Tevatron*, *Comput. Phys. Commun.* **182** (2011) 2605 [1102.1898].

[189] P. Bechtle, O. Brein, S. Heinemeyer, O. Stål, T. Stefaniak, G. Weiglein et al., HiggsBounds − 4: *Improved Tests of Extended Higgs Sectors against Exclusion Bounds from LEP, the Tevatron and the LHC*, *Eur. Phys. J. C* **74** (2014) 2693 [1311.0055].

[190] P. Bechtle, D. Dercks, S. Heinemeyer, T. Klingl, T. Stefaniak, G. Weiglein et al., *HiggsBounds-5: Testing Higgs Sectors in the LHC 13 TeV Era*, *Eur. Phys. J. C* **80** (2020) 1211 [2006.06007].

[191] H. Bahl, T. Biekötter, S. Heinemeyer, C. Li, S. Paasch, G. Weiglein et al., *HiggsTools: BSM scalar phenomenology with new versions of HiggsBounds and HiggsSignals*, *Comput. Phys. Commun.* **291** (2023) 108803 [2210.09332].

[192] H. Bahl, V.M. Lozano, T. Stefaniak and J. Wittbrodt, *Testing exotic scalars with HiggsBounds*, *Eur. Phys. J. C* **82** (2022) 584 [2109.10366].

[193] CMS collaboration, *A portrait of the Higgs boson by the CMS experiment ten years after the discovery.*, *Nature* **607** (2022) 60 [2207.00043].

[194] ATLAS collaboration, *A detailed map of Higgs boson interactions by the ATLAS experiment ten years after the discovery*, *Nature* **607** (2022) 52 [2207.00092].

[195] P. Bechtle, S. Heinemeyer, O. Stål, T. Stefaniak and G. Weiglein, *HiggsSignals: Confronting arbitrary Higgs sectors with measurements at the Tevatron and the LHC*, *Eur. Phys. J. C* **74** (2014) 2711 [1305.1933].

[196] P. Bechtle, S. Heinemeyer, O. Stål, T. Stefaniak and G. Weiglein, *Probing the Standard Model with Higgs signal rates from the Tevatron, the LHC and a future ILC*, *JHEP* **11** (2014) 039 [1403.1582].

[197] P. Bechtle, S. Heinemeyer, T. Klingl, T. Stefaniak, G. Weiglein and J. Wittbrodt, *HiggsSignals-2: Probing new physics with precision Higgs measurements in the LHC 13 TeV era*, *Eur. Phys. J. C* **81** (2021) 145 [2012.09197].

[198] D. Eriksson, J. Rathsman and O. Stal, *2HDMC: Two-Higgs-Doublet Model Calculator Physics and Manual*, *Comput. Phys. Commun.* **181** (2010) 189 [0902.0851].

[199] A. Djouadi, J. Kalinowski and M. Spira, *HDECAY: A Program for Higgs boson decays in the standard model and its supersymmetric extension*, *Comput. Phys. Commun.* **108** (1998) 56 [hep-ph/9704448].

[200] HDECAY collaboration, *HDECAY: Twenty$_{++}$ years after*, *Comput. Phys. Commun.* **238** (2019) 214 [1801.09506].

[201] R. Harlander, M. Mühlleitner, J. Rathsman, M. Spira and O. Stål, *Interim recommendations for the evaluation of Higgs production cross sections and branching ratios at the LHC in the Two-Higgs-Doublet Model*, 1312.5571.

[202] T. Enomoto and R. Watanabe, *Flavor constraints on the Two Higgs Doublet Models of Z_2 symmetric and aligned types*, *JHEP* **05** (2016) 002 [1511.05066].

[203] A. Arbey, F. Mahmoudi, O. Stal and T. Stefaniak, *Status of the Charged Higgs Boson in Two Higgs Doublet Models*, *Eur. Phys. J. C* **78** (2018) 182 [1706.07414].

[204] Heavy Flavor Averaging Group, *Rare B Decays*, 2022.

[205] F. Mahmoudi, *SuperIso: A Program for calculating the isospin asymmetry of $B \longrightarrow K^*$ gamma in the MSSM*, *Comput. Phys. Commun.* **178** (2008) 745 [0710.2067].

[206] F. Mahmoudi, *SuperIso v2.3: A Program for calculating flavor physics observables in Supersymmetry*, *Comput. Phys. Commun.* **180** (2009) 1579 [0808.3144].

[207] F. Mahmoudi, *SuperIso v3.0, flavor physics observables calculations: Extension to NMSSM*, *Comput. Phys. Commun.* **180** (2009) 1718.

[208] M. Muhlleitner, M.O.P. Sampaio, R. Santos and J. Wittbrodt, *The N2HDM under Theoretical and Experimental Scrutiny*, *JHEP* **03** (2017) 094 [1612.01309].

[209] K. Enomoto, S. Kanemura and Y. Mura, *Electroweak baryogenesis in aligned two Higgs doublet models*, *JHEP* **01** (2022) 104 [2111.13079].

[210] G.C. Dorsch, S.J. Huber, T. Konstandin and J.M. No, *A Second Higgs Doublet in the Early Universe: Baryogenesis and Gravitational Waves*, *JCAP* **05** (2017) 052 [1611.05874].

[211] P. Basler, M. Krause, M. Muhlleitner, J. Wittbrodt and A. Wlotzka, *Strong First Order Electroweak Phase Transition in the CP-Conserving 2HDM Revisited*, *JHEP* **02** (2017) 121 [1612.04086].

[212] D. Gonçalves, A. Kaladharan and Y. Wu, *Electroweak phase transition in the 2HDM: Collider and gravitational wave complementarity*, *Phys. Rev. D* **105** (2022) 095041 [2108.05356].

[213] G.C. Dorsch, S.J. Huber and J.M. No, *A strong electroweak phase transition in the 2HDM after LHC8*, *JHEP* **10** (2013) 029 [1305.6610].

[214] G.C. Dorsch, S.J. Huber, K. Mimasu and J.M. No, *The Higgs Vacuum Uplifted: Revisiting the Electroweak Phase Transition with a Second Higgs Doublet*, *JHEP* **12** (2017) 086 [1705.09186].

[215] A. Djouadi, W. Kilian, M. Muhlleitner and P.M. Zerwas, *Production of neutral Higgs boson pairs at LHC*, *Eur. Phys. J. C* **10** (1999) 45 [hep-ph/9904287].

[216] J. Baglio, A. Djouadi, R. Gröber, M.M. Mühlleitner, J. Quevillon and M. Spira, *The measurement of the Higgs self-coupling at the LHC: theoretical status*, *JHEP* **04** (2013) 151 [1212.5581].

[217] G. Degrassi, P.P. Giardino, F. Maltoni and D. Pagani, *Probing the Higgs self coupling via single Higgs production at the LHC*, *JHEP* **12** (2016) 080 [1607.04251].

[218] ATLAS collaboration, *Constraints on the Higgs boson self-coupling from single- and double-Higgs production with the ATLAS detector using pp collisions at s=13 TeV*, *Phys. Lett. B* **843** (2023) 137745 [2211.01216].

[219] O.J.P. Eboli, G.C. Marques, S.F. Novaes and A.A. Natale, *TWIN HIGGS BOSON PRODUCTION*, *Phys. Lett. B* **197** (1987) 269.

[220] E.W.N. Glover and J.J. van der Bij, *HIGGS BOSON PAIR PRODUCTION VIA GLUON FUSION*, *Nucl. Phys. B* **309** (1988) 282.

[221] S. Dawson, S. Dittmaier and M. Spira, *Neutral Higgs boson pair production at hadron colliders: QCD corrections*, *Phys. Rev. D* **58** (1998) 115012 [hep-ph/9805244].

[222] S. Borowka, N. Greiner, G. Heinrich, S.P. Jones, M. Kerner, J. Schlenk et al., *Higgs Boson Pair Production in Gluon Fusion at Next-to-Leading Order with Full Top-Quark Mass Dependence*, *Phys. Rev. Lett.* **117** (2016) 012001 [1604.06447].

[223] S. Borowka, N. Greiner, G. Heinrich, S.P. Jones, M. Kerner, J. Schlenk et al., *Full top quark mass dependence in Higgs boson pair production at NLO*, *JHEP* **10** (2016) 107 [1608.04798].

[224] J. Baglio, F. Campanario, S. Glaus, M. Mühlleitner, M. Spira and J. Streicher, *Gluon fusion into Higgs pairs at NLO QCD and the top mass scheme*, *Eur. Phys. J. C* **79** (2019) 459 [1811.05692].

[225] J. Davies, G. Heinrich, S.P. Jones, M. Kerner, G. Mishima, M. Steinhauser et al., *Double Higgs boson production at NLO: combining the exact numerical result and high-energy expansion*, *JHEP* **11** (2019) 024 [1907.06408].

[226] J. Baglio, F. Campanario, S. Glaus, M. Mühlleitner, J. Ronca, M. Spira et al., *Higgs-Pair Production via Gluon Fusion at Hadron Colliders: NLO QCD Corrections*, *JHEP* **04** (2020) 181 [2003.03227].

[227] J. Baglio, F. Campanario, S. Glaus, M. Mühlleitner, J. Ronca and M. Spira, $gg \to HH$: *Combined uncertainties*, *Phys. Rev. D* **103** (2021) 056002 [2008.11626].

[228] J. Alison et al., *Higgs boson potential at colliders: Status and perspectives*, *Rev. Phys.* **5** (2020) 100045 [1910.00012].

[229] *LHC Higgs WG4 group twiki*, *https://twiki.cern.ch/twiki/bin/view/LHCPhysics/LHCHWGHH* .

[230] D. de Florian and J. Mazzitelli, *Higgs Boson Pair Production at Next-to-Next-to-Leading Order in QCD*, *Phys. Rev. Lett.* **111** (2013) 201801 [1309.6594].

[231] J. Grigo, K. Melnikov and M. Steinhauser, *Virtual corrections to Higgs boson pair production in the large top quark mass limit*, *Nucl. Phys. B* **888** (2014) 17 [1408.2422].

[232] J. Davies, F. Herren, G. Mishima and M. Steinhauser, *Real corrections to Higgs boson pair production at NNLO in the large top quark mass limit*, *JHEP* **01** (2022) 049 [2110.03697].

[233] M. Grazzini, G. Heinrich, S. Jones, S. Kallweit, M. Kerner, J.M. Lindert et al., *Higgs boson pair production at NNLO with top quark mass effects*, *JHEP* **05** (2018) 059 [1803.02463].

[234] E. Bagnaschi, G. Degrassi and R. Gröber, *Higgs boson pair production at NLO in the POWHEG approach and the top quark mass uncertainties*, *Eur. Phys. J. C* **83** (2023) 1054 [2309.10525].

[235] H.-Y. Bi, L.-H. Huang, R.-J. Huang, Y.-Q. Ma and H.-M. Yu, *Electroweak Corrections to Double Higgs Production at the LHC*, *Phys. Rev. Lett.* **132** (2024) 231802 [2311.16963].

[236] S. Borowka, C. Duhr, F. Maltoni, D. Pagani, A. Shivaji and X. Zhao, *Probing the scalar potential via double Higgs boson production at hadron colliders*, *JHEP* **04** (2019) 016 [1811.12366].

[237] M. Mühlleitner, J. Schlenk and M. Spira, *Top-Yukawa-induced corrections to Higgs pair production*, *JHEP* **10** (2022) 185 [2207.02524].

[238] J. Davies, G. Mishima, K. Schönwald, M. Steinhauser and H. Zhang, *Higgs boson contribution to the leading two-loop Yukawa corrections to gg → HH*, *JHEP* **08** (2022) 259 [2207.02587].

[239] J. Davies, K. Schönwald, M. Steinhauser and H. Zhang, *Next-to-leading order electroweak corrections to $gg \to HH$ and $gg \to gH$ in the large-m_t limit*, *JHEP* **10** (2023) 033 [2308.01355].

[240] G. Heinrich, S. Jones, M. Kerner, T. Stone and A. Vestner, *Electroweak corrections to Higgs boson pair production: the top-Yukawa and self-coupling contributions*, *JHEP* **11** (2024) 040 [2407.04653].

[241] T. Plehn, M. Spira and P.M. Zerwas, *Pair production of neutral Higgs particles in gluon-gluon collisions*, *Nucl. Phys. B* **479** (1996) 46 [hep-ph/9603205].

[242] D.T. Nhung, M. Muhlleitner, J. Streicher and K. Walz, *Higher Order Corrections to the Trilinear Higgs Self-Couplings in the Real NMSSM*, *JHEP* **11** (2013) 181 [1306.3926].

[243] C. Borschensky, T.N. Dao, M. Gabelmann, M. Mühlleitner and H. Rzehak, *The trilinear Higgs self-couplings at $\mathcal{O}(\alpha_t^2)$ in the CP-violating NMSSM*, *Eur. Phys. J. C* **83** (2023) 118 [2210.02104].

[244] H. Abouabid, A. Arhrib, D. Azevedo, J.E. Falaki, P.M. Ferreira, M. Mühlleitner et al., *Benchmarking di-Higgs production in various extended Higgs sector models*, *JHEP* **09** (2022) 011 [2112.12515].

[245] A. Buckley, J. Ferrando, S. Lloyd, K. Nordström, B. Page, M. Rüfenacht et al., *LHAPDF6: parton density access in the LHC precision era*, *Eur. Phys. J. C* **75** (2015) 132 [1412.7420].

[246] J.R. Andersen et al., *Les Houches 2013: Physics at TeV Colliders: Standard Model Working Group Report*, 1405.1067.

[247] S. Dulat, T.-J. Hou, J. Gao, M. Guzzi, J. Huston, P. Nadolsky et al., *New parton distribution functions from a global analysis of quantum chromodynamics*, *Phys. Rev. D* **93** (2016) 033006 [1506.07443].

[248] CMS collaboration, *Constraints on the Higgs Boson Width from Off-Shell Production and Decay to Z-Boson Pairs*, *Phys. Lett. B* **736** (2014) 64 [1405.3455].

[249] M. Cepeda et al., *Report from Working Group 2: Higgs Physics at the HL-LHC and HE-LHC*, *CERN Yellow Rep. Monogr.* **7** (2019) 221 [1902.00134].

[250] R. Grober, M. Muhlleitner and M. Spira, *Higgs Pair Production at NLO QCD for CP-violating Higgs Sectors*, *Nucl. Phys. B* **925** (2017) 1 [1705.05314].

[251] J. Baglio, F. Campanario, S. Glaus, M. Mühlleitner, J. Ronca and M. Spira, *Full NLO QCD predictions for Higgs-pair production in the 2-Higgs-doublet model*, *Eur. Phys. J. C* **83** (2023) 826 [2303.05409].

[252] M. Capozi and G. Heinrich, *Exploring anomalous couplings in Higgs boson pair production through shape analysis*, *JHEP* **03** (2020) 091 [1908.08923].

[253] F. Arco, S. Heinemeyer and M.J. Herrero, *Triple Higgs couplings in the 2HDM: the complete picture*, *Eur. Phys. J. C* **82** (2022) 536 [2203.12684].

[254] F. Arco, S. Heinemeyer and M.J. Herrero, *Sensitivity to triple Higgs couplings via di-Higgs production in the 2HDM at e^+e^- colliders*, *Eur. Phys. J. C* **81** (2021) 913 [2106.11105].

[255] CMS collaboration, *Search for heavy Higgs bosons decaying to a top quark pair in proton-proton collisions at $\sqrt{s} = 13$ TeV*, *JHEP* **04** (2020) 171 [1908.01115].

[256] G. Buchalla, M. Capozi, A. Celis, G. Heinrich and L. Scyboz, *Higgs boson pair production in non-linear Effective Field Theory with full m_t-dependence at NLO QCD*, *JHEP* **09** (2018) 057 [1806.05162].

[257] P. Bechtle, S. Heinemeyer, O. Stal, T. Stefaniak and G. Weiglein, *Applying Exclusion Likelihoods from LHC Searches to Extended Higgs Sectors*, *Eur. Phys. J. C* **75** (2015) 421 [1507.06706].

[258] ATLAS collaboration, *Search for resonant and non-resonant higgs boson pair production in the $b\bar{b}\tau^+\tau^-$ decay channel using 13 tev pp collision data from the atlas detector*, *JHEP* **07** (2023) 040 [2209.10910].

[259] M. Krause, *On the Renormalization of the Two-Higgs-Doublet Model*, Master's thesis, KIT, Karlsruhe, TP, 2016.

[260] R. Mertig, M. Böhm and A. Denner, *Feyn calc - computer-algebraic calculation of feynman amplitudes*, *Computer Physics Communications* **64** (1991) 345.

[261] V. Shtabovenko, R. Mertig and F. Orellana, *New Developments in FeynCalc 9.0*, *Comput. Phys. Commun.* **207** (2016) 432 [1601.01167].

[262] T. Hahn, *Generating Feynman diagrams and amplitudes with FeynArts 3*, *Comput. Phys. Commun.* **140** (2001) 418 [hep-ph/0012260].

[263] T. Hahn and M. Perez-Victoria, *Automatized one loop calculations in four-dimensions and D-dimensions*, *Comput. Phys. Commun.* **118** (1999) 153 [hep-ph/9807565].

[264] T. Hahn, *Automatic loop calculations with FeynArts, FormCalc, and LoopTools*, *Nucl. Phys. B Proc. Suppl.* **89** (2000) 231 [hep-ph/0005029].

[265] S. Amoroso et al., *Les Houches 2019: Physics at TeV Colliders: Standard Model Working Group Report*, in *11th Les Houches Workshop on Physics at TeV Colliders: PhysTeV Les Houches*, 3, 2020 [2003.01700].

[266] G. Heinrich, J. Lang and L. Scyboz, *SMEFT predictions for $gg \rightarrow hh$ at full NLO QCD and truncation uncertainties*, *JHEP* **08** (2022) 079 [2204.13045].

[267] L. Alasfar et al., *Effective Field Theory descriptions of Higgs boson pair production*, *SciPost Phys. Comm. Rep.* **2024** (2024) 2 [2304.01968].

[268] R.V. Harlander, S. Liebler and H. Mantler, *SusHi: A program for the calculation of Higgs production in gluon fusion and bottom-quark annihilation in the Standard Model and the MSSM*, *Comput. Phys. Commun.* **184** (2013) 1605 [1212.3249].

[269] R.V. Harlander, S. Liebler and H. Mantler, *SusHi Bento: Beyond NNLO and the heavy-top limit*, *Comput. Phys. Commun.* **212** (2017) 239 [1605.03190].

[270] CMS collaboration, *Search for Higgs boson pair production in the $\gamma\gamma b\overline{b}$ final state in pp collisions at $\sqrt{s} = 13$ TeV*, *Phys. Lett. B* **788** (2019) 7 [1806.00408].

[271] ATLAS collaboration, *Search for Higgs boson pair production in the two bottom quarks plus two photons final state in pp collisions at $\sqrt{s} = 13$ TeV with the ATLAS detector*, *Phys. Rev. D* **106** (2022) 052001 [2112.11876].

[272] ATLAS collaboration, *Search for resonant pair production of Higgs bosons in the $b\overline{b}b\overline{b}$ final state using pp collisions at $\sqrt{s} = 13$ TeV with the ATLAS detector*, *Phys. Rev. D* **105** (2022) 092002 [2202.07288].

[273] ATLAS collaboration, *Combination of Searches for Resonant Higgs Boson Pair Production Using pp Collisions at s=13 TeV with the ATLAS Detector*, *Phys. Rev. Lett.* **132** (2024) 231801 [2311.15956].

[274] CMS collaboration, *Searches for Higgs boson production through decays of heavy resonances*, *Phys. Rept.* **1115** (2025) 368 [2403.16926].

[275] CMS collaboration, *Search for resonant pair production of Higgs bosons in the $b\overline{b}b\overline{b}$ final state using large-area jets in proton-proton collisions at $\sqrt{s} = 13$ TeV*, *JHEP* **02** (2025) 040 [2407.13872].

[276] CMS collaboration, *Search for a heavy pseudoscalar boson decaying to a Z and a Higgs boson at $\sqrt{s} = 13$ TeV*, *Eur. Phys. J. C* **79** (2019) 564 [1903.00941].

[277] ATLAS collaboration, *Search for heavy resonances decaying into a Z or W boson and a Higgs boson in final states with leptons and b-jets in 139 fb^{-1} of pp collisions at $\sqrt{s} = 13$ TeV with the ATLAS detector*, *JHEP* **06** (2023) 016 [2207.00230].

[278] ATLAS collaboration, *Search for charged Higgs bosons decaying into a top quark and a bottom quark at $\sqrt{s} = 13$ TeV with the ATLAS detector*, *JHEP* **06** (2021) 145 [2102.10076].

[279] CMS collaboration, *Searches for additional Higgs bosons and for vector leptoquarks in $\tau\tau$ final states in proton-proton collisions at $\sqrt{s} = 13$ TeV*, *JHEP* **07** (2023) 073 [2208.02717].

[280] ATLAS collaboration, *Search for heavy Higgs bosons decaying into two tau leptons with the ATLAS detector using pp collisions at $\sqrt{s} = 13$ TeV*, *Phys. Rev. Lett.* **125** (2020) 051801 [2002.12223].

[281] ATLAS collaboration, *Search for a heavy Higgs boson decaying into a Z boson and another heavy Higgs boson in the $\ell\ell bb$ and $\ell\ell WW$ final states in pp collisions at $\sqrt{s} = 13$ TeV with the ATLAS detector*, *Eur. Phys. J. C* **81** (2021) 396 [2011.05639].

[282] T. Plehn, A. Butter, B. Dillon, T. Heimel, C. Krause and R. Winterhalder, *Modern Machine Learning for LHC Physicists*, 2211.01421.

[283] M. Feickert and B. Nachman, *A Living Review of Machine Learning for Particle Physics*, 2102.02770.

[284] M. Abdughani, J. Ren, L. Wu, J.M. Yang and J. Zhao, *Supervised deep learning in high energy phenomenology: a mini review*, *Commun. Theor. Phys.* **71** (2019) 955 [1905.06047].

[285] F. Arco, S. Heinemeyer and M.J. Herrero, *Sensitivity and constraints to the 2HDM soft-breaking Z_2 parameter m_{12}*, *Phys. Lett. B* **835** (2022) 137548 [2207.13501].

[286] A. Lenzi, J. Bessac, J. Rudi and M.L. Stein, *Neural networks for parameter estimation in intractable models*, 2021.

[287] A. Paszke, S. Gross, F. Massa, A. Lerer, J. Bradbury, G. Chanan et al., *Pytorch: An imperative style, high-performance deep learning library*, 2019.

[288] M. Quiros, *Finite temperature field theory and phase transitions*, in *ICTP Summer School in High-Energy Physics and Cosmology*, pp. 187–259, 1, 1999 [hep-ph/9901312].

[289] P.B. Arnold and O. Espinosa, *The Effective potential and first order phase transitions: Beyond leading-order*, *Phys. Rev. D* **47** (1993) 3546 [hep-ph/9212235].

[290] D. Curtin, P. Meade and H. Ramani, *Thermal Resummation and Phase Transitions*, *Eur. Phys. J. C* **78** (2018) 787 [1612.00466].

[291] D. Croon, O. Gould, P. Schicho, T.V.I. Tenkanen and G. White, *Theoretical uncertainties for cosmological first-order phase transitions*, *JHEP* **04** (2021) 055 [2009.10080].

[292] O. Gould and T.V.I. Tenkanen, *On the perturbative expansion at high temperature and implications for cosmological phase transitions*, *JHEP* **06** (2021) 069 [2104.04399].

[293] O. Gould and T.V.I. Tenkanen, *Perturbative effective field theory expansions for cosmological phase transitions*, 2309.01672.

[294] C.L. Wainwright, *CosmoTransitions: Computing Cosmological Phase Transition Temperatures and Bubble Profiles with Multiple Fields*, *Comput. Phys. Commun.* **183** (2012) 2006 [1109.4189].

[295] T. Biekötter, S. Heinemeyer, J.M. No, M.O. Olea and G. Weiglein, *Fate of electroweak symmetry in the early Universe: Non-restoration and trapped vacua in the N2HDM*, *JCAP* **06** (2021) 018 [2103.12707].

[296] A.D. Linde, *Fate of the False Vacuum at Finite Temperature: Theory and Applications*, *Phys. Lett. B* **100** (1981) 37.

[297] S. Baum, M. Carena, N.R. Shah, C.E.M. Wagner and Y. Wang, *Nucleation is more than critical: A case study of the electroweak phase transition in the NMSSM*, *JHEP* **03** (2021) 055 [2009.10743].

[298] M.O. Olea Romacho, *Higgs physics as a window to the electroweak epoch*, Ph.D. thesis, U. Hamburg (main), Hamburg U., 2022.

[299] M. Carena, C. Krause, Z. Liu and Y. Wang, *New approach to electroweak symmetry nonrestoration*, *Phys. Rev. D* **104** (2021) 055016 [2104.00638].

[300] P. Meade and H. Ramani, *Unrestored Electroweak Symmetry*, *Phys. Rev. Lett.* **122** (2019) 041802 [1807.07578].

[301] I. Baldes and G. Servant, *High scale electroweak phase transition: baryogenesis \& symmetry non-restoration*, *JHEP* **10** (2018) 053 [1807.08770].

[302] O. Matsedonskyi and G. Servant, *High-Temperature Electroweak Symmetry Non-Restoration from New Fermions and Implications for Baryogenesis*, *JHEP* **09** (2020) 012 [2002.05174].

[303] A. Glioti, R. Rattazzi and L. Vecchi, *Electroweak Baryogenesis above the Electroweak Scale*, *JHEP* **04** (2019) 027 [1811.11740].

[304] D. Bodeker and W. Buchmuller, *Baryogenesis from the weak scale to the grand unification scale*, *Rev. Mod. Phys.* **93** (2021) 035004 [2009.07294].

[305] J.A. Harvey, E.W. Kolb, D.B. Reiss and S. Wolfram, *Calculation of Cosmological Baryon Asymmetry in Grand Unified Gauge Models*, *Nucl. Phys. B* **201** (1982) 16.

[306] S. Weinberg, *Cosmological production of baryons*, *Phys. Rev. Lett.* **42** (1979) 850.

[307] D.V. Nanopoulos and S. Weinberg, *Mechanisms for cosmological baryon production*, *Phys. Rev. D* **20** (1979) 2484.

[308] A.Y. Ignatiev, N.V. Krasnikov, V.A. Kuzmin and A.N. Tavkhelidze, *Universal CP Noninvariant Superweak Interaction and Baryon Asymmetry of the Universe*, *Phys. Lett. B* **76** (1978) 436.

[309] M. Yoshimura, *Origin of cosmological baryon asymmetry*, *Physics Letters B* **88** (1979) 294.

[310] G.C. Dorsch, S.J. Huber, K. Mimasu and J.M. No, *Echoes of the Electroweak Phase Transition: Discovering a second Higgs doublet through $A_0 \to ZH_0$*, *Phys. Rev. Lett.* **113** (2014) 211802 [1405.5537].

[311] ATLAS collaboration, *Search for a CP-odd Higgs boson decaying into a heavy CP-even Higgs boson and a Z boson in the $\ell^+\ell^- t\bar{t}$ and $\nu\bar{\nu}b\bar{b}$ final states using 140 fb^{-1} of data collected with the ATLAS detector*, *JHEP* **02** (2024) 197 [2311.04033].

[312] ATLAS collaboration, *Search for a heavy Higgs boson decaying into a Z boson and another heavy Higgs boson in the $\ell\ell bb$ final state in pp collisions at $\sqrt{s} = 13$ TeV with the ATLAS detector*, *Phys. Lett. B* **783** (2018) 392 [1804.01126].

[313] CMS collaboration, *Search for neutral resonances decaying into a Z boson and a pair of b jets or τ leptons*, *Phys. Lett. B* **759** (2016) 369 [1603.02991].

[314] CMS collaboration, *Search for heavy neutral Higgs bosons A and H in the t̄tZ channel in proton-proton collisions at 13 TeV*, 2412.00570.

[315] CMS collaboration, *Search for charged Higgs bosons decaying into a top and a bottom quark in the all-jet final state of pp collisions at $\sqrt{s}$ = 13 TeV*, *JHEP* **07** (2020) 126 [2001.07763].

[316] CMS collaboration, *Search for a charged Higgs boson decaying into a heavy neutral Higgs boson and a W boson in proton-proton collisions at $\sqrt{s}$ = 13 TeV*, *JHEP* **09** (2023) 032 [2207.01046].

[317] CMS collaboration, *Observation of four top quark production in proton-proton collisions at s=13TeV*, *Phys. Lett. B* **847** (2023) 138290 [2305.13439].

[318] ATLAS collaboration, *Observation of four-top-quark production in the multilepton final state with the ATLAS detector*, *Eur. Phys. J. C* **83** (2023) 496 [2303.15061].

[319] S. Gori, I.-W. Kim, N.R. Shah and K.M. Zurek, *Closing the Wedge: Search Strategies for Extended Higgs Sectors with Heavy Flavor Final States*, *Phys. Rev. D* **93** (2016) 075038 [1602.02782].

[320] CMS collaboration, *Search for new neutral Higgs bosons through the H→ ZA → $\ell^+\ell^-$b̄b process in pp collisions at $\sqrt{s}$ = 13 TeV*, *JHEP* **03** (2020) 055 [1911.03781].

[321] CMS collaboration, *Search for dilepton resonances from decays of (pseudo)scalar bosons produced in association with a massive vector boson or top quark anti-top quark pair at $\sqrt{s}$ = 13 TeV*, Tech. Rep. CMS-PAS-EXO-21-018 (2022).

[322] ATLAS collaboration, *Search for heavy neutral Higgs bosons produced in association with b-quarks and decaying into b-quarks at $\sqrt{s}$ = 13 TeV with the ATLAS detector*, *Phys. Rev. D* **102** (2020) 032004 [1907.02749].

[323] ATLAS collaboration, *Search for low-mass resonances decaying into two jets and produced in association with a photon using pp collisions at $\sqrt{s}$ = 13 TeV with the ATLAS detector*, *Phys. Lett. B* **795** (2019) 56 [1901.10917].

[324] K. Kainulainen, V. Keus, L. Niemi, K. Rummukainen, T.V.I. Tenkanen and V. Vaskonen, *On the validity of perturbative studies of the electroweak phase transition in the Two Higgs Doublet model*, *JHEP* **06** (2019) 075 [1904.01329].

[325] A. Ekstedt, P. Schicho and T.V.I. Tenkanen, *DRalgo: A package for effective field theory approach for thermal phase transitions*, *Comput. Phys. Commun.* **288** (2023) 108725 [2205.08815].

[326] L. Niemi, M.J. Ramsey-Musolf, T.V.I. Tenkanen and D.J. Weir, *Thermodynamics of a Two-Step Electroweak Phase Transition*, *Phys. Rev. Lett.* **126** (2021) 171802 [2005.11332].

[327] P.M. Schicho, T.V.I. Tenkanen and J. Österman, *Robust approach to thermal resummation: Standard Model meets a singlet*, *JHEP* **06** (2021) 130 [2102.11145].

[328] P. Schicho, T.V.I. Tenkanen and G. White, *Combining thermal resummation and gauge invariance for electroweak phase transition*, *JHEP* **11** (2022) 047 [2203.04284].

[329] F. Arco, S. Heinemeyer and M. Mühlleitner, *Large One-Loop Effects of BSM Triple Higgs Couplings on Double Higgs Production at e^+e^- Colliders*, 2505.02947.

[330] J.M. Torndal and J. List, *Higgs self-coupling measurement at the International Linear Collider*, in *International Workshop on Future Linear Colliders*, 7, 2023 [2307.16515].

[331] E. Witten, *Cosmic Separation of Phases*, *Phys. Rev. D* **30** (1984) 272.

[332] C.J. Hogan, *Gravitational radiation from cosmological phase transitions*, *Mon. Not. Roy. Astron. Soc.* **218** (1986) 629.

[333] LISA collaboration, *Laser Interferometer Space Antenna*, 1702.00786.

[334] M. Hindmarsh, S.J. Huber, K. Rummukainen and D.J. Weir, *Gravitational waves from the sound of a first order phase transition*, *Phys. Rev. Lett.* **112** (2014) 041301 [1304.2433].

[335] M. Hindmarsh, S.J. Huber, K. Rummukainen and D.J. Weir, *Numerical simulations of acoustically generated gravitational waves at a first order phase transition*, *Phys. Rev. D* **92** (2015) 123009 [1504.03291].

[336] M. Hindmarsh, *Sound shell model for acoustic gravitational wave production at a first-order phase transition in the early Universe*, *Phys. Rev. Lett.* **120** (2018) 071301 [1608.04735].

[337] M. Hindmarsh, S.J. Huber, K. Rummukainen and D.J. Weir, *Shape of the acoustic gravitational wave power spectrum from a first order phase transition*, *Phys. Rev. D* **96** (2017) 103520 [1704.05871].

[338] C. Caprini and R. Durrer, *Gravitational waves from stochastic relativistic sources: Primordial turbulence and magnetic fields*, *Phys. Rev. D* **74** (2006) 063521 [astro-ph/0603476].

[339] G. Gogoberidze, T. Kahniashvili and A. Kosowsky, *The Spectrum of Gravitational Radiation from Primordial Turbulence*, *Phys. Rev. D* **76** (2007) 083002 [0705.1733].

[340] C. Caprini, R. Durrer and G. Servant, *The stochastic gravitational wave background from turbulence and magnetic fields generated by a first-order phase transition*, *JCAP* **12** (2009) 024 [0909.0622].

[341] A. Roper Pol, S. Mandal, A. Brandenburg, T. Kahniashvili and A. Kosowsky, *Numerical simulations of gravitational waves from early-universe turbulence*, *Phys. Rev. D* **102** (2020) 083512 [1903.08585].

[342] P. Auclair, C. Caprini, D. Cutting, M. Hindmarsh, K. Rummukainen, D.A. Steer et al., *Generation of gravitational waves from freely decaying turbulence*, *JCAP* **09** (2022) 029 [2205.02588].

[343] C. Caprini et al., *Detecting gravitational waves from cosmological phase transitions with LISA: an update*, *JCAP* **03** (2020) 024 [1910.13125].

[344] J. Ellis, M. Lewicki and J.M. No, *On the Maximal Strength of a First-Order Electroweak Phase Transition and its Gravitational Wave Signal*, *JCAP* **04** (2019) 003 [1809.08242].

[345] B. Laurent and J.M. Cline, *Fluid equations for fast-moving electroweak bubble walls*, *Phys. Rev. D* **102** (2020) 063516 [2007.10935].

[346] W.-Y. Ai, B. Laurent and J. van de Vis, *Model-independent bubble wall velocities in local thermal equilibrium*, *JCAP* **07** (2023) 002 [2303.10171].

[347] G.C. Dorsch, S.J. Huber and T. Konstandin, *Bubble wall velocities in the Standard Model and beyond*, *JCAP* **12** (2018) 034 [1809.04907].

[348] LISA collaboration, *Science Requirements Document*, *https://www.cosmos.esa.int/web/lisa/lisa-documents*, Tech. Rep. ESA-L3-EST-SCI-RS-001 (2018).

[349] AEDGE collaboration, *AEDGE: Atomic Experiment for Dark Matter and Gravity Exploration in Space*, *EPJ Quant. Technol.* **7** (2020) 6 [1908.00802].

[350] S. Kawamura et al., *The Japanese space gravitational wave antenna: DECIGO*, *Class. Quant. Grav.* **28** (2011) 094011.

[351] S. Kawamura et al., *Current status of space gravitational wave antenna DECIGO and B-DECIGO*, *PTEP* **2021** (2021) 05A105 [2006.13545].

[352] V. Corbin and N.J. Cornish, *Detecting the cosmic gravitational wave background with the big bang observer*, *Class. Quant. Grav.* **23** (2006) 2435 [gr-qc/0512039].

[353] E. Di Valentino, S. Gariazzo and O. Mena, *Most constraining cosmological neutrino mass bounds*, *Phys. Rev. D* **104** (2021) 083504 [2106.15267].

[354] M. Laine and A. Vuorinen, *Basics of Thermal Field Theory*, vol. 925, Springer (2016), 10.1007/978-3-319-31933-9, [1701.01554].

[355] M. Laine, M. Meyer and G. Nardini, *Thermal phase transition with full 2-loop effective potential*, *Nucl. Phys. B* **920** (2017) 565 [1702.07479].

[356] M. Garny and T. Konstandin, *On the gauge dependence of vacuum transitions at finite temperature*, *JHEP* **07** (2012) 189 [1205.3392].

[357] H.H. Patel and M.J. Ramsey-Musolf, *Baryon Washout, Electroweak Phase Transition, and Perturbation Theory*, *JHEP* **07** (2011) 029 [1101.4665].

[358] N.K. Nielsen, *On the Gauge Dependence of Spontaneous Symmetry Breaking in Gauge Theories*, *Nucl. Phys. B* **101** (1975) 173.

[359] M.E. Shaposhnikov, *Finite temperature effective theories*, *Subnucl. Ser.* **34** (1997) 360 [hep-ph/9610247].

[360] R.R. Parwani, *Resummation in a hot scalar field theory*, *Phys. Rev. D* **45** (1992) 4695 [`hep-ph/9204216`].

[361] C.G. Boyd, D.E. Brahm and S.D.H. Hsu, *Resummation methods at finite temperature: The Tadpole way*, *Phys. Rev. D* **48** (1993) 4963 [`hep-ph/9304254`].

[362] H. Bahl, M. Carena, A. Ireland and C.E.M. Wagner, *Improved thermal resummation for multi-field potentials*, *JHEP* **09** (2024) 153 [`2404.12439`].